

University of South Wales



2059231

 *Bound by*
Abbey
Bookbinding Co.
105 Cathays Terrace, Cardiff CF24 4HU
South Wales, U.K. Tel: (029) 2039 5882
www.bookbindersuk.com

IMPROVING THE PERFORMANCE OF AEROFOIL SECTIONS USING MOMENTUM TRANSFER VIA A SECONDARY FLOW

Oliver Breitfeld

A submission presented in partial fulfilment of the requirements of the
University of Glamorgan/Prifysgol Morgannwg for the degree of
Doctor of Philosophy

June 2002

Declaration

This is to certify that this thesis has not been presented, or is not currently submitted for any degree other than the degree of Doctor of Philosophy at the University of Glamorgan.

Signed

Oliver Breitfeld

Candidate.

Certificate of Research

This is to certify that, except where specific reference is made, the work described in this thesis is original work, and is the work of the candidate.

Signed

Oliver Breitfeld

Candidate.

Signed

[Signature]

Director of Studies.

Date

20.06.02

To my family
for their encouragement
and support.

Acknowledgements

I would like to thank my director of studies, Dr. Talal Maksoud, and my second supervisors Prof. John Ward and Dr. Mike Wilson, for their supervision during the course of this PhD. Without their guidance and expertise this work would not have been completed.

Special thanks to all the members of staff who were involved in the project. I wish to express sincere thanks to Gwyn Jenkins and Mike Williams who made the excellent construction of the experimental set up for this project possible. Thanks are also due to the University of Bath for the use their wind tunnel facilities which enabled me to undertake the experimental measurements.

My thanks go to Dr. Hans-Gerhard Groß for his advice and discussion on genetic algorithms and computing issues. I would also like to thank Dr. Sara Correia for fruitful discussions on computational fluid dynamics.

Finally, I would like to thank my parents, my brother and my friends. Special thanks to Dr. Elizabeth Wild who supported me throughout this project.

Abstract

Aerodynamic flow control can improve aerofoil performance by influencing the natural growth of boundary layers, which develop on the surface of vehicles moving in viscous fluids. Many active and passive techniques have been developed to reduce drag and/or increase the lift of aerofoil sections.

The work presented in this thesis is concerned with the active excitation of the boundary layer on the suction side of aerofoil sections through momentum transfer via a secondary flow. The secondary flow was achieved by air passing through an air breathing device (ABD) which was implemented in the aerofoil surface. This resulted in an almost tangential and uni-directional fluid interaction. Numerical and experimental work showed a beneficial influence of the secondary flow on the aerodynamic characteristics of the studied aerofoil sections.

A Taguchi analysis was initially used to confirm findings from previous work on the use of an ABD on a NACA0012 aerofoil section. The resulting parameter ranking showed general agreement with previous data in that the most important parameters are the gap-size i.e. the length over which the two fluids are in contact and the velocity gradient between the two fluids.

However, it also raised questions that required an additional in-depth analysis of the parameters governing the flow control process. Due to the greater importance to the modern aviation industry of the NACA65-415 aerofoil section this particular cambered aerofoil section was used for further investigations. This study highlighted the importance of the velocity gradient between the main and secondary flows as well as the location of interaction of the ABD. In addition the gap-size is also important. Consideration of the power requirements for the ABD indicated that this may limit exploitation of the device.

An evolutionary search strategy based on genetic algorithms, was employed to optimise the air breathing geometry. This optimisation produced non-intuitive geometries which revealed the importance of promoting an inner fluid recirculation in the device.

Finally experimental data in a closed loop wind-tunnel showed trends which were in general agreement with the numerical predictions. However, the measurements indicated significantly greater enhancements of lift forces than those predicted by the numerical investigation.

Contents

Contents	i
List of Figures	iv
List of Tables	ix
Nomenclature	xi
1 Introduction	1
2 Flow Control	4
2.1 The Governing Equations	4
2.2 Boundary Layer Concepts	6
2.3 Flow Control	9
2.3.1 Reduction of Laminar Skin Friction	10
2.3.2 Transition Delay	11
2.3.3 Turbulent Drag Reduction	13
2.3.4 Separation Control	14
2.3.5 Interrelation of Flow Control Techniques	14
2.3.6 Momentum Transfer	16
3 The Application of Computational Fluid Dynamics to Determine the Aerodynamic Characteristics of Aerofoil Sections	23
3.1 Solution Procedure for the Control Volume Method	25
3.2 Model Validation	32
3.2.1 Computational Set-Up	33

3.2.2	Validation of the Computations for a Smooth Aerofoil Section . . .	38
4	CFD Study	45
4.1	Representation of the Aerofoil Section with an ABD	45
4.2	Taguchi Analysis	47
4.2.1	Taguchi Analysis of the Momentum Transfer by means of an ABD	48
4.2.2	Validation of the Taguchi Analysis	52
4.3	Parametric Study of an ABD on a NACA65-415 Aerofoil Section	55
4.3.1	Impact of the Parameters on the Aerodynamic Characteristics of the Aerofoil Section	56
4.3.2	Impact of the ABD on the Near Wall Flow	65
4.3.3	Impact on the Pressure Distribution	72
4.3.4	Flow Visualisation	76
4.3.5	Effect of the ABD Power Consumption on the overall Improve- ment in Aerodynamic Characteristics of the Aerofoil Section . .	77
4.3.6	Notes on the CFD Set-Up	83
4.3.7	Discussion	85
5	Optimisation of the ABD by Genetic Algorithms and CFD	88
5.1	Genetic Algorithms	88
5.2	Optimisation	92
5.2.1	Structure and Set-Up	92
5.2.2	Results	99
5.2.3	Discussion	109
6	Wind Tunnel Experiments	110
6.1	The Wind Tunnel	110
6.2	Construction of the Aerofoil Section	111
6.3	Aerodynamic Characteristics of the Aerofoil	117
6.3.1	The Smooth Aerofoil Section	119
6.3.2	Effect of the ABD on the Aerofoil Performance	120
6.4	Pressure Distributions	123

6.4.1	Installation of the Pressure Transducers	124
6.4.2	Validation of the Pressure Measurements	125
6.4.3	Effects of the ABD on the Pressure Distributions	127
6.5	Flow Visualisation	136
6.6	Power Requirements	141
6.7	Discussion	142
7	Conclusions and Recommendations for Further Work	145
7.1	Conclusions	145
7.2	Recommendations for Further Work	148
	Bibliography	150
A	CFD	156
A.1	Differencing Schemes	156
A.2	Specification of Grid Types	159
A.3	Grid Geometric Propagation Formulae	160
A.4	Command File	161
B	Experimental Details	162
B.1	ABD Velocity Distribution	162
B.2	Details of the Force Balance System	163
B.3	Correction Procedure for the Force Balance System	165
B.4	Pressure Transducer CTQH-187	166
B.4.1	Calibration	166
B.5	A/D-Card	167
B.6	Pressure Distributions for various Angles of Attack ($Re = 1.02 \times 10^6$) .	167

List of Figures

2.1	Boundary Layer Development on an Aerofoil Suction Side	8
2.2	Aerofoil Performance as a Function of the Chord Reynolds-number [8] .	9
2.3	Interrelation between Flow Control Goals	15
2.4	Arrangements for MSBC	17
2.5	Principle of the ABD	18
3.1	Node Notation	26
3.2	Mesh on the NACA0012 Aerofoil Section at 0° Angle of Attack	34
3.3	Mesh on the NACA65-415 Aerofoil Section at 12° Angle of Attack . .	35
3.4	Validation of the Drag Coefficient for the NACA 0012 Aerofoil Section	40
3.5	Validation of the Lift Coefficient for the NACA 0012 Aerofoil Section .	41
3.6	Validation of the Drag Coefficient for the NACA 65-415 Aerofoil Section	42
3.7	Validation of the Lift Coefficient for the NACA 65-415 Aerofoil Section	43
4.1	Curved ABD Shape with Multi-block Topology	46
4.2	Geometric ABD Parameter	49
4.3	Percentage Variation versus Angle of Attack	56
4.4	Improvements in Aerodynamic Characteristics versus Angle of Attack .	57
4.5	Wake U-Velocity Distribution with and without Flow Control	58
4.6	The Effects of the ABD Location on the Aerodynamic Characteristics	59
4.7	The Effect of the ABD Gap-Size on the Aerodynamic Characteristics .	60
4.8	The Effects of the Injection Coefficient, C_i , on the Aerodynamic Char- acteristics	61
4.9	Geometry and Grid for a Curved ABD with $R = 5\%$ Chord	62

4.10 The Effect of the Radius of Curvature of the ABD on the Aerodynamic Characteristics	62
4.11 The Effect of the Chord Reynolds-number on the Aerodynamic Characteristics	64
4.12 The Effects of the ABD Depth on the Aerodynamic Characteristics . .	64
4.13 Percentage Variation of C_D , C_L and L/D with increasing Chord Length at $Re = 3.4 \times 10^6$	65
4.14 Impact of the Gap-Size on the Near Wall Velocity Profile	67
4.15 Impact of C_i on the Near Wall Velocity Profile	68
4.16 Impact of the Shape on the Near Wall Velocity Profile	69
4.17 Velocity Distribution at the ABD Trailing Edge for Different ABD Locations	70
4.18 Variation of Total Pressure at a) 50% and b) 70% Chord for the Base Parameter Set and $C_i=2.5$. The ABD is located at 60% Chord	71
4.19 Variation of the Pressure Gradient $[dp/dx_1]$ between the Smooth Aerofoil and with an ABD with C_i of 2.5	71
4.20 Effect of C_i on the Pressure Distribution	72
4.21 Local Effect of C_i on the Pressure Distribution	73
4.22 Effect of the Gap-Size on the Pressure Distribution	74
4.23 Local Effect of the Gap-Size on the Pressure Distribution	75
4.24 Effect of the Injection and Suction Angle on the Pressure Distribution	75
4.25 Local Effect of the Injection and Suction Angle on the Pressure Distribution	76
4.26 Velocity Vector at the location of flow control for a Curved and Parallel ABD Arrangement	77
4.27 Shaded Velocity Contours at the location of flow control	77
4.28 Impact of the Angle of Attack on the Effective ABD Performance . . .	79
4.29 Impact of the ABD Location on the Effective ABD Performance . . .	80
4.30 Impact of the Gap-Size on the Effective ABD Performance	81
4.31 Impact of C_i on the Effective Performance	81
4.32 Impact of the Reynolds-number on the Effective ABD Performance . .	82

4.33	Impact of the ABD Depth on the Effective ABD Performance	83
5.1	Resulting Aerofoil Shape due to GA Optimisation [48]	91
5.2	a) Straight Micropump before Optimisation and b) Micropump after Optimisation [44]	92
5.3	Example for Single Point Cross-over	93
5.4	Example for Single Point Flip Mutation	93
5.5	Flow Charts for the Genetic Algorithm	94
5.6	Flow Charts for the Fitness Function	95
5.7	Principle Structure for Creation of an Optimal ABD by GAs	96
5.8	Coarse Grid around NACA65-415 Aerofoil Section for GA optimisation	97
5.9	a) Convergence of the Averaged Fitness, C_D , C_L and Δp , and b) Con- vergence of Fitness for Evolution 1.1	100
5.10	a) Convergence of the Averaged Fitness, C_D , C_L and Δp , and b) Con- vergence of Fitness for Evolution 1.2	101
5.11	a) Convergence of the Averaged Fitness, C_D , C_L and Δp , and b) Con- vergence of Fitness for Evolution 1.3	102
5.12	Best Individual Case of Evolution 1.1	103
5.13	Best Individual Case of Evolution 1.2	103
5.14	Best Individual Case of Evolution 1.3	103
5.15	ABD Models to Study Characteristics of Evolutionary Results	105
5.16	Pressure Distribution due to Different ABD Models	106
5.17	Total Pressure Distribution due to Different ABD Models	107
5.18	Velocity Profiles due to Different ABDs Upstream and Downstream of the Point of Interaction	108
5.19	Velocity Vectors for a) the ABD Model with an even depth and b) the ABD Model with a ‘pocket’	108
6.1	Aerofoil Section	112
6.2	NACA65-415 Aerofoil Section With ABD Insert	113
6.3	Injection Air Distributor System	114

6.4	From bottom to top: Pressure Distributor, Pressure Tapping System, and Separation Wall with 3mm bore holes	115
6.5	Velocity Distribution along the Interaction Zone	116
6.6	Model Structure	117
6.7	Aerofoil Section with Blank Insert	118
6.8	Drag Coefficient versus Angle of Attack	120
6.9	Lift Coefficient versus Angle of Attack	121
6.10	Effect of the ABD on C_L at various Angles of Attack ($Re = 1.02 \times 10^6$)	122
6.11	Effect of the ABD on C_L at various Angles of Attack ($Re = 0.68 \times 10^6$)	123
6.12	Percentage Change of C_L	124
6.13	Effect of the ABD on C_D at various Angles of Attack ($Re = 1.02 \times 10^6$)	125
6.14	Effect of the ABD on C_D at various Angles of Attack ($Re = 0.68 \times 10^6$)	126
6.15	Principle of Pressure Tapping	126
6.16	Validation of Pressure Readings for 0° and 12°	127
6.17	Validation of Pressure Readings for -4° and 8°	128
6.18	Effects of the ABD on the Pressure Distribution at -8° Angle of Attack	128
6.19	Effects of the ABD on the Pressure Distribution at 0° Angle of Attack	129
6.20	Effects of the ABD on the Pressure Distribution at 8° Angle of Attack	129
6.21	Effects of the ABD on the Pressure Distribution at 16° Angle of Attack	130
6.22	Experimental Lift Coefficient versus Angle of Attack ($Re = 0.68 \times 10^6$)	133
6.23	Experimental Lift Coefficient versus Angle of Attack ($Re = 1.02 \times 10^6$)	134
6.24	Percentage Variation of C_L due to the Experimental Pressure Distribu- tion	135
6.25	Percentage Variation of C_L due to the Experimental Pressure Distribution	136
6.26	Flow Visualisation for $Re = 1.02 \times 10^6$ for the Smooth Aerofoil Section and the ABD with $C_i = 1.5$, (i.e. $\dot{V} = 34 \text{ m}^3/\text{h}$)	138
6.27	Flow Visualisation for $Re = 0.68 \times 10^6$ for the Smooth Aerofoil Section and the ABD with $C_i = 2.5$ (i.e. $\dot{V} = 34 \text{ m}^3/\text{h}$)	139
6.28	Flow Visualisation for $Re = 0.68 \times 10^6$ for the ABD with $C_i = 2.0$ (i.e. $\dot{V} = 28.8 \text{ m}^3/\text{h}$) and the ABD with $C_i = 1.5$ (i.e. $\dot{V} = 21.6 \text{ m}^3/\text{h}$) . . .	140
6.29	Power Requirements for the ABD versus C_i ($Re = 0.68 \times 10^6$)	141

A.1	Control Volume Notation	156
A.2	Specification of Grid Types	159
B.1	Model for Tapered Internal Ducting	162
B.2	Predicted Velocity Distribution along Interaction Zone Centre Line . .	163
B.3	Virtual Axis Six-Component Wind Tunnel Force Balance System with Vacuum Pump for Fluid Removal	164
B.4	Experimental Set Up	165
B.5	Effect of the ABD on the Pressure Distribution at -8° Angle of Attack ($Re = 1.02 \times 10^6$)	167
B.6	Effect of the ABD on the Pressure Distribution at -4° Angle of Attack ($Re = 1.02 \times 10^6$)	168
B.7	Effect of the ABD on the Pressure Distribution at 0° Angle of Attack ($Re = 1.02 \times 10^6$)	168
B.8	Effect of the ABD on the Pressure Distribution at 4° Angle of Attack ($Re = 1.02 \times 10^6$)	169
B.9	Effect of the ABD on the Pressure Distribution at 8° Angle of Attack ($Re = 1.02 \times 10^6$)	169
B.10	Effect of the ABD on the Pressure Distribution at 12° Angle of Attack ($Re = 1.02 \times 10^6$)	170
B.11	Effect of the ABD on the Pressure Distribution at 16° Angle of Attack ($Re = 1.02 \times 10^6$)	170
B.12	Effect of the ABD on the Pressure Distribution for 20° Angle of Attack ($Re = 1.02 \times 10^6$)	171

List of Tables

2.1	ABD Dimensions from Pioneering Work [1]	19
2.2	Summary of the Aerodynamic Effects of some Active Flow Control Techniques	22
3.1	Data for Grid-Independent Computation	34
3.2	Data for NACA0012 Validation	43
3.3	Data for NACA65-415 Validation	44
3.4	Percentage Variation of Predicted Drag Coefficients from the Aerofoil Section with Standard Surface Roughness	44
4.1	ABD Inlet and Outlet Turbulence Levels	47
4.2	Parameter Levels	48
4.3	L_8 -Array Parameter Combination	49
4.4	Simulation Results	50
4.5	Percentage Change in C_L , C_D and L/D due to the presents of an ABD	50
4.6	Response Table	51
4.7	Ranking of the Flow Control Parameters	52
4.8	Comparison of Taguchi Prediction and CFD Results	53
4.9	Levels for Confirmation Run	54
4.10	Comparison of Taguchi Prediction and CFD Results for the Confirmation Run	54
4.11	Values for the Common Base Case	55
4.12	Variation of the Aerodynamic Characteristics with the Reynolds-number	63
4.13	Proportion of P_{ABD} to P_D	83

4.14	Effects of CFD Parameter on Momentum Transfer via a Secondary Flow through the ABD	85
5.1	Refined Results of Best Individuals	102
5.2	Results for ABD Models	106
6.1	Values of Lift Coefficients by Different Techniques for a Smooth Aerofoil Section	132

Nomenclature

Symbols	Names	Units
A	surface	(m ²)
C_D	drag coefficient	-
C_i	injection coefficient,	-
C_L	lift coefficient	-
C_p	pressure coefficient	-
$C_\mu, C_{1\epsilon}, C_{1\epsilon}$	constants for $k - \epsilon$ and RNG $k - \epsilon$ turbulence model	-
D	drag force	(N)
E	log-law constant	-
L	lift force	(N)
L/D	aerofoil performance	-
L_8	two factor level array for 7 parameter	-
P	power	(W)
P	rate of production of turbulence	
	kinetic energy	(W/m ³)
PF	penalty factor	-
P_D	power for forward motion	(W)
P_L	power for lift	(W)
$P_L/P_{D_{eff}}$	effective aerofoil performance	-
P_{ABD}	power to drive secondary flow	(W)
$P_{D_{eff}}$	effective power for forward motion	(W)
Pe	Peclet number	-
R	radius	(m)
Re	Reynolds-number	-
$-\rho \overline{u'_i u'_j}$	Reynolds-stress	(N/m ²)
S	source	-
T	temperature	(K)
T_i	turbulence intensity	-
U_i	injection velocity	(m/s)
U_s	velocity of a moving surface	(m/s)

U_{∞}	free stream velocity	(m/s)
\dot{V}	volume flow rate	(m ³ /s)
\overline{T}	overall experimental average	-
\overline{T}_{level}	average of individual	-
	percentage changes	-
\overline{u}_i	time averaged velocity component	(m/s)
\overline{y}_i	mean response of levels	-
b	body force	(N)
c	chord	(m)
d	total derivative	-
k	turbulent kinetic energy	(m ² /s ²)
n	number of experiments	-
p	pressure	(Pa)
q_{∞}	dynamic pressure of the free stream	(Pa)
t	time	(s)
u^+	non-dimensionalised boundary layer velocity	-
u_1, u_2	velocities tangential and normal to a solid surface	(m/s)
u'_i	velocity component of turbulent fluctuation	(m/s)
u_i, u_j, u_k	velocity components for Cartesian co-ordinate system	(m/s)
u_{ABD}	velocity of secondary flow inside the ABD	(m/s)
x_1, x_2	directions tangential and normal to surfaces	-
x_i, x_j	directions in Cartesian co-ordinate system	-
y^+	non-dimensionalised boundary layer co-ordinate	-
y_o^+	non-dimensional boundary layer co-ordinate for laminar sublayer	-
y_i	individual percentage variation	-
y_p	distance of the near wall node	(m)

Greek Symbols	Names	Units
Γ	diffusion coefficient	-
Δ	difference	-
δ	distance	(m)
δ_{ij}	Kronecker delta	-
ϵ	energy dissipation	(m ² /s ³)
θ	local surface angle	(°)
κ	von Karman constant	-
λ	normal stress component due to volumetric deformation	(N/m ²)
μ	molecular coefficient of viscosity	(kg/ms)
μ_t	eddy viscosity	(kg/ms)
ν	kinematic viscosity	(m ² /s)
∂	partial derivative	-
$\overline{\phi}$	time averaged quantity	-
ϕ	general scalar quantity	-
ϕ'	variation of ϕ due to turbulent fluctuation	-
ρ	density	(kg/m ³)
σ	normal stress	(N/m ²)
σ_k	turbulent Prandtl number	-
τ	tangential stress	(N/m ²)

Subscripts

E	nodal point east
$Jones$	Jones traverse method
P	nodal point
W	nodal point west
∞	free stream condition
ϕ	general scalar quantity
$at.$	atmospheric condition
e	east face
eff	effective
far	far field
i	injection
i, j, w	tensor notation for component in Cartesian co-ordinate space
max	maximum
num	numerical predictions
p	pressure
rms	root-mean-square

<i>s</i>	surface
<i>surf.</i>	surface
<i>t</i>	turbulent
<i>w</i>	wall
<i>w</i>	west face
<i>w.f.</i>	wall force

Abbreviations

<i>ABD</i>	Air Breathing Device
<i>ASM</i>	Algebraic Stress Model
<i>BLC</i>	Boundary Layer Control
<i>CFD</i>	Computational Fluid Dynamics
<i>CPU</i>	Central Processing Unit
<i>DNS</i>	Direct Numerical Simulation
<i>GA</i>	Genetic Algorithm
<i>HLFC</i>	Hybrid Laminar Flow Control
<i>LE</i>	Leading Edge
<i>LEBU</i>	Large Eddy Break-Up
<i>LES</i>	Large Eddy Simulation
<i>LFC</i>	Laminar Flow Control
<i>MEMS</i>	Micro Electrical Mechanical Systems
<i>MSBC</i>	Moving Surface Boundary Layer Control
<i>MT</i>	Momentum Transfer
<i>NACA</i>	National Advisory Committee for Aeronautics
<i>NFL</i>	Natural Laminar Flow
<i>PDE</i>	Partial Differential Equation
<i>RANS</i>	Reynolds Average Navier-Stokes Solver
<i>RDF</i>	Reduction Factor
<i>RSM</i>	Reynolds Stress Model
<i>TBL</i>	Turbulent Boundary Layer
<i>TE</i>	Trailing Edge

Chapter 1

Introduction

The performance of aerodynamic and hydrodynamic vehicles is predominantly influenced by the existence of a thin boundary layer over the surface of the vehicle. The boundary layer develops due to fluid attachment to the solid surface (i.e. the no-slip condition), viscosity effects and a velocity difference between the solid and the fluid. At their onset, boundary layers are characterised by laminar fluid motion which changes subsequently into a turbulent state with randomly fluctuating fluid particles as a result of disturbances and/or insufficient energy content in the fluid within the boundary layer. As a result of the boundary layer, shear and pressure forces act against the vehicle's forward motion. Adverse conditions within the flow region adjacent to the surface may bring the flow in the boundary layer to rest and particles of fluid are forced away from the surface. The flow is then said to be 'separated', and this contributes strongly to pressure drag. It is important to control the state of the boundary layer to keep drag forces to a minimum and to prevent potential aerodynamic failure of the devices (e.g. stall of lift surfaces) due to flow separation. Both issues are of particular interest to the aviation industry and consequently have been the focus of research for the past century.

A world in which air traffic is growing rapidly requires efficient and safe air transportation. Improved cruise conditions results in cost reductions due to increased payload and operational range. Augmentation of the lift performance of wings primarily affects take off and landing performance. Thus higher take-off and landing loads, reduced noise levels due to lower thrust requirements as well as shorter landing and

take-off distances can all result from improved boundary layer control (BLC). Better lift performance also improves aviation safety as a result of reduced approach landing velocities.

A large number of flow control devices have been investigated and installed in the wings or fuselages of aircraft. However, many of these devices have been unsuccessful often as a result of negative side effects. Thus reduction of shear forces can also lead to an increase in pressure drag and vice versa. Considerations such as the auxiliary energy consumption of active devices, the additional weight, practicality, retrofit-ability and maintenance requirements also restrict the application of BLC for modern aircraft. All the effects associated with a certain flow control technique need careful balancing and appropriate adaptation to meet specific applications. A one-size-fits-all solution is difficult or virtually impossible to achieve.

The work described in this thesis concentrates on augmenting the performance of aerofoil sections using a novel momentum transfer (MT) technique via a secondary flow. This flow control method is based on the interaction of a tangential secondary flow with the boundary layer on the suction side of an aerofoil section. To ensure momentum transmission into the external boundary layer the velocity ratio between the secondary flow and the free stream must be greater than unity. The method uses a so-called air breathing device (ABD), which achieves the required momentum transfer without any net mass exchange between the external and secondary tangential flows. The secondary flow requires auxiliary energy, so that the effectiveness and the efficiency of the ABD should be optimised. Therefore, numerical studies on the parameters governing the performance and the efficiency of the technique were conducted to provide a comprehensive understanding of the behaviour of this present flow control technique. Attempts were made to optimise the geometrical and flow parameters of the ABD using both Taguchi's method as well as by means of genetic algorithms (GAs) in combination with computational fluid dynamics (CFD). Measurements in a wind tunnel were used to confirm the benefits of momentum transfer via secondary flow.

Chapter 2 presents the main literature review and includes a brief introduction to the flow equations (i.e. the Navier-Stokes equations) and the concept of boundary layer, followed by a description of typical flow control techniques for different boundary layer

conditions. Particular attention is given to momentum transfer techniques. Chapter 3 provides an introduction to the simulation method (control volume technique, Reynolds-Averaged-Navier-Stokes method) which was used in this thesis. The specifications of the numerical methods and mathematical models are then discussed. The validity of the computational set-up was established by comparing the predictions for the drag and lift coefficients with previously published data for two different aerofoil sections (a symmetric NACA0012 aerofoil section and a cambered NACA65-415 section). For both aerofoil sections the effects of flow control using an ABD were studied numerically in Chapter 4. A Taguchi analysis was undertaken for the NACA0012 aerofoil section in order to confirm the findings of previous work [1] and to establish the main parameters governing momentum transfer via the secondary ABD flow. The effects of individual ABD geometrical and flow parameters on the aerodynamic characteristics of the NACA65-415 aerofoil section and the efficiency of the ABD are also described in this chapter. The cambered NACA65-415 aerofoil section was chosen for this study due to its greater significance to the modern aviation industry than the symmetrical NACA0012 section. Chapter 5 of this thesis deals with the optimisation of the ABD. This optimisation employed genetic algorithms in conjunction with CFD predictions of the system. Experimental studies were conducted to validate the numerical results and these are presented in Chapter 6. These experiments involved measurements of lift and drag using an accurate force balance as well as individual pressure readings over the surface of the aerofoil section. Qualitative assessment of the effects of flow control using the ABD was undertaken by flow visualisation using tufts on the trailing section of the aerofoil. The final chapter (Chapter 7) contains overall consideration of the conclusions from this work and recommendations for further research on the use of an ABD to transfer momentum via a secondary flow.

Chapter 2

Flow Control

2.1 The Governing Equations

The physics of fluid flows are governed by a set of equations based on the conservation of various quantities. For a control volume $dx dy dz$, the input and output of any quantity must be balanced. The *continuity equation* ensures the conservation of mass for a three-dimensional, time dependent and compressible flow by:

$$\frac{\partial \rho}{\partial t} + \frac{\partial}{\partial x_i}(\rho u_i) = 0 \quad (2.1)$$

The Newtonian law, i.e. the equation for conservation of momentum, for fluid particles can be written in index notation for Cartesian co-ordinate systems as:

$$\frac{\partial(\rho u_i)}{\partial t} + \frac{\partial}{\partial x_j}(\rho u_i u_j) = b_i - \frac{\partial p}{\partial x_i} + \frac{\partial \tau_{ij}}{\partial x_j} \quad (2.2)$$

where the first term accounts for transient (i.e. local) flow movements, the second term on the left hand side describes the variation of momentum due to changes of position (convection). The right hand side of Equation 2.2 comprises the body forces, b_i , such as gravity or centrifugal forces, a term for pressure and the diffusion term. For spatial flows of Newtonian fluids shear stresses arise as a consequence of friction. These stresses can be expressed by a generalisation of Newton's law of friction:

$$\tau_{ij} = \mu \left(\frac{\partial u_i}{\partial x_j} + \frac{\partial u_j}{\partial x_i} \right) - \frac{2}{3} \mu^* \frac{\partial u_i}{\partial x_i} \delta_{ij} \quad (2.3)$$

Here μ^* arises from Stokes hypothesis ($3\lambda + 2\mu^* = 0$). Using this relationship reduces the amount of material properties which describe the field of tension within a compressible fluid from two to one, so that it can be used in the above equation. Lambda (λ) accounts for the stresses due to volumetric deformation. Stokes hypothesis is still a matter of current debate, but provides a good approximation for gases [2]. Equations 2.2 and 2.3 apply to transient, compressible and laminar flow [3]. The Kröencker delta δ_{ij} in equation 2.3 includes the normal stress contribution when $i=j$ since $\delta_{ij} = 1$ in this case and otherwise $\delta_{ij} = 0$.

Turbulent flows are characterised by random fluctuations of flow quantities. In fluid dynamics a stochastic approach is used to account for these fluctuations by dividing the time dependent quantity $\phi(t)$ into a time independent mean value $\bar{\phi}$ and time dependent fluctuations ϕ' around the mean value, thus $\phi(t) = \bar{\phi} + \phi'$. Time averaging of these fluctuations is by definition zero. The superposition of these fluctuations on the mean motion causes additional stresses:

$$-\rho \overline{u'_i u'_j} \quad (2.4)$$

These stresses are referred to as ‘apparent’ or Reynolds-stresses [4]. Inserting the mean velocity components into Equation 2.2 and adding the apparent stresses leads to the Reynolds equation, which reads:

$$\frac{\partial(\rho \bar{u}_i)}{\partial t} + \frac{\partial}{\partial x_j}(\rho \bar{u}_i \bar{u}_j + \overline{\rho u'_i u'_j}) = b_i - \frac{\partial p}{\partial x_i} + \frac{\bar{\tau}_{ij}}{\partial x_j} \quad (2.5)$$

here, $\bar{\tau}_{ij}$ evolves from the mean viscous stress tensor:

$$\bar{\tau}_{ij} = \mu \left(\frac{\partial \bar{u}_i}{\partial x_j} + \frac{\partial \bar{u}_j}{\partial x_i} \right) - \frac{2}{3} \mu^* \frac{\partial \bar{u}_i}{\partial x_i} \delta_{ij} \quad (2.6)$$

Solution of the Navier-Stokes equations can only be obtained for some special cases for low Reynolds numbers [3]. For high Reynolds numbers many problems are solved using boundary layer theory. In particular, Reynolds-stresses add further unknowns to the momentum equations. To account for these turbulence quantities the problem has to be *closed* by additional relations, and this is known as turbulence modelling. For non-isothermal flows the *energy equation* is added to the set of equations.

2.2 Boundary Layer Concepts

The boundary layer concept provides the link between theoretical hydrodynamics and the more empirical approaches. Before the boundary layer concept was introduced the theoretical approach was based on Euler's equations of motion and did not give sufficiently accurate answers for many practical problems. Although the Navier-Stokes equations which involve viscous effects, were known, their mathematical complexity limited their practical application [4]. Thus engineers relied largely on empirical results. In 1904 L. Prandtl [5] introduced the concept of a boundary layer. This theory divides the flow into a region where potential flow theory is valid and a layer which is governed by wall and viscous effects. In external flows this layer is relatively thin but has a significant influence on most aerodynamic problems.

A boundary layer develops due to fluid particles adhering to a solid surface (i.e. no-slip condition), and viscous effects due to a velocity difference between solid surface and the main fluid flow. Within a small distance from the wall these viscous effects result in a velocity profile through the boundary layer in which the velocity gradually changes from the wall value (zero) to the mainstream value (Figure 2.1). The smooth transition which occurs from the boundary layer to the potential flow region makes it difficult to identify a clear border between the two regions. Normally the edge of the layer is defined as the position where the local velocity is 99% of the mainstream value. In the undisturbed region the velocity gradients are small so that viscous effects may be neglected. The product of the velocity gradient at the wall, $[\partial u_1 / \partial x_2]_w$, and the coefficient of molecular viscosity, μ , of the fluid results in local skin friction drag. The reader should note that the indices i and j are replaced by 1 and 2 in this case which indicates the directions tangential and normal to walls, respectively.

Initially at onset boundary layers are always laminar. The flow in the layer is, however, sensitive to small disturbances, resulting in two-dimensional so-called Tollmien-Schlichting waves [4]. At a critical Reynolds-number these waves gain amplitude and non-linear effects take place, i.e. the onset of three-dimensional structures. Hairpin vortices due to tertiary instabilities cause a rapid break-down into turbulent flow [6]. At low Reynolds-numbers the initial linear instabilities caused by moderate disturbances

may decay so that the boundary layer remains laminar.

In external flows the process of transition from laminar to turbulent flow can be influenced by the magnitude of the Reynolds-number, pressure gradients, surface roughness, radiated sound, surface vibration and free stream turbulence. As a result of Reynolds-stresses (Equation 2.4) the skin friction drag of turbulent boundary layers can be of an order of magnitude higher than the skin friction of the laminar boundary layer. Due to the momentum conducting properties of turbulent boundary layers the velocity distribution in the turbulent case gains a ‘fuller’ profile, so that $[\partial u_1 / \partial x_2]_w$ increases. Entrainment between turbulent fluid layers is caused by the fluctuation of the fluid particles which transmits momentum close to the solid surface. The energy for this process is taken from the flow external to the boundary layer. Near smooth walls the turbulent fluctuations in the flow diminish with a consequent reduction in the Reynolds-stresses, so that even in turbulent boundary layers wall shear forces are generated by viscous effects only [4]. In any other region of the flow, turbulent stresses are much greater than the stress contribution due to viscosity. Strong disturbances (i.e. $u'_{rms}/U_\infty \geq 10\%$) bypass the relatively slow amplification procedure, leading to transition at much lower Reynolds-numbers [7].

Shear forces, turbulent stresses and adverse pressure gradients all result in energy dissipation within the boundary layer. This loss decelerates the near wall flow until $[\partial u_1 / \partial x_2]_w$ becomes zero (Figure 2.1, Position 3). The flow downstream of this point is said to be ‘separated’ and the boundary layer approximations are no longer valid [7]. At the separation point the fluid starts to reverse its motion, and vortex flow is initiated downstream of this separation point with a consequent depression in pressure. Oncoming fluid particles cannot penetrate the vortex layer so that the streamlines depart from the body causing a widening of the wake region. The effects of increased displacement, and the pressure depression in the wake, both contribute to the pressure drag on the body. Furthermore, separation guides the streamlines away from the aerofoil shape so that circulation around the body, i.e lift, is reduced. As explained previously the momentum transfer properties which result in a ‘full’ velocity profile make turbulent boundary layers more resistant to separation than laminar boundary layer.

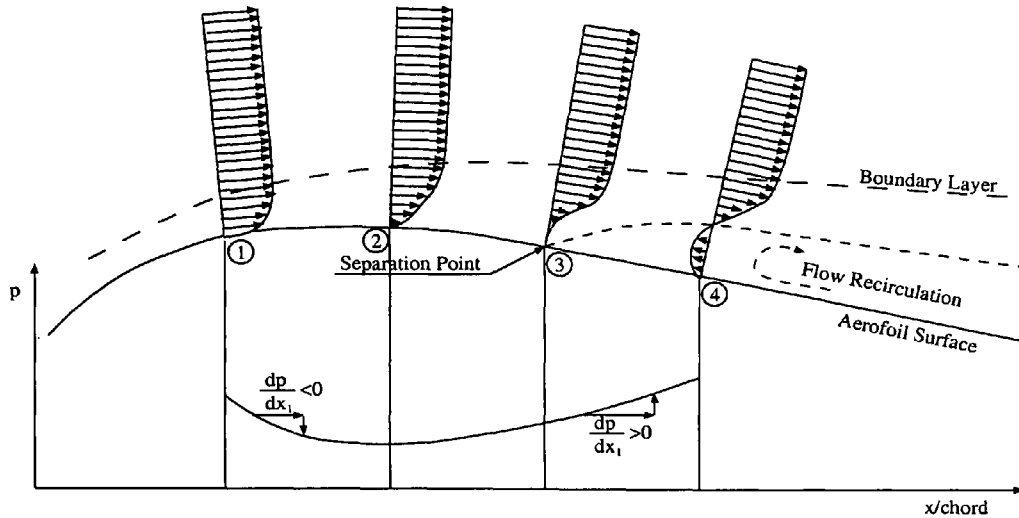


Figure 2.1: Boundary Layer Development on an Aerofoil Suction Side

Flow Conditions on Aerofoil Sections

Aerofoil sections are operated at Reynolds-numbers between $10^2 < Re < 10^9$ where the chord length is the characteristic dimension and Re is based on mainstream velocity. Their aerodynamic characteristics are governed by the phenomena explained previously in this chapter. Below $Re = 10^4$ boundary layers are always laminar. Vehicles operating within this range (small model aeroplanes) experience stall conditions at moderate angles of attack, due to abrupt separation of the laminar boundary layer. Therefore the aerofoil performance, which is usually characterised by the rate of lift-to-drag forces, L/D , is relatively poor. For $10^4 < Re < 10^6$ the aerodynamic characteristics of aerofoil sections improve dramatically (Figure 2.2).

Increasing the Reynolds-number above 10^6 results in only moderate improvements in L/D and large aeroplanes are operated in this range. At these Reynolds-numbers the separation starts at the trailing edge and proceeds upstream with increasing angle of attack and this is called trailing edge stall.

For $10^4 \leq Re \leq 10^6$ *separation bubbles* can occur. These bubbles are a local flow separation which are subsequently forced to re-attach to the surface by the entrainment of momentum from 'high-speed' fluid. Downstream of the separation bubble the flow in the boundary layer is governed by turbulent phenomena. Within this Reynolds-number

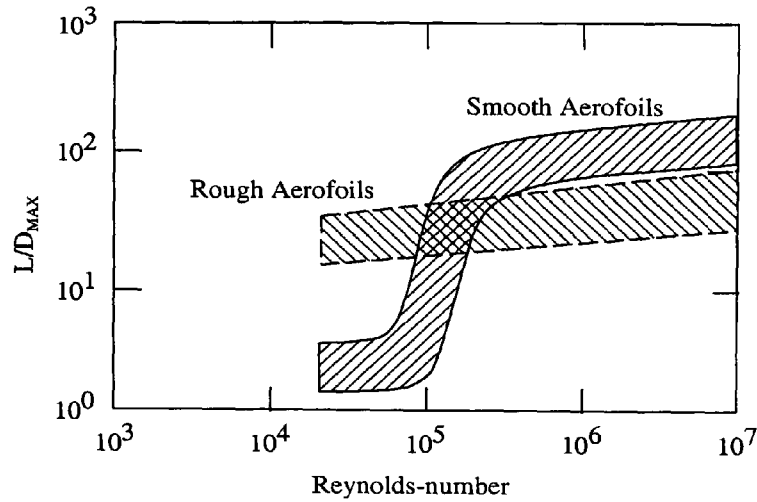


Figure 2.2: Aerofoil Performance as a Function of the Chord Reynolds-number [8]

range separation bubbles are more likely at the lower Reynolds-numbers [8].

The undesirable effects resulting from the different regimes of boundary layer in external flows over lift devices provide an impetus for modifications to flows in order to obtain improved aerodynamic performance. In the following section the major goals of flow control are explained and a brief review of most flow control devices is presented.

2.3 Flow Control

Flow control applied to aerofoil sections aims to increase the overall performance by enhancing L/D . Lift improvements largely affect the allowable overall take-off loads, take-off distance, and noise levels as a result of lowered thrust requirements for large aircraft [9]. Lower noise levels also require less equipment for engine silencing leading to a reduced net weight of the aircraft. Also, a flow control device that substantially augments the lift characteristics may lessen the need for mechanical high lift devices such as trailing or leading edge flaps, slats and slots. These devices require heavy support structures and impose high maintenance costs and their bulky drive systems also result in ‘bumps’ on the aerofoil surface. The elimination of such devices would have a positive impact on the overall take-off weight of an aircraft and improve cruising conditions [10]. Reduced drag improves aircraft efficiency and can lead to an increased

operational range, reduced fuel costs, higher payloads or even increased speed [7].

By definition flow control interferes with the natural development of the boundary layer. Depending on the state of the boundary layer and the targeted flow phenomena, flow control can be classified into techniques and methods which attempt to:

- reduce laminar skin friction,
- delay transition or re-laminarise the boundary layer,
- reduce turbulent skin friction,
- reduce displacement effects with turbulent boundary layers,
- postpone separation or bring about re-attachment of the boundary layer.

Devices used for these techniques are either passive or active. Active devices require auxiliary power, thus their success strongly depends on the net savings which can be achieved. So-called ‘predetermined’ active flow control devices use a steady or unsteady energy input without regard to the particular state of the boundary layer whereas ‘reactive’ devices are sensitive to the state of near wall flow. The latter type has gained increasing attention due to improved manufacturing methods for micro-devices and the availability of complex control systems [11].

2.3.1 Reduction of Laminar Skin Friction

Boundary layer flows at Reynolds-numbers $< 10^6$, (based on the distance from the leading edge of an aerofoil) are mainly laminar so that ways of reducing the laminar shear stress ($\tau = \mu[\partial u_1/\partial x_2]$) are necessary. The ‘wall velocity gradient’, $\partial u_1/\partial x_2$, can be reduced by adverse pressure gradients (i.e. $dp/dx_1 > 0$) or by mass injection at the solid surface. Alternatively, the coefficient of molecular viscosity can be increased by surface heating for gases or surface cooling in liquids, which thickens the boundary layer and also reduces the wall velocity gradient. However, it should be noted that these methods promote instabilities and can lead to laminar-to-turbulent transition and/or separation.

2.3.2 Transition Delay

Transition delay finds application within the range of $10^6 < \text{Re} < 4 \times 10^7$ (again based on the distance from the aerofoil leading edge) [7]. Laminar boundary layers produce substantially lower skin friction than turbulent boundary layers so that means that extending this region of flow as far as possible is desirable. A further advantage is that vibrations resulting from turbulence effects which can cause structural, aerodynamic (flutter) and comfort problems (noise) are reduced.

As discussed in Section 2.1 transition is initiated by disturbances which increase in amplitude when a critical Reynolds-number is reached. Transition can be postponed either by avoidance of disturbances or by stabilising the boundary layer using ‘stability modifiers’. Disturbances can be minimised by reducing surface roughness, radiated sound or surface vibration. Tertiary instabilities such as cross-flows or three-dimensional vortices (e.g. Taylor-Görtler vortices) can be minimised by making surfaces less concave and reducing the sweep of the lift surface [7].

Stability modifier influencing the shape of the velocity profile at the wall, so that the ratio of displacement thickness to momentum thickness is kept small, hence a ‘full’ velocity profile (i.e. strong curvature) is maintained. Possible methods for stabilising the laminar boundary layer can be derived from the two-dimensional boundary layer equation for flows along a surface with a small curvature [7]:

$$\left[\rho \frac{\partial u_1}{\partial t} \right]_w + \left[\rho u_1 \frac{\partial u_1}{\partial x_1} \right]_w + \left[\rho u_2 \frac{\partial u_1}{\partial x_2} \right]_w + \frac{dp}{dx_1} - \frac{d\mu}{dT} \left[\frac{\partial T}{\partial x_2} \frac{\partial u_1}{\partial x_2} \right]_w = \left[\mu \frac{\partial^2 u_1}{\partial x_2^2} \right]_w \quad (2.7)$$

This equation is derived from the Navier-Stokes equations. All terms on the left hand side of Equation 2.7 can influence the curvature of the velocity profile so that it remains negative and hence stabilises the laminar boundary layer.

The first three terms are affected by *wave cancellation devices* such as compliant walls or micro-electro-mechanical-systems (MEMS). Compliant walls have been suggested following observations of dolphins. It is suspected that their high gliding speeds arise from the flexibility of their skins and this maintains laminar flow. These compliant walls can consist of flexible coatings with a low modulus of rigidity. They result in a damping of instabilities due to formation of surface waves caused by the stress field of

the fluid. Alternatively, actively driven flexible surfaces can alter the boundary layer so that a ‘full’ velocity profile is achieved [7, 11, 12, 13]. MEMS are micro actuators which cancel the growth of disturbances [11].

Boundary layers are caused by the velocity difference between the wall and the free stream. Movement of the wall with the free stream reduces this difference and this affects the second term in Equation 2.7 and helps to delay transition [2].

Natural laminar flow (NLF) is achieved by creating a favourable pressure gradient on the suction side of an aerofoil section ($dp/dx_1 < 0$). This can be achieved by shaping aerofoil sections (so-called laminar aerofoils), so that the point of minimum pressure occurs as far downstream as possible. Due to a large pressure increase behind this point the flow is likely to separate so that, if the shape is not carefully chosen, the pressure drag penalties may exceed the savings from the larger laminar section of the boundary layer [4]. The maintenance of NLF can be adversely affected by three-dimensional flows, such as cross-flow vortex instabilities on swept wings, so that the use of laminar aerofoils find only limited application on large aeroplanes [13].

Withdrawing fluid from a boundary layer through porous regions or transverse slots in the surface results in $[u_2]_w > 0$. This method inhibits boundary layer growth so that a critical boundary layer thickness is not reached and instabilities are not amplified. For economic reasons the amount of withdrawn fluid should be kept to a minimum, since the requirements for auxiliary power and difficulties with the disposal of the withdrawn fluid reduce the efficiency of the method. Real flight tests have been conducted by American and European institutions and these indicated the considerable potential for LFC (Laminar Flow Control) by means of surface suction. However, uncertainties with regard to requirements for additional maintenance and long term structural integrity of these systems prevented suction from being used on commercial aircraft [14, 13, 15, 16]. Methods combining NLF and LFC are commonly referred to as hybrid laminar flow control (HLFC).

Cooling the surface affects the fluid viscosity¹. Hence with gases $d\mu/dT$ is > 0 and $[\partial T/\partial x_2]_w$ is > 0 . The reduced viscosity causes a ‘fuller’ velocity profile at the wall and the critical Reynolds-number (based on the distance from the leading edge) is

¹In gases viscous effects decrease with a drop in temperature whereas the opposite is true for liquids

substantially increased. This technique, however, is difficult to achieve and may only be applicable when cryogenic-fuels are burned in the aircraft propulsion system [7].

2.3.3 Turbulent Drag Reduction

In many practical applications laminar flows cannot be maintained. This is the case when the Reynolds-number exceeds $\approx 4 \times 10^7$ or structural disturbances such as doors, windows, windscreen wipers and pitot static tubes cause transition [17], so that methods of interfering with the turbulent structure of the near wall flow have been sought.

Surface heating with gases increases the fluid viscosity and hence reduces the velocity gradient at the wall (i.e. boundary layer thickening), and this leads to the reduction of turbulent skin friction drag. This heating can be difficult to achieve since, for example, the use of waste heat from cooling systems of the aircraft propulsion unit would require major changes to both the wing box and the cooling systems [17].

Tangential slot injection of ‘low momentum fluid’ also thickens the boundary layer and reduces turbulent skin friction. This method can yield substantial benefits, but net savings depend on the magnitude of the losses in the injection system and a sufficiently ‘low-loss’ air source has not yet been developed [17]. The danger in boundary layer thickening lies in the potential promotion of separation which diminishes any benefits through increased pressure drag.

Riblets damp the turbulence within the boundary layer which reduces the associated energy dissipation. These devices consist of rows of small V-shaped grooves which are aligned in a stream-wise direction on the aerofoil surface. Due to their suitability for retrofit applications and their passive action much attention has been given to the subject, see for example [17, 18].

Adaptation of the wall structure by compliant coatings can be used for transition control but also has potential to reduce turbulent drag due to suppression of the ‘bursting’ of the turbulent boundary layers [12].

Large eddy breakup devices (LEBUs) shaped as aerofoil sections may be placed in the outer region of the boundary layer to alter the turbulent structure of the flow. Despite the additional pressure and skin friction drag from the LEBUs, net savings may be achieved due to the reduction of near wall fluctuations [12].

2.3.4 Separation Control

Perhaps the most important objective of boundary flow interference is the control of flow separation. Separation governs the stall, lifting performance, pressure recovery and the associated pressure drag of aerofoil sections [11]. As stated above separation occurs when the energy loss is sufficient to cause a reversal in the velocity profile (Figure 2.1) of the boundary layer. When the flow is separated, the gradient $[\partial^2 u_1 / \partial x_2^2]$ at the wall is greater than zero, i.e. positive. Therefore, a velocity profile as ‘full’ as possible is beneficial for separation delay as well as for stabilising a laminar boundary layer. This becomes apparent by re-writing Equation 2.7 for separation control [7] as follows:

$$\left[\rho u_2 \frac{\partial u_2}{\partial x_2} \right]_w + \frac{dp}{dx_1} - \frac{d\mu}{dT} \left[\frac{\partial T}{\partial x_2} \frac{\partial u_1}{\partial x_2} \right]_w = \left[\mu \frac{\partial^2 u_1}{\partial x_2^2} \right]_w \quad (2.8)$$

The left hand side of Equation 2.8 includes terms for wall suction (term 1), favourable pressure gradient (term 2) and surface cooling (term 3) to keep $[\partial^2 u_1 / \partial x_2^2]$ as negative as possible. The methods for separation control are similar to those for transition delay, although their detailed application may differ. For example, on streamlined bodies a sufficiently steep adverse pressure gradient causes a boundary layer to separate. Sufficient suction at this point can delay or even prevent flow divergence from the wall. In this case, suction is applied downstream to the point of minimum pressure in contrast to LFC where the fluid is withdrawn upstream of this point.

For applications where the pressure drag due to flow separation is significantly higher than the contribution of skin friction drag, artificial initiation of a turbulent boundary layer postpones separation.

2.3.5 Interrelation of Flow Control Techniques

This last case of preventing separation by initiation of transition shows that the effects of flow control techniques are not exclusive to a particular phenomena. Thus the application of a technique may have beneficial effects on one aspect of aerofoil behaviour but adverse effects elsewhere so that the overall effects are often a compromise. Another example of this is surface heating to reduce local skin friction drag with laminar and turbulent boundary layers flows. The resultant boundary layer thickening, however,

also promotes separation and/or transition of the laminar boundary layers. Both of these affect lift and drag of the body.

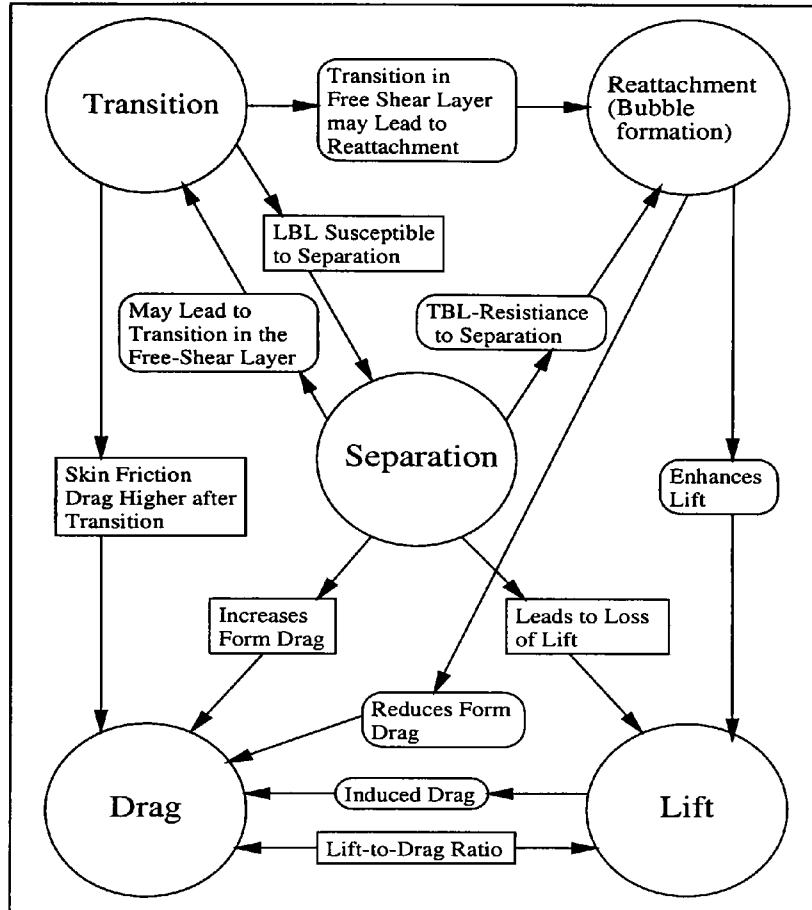


Figure 2.3: Interrelation between Flow Control Goals

Figure 2.3 [8] shows the interrelationships between flow control goals and the associated flow phenomena. A comprehensive review on the interrelation of flow control devices is given by Gad-el-Hak [8].

This strong interdependence of the effects of flow control methods makes it difficult to clearly distinguish the various classifications. The overall subject is vast so that the remainder of this review is restricted to a selection of active flow control devices which are relevant to the present work. In particular emphasis is placed on momentum transfer into the boundary layer of an external flow and this is discussed in the next subsection. It must be stressed that the vast amount of literature on flow control, accumulated over

the last century or so, is too great to be reviewed and discussed within this thesis.

2.3.6 Momentum Transfer

Momentum transfer into the near wall flow has been known for some decades as an effective means of enhancing aerodynamic characteristics of aerofoil sections. A simple application of the technique is a rotating cylinder placed into a cross-flow. The boundary layer development is inhibited on the side where the fluid and cylinder surface move in the same direction. The reduced or even reversed relative motion between the fluid attached to the surface and the free stream causes increased circulation (i.e. lift) and the total drag is reduced due to delayed flow separation. The discovery of this phenomenon, as described by Prandtl in 1925 [19], led to various attempts to transfer momentum into the boundary layer of aerofoil sections.

A rotating cylinder placed within the body of a lifting device is known as ‘moving surface boundary layer control’ (MSBC). The almost tangential interaction between the cylinder and the fluid adjacent to the wall can enhance considerably the aerodynamic characteristics of aerofoil sections. Application of MSBC at the wing-tip postpones stall to higher angles of attack [20, 21]. As reported by Modi et al [20], the lift coefficient of a symmetrical Joukowski aerofoil section, placed in a low-speed, low-turbulence wind-tunnel, was multiplied by about 2.3, at 28° angle of attack for $U_s/U_\infty = 4$. U_s and U_∞ are the velocity of the moving surface and the free stream velocity, respectively. This trend was confirmed by Chew et al [21] who used numerical predictions to find a lift-to-drag, L/D , improvement from 20 to 60 at 10° angle of attack for the same type of wing. Chew [21] stated that the leading edge arrangement has little affect on the drag coefficient, C_D , at angles of attack of less than 12° .

A truncated trailing edge arrangement (Figure 2.4) for the rotating cylinders enhances flow circulation with a consequent improvement in the lift of an aerofoil section [20, 22]. However, the stall region remains unaffected.

A rotating cylinder mounted in the upper surface can also contribute to augmentation of the lift coefficient, C_L , and delay in the onset of stall. The effectiveness is location dependent and whilst at rest their protrusion into the upper surface flow has an adverse effect on the aerofoil performance [20]. Irrespective of the position of the

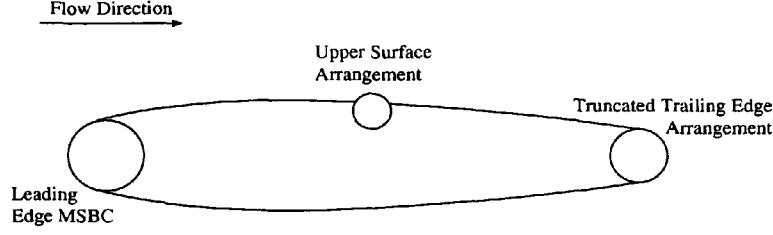


Figure 2.4: Arrangements for MSBC

device, the impact of MSBC is directly related to the moving surface to free stream velocity ratio. Modi et al [23] and Tennant et al [22] all reported a sensitivity to the gap between the rotating cylinder and the stationary aerofoil surface and moving surfaces are technically difficult to implement [4].

Separation can also be delayed by ‘tangential slot-injection’, i.e. momentum transfer from wall jets. This method supplies momentum into the boundary layer and re-energises the near wall fluid layers which are likely to separate. The injection velocity must be greater than the free stream velocity (i.e. $U_i/U_\infty > 1$). A wall jet placed immediately in front of a flap is particularly successful in improving the lift coefficient, C_L . This technique has been used on high-speed military aircraft (e.g. the Lockheed F-104), since these have small wing areas and cannot make use of other high lift devices [24]. High momentum injection can also cause *super-circulation* [4]. This so-called jet flap effect describes the occurrence of near wall velocities higher than the potential flow theory would suggest. Tangential slot-injection is sensitive to a variety of parameters (including the extent of the mixing region, the turbulence intensities in both the free stream and injected flow, the boundary layer pressure gradient, the injection angle, and the slot lip-thickness) [25]. Mass injection has only been used on ‘slotted wing’ designs for commercial aircraft, where the pressure difference between the suction and high pressure sides of the wing drives the injection of air. These are known as either ‘slotted flap wings’ or ‘leading-edge slat wings’ [26]. The efficiency of slot-injection is significantly reduced by the high ram-drag penalties resulting from fluid collection.

Therefore, periodic addition of momentum through tangential slots, without mass-injection is under investigation [24]. Seifert and Pack [27] used periodic excitation of the boundary layer to prevent separation. The method proved to be beneficial on a

NACA0015 aerofoil section when the device was placed a small distance upstream of the separation point. For incompressible flows $C_{L_{max}}$ can be improved by 15% and stall was substantially postponed. Ravindran [28] confirmed the potential benefits of this method by means of numerical predictions. Periodic or oscillatory excitation of the external flow over an aerofoil section is frequently referred to as synthetic jets. The unsteady suction and blowing principle transfers momentum into the boundary layer with no net exchange of mass and is a promising technique with low power requirements. The efficiency of the device is sensitive to the location of flow control.

Maksoud et al [29] described pioneering work at the University of Glamorgan whereby a fluid sub-layer i.e. a *secondary flow* was used to transfer momentum into the boundary layer of an external flow. The transfer of momentum was achieved via a transverse groove on the suction side of a NACA0012 aerofoil section. A so-called air breathing device (ABD) was developed and incorporated a tangential injection-suction principle without mass exchange, as depicted in Figure 2.5. Al-Shihry [1] conducted

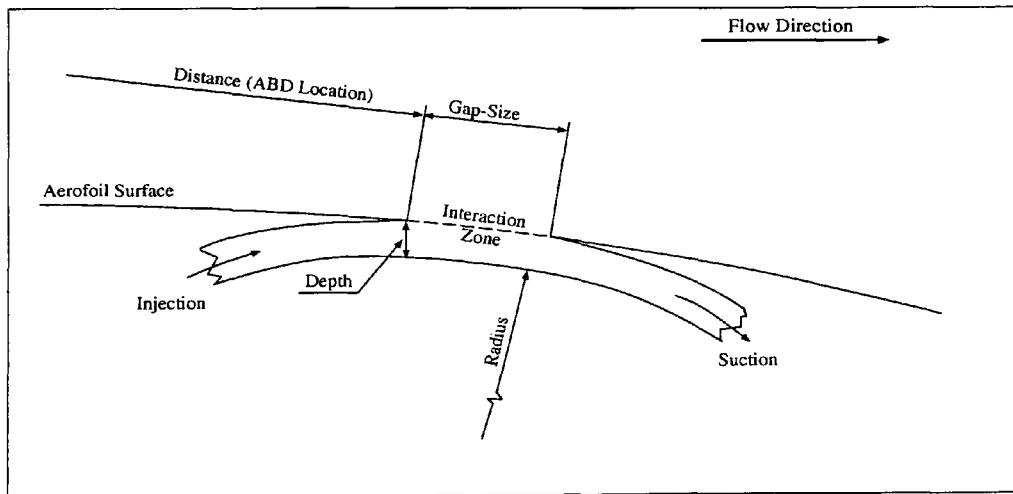


Figure 2.5: Principle of the ABD

both experimental and numerical studies at a chord Reynolds-number of 4×10^5 . A low-speed wind-tunnel with testing-cross-section dimensions of $0.3 \times 0.3 \text{ m}^2$ was used in the experiments. The location and interaction zone for momentum transfer was limited by the chord length of the model (chord = 0.15 m). Two different ABDs were used with the geometrical parameters shown in Table 2.1. Experiments were undertaken

for a range of $-2^\circ < \alpha < 14^\circ$ angles of attack and flow rate coefficients between 1.0 and 2.5 and these resulted in a maximum lift augmentation of 35%. Corresponding drag reductions were not explicitly mentioned. The flow rate coefficient is defined as the velocity ratio between the secondary flow and the free stream, U_{ABD}/U_∞ . Al-Shihry validated his numerical predictions by means of the wind tunnel experiments and subsequently conducted a wide range of numerical simulations. Drag reductions up to 50% and lift enhancements of around 35% were obtained with an interaction zone extending over 6.3% of the chord length with a flow rate coefficient of 2.5. From this Al-Shihry concluded that the flow rate coefficient had the strongest impact on lift and drag. For a secondary flow velocity of the same magnitude as the free stream velocity, flow disturbance occurred, resulting in an increased drag. Therefore, the flow rate coefficient must be sufficiently large to beneficially transfer momentum into the boundary layer. Al-Shihry observed that the introduced momentum only affected the velocity profile of the boundary layer downstream of the flow control device, whereas, a decrease in pressure occurs over the whole upper aerofoil surface.

Table 2.1: ABD Dimensions from Pioneering Work [1]

	Distance	Gap-Size	Radius	Depth
Model 1	38%	3.3%	3.3%	3.3%
Model 2	38%	4%	13.3%	4%

All dimensions are related to the aerofoil chord length (see Figure 2.5)

An increase in *gap-size* allowed greater interaction so that more momentum can be transferred, thereby producing greater reductions in drag. Al-Shihry used gap-sizes of 4%, 5.3%, and 6.3% chord at different locations on the suction surface of the aerofoil section. He reported that installing the ABD relatively near the leading edge resulted in greater lift improvements with the small (4%) interaction zone, whereas, the improvement increased with gap-size as the device moved further away from the leading edge. All the locations chosen for the ABD were downstream of the point of minimum pressure. It was also reported that the injection and the suction angles influence the performance of the device and that an ABD with curvature has greater impact on momentum transfer than a parallel system. The depth of the injection and suction slots

did not appear to have a significant effect on drag reduction or lift improvement.

Al-Shihry's work [1] used a flow rate coefficient to define the velocity ratio between the secondary flow and the free stream. This is appropriate as long as the flow direction within the region of interaction is parallel to the replaced aerofoil surface. For non-parallel ABDs the specification of this flow rate coefficient is more difficult. In the present study the injection coefficient, C_i , is used, in which the injection velocity of the secondary flow at the injection slot of the ABD is used. This parameter, does not provide information about the injection direction or the velocity distribution within the flow interaction zone.

Rationale behind this Present Work

The overall motivation for the present study is the general need for improved efficiency of aircraft. In particular it is based on the initial promise of a method of using a secondary flow to transfer momentum to the boundary layer on aerofoil sections.

The potential effects of improved performances of wing sections due to flow control can be summarised as:

- reduced costs due to improved cruise condition (drag reductions),
- higher take-off and landing pay loads (lift improvements),
- reduced take-off and landing distances (lift improvements),
- reduced noise levels due to lower thrust requirements (lift improvements),
- reduced take-off and landing weight of the aircraft due to less noise reduction equipment for jet engines (lift improvements),
- reduced take-off weight of the aircraft due to reduced demand for mechanical high lift devices and their bulky drive system (lift improvements),
- improved aviation safety due to reduced approach landing velocities (lift improvements).

Although, the above summary mainly highlights the need for lift improvements, drag reductions are no less important due the high proportion of time spent at cruising conditions.

Momentum transfer via a secondary flow has exhibited the potential to augment the performance of aerofoil sections [1] and may possibly avoid some of the drawbacks of other momentum transfer devices. An ABD provides structural flexibility due the use of air as the momentum transmitter. Full or partial air re-circulation of the secondary flow may provide an efficient flow control technique, since penalties due to fluid collection as occurs with blowing or disposal of the fluid (i.e. for suction) can be avoided.

Table 2.2 compares the aerodynamic benefits and disadvantages for a range of active flow control techniques. From this the advantages of momentum transfer without mass exchange (such as can occur with MSBC, synthetic jets and MT via a secondary flow through an ABD) is apparent. Momentum transfer without mass exchange has little known disadvantage on the the aerodynamic performance of wing sections in subsonic conditions. Disadvantages may arise, however, from possible failure of these devices, with consequent inevitable alterations to the aerofoil shape or surface properties and a resultant deterioration in aerofoil performance. In addition there is the need for auxiliary power to drive the devices.

Al-Shihry [1] used a NACA0012 aerofoil section to study momentum transfer by means of an ABD via a secondary flow. His work was aimed at the study of the individual parameters governing momentum transfer by means of this air breathing device. However, the interaction of these parameters was not clarified, so that the geometry and flows of the ABD were not optimised. The numerical simulations were set up to correspond to the conditions of the experimental tests. However, these tests and hence the conclusions may have been influenced by boundary conditions such as wall effects and/or wind-tunnel blockage.

The present work is aimed at overcoming some limitations of Al-Shihry's study particularly with respect to the range of Reynolds-numbers. The numerical work also largely removes the effects of interference from the boundaries of the domain of interest.

A Taguchi analysis was employed to study the effects of the ABD parameters when the device was installed on a NACA0012 aerofoil section. The work was subsequently

Table 2.2: Summary of the Aerodynamic Effects of some Active Flow Control Techniques

Techniques	Advantages	Disadvantages
Suction	Drag Reduction Transition Delay Separation Delay	Momentum Loss
Injection ($C_i < 1$)	Drag Reduction	Separation Promotion
Injection ($C_i > 1$)	Momentum Enhancement Separation Delay	Increased Skin Friction Transition Promotion
Heating (Gas)	Turbulent Drag Reduction	Separation Promotion
Cooling (Gas)	Drag Reduction Transition Delay	Separation Promotion
Momentum Introduction without mass exchange	Separation Delay Drag Reduction Circulation Improvement	

extended to a cambered aerofoil section. This cambered aerofoil was studied experimentally and numerically. The work was extended to study the parameters affecting the ABD performance in more detail. In order to try to optimise the performance a computer based semi-stochastic optimisation tool was utilised. Attempts were made to optimise the geometry of the ABD using genetic algorithms in combination with CFD predictions. The numerical predictions were validated against published data (for the smooth case) and by means of measurements in a large, sophisticated wind tunnel at the University of Bath thereby removing some of the restrictions which result from the small size of the tunnel in the previous work.

Chapter 3

The Application of Computational Fluid Dynamics to Determine the Aerodynamic Characteristics of Aerofoil Sections

Physical experiments are the most reliable source of information for flow characteristics of aerofoil sections. However, laboratory work is often subject to limitations caused by restrictions on the model dimensions and disturbances to the flow by the measurement equipment, etc. Moreover the experimental solution of these problems is often prohibitively expensive or virtually impossible. For fluid dynamic and thermodynamic processes computational fluid dynamics (CFD) provides a powerful alternative tool to overcome many of these limitations. Relatively low costs, speed, completeness of information and the ability to achieve flow predictions for non-scaled model dimensions are the strengths of CFD. However, drawbacks of the technique are those associated with theoretical methods namely errors and the assumptions of the mathematical models and numerical methods. Thus a computational model always has to be validated.

The programs included in most commercial CFD packages can be divided into the three main applications; the pre-processor, the solver, and the post-processor. Within the pre-processor the physical flow system is modelled by means of a mesh of discrete grid points which is applied to the flow domain. This data is then written to a file to be further processed by the solver. Depending on the formulation of the solution strategy the mesh consists of either structured or unstructured hexahedron and/or unstructured

tetrahedron meshes. Pre-processing also includes solver, fluid and model specifications.

Different solution principles are used for CFD, based mainly on either finite element, finite difference or control volume formulations. All of these have merits and disadvantages with respect to efficiency, accuracy, and flexibility. The solver used in the present study, was based on the control volume formulation and can be regarded as a ‘quasi-hybrid’ method, due to the use of a finite element mesh and their formal equivalence to the finite difference method [30].

The inclusion of turbulence into the computation further divides CFD methods into:

- direct numerical simulation (DNS),
- large eddy simulation (LES), and
- Reynolds-Averaged Navier-Stokes (RANS) techniques.

DNS codes are based on the idea that turbulence, independent of its scale and complexity can be represented as viscous flow which locally obeys the Navier-Stokes equation. The resultant necessity for sufficiently fine grids makes this method impractical for many applications with present computer technology [31]. Large eddy simulation as the name suggests accounts for turbulence by simulating the larger eddies [32]. This approach is of increasing interest and is implemented in some commercial CFD codes. However, the LES method is still not as widely used and has not been validated for such a range of applications as the RANS method. The RANS method is based on the stochastic evaluation of the turbulent behaviour of the flow. Here, the mean flow variables are described by their time averaged quantities and the additional Reynolds-stresses, as discussed in 2.1. This technique proved to be economical but has its drawbacks due to the methods used to account for the Reynolds-stresses (turbulence modelling) and the treatment of the near wall flow (wall functions). A variety of turbulence models are available for the RANS method, with varying suitability for different flow phenomena, such as jets, wakes, wall bounded flows and swirling flows. These models have great influence on the accuracy, duration and stability of the solution process. The application of one turbulence model to the entire computational domain complicates the selection of an appropriate turbulence model for a given CFD problem.

Finally, post-processing modules of the code cover reduction and analysis of the predicted data and graphical visualisation of the flows. This includes for example vector plots, contour plots and discrete values for all quantities for the entire computational domain.

3.1 Solution Procedure for the Control Volume Method

The control volume code (CFX) used in this study employs a curvilinear coordinate transformation to map the physical flow domain to a rectangular domain in computational space. All the equations to be solved are discretised with respect to the computational space. The general differential form of these equations reads:

$$\underbrace{\frac{\partial(\rho\bar{\phi})}{\partial t}}_{unsteady} + \underbrace{\frac{\partial}{\partial x_j}(\rho\bar{u}_j\bar{\phi})}_{convection} = \underbrace{\frac{\partial}{\partial x_j}\left(\Gamma_{eff}\frac{\partial\bar{\phi}}{\partial x_j}\right)}_{diffusion} + \underbrace{S_{\phi}}_{source} \quad (3.1)$$

where $\bar{\phi}$ represents any mean quantity involved in the computation and Γ_{eff} stands for the effective diffusion coefficient for the variable ϕ . For example, the momentum equation is obtained by using velocity components for ϕ . In this case the effective diffusion coefficient includes the dynamic viscosity, μ , of the fluid and stresses due to turbulence. Pressure is treated externally by a ‘pressure-velocity coupling’ algorithm. Equation 3.1 is integrated over the control volume and subsequently discretised by obtaining algebraic equations for each quantity at each cell (control volume) centre. All the terms in the above equation are discretised using second-order central differencing, apart from the convection term. Second-order central differencing calculates the quantity ϕ_P at the centre of the control volume by involving one node upstream, E, and one downstream, W, to the grid point, as shown in Figure 3.1. Thus, for example, for a uniform ($\Delta x_{PE} = \Delta x_{WP} = \Delta x$) and rectangular grid second-order central differencing for the diffusion term gives:

$$\left(\frac{\Gamma_e A_e}{\Delta x} + \frac{\Gamma_w A_w}{\Delta x}\right) \phi_P = \left(\frac{\Gamma_w A_w}{\Delta x}\right) \phi_W + \left(\frac{\Gamma_e A_e}{\Delta x}\right) \phi_E \quad (3.2)$$

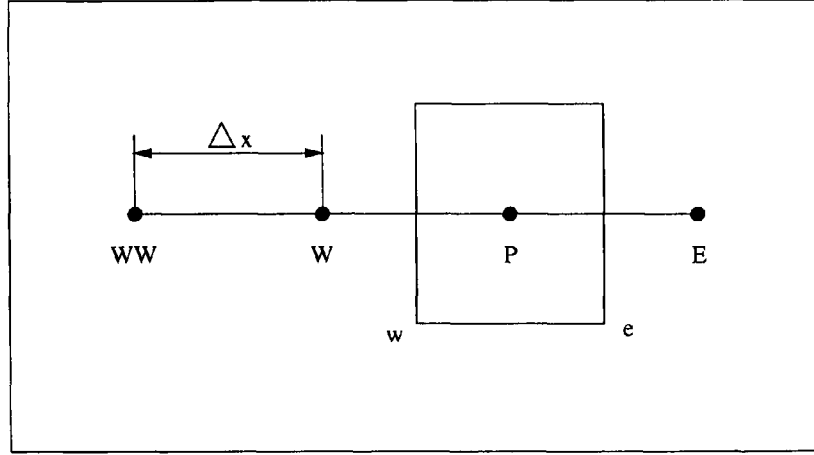


Figure 3.1: Node Notation

The involvement of an upstream and downstream node results in quadratic reduction of any discretisation error when the node distance is reduced.

The treatment of the convection terms determines the accuracy of the solution. These terms are problematic because the more accurate schemes tend to be relatively less robust or slower; a choice of discretisation methods is available. Second-order central differencing may not be a good choice for these terms due to instabilities and the possibility of non-physical solutions [30]. The discretisation of the convection terms is often done by upwind schemes. First-order upwind uses the value of ϕ at the face from the next upwind point, i.e. $\phi_w = \phi_W$ and $\phi_e = \phi_P$. This scheme is very efficient but suffers from numerical diffusion. Second-order upwind extrapolates from two upwind points to the face and is second-order accurate. Involving two upwind points and one downstream point to calculate ϕ at the face is used by the QUICK (Quadratic Upwind Differencing) scheme. Here, a parabola is used to approximate the variable profile [33]. This scheme is third-order accurate. Differencing schemes can also be blended to improve their performance. The HYBRID scheme uses first-order upwind for convective driven flows and switches to central differencing when the flow is diffusion dominated. Thus the simulation is improved compared to the first-order upwind scheme since second-order central differencing is used across streams and where the flow velocity is small [30]. The HYBRID scheme is only slightly more expensive than the first-order upwind scheme. In the above discussion the flow proceeded from left hand side, W, to

right hand side, E , of the page. A more detailed discussion of differencing schemes can be found in Appendix A.1.

The algebraic equations obtained by discretisation are passed to a linear equation solver. A flow simulation is achieved by *inner iterations* and *outer iterations*. Inner iterations provide spacial coupling of each variable within the domain, whilst the other variables are kept at a fixed value. The non-linear nature of the governing equations requires an iterative solution process where the coefficients of the algebraic expressions (i.e. matrix coefficients) are up-dated for each cycle. The inner iterations are halted either after a maximum number of iterations or when a residual reduction factor has been satisfied. When convergence of the inner iterations is achieved the variables are linked to each other by another iterative process, the so-called outer iterations. The convergence of the outer iterations indicate the quality of the solution [30]. Commonly, a computation is halted when a defined mass source residual is reached or the convergence of the residuals is stationary. Further details of the linear equation solver and the iterative solution processes of non-linear equations are given by, for example, Anderson et al [34], Abbot and Basco [32], and Versteeg and Malalasekera [35].

Pressure-Velocity Coupling

In general purpose CFD problems the initial pressure and velocity fields within the domain are usually unknown. Due to the close coupling of the governing equations, their non-linearity and the lack of a transport equation for pressure in incompressible flows, an iterative algorithm is used to approach a solution for both pressure and velocity. In compressible flows the equation of state ($p = \rho RT$) can be utilised to obtain the pressure, by using the continuity equation as a transport equation for density and the energy equation for temperature. This is not possible in incompressible computations since ρ is constant and is thus not linked to the pressure.

Pressure-velocity coupling algorithms use an iterative predictor-corrector strategy. An initially guessed pressure field is used to compute the predicted velocity components. These velocity components are then employed to update the pressures at each ‘node’ and the whole iterative procedure is continued until convergence is achieved. As for any other inner iterative procedure pressure-velocity coupling is controlled by a minimum

number of iterations, a maximum number of iterations and a residual reduction factor.

Turbulence Treatment

The stochastic approach used to account for turbulence which is used in this thesis is based on the time averaged Reynolds-equation (Equation 2.5) also known as Reynolds-Averaged Navier-Stokes equation.

As described in Section 2.1 a fluctuating quantity, $\phi(t)$, is divided into a time independent mean value, $\bar{\phi}$, and the fluctuating part, ϕ' . The Reynolds-Averaged Navier-Stokes equation is solved for the mean quantity apart from the additional stress contribution of the fluctuating part of, $\phi(t)$, as will be seen later in this section. Due to an overlap of unknowns, the *closure* problem requires treatment of the additional terms by so-called turbulence models. Classical closure methods include two-equation models, Reynolds stress models (RSM) and algebraic stress models (ASM). The latter models (RSM, ASM) solve equations for the individual components of the Reynolds-stresses. The two-equation, or two PDE (Partial Differential Equation), models are based on the ‘eddy viscosity hypothesis’ which assumes a linear relationship between the Reynolds-stresses and the mean velocity gradient. In Cartesian tensor form this is expressed as:

$$-\rho \overline{u'_i u'_j} = \mu_t \left(\frac{\partial \bar{u}_i}{\partial x_j} + \frac{\partial \bar{u}_j}{\partial x_i} \right) - \frac{2}{3} \rho k \delta_{ij} \quad (3.3)$$

where $k = \frac{1}{2} \overline{u'_i u'_i}$ [33] and represents the turbulent kinetic energy, μ_t stands for the eddy viscosity and δ_{ij} is the Kröneckers delta. The indices can be replaced by 1, 2 or 3 which then denote the components of the quantity in Cartesian co-ordinate space. The last term in Equation 3.3 makes the equation applicable to normal stresses since $\delta_{ij} = 1$ if $i = j$ and $\delta_{ij} = 0$ for $i \neq j$, so that the contribution of the normal stresses are involved when the first term on the right hand side of Equation 3.3 equals zero.

Probably the most widely employed and validated eddy viscosity turbulence model is the $k - \epsilon$ model. This $k - \epsilon$ model uses a relationship between the turbulent kinetic energy and the energy dissipation, ϵ , to compute the effective viscosity, μ_{eff} .

$$\mu_{eff} = \mu + \mu_t \quad (3.4)$$

where

$$\mu_t = C_\mu \rho \frac{k^2}{\epsilon} \quad (3.5)$$

where μ_t and μ represent the turbulent viscosity and dynamic molecular viscosity, respectively, and C_μ is a dimensionless model constant. The transport equations for the turbulent kinetic energy and the energy dissipation in conservation form are:

$$\frac{\partial(\rho k)}{\partial t} + \frac{\partial}{\partial x_j}(\rho \bar{u}_j k) = \frac{\partial}{\partial x_j} \left[\left(\mu + \frac{\mu_t}{\sigma_k} \right) \frac{\partial k}{\partial x_j} \right] + P - \rho \epsilon \quad (3.6)$$

and

$$\frac{\partial(\rho \epsilon)}{\partial t} + \frac{\partial}{\partial x_j}(\rho \bar{u}_j \epsilon) = \frac{\partial}{\partial x_j} \left[\left(\mu + \frac{\mu_t}{\sigma_\epsilon} \right) \frac{\partial \epsilon}{\partial x_j} \right] + C_{1\epsilon} P \frac{\epsilon}{k} - C_{2\epsilon} \rho \frac{\epsilon^2}{k} \quad (3.7)$$

where

$$P = \mu_t \left(\frac{\partial \bar{u}_i}{\partial x_j} + \frac{\partial \bar{u}_j}{\partial x_i} \right) \frac{\partial \bar{u}_i}{\partial x_j} \quad (3.8)$$

Equation 3.4 to 3.7 contain five adjustable constants. Commonly used values for these constants are [30]: $C_\mu = 0.09$, $\sigma_k = 1$, $\sigma_\epsilon = 1.3$, $C_{1\epsilon} = 1.44$ and $C_{2\epsilon} = 1.92$. P is the rate of production of turbulent kinetic energy. The $k - \epsilon$ model assumes isotropic behaviour of the Reynolds-stresses by Equation 3.3 [35].

Boundary Conditions

Within the boundary layer at a wall the physical phenomena of turbulence occurs at random, microscopic, spatial and temporal levels, the detail of which cannot be captured without the use of an uneconomical, highly defined grid spacing. This difficulty in achieving an exact solution is compounded by the limited accuracy of the transport equations. Therefore, the flow behaviour in the near wall regions is often approximated by so-called wall functions. No slip conditions exist at a wall and the shear stress is therefore governed by:

$$\tau_i = \left(\mu \frac{\partial \bar{u}_i}{\partial x_2} \right)_{wall} \quad (3.9)$$

3.1. SOLUTION PROCEDURE FOR THE CONTROL VOLUME METHOD

After transition the boundary layer consists of an laminar sub-layer and a turbulent region. For high Reynolds-numbers the laminar sub-layer is very small and is neglected to simplify the approximation of near wall flow. Turbulent velocity profiles are logarithmic and are described by the dimensionless velocity, u^+ , with [35]:

$$u^+ = \frac{1}{\kappa} \ln(Ey^+) \quad (3.10)$$

where κ is the von Karman constant ($\kappa = 0.41$), E is the so-called log law constant and y^+ is the dimensionless normal distance from the wall¹. For hydraulic smooth walls E equals 9.793 [30]. The equation for y^+ reads:

$$y^+ = \frac{\sqrt{\rho\tau_k}}{\mu} x_2 \quad (3.11)$$

where τ_k is the shear stress of a turbulent boundary layer at the wall. It is assumed that this shear stress can be related to the turbulent kinetic energy as [33]:

$$\tau_k = \rho C_\mu^{1/4} \kappa \sqrt{k} \frac{\overline{u_t}}{\ln(Ey_P^+)} \quad (3.12)$$

where $\overline{u_t}$ is the shear velocity parallel to the wall and y_P^+ is the dimensionless nodal distance from the wall. Thus the wall function is linked to the laminar sub-layer nearest to the wall. The production of turbulent kinetic energy may be computed by [33]:

$$P \approx \tau_k \frac{\partial \overline{u_t}}{\partial x_2} \quad (3.13)$$

This is an approximation to Equation 3.8. Within the first grid layer the (i.e. in the individual cell centres) energy dissipation is defined as [33]:

$$\epsilon_P = \frac{C_\mu^{3/4} k_P^{3/2}}{\kappa y_p} \quad (3.14)$$

where the subscript P relates all variables to the cells within the first grid layer at the wall.

Proper operation of the wall function is only ensured when the laminar sublayer is located within the first grid layer at the wall. The interface of the laminar sub-layer and

¹Most literature describes the dimensionless normal distance from the wall by the variable y^+ . Therefore this convention will be used here too, despite use of x_2 for the actual distance normal to the wall.

the turbulent region of the boundary layer is determined at $y_o^+ = 11.225^2$. Therefore the nodal distance to the wall must be well above y_o^+ . Values greater than 30 for y^+ are recommended [33].

The disadvantage of this approach in turbulent computations is the global assignment to all solid walls within the domain. Thus laminar regions are ignored and where the flow is separated or re-attached the conditions for the wall functions are not satisfied and the numerical result might be wrong [33]. So-called two-layer models should be used for such flows. These models require a y^+ at approximately one and further 20 to 30 grid points across the boundary layer (normal to the wall) and are therefore computationally very expensive. In laminar computations the boundary layer is approximated by a parabolic velocity profile.

Flow boundaries are used to introduce a mass flow into or discharge fluid out of the domain. Inlets or mass-flow boundaries and pressure boundaries are commonly used for this purpose.

- **Inlets** are subject to *Dirichlet* conditions (i.e. provision of a fixed boundary value), thus all velocity components, turbulent quantities and additional scalars need to be specified. For the supersonic case the inlet pressure also needs to be specified, whereas in subsonic flows pressure is extrapolated to the domain boundaries from downstream in the domain [30].
- A fluid can either enter or leave the domain through **mass-flow boundaries**. Here, the fluid mass flow through each mass-flow boundary within the domain is specified. This boundary type is subject to *Neumann* conditions (i.e. the gradients of all transported variables are defined). For all variables the normal gradients are set to zero ($\partial\bar{\phi}_i/\partial n = 0$, where n is the outward normal direction) apart from the velocity. Velocity is given constant normal gradients. The discrepancy between actual inflow and outflow rates is computed and subsequently corrected by scaling the velocity field at the boundary [30].
- At **pressure boundaries** a fixed pressure is set (Dirichlet conditions on pressure) and Neumann conditions are imposed on all the other transported variables

²This value refers to the default CFXTM code specification.

($\partial\bar{\phi}_i/\partial n = 0$). At pressure outlets all these variables are extrapolated from upstream. As for mass-flow boundaries the flow can enter and leave the domain through pressure boundaries, except that supersonic inflows would be inappropriate [30].

3.2 Model Validation

As discussed at the beginning of this chapter, the accuracy of numerical methods and mathematical models is limited. Therefore, these numerical models require validation using data from physical experiments.

In order to assess the reliability of the numerical predictions of flow control in the present study, prior validation of the models was carried out for two different ‘smooth’ aerofoil sections. Initially, a NACA0012 aerofoil section was investigated since, as discussed in Section 2.3.6, this wing type had been used in previous studies of the potential benefits of momentum transfer via secondary flow [1]. The use of this NACA0012 aerofoil section (see Figure 3.2) was also intended to extend these previous studies to different flow conditions, such as higher Reynolds-numbers and higher Mach-numbers. The free stream conditions were changed to provide a flow domain that was sufficiently large to avoid significant influence of the external boundary condition on the solution of the flow near to the aerofoil section.

A further validation study was carried out for a cambered NACA65-415 aerofoil type (see Figure 3.3). This aerofoil section was chosen due to:

- the camber of the aerofoil,
- the point of minimum pressure occurs at 50% chord,
- the maximum thickness is 15% of the chord length,
- the availability of experimental data.

The use of a cambered aerofoil section makes this study of the application of momentum transfer relevant to a modern wing-type. Cambered aerofoil sections are preferred to symmetrical types due to their generally better performance. Downstream of the point

of minimum pressure (i.e. at 50% chord) a strong increase of the static pressure results in adverse conditions so that significant boundary layer growth can be expected. Thus, the impact of momentum transfer on the onset of trailing edge separation at moderate angles of attack may be highlighted. So far, as the experimental studies are concerned, the use of an aerofoil section with a maximum thickness of 15% chord would assist in the installation of an air supply and discharge system in a physical model. A further reason is that data is available [26] for validation purposes.

3.2.1 Computational Set-Up

The computation of fluid dynamics problems by means of CFD requires the following initial set of data:

- a grid representing the physical domain of the problem,
- an input ‘command file’ specifying boundary conditions, fluid parameters, numerical schemes, mathematical models and convergence (stopping) criteria, etc.

The solver processes the data depending on the formulation of the solution strategy and provides the results of output quantities in either text or binary format for data reduction or flow visualisation, respectively³.

The present study employs a commercial code⁴ based on the control volume formulation, discretising the integrated form of the Reynolds-Averaged-Navier-Stokes equations. A multi-block structure represents the physical domain, described by a structured grid of regular/irregular hexahedrons.

The physical domain around both aerofoil sections (NACA0012 and NACA65-415) consisted of a ‘C-grid’ (Appendix A.2) surrounding the aerofoil itself and an ‘H-grid’ downstream of the section (Figures: 3.2 and 3.3).

In order to ensure a cell structure as orthogonal as possible the ‘C-grid’ was divided into two sections by halving the domain at the wing tip. By doing so, the cells in the vicinity of the aerofoil sections remained unaffected in shape and distance at all the

³Pre-processor, Solver, and Post-processor are provided by the commercial CFD package used

⁴CFX distributed by AEA-Technology plc.

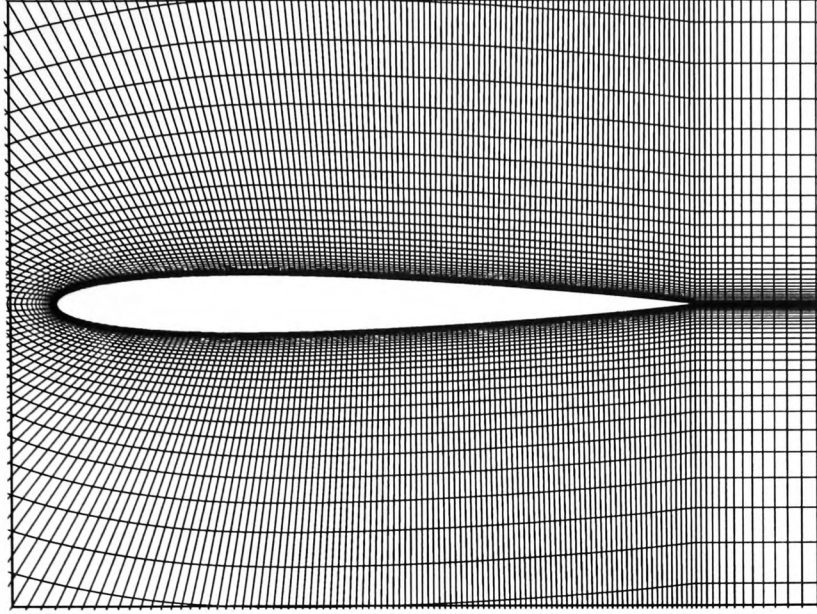


Figure 3.2: Mesh on the NACA0012 Aerofoil Section at 0° Angle of Attack

angles of attack under investigation. To keep the computational time to a minimum, the grid spacing increased progressively with an increase in distance from the aerofoil surface (see Figure 3.2 and 3.3). A uniform mesh was assigned tangentially to the aerofoil geometry whilst, on the outer ‘C’, the mesh propagated with decreasing cell sizes from its centre. Such distribution develops naturally when an orthogonal cell structure at the aerofoil is attempted since a large proportion of the aerofoil surface is almost horizontal.

Table 3.1: Data for Grid-Independent Computation

	cell no.	prop. type	prop. factor
Aerofoil	250	uniform	1
‘C-grid’	250	two way	1.05
‘H-grid’ in x	50	one way	1.1
‘H-grid’ in y	98	two way	1.17

A grid independence study resulted in a computational domain having the cell numbers and propagation ratios given in Table 3.1. As can be seen in Figures 3.2 and 3.3 the smallest mesh dimensions within the ‘H-grid’ are located at the trailing edge

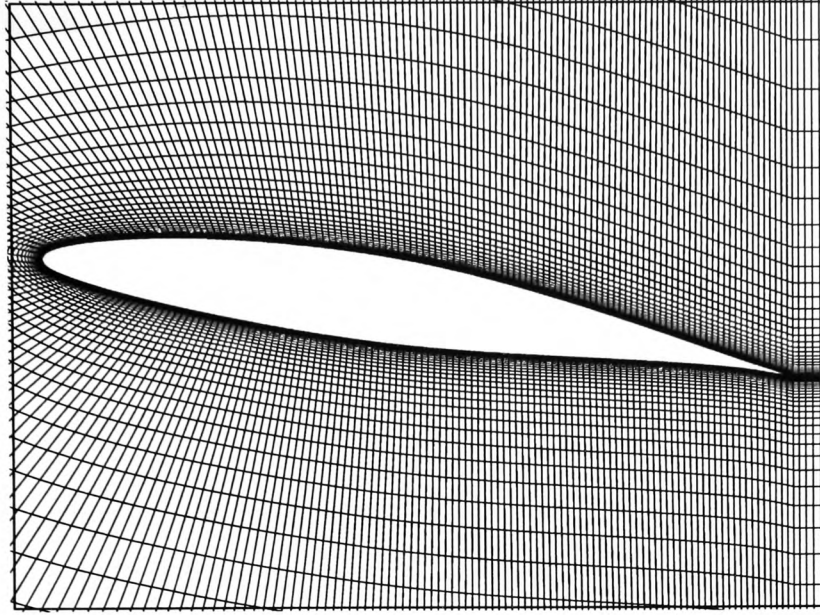


Figure 3.3: Mesh on the NACA65-415 Aerofoil Section at 12° Angle of Attack

of the aerofoil sections. In order to establish a grid point distance, y , normal to the aerofoils which satisfied the requirements of the wall function approach for a turbulent boundary layer (i.e. $y^+ > 30$), a flat plate approximation for y^+ was used [2], where:

$$y^+ = 0.172\left(\frac{y_P}{L}\right)Re^{0.9} \quad (3.15)$$

where L stands for the characteristic length (i.e. the chord length) and Re represents the Reynolds-number based on this chord length. Therefore, y_P was assigned at the trailing edge of the aerofoil section. This approximation yielded good results so that wall function requirements were satisfied for almost all computations. Further grid point data were obtained by use of the grid propagation formulae shown in Appendix A.3.

The far-field boundaries were located ten chord lengths from the aerofoils, to avoid any significant influence of the boundary conditions on the flow in the vicinity of the aerofoil. Also, smaller domains could not be used due to convergence difficulties.

Solver Specification

In the following section the specification of the most important input settings for the computation of the smooth aerofoil sections is discussed. A complete command file is given in Appendix A.4.

The convection terms of the transport equations for momentum are discretised by a total variation diminishing (TVD) scheme. Due to the type of flux limiter setting, the scheme is referred to as the ‘Van Leer’ scheme. TVD schemes are modifications of higher-order upwind schemes which use two upwind points (W and WW; see Figure 3.1) to compute values of fluid quantities at the west face of the control volume. The east face quantities are predicted as functions of the west point and the control volume centre itself [30]. TVD schemes ensure oscillation free solutions [35] and therefore have been found to be useful in flows with high velocity and pressure gradients [30]. All the other equations were discretised using a HYBRID scheme, which uses central differencing when the mesh Péclet, Pe , number is smaller than 2 (i.e. in diffusion dominated problems). If $Pe \geq 2$ the scheme switches to upwind differencing (i.e. convection dominated calculation). The mesh Péclet number is governed by the ratio of convection to diffusion quantities ($Pe = (\rho u)/(\Gamma/\delta x)$) and is therefore a measure of the relative strength of the two phenomena [35]. Default linear equation solver was employed to solve the discretised finite volume approximations.

Turbulence was treated using the RNG $k - \epsilon$ turbulence model which is a modification of the standard $k - \epsilon$ model (Equation 3.6 and 3.7) for high Reynolds-number flows [30]. The scheme derives from a so-called re-normalisation group (RNG) analysis of the Navier-Stokes equation and differs from the standard $k - \epsilon$ model in the set of model constants and in modification of the ϵ -equation, as follows:

$$\frac{\partial(\rho k)}{\partial t} + \frac{\partial(\rho \bar{u}_j k)}{\partial x_j} = \frac{\partial}{\partial x_j} \left[\left(\mu + \frac{\mu_t}{\sigma_k} \right) \frac{\partial k}{\partial x_j} \right] + P - \rho \epsilon \quad (3.16)$$

and

$$\frac{\partial(\rho \epsilon)}{\partial t} + \frac{\partial(\rho \bar{u}_j \epsilon)}{\partial x_j} = \frac{\partial}{\partial x_j} \left[\left(\mu + \frac{\mu_t}{\sigma_k} \right) \frac{\partial \epsilon}{\partial x_j} \right] + C_{1\epsilon}^* P \frac{\epsilon}{k} - C_{2\epsilon} \rho \frac{\epsilon^2}{k} \quad (3.17)$$

where, $C_\mu = 0.0845$, $\alpha_k = \alpha_\epsilon = 1.39$, $C_{1\epsilon} = 1.42$, $C_{2\epsilon} = 1.68$ and

$$C_{1\epsilon}^* = C_{1\epsilon} - \frac{\eta(1 - \eta/\eta_o)}{1 + \beta\eta^3}$$

where $\eta = \sqrt{\frac{P}{\mu_t}} \frac{k}{\epsilon}$, $\eta_o = 4.377$ and $\beta = 0.012$ [30]. For the present case the model was found to be useful, since it is only slightly more computationally expensive to run than the standard model and provided improved performance at stagnation points and with flows with large strains (i.e. for curved boundary layer) [35].

All computations were halted when all quantities showed stationary convergence. This was generally achieved after 1000 outer iterations. For the 16° attack case ‘false timesteps’ under-relaxation was used to converge the computation after a total of 5000 iterations.

Pressure-velocity coupling was achieved by an Pressure Implicit with Splitting of Operators (PISO) technique. The PISO method uses a second pressure-velocity coupling equation to improve the solution of the momentum equations whilst maintaining continuity. Although, the number of inner iterations is increased, the more accurate solution of the momentum equations may reduce the overall number of outer iterations [30].

Default (no slip, no heat transfer) boundary conditions were assigned to the aerofoil surfaces. Within the grid generation package inlet conditions were pre-assigned to boundaries upstream of the aerofoil section on the outer ‘C-grid’ and were specified as follows:

```
>>MODEL BOUNDARY CONDITIONS
>>INLET BOUNDARIES
PATCH NAME 'INLET1'
U VELOCITY 5.0000E+01 (m/s)
V VELOCITY 0.0000E+00 (m/s)
K 1.0000E-04 (m2/s2)
EPSILON 1.0000E-04 (m2/s3)
```

The use of the turbulence model requires specification of turbulence quantities at the inlet boundary. Due to the size of the domain and the inevitable viscous damping of

turbulence, all the turbulence quantities specified at the inlet decayed before the flow reached the aerofoil section, so that these quantities were kept at the default low levels. All the other outer boundaries were subjected to pressure boundary conditions with the pressure assumed to be atmospheric (i.e. $p_{at.} = 1013 \text{ mbar}$, see Appendix A.4).

It should be noted that it was not possible to find the optimal solution procedure for the aerofoil computation. The number of available computational options and the limitations on computational expense constrained the configurations which were studied. This present model, nevertheless, yielded valid and representative results as described in the next section.

3.2.2 Validation of the Computations for a Smooth Aerofoil Section

The performance of aerofoil sections is determined by non-dimensional parameters, which relate the drag, D , and lift, L , forces acting upon the section to the velocity head in the main stream, q_∞ , and the plan area of the wing, A . The resultant so-called drag, C_D , and lift, C_L , coefficients are then defined as:

$$C_D = \frac{D}{\frac{1}{2}\rho U_\infty^2 A} = \frac{D}{q_\infty A} \quad (3.18)$$

$$C_L = \frac{L}{\frac{1}{2}\rho U_\infty^2 A} = \frac{L}{q_\infty A} \quad (3.19)$$

For the two-dimensional case the section drag and lift coefficients are related to a unit span of the aerofoil (i.e. $\text{span} = 1 \text{ m}$), thus the area of the aerofoil section is represented by the chord length. Lift and drag forces are mutually perpendicular with the drag force aligned parallel to the main flow direction.

These forces can be measured in several different ways. In wind-tunnel tests direct measurement with a balance system usually provides the most reliable data for lift and drag. In free-flight experiments pressure measurements from tappings on the wing and wake profile analysis may approximate the performance of wings.

In the present validation the computed lift force was determined by the integration of all the pressure and shear components in the lift direction so that [36]:

$$L = \oint_s p dA \cos\theta + \oint_s \tau_w dA \sin\theta \quad (3.20)$$

where s denotes the integral over the surface of the wing section. The required data are provided by the computer model and can be converted directly into the appropriate coefficient.

The drag coefficient was obtained in two different ways. The first approach is analogous to the lift force determination and employed the wall forces computed by the code so that [36]:

$$D = \oint_s p dA \sin\theta + \oint_s \tau_w dA \cos\theta \quad (3.21)$$

Secondly, the drag coefficient was computed from the wake pressure and velocity profiles. The profile drag of a body, can be defined by the changes of the velocity profile in the far field, when the static pressure has recovered, by:

$$D = \int_{-\infty}^{+\infty} \rho u_{far} (U_{\infty} - u_{far}) dy_{far} \quad (3.22)$$

Jones [37] assumed that the total pressure does not change within the wake region and devised a wake traverse method which yields the drag coefficient by:

$$C_D = 2 \int_{-\infty}^{+\infty} \sqrt{\frac{P_{(total)} - P_{(stat)}}{P_{(total)\infty} - P_{(stat)\infty}}} \left[1 - \sqrt{\frac{P_{(total)} - P_{(stat)\infty}}{P_{(total)\infty} - P_{(stat)}}} \right] d\left(\frac{y}{c}\right) \quad (3.23)$$

Theoretically, Equations 3.22 and 3.23 only need to be integrated across the wake, due to zero-differences in the quantities outside the wake region. In practice it is difficult to determine exactly the extent of the wake region, particularly for lifting surfaces. Therefore, three different integration ranges (80% chord, 60% chord and 40% chord) were compared for 0° , 4° and 8° angles of attack at one chord length behind the aerofoil section. Over this range a maximum difference in C_D of 3.9% was found at 8° angle of attack (i.e. with the widest wake). This showed the relative insensitivity of the results to the integration range. However, in order to ensure capture of virtually all of the wake at higher angles the drag calculations were conducted with the largest of the above integration ranges. The flow characteristics of the wake were obtained from

a post-processing-tool in the CFD software, which allowed plotting and storage of the required data along a specified line within the domain. These calculation procedures enabled the section lift and drag coefficients to be obtained and plotted as a function of the angle of attack.

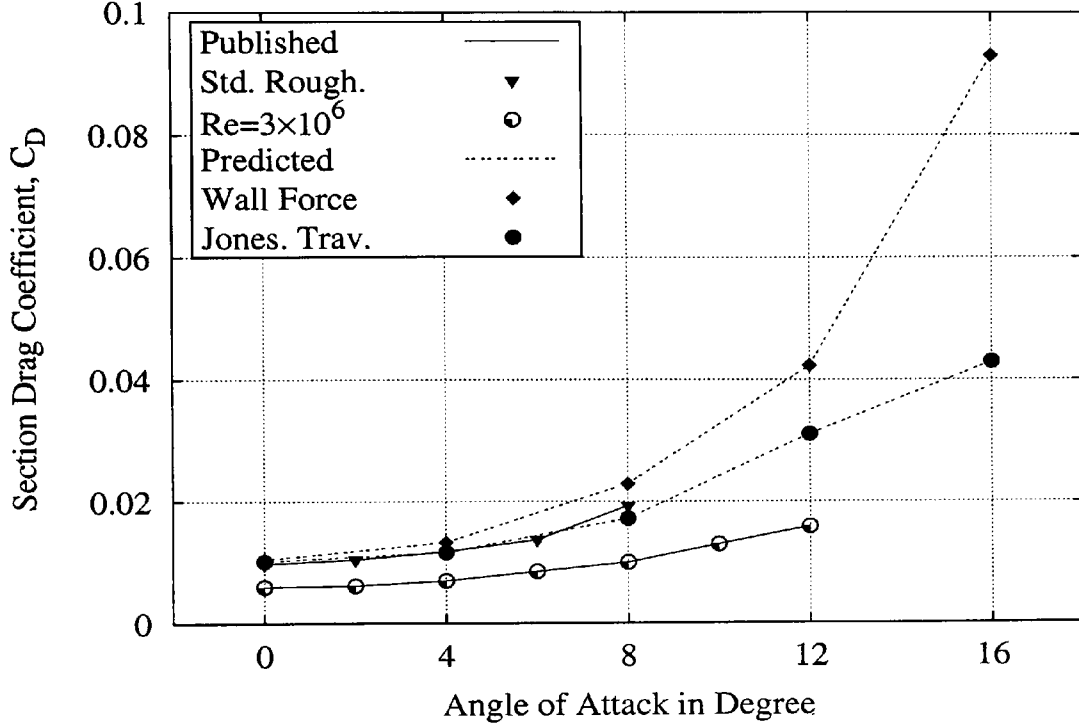


Figure 3.4: Validation of the Drag Coefficient for the NACA0012 Aerofoil Section

In Figures 3.4, 3.5, 3.6, and 3.7 the results of the numerical analysis are plotted against previously published data from Abbott and von Doenhoff [26] for two different aerofoil sections. Abbott and von Doenhoff obtained their results in the NACA two-dimensional low-turbulence wind tunnel. The tunnel had a test section 0.91 m in width and with a height of 2.28 m, and the models used in their tests had a chord length of 0.61 m. Integration of the measured pressures from the upper and lower tunnel walls provided the lift coefficients and the drag coefficients were obtained from measurements in the wake region. In Figures 3.4, 3.5, 3.6, and 3.7 the published data are denoted with *Std. Rough.* and $Re = 3 \times 10^6$. The first of these refers to measurements in which 0.28 mm diameter grain carborundum particles were installed over 5% to 10% of the chord to simulate a rough aerofoil section surface. These aerofoils were then tested

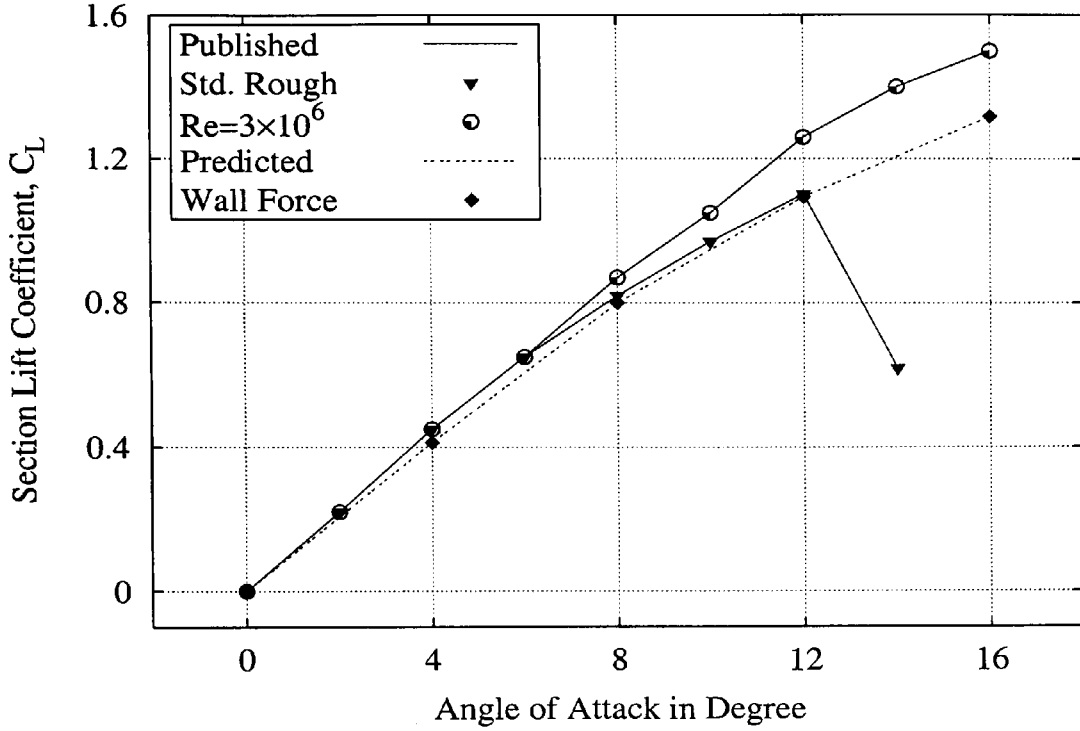


Figure 3.5: Validation of the Lift Coefficient for the NACA0012 Aerofoil Section

at a Reynolds-number of 6×10^6 . Abbott and von Doenhoff also employed a smooth aerofoil section at a Reynolds-number of 3×10^6 which was close to that in the present calculations (3.4×10^6).

Figures 3.4 and 3.5, 3.6, and 3.7 show that the magnitude of the predicted drag coefficients for both the Jones traverse wake method and for wall force integration, do not closely agree with the data published for the ‘smooth’ aerofoil section. Closer agreement was achieved by comparing the predictions to the published results for the ‘rough’ aerofoil sections. This is particularly true when Jones wake traverse method is employed to calculate C_D . The discrepancies in the assessment of the drag forces probably stemmed from the wall function approach which is used in the RANS method. This method is not capable of dealing with laminar-turbulent transition regions, see [38], and this affects the local skin friction drag and the boundary layer thickness. Integration of the skin friction plays a major role when determining the drag via a wall force integration and this is likely to have led to over-predictions of the drag coefficients. Instant sudden transition results in elevated displacement effects by the boundary layer

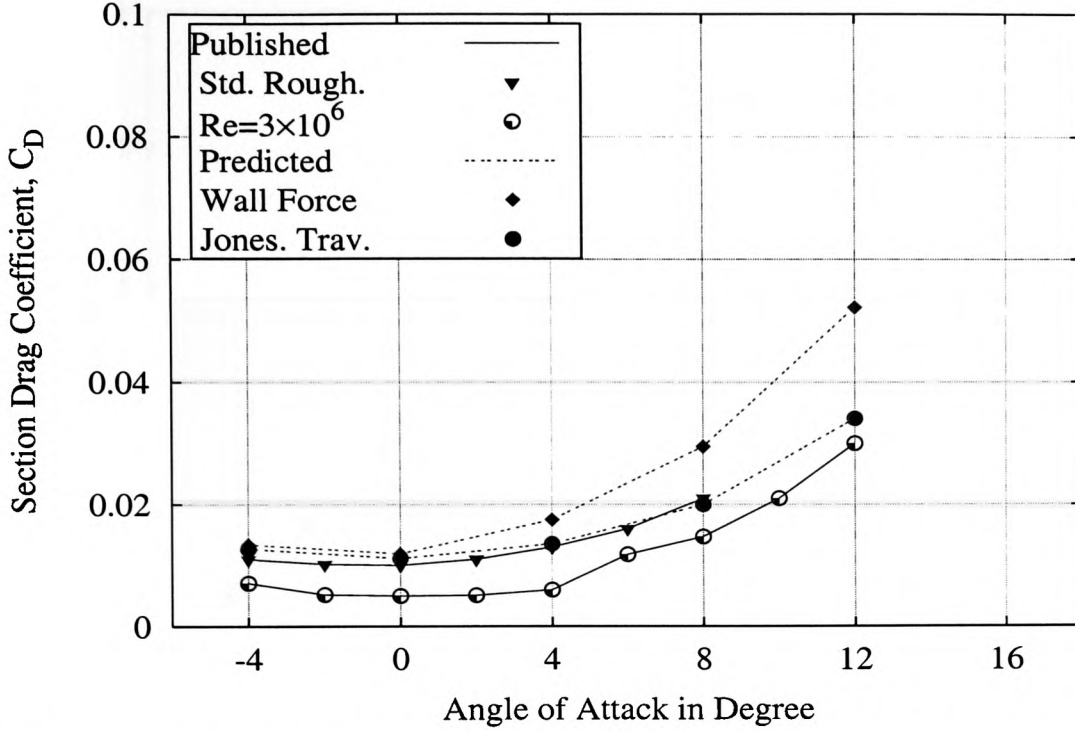


Figure 3.6: Validation of the Drag Coefficient for the NACA65-415 Aerofoil Section

with a consequent widening of wake, so that wake integration also predicts a higher drag resistance as shown in the figures. The application of artificial roughness over parts of the aerofoil section by Abbott and von Doenhoff [26] triggered almost instant transition so that there is agreement between the published data for this situation and the predicted C_D using the wake method of Jones (see Figures 3.4 and 3.6). As the angle of attack increased the results from wall force integration increasingly diverged from the data obtained from the wake method and the published experimental results. The aerofoil shape is only approximated by the CFD grid and this can lead to misalignment of the angle of the force vector. This is of particular significance at high angles of attack, see Klausmeyer and Lin [39].

The predicted characteristics of the simulated aerofoil sections together with additional information about convergence and the efficiency of the computation are presented in Tables 3.2 and 3.3. ‘RDF’ stands for ‘reduction factor’ and represents the normalised average mass source residual. The indices w.f. refer to the evaluation of C_L and C_D by integration of the forces at the wall.

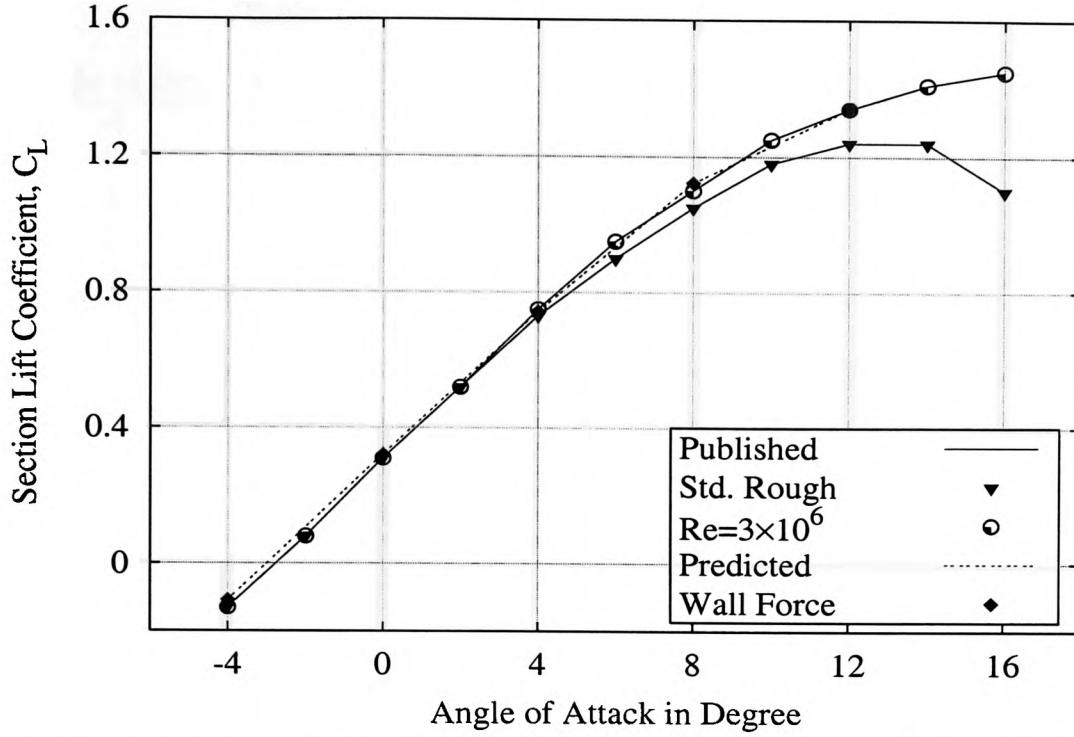


Figure 3.7: Validation of the Lift Coefficient for the NACA65-415 Aerofoil Section

Implementation of ‘false time steps’ under-relaxation was needed to converge the NACA0012 aerofoil section at 16° angle of attack due to unsteady separated flow. This approach achieved a ‘quasi’ steady state solution.

In Table 3.4 the percentage variations for both of the predicted drag calculations (based on the published drag coefficients for the aerofoil with standard surface roughness) are presented.

Overall, the reasonable agreement with the published data provided adequate vali-

Table 3.2: Data for NACA0012 Validation

Angle of Inc.	$C_{L_{w.f.}}$	$C_{D_{w.f.}}$	C_D Jones	$RDF \times 10^4$	CPU Time in sec.
0	0.0000	0.0105	0.0102	2.286	9529
4	0.4130	0.0133	0.0116	2.286	9671
8	0.8000	0.0229	0.0172	2.204	14390
12	1.0940	0.0423	0.0311	1.878	47490
16*	1.3180	0.0930	0.0429	1.878	47870

*This result was achieved by using a ‘false time stepping’ strategy

Table 3.3: Data for NACA65-415 Validation

Angle of Inc.	$C_{L_{w.f.}}$	$C_{D_{w.f.}}$	$C_{D_{Jones}}$	$RDF \times 10^4$	CPU Time in sec.
-4	-0.1080	0.0134	0.012713	2.041	9237
0	0.32141	0.0119	0.011139	2.122	9529
4	0.74331	0.0175	0.013543	2.286	9671
8	1.12290	0.0295	0.019971	2.286	14390
12	1.34010	0.0522	0.034094	3.184	47490

Table 3.4: Percentage Variation of Predicted Drag Coefficients from the Aerofoil Section with Standard Surface Roughness

	NACA0012		NACA65-415	
	$C_{D_{w.f.}}$	$C_{D_{Jones}}$	$C_{D_{w.f.}}$	$C_{D_{Jones}}$
	in %			
-4	-	-	21.81	15.57
0	7.14	4.08	19.00	11.39
4	12.70	-1.44	34.46	4.17
8	18.65	-2.14	40.80	4.90

dition of the computational set up for the numerical predictions of the aerofoil sections. This study of the drag and lift coefficients for the smooth aerofoil also indicates that the Jones wake integration method should be used to predict drag whilst wall force integration can be employed for lift calculations.

Chapter 4

CFD Study

4.1 Representation of the Aerofoil Section with an ABD

The incorporation of an air breathing device into the upper surface of the aerofoil section required changes to the computational domain which was used for the validation exercise, as described earlier (Section 3.2). The multi-block structure of the CFD code allowed the division of the ‘C-structured’ domain around the aerofoil section and Figure 4.1 indicates the block topology which was employed on the suction side of the aerofoil. Block 3 extended from the wing tip to the leading edge of the ABD; Block 2 covered the interaction zone between the ABD flow and the mainstream; and Block 1 started at the rear of the ABD and ended at the aerofoil trailing edge. The outer boundaries of these blocks were fixed by dividing the C domain into sections which corresponded the cells in the different blocks on the surface of the aerofoil section. The fourth block which covered the high pressure side of the aerofoil section is not shown in Figure 4.1. Although, as an alternative *constraints* can be used to connect blocks with different edge length, the current division of the domain provided more control over mesh refinement over the interaction zone. Along this interaction zone the tangential control volume dimension was set to a constant width of 0.0025% of the chord length. The grid distribution upstream and downstream of the interaction zone was propagated towards the trailing and leading edges of the aerofoil section to match the control volume dimensions as used previously for the model validation exercise. The propagation ratios were evaluated

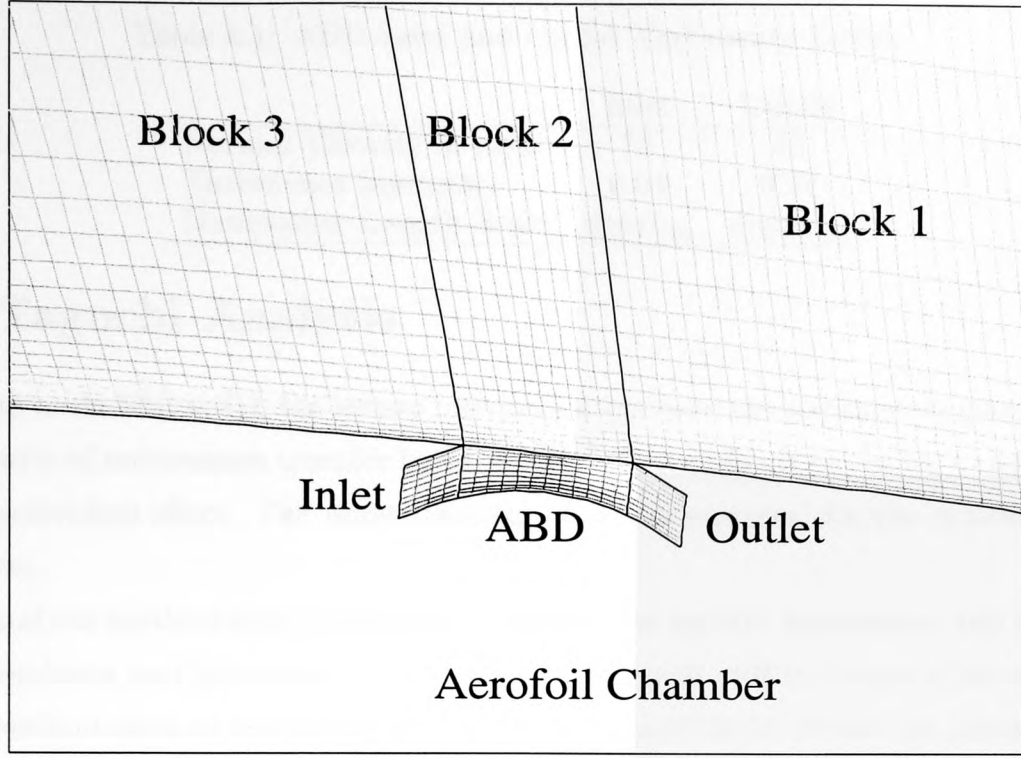


Figure 4.1: Curved ABD Shape with Multi-block Topology

from the grid propagation formulae in Appendix A.3. A symmetric grid propagation with a propagation ratio of 1.16 was chosen for the cross-stream direction of the ABD. The number of cells varied with the depth of the ABD in order to keep $y^+ > 30$. All remaining mesh properties were kept at the settings in Table 3.1.

The ‘basic’ ABD configuration was a rectangular block attached underneath the aerofoil surface where both flow boundaries were subjected to inlet conditions with equal inlet and outflow velocities. The turbulent flow computations also required specification of the turbulence properties at inlet boundaries. The turbulence intensity was set to 4% and the dissipation length scale was set according to the inlet/outlet depth of the ABD. The incorporation of an additional block and the changes in the grid distribution caused slight variations in aerofoil performance. In order to avoid error accumulation, the aerofoil characteristics, C_D and C_L , were assessed for each individual model topology with and without flow control. A smooth aerofoil section was simulated by closing the interaction zone.

Table 4.1: ABD Inlet and Outlet Turbulence Levels

	Inlet	Outlet
Normal Velocity in m/s	75	75
Turbulence Intensity	0.04	0.04
Dissipation Length Scale	$depth_{in}$	$depth_{out}$

4.2 Taguchi Analysis

According to Al-Shihry [1], the strong interaction between the parameters governing the performance of momentum transfer by an ABD made it difficult to obtain a clear picture of each individual effect. The understanding of this is essential for the optimisation of the device.

An analysis methodology, originally developed for quality assessment and optimisation of products and processes, was devised by Taguchi [40] in Japan after world war II. The method aims to assess the strength of each considered *factor* (or parameter) on the ‘quality variation of the product’. In the present study the quality of the product refers to the performance of the aerofoil section. The Taguchi analysis is based on a so-called *loss-function* and the general features of *orthogonal arrays*. A loss-function describes with a positive parabolic relation the optimal use of factors at the point of inflection. Any variation from this optimal parameter setting results in an increased loss in performance.

The results of a test series can be analysed using orthogonal arrays in order to separate the effects of each factor from the effects of the other factors. These factors are related in such a way that each *level* of every factor occurs an equal number of times. A level is a value of a factor that is kept constant throughout the analysis. Due to the recurrence of each factor the orthogonal array can be reduced in size by a carefully chosen set of experiments. This reduced orthogonal array and the provision of tabulated sets of *standard arrays* are advantages of the Taguchi method and make it cost-effective and easy to use [40].

4.2.1 Taguchi Analysis of the Momentum Transfer by means of an ABD

For the present study, which involved a NACA0012 aerofoil section, a L_8 -array was chosen using *two levels* for the factors. This type of Taguchi array allowed the study of seven individual parameters at two different levels by means of eight numerical simulations (or sets of data) which replaced the full 2^7 ($= 128$) simulations.

In order to assess the importance of parameters governing momentum transfer by an ABD, the two levels for each parameter needed to have considerable differences. This, however, had to be within a reasonable range due to uncertainties in the numerical predictions. In particular the Reynolds-numbers and angles of attack were chosen to ensure that similar convergence levels of the computations could be retained. In Table

Table 4.2: Parameter Levels

No.	Parameter	Level 1	Level 2	Units
1.	Reynolds-number	3.4×10^6	5.1×10^6	-
2.	C_i	1.5	2.0	-
3.	Distance	30	50	%
4.	Gap-Size	1.0	3.0	%
5.	Depth	2.0	1.0	%
6.	Shape	par	curved	-
7.	Angle of Attack	4	6	$^\circ$

4.2 *par* stands for a parallel interaction zone and *curved* represents an air breathing system as shown in Figure 4.1. Figure 4.2 explains all the geometric ABD parameters specified in Table 4.2. The Reynolds-number is based the chord length and the injection coefficient, C_i , determines the injection velocity with respect to the free stream velocity.

To construct a curved ABD the aerofoil section was rotated so that the ABD was located parallel to the y-axis of the domain. Vertices were created at $\Delta x = \pm 1\%$ chord and $\Delta y = -0.5\%$ chord from the lower leading and trailing edge of the ABD. A *spline* curve was used to create the bottom surface of the ABD by connecting the newly created lower leading and trailing edges and the previous lower leading and trailing edge of the ABD. Due to the relatively small injection and suction angles into the device only minor deformation was caused to the cell structure within the ABD, so that the

implementation of this flow control device did not interfere with the mesh representing the external domain.

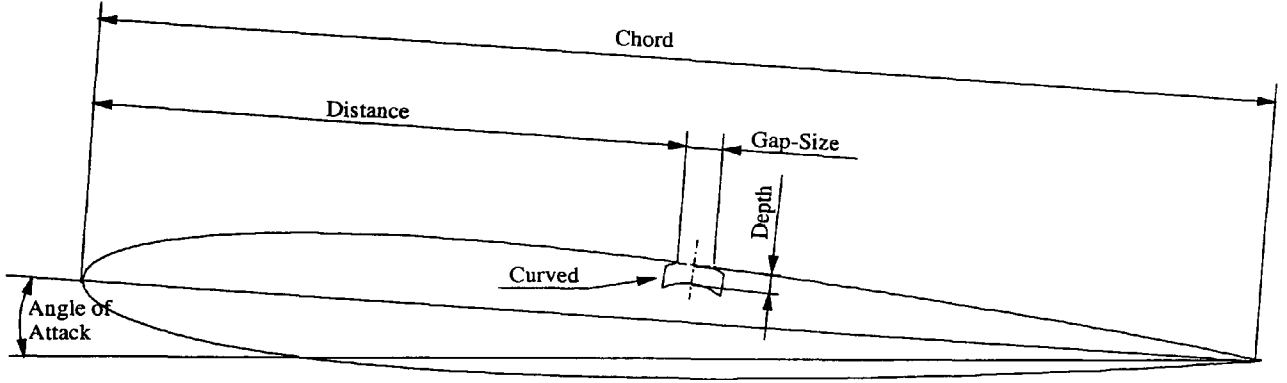


Figure 4.2: Geometric ABD Parameter

The structure of the L_8 -array Taguchi method resulted in the parameter combination shown in Table 4.3. The resultant aerofoil characteristics with flow control and for the

Table 4.3: L_8 -Array Parameter Combination

Test	$Re \times 10^{-6}$	C_i	Dist. in %	Gap in %	Angle in $^\circ$	Shape	Depth in %
1	3.4	1.5	30	1	4	par	2
2	3.4	1.5	30	3	6	curved	1
3	3.4	2.0	50	1	4	curved	1
4	3.4	2.0	50	3	6	par	2
5	5.1	1.5	50	1	6	par	1
6	5.1	1.5	50	3	4	curved	2
7	5.1	2.0	30	1	6	curved	1
8	5.1	2.0	30	3	4	par	2

The percentages of the geometrical parameters are related to the chord length of the aerofoil section

corresponding smooth aerofoil sections are given in Table 4.4. Slight differences of the drag and lift coefficients of the smooth aerofoil section at the same Reynolds-number and angle of attack were caused by the small variations of the grid on the suction side due to different gap-sizes and locations of the ABD. As mentioned in the last paragraph of section 4.1, the aerodynamic characteristics of the smooth aerofoil section were computed for each geometry individually by closing the interaction zone of the

Table 4.4: Simulation Results

Test	C_D	$C_{D_{ABD}}$	C_L	$C_{L_{ABD}}$	L/D	L/D_{ABD}
1.	0.0114	0.0111	0.4138	0.4138	36.40	37.27
2.	0.0134	0.0128	0.6094	0.6158	45.44	48.02
3.	0.0118	0.0116	0.4085	0.4110	34.62	35.42
4.	0.0139	0.0130	0.6059	0.6152	43.52	47.26
5.	0.0132	0.0129	0.6121	0.6135	46.19	47.55
6.	0.0111	0.0106	0.4123	0.4160	36.92	38.98
7.	0.0127	0.0121	0.6151	0.6192	48.31	51.13
8.	0.0109	0.0095	0.4148	0.4217	38.15	44.36

ABD.

The present application of the Taguchi method used a percentage change of the lift and drag coefficients to avoid the overwhelming influence of the angle of attack on the magnitude of the coefficients. Thus, at 6° angle of attack C_D was about 17% and C_L about 45% higher than the coefficient at 4° attack. The percentage variation was

Table 4.5: Percentage Change in C_L , C_D and L/D due to the presents of an ABD

Test	ΔC_D in %	ΔC_L in %	$\Delta L/D$ in %
1.	-2.69	-0.01	2.39
2.	-4.36	1.05	5.67
3.	-1.65	0.63	2.31
4.	-6.50	1.52	8.59
5.	-2.63	0.23	2.94
6.	-4.20	0.89	5.58
7.	-4.89	0.66	5.83
8.	-12.56	1.66	16.27

determined by:

$$\frac{a - b}{b} \times 100\% \quad (4.1)$$

where a and b represent the particular aerodynamic characteristics of the aerofoil section, C_D , C_L , and L/D , with and without flow control, respectively. The resultant percentage changes are presented in Table 4.5 and were used to perform a *level average*

analysis.

$$\bar{T}_{level} = \sum_{i=1}^n \frac{y_{i level}}{n} \quad (4.2)$$

where \bar{T}_{level} represents the average percentage change of the aerodynamic characteristic of the aerofoil for one parameter, y_i and n stand for the individual percentage change for the considered level and the total number of tests per level (i.e. four in the present case), respectively. Application of Formula 4.2 to the data in Table 4.5 resulted in the *response* of each factor and this is displayed in Table 4.6. For example, the level average for the lower Reynolds-number ($Re = 3.4 \times 10^6$) with respect to drag arose from the average ΔC_D of Test 1 to 4 (Table 4.5). The level average with C_i of 1.5 was computed using ΔC_D from Test 1, 2, 5 and 6 and so forth. The difference between the two levels indicates the potential influence of the parameters on the performance of the ABD. A list or *ranking* of the parameters according to the magnitude of the level differences is shown in Table 4.7.

Table 4.6: Response Table

Parameter	ΔC_D in %			ΔC_L in %			$\Delta L/D$ in %		
	Level 1	Level 2	Difference	Level 1	Level 2	Difference	Level 1	Level 2	Difference
Reynolds-number	-3.80	-6.07	2.27	0.80	0.86	0.06	4.74	7.66	2.91
C_i	-3.47	-6.40	2.92	0.54	1.12	0.58	4.14	8.25	4.10
Distance	-6.12	-3.74	2.37	0.84	0.82	0.02	7.54	4.85	2.68
Gap Size	-2.96	-6.90	3.94	0.37	1.28	0.90	3.37	9.03	5.66
Angle of A.	-5.27	-4.59	0.68	0.79	0.87	0.08	6.64	5.76	0.87
Shape	-6.09	-3.77	2.31	0.85	0.81	0.04	7.55	4.85	2.70
Depth	-6.49	-3.38	3.10	1.01	0.64	0.36	8.21	4.19	4.01

For the range of variables considered in this Taguchi analysis the performance of the momentum transfer device (i.e. the ABD) was most clearly influenced by the gap-size, C_i , and the depth of the ABD. Almost all the parameters, apart from the angle of attack, resulted in significant effects on the reduction in drag. The effects on C_L were less marked but were mainly governed by the gap-size. The Reynolds-number, distance,

Table 4.7: Ranking of the Flow Control Parameters

Rank	C_D	C_L	L/D
1	Gap.	Gap.	Gap.
2	Depth	C_i	C_i
3	C_i	Depth	Depth
4	Dist.	Angle	Re
5	Shape	Re	Shape
6	Re	Shape	Dist.
7	Angle	Dist.	Angle

angle of attack, and the shape of the ABD appeared to have little effects on lift. The effects of the variables on the basic aerodynamic characteristics of the aerofoil, C_D , and C_L , resulted in rankings for the lift-to-drag ratio, L/D , which were clearly governed by the variations of the gap-size, C_i , and the depth of the ABD.

From the rankings of the relative effects of the individual parameters, some preliminary conclusions can be drawn on the momentum exchange mechanism as a result of the secondary flow in the ABD. The effects are primarily related to the relative momentum of the secondary flow and the length over which the interaction occurs. The importance of the gap-size shows that insufficient momentum can be transferred to significantly augment the aerodynamic characteristics of the aerofoil, unless the length of the transfer zone is large. Increased interaction enhanced the ABD performance. As with most momentum transfer methods the velocity ratio between the fluid or solid providing momentum and the fluid receiving momentum is an important factor. The strong positive influence of the depth of the ABD may well be related to the total momentum of the secondary flow as a result of increased mass flow rate through the ABD duct. In Table 4.7 the Reynolds-number and the angle of attack have low ranking and this suggests that the relative performance of the ABD is insensitive to these parameters.

4.2.2 Validation of the Taguchi Analysis

In order to use the results of the Taguchi analysis with confidence the validity of the method required confirmation. For this purpose a prediction formula can be used to simulate any combination of levels. This is based on the *overall experimental average*,

\bar{T} :

$$\bar{T} = \sum_{i=1}^n \frac{y_{i \text{ test}}}{n} \quad (4.3)$$

Here the average is computed for all percentage changes for the aerodynamic characteristics of the aerofoil, C_D , C_L , and L/D). For the L_8 -array the prediction calculation is given by:

$$\hat{y} = A_i + B_i + C_i + D_i + E_i + F_i - 6\bar{T} \quad (4.4)$$

where A_i , B_i etc. are the values of \bar{T}_{level} (Table 4.6) for the individual parameters.

The most favourable situation for momentum transfer by the ABD was obtained from the response table by choosing the levels for each individual parameter that provide the most favourable response, i.e the lower value for C_D and the higher value for C_L and L/D . By chance a combination of these most favourable factor levels for L/D has already been used (i.e. *Test 8* in Table 4.3). Thus this case was used to compare the values from the Taguchi prediction method with the computed results from the CFD analysis to estimate the validity of the Taguchi analysis. Good agreement between

Table 4.8: Comparison of Taguchi Prediction and CFD Results

Aerofoil Characteristic	CFD	Taguchi	$ \frac{CFD}{\bar{T}_{Taguchi}} - 1 $
Drag Coefficient, C_D	-12.56%	-13.75%	0.086
Lift Coefficient, C_L	1.66%	1.76%	0.056
Overall Efficiency, L/D	16.27%	17.68%	0.079

the Taguchi predictions and the CFD results were achieved, see Table 4.8. However a further exercise was undertaken using a combination of values which had not been previously investigated (see Table 4.9). Greater differences between the two methods, as shown in Table 4.10, were now observed. The Taguchi prediction formula over-predicted the drag reduction by 11% whilst the two values for the lift coefficient differ by 46%, since relatively small variations in the value of C_L may cause substantial percentage differences.

Overall, the Taguchi method indicated that the size of the interaction zone (i.e. the gap-size of the ABD) was the most influential parameter for promoting enhanced

Table 4.9: Levels for Confirmation Run

Parameter	Level	Value
Reynolds-number	2	5.1×10^6
C_i	2	2.0
Distance	1	30%
Gap-Size	2	3.0%
Angle of Attack	1	6°
Shape	1	par
Depth	1	2.0%

Table 4.10: Comparison of Taguchi Prediction and CFD Results for the Confirmation Run

Aerofoil Characteristic	CFD	Taguchi	$ \frac{CFD}{Taguchi} - 1 $
Drag Coefficient, C_D	-11.63%	-13.07%	0.11
Lift Coefficient, C_L	1.00%	1.86%	0.46
Overall Efficiency, L/D	14.37%	16.80%	0.14

momentum transfer. In addition drag was substantially reduced by increasing the depth of the ABD and the velocity ratio C_i (i.e. increasing the injection velocity of the secondary flow). The analysis suggested that the impact of the ABD on the lift coefficient is limited and much greater percentage improvements can be achieved with respect to the drag coefficient. The importance of the gap-size and C_i with respect to C_D confirmed the conclusions of previous work by Al-Shihry [1].

However the importance of the ABD depth as an influential parameter had not been found previously and this required further investigation. The differences in the variations between Taguchi predictions and CFD suggested that further investigations using Taguchi's method would only have limited value. The two level factor analysis does not account for any non-linear interactions between the parameters and this may have contributed to the differences in the predictions.

Although the Taguchi study provided a general insight into the main parameters governing momentum transfer from the ABD via the secondary flow it does not shed light on the aerodynamic phenomena involved in the method. In order to obtain a better understanding of these phenomena a detailed parametric investigation was conducted

on a cambered aerofoil section.

4.3 Parametric Study of an ABD on a NACA65-415 Aerofoil Section

The assessment of momentum transfer by an ABD on a cambered aerofoil section required a comprehensive parametric study. This study aimed to provide a detailed investigation of all the factors (parameters), whereas the Taguchi analysis was mainly concerned at ranking the importance of parameters. Therefore, a set of parameters were chosen as the base case and each of these were then varied independently in turn. The percentage changes (when compared to the smooth aerofoil) for all three aerodynamic characteristics of the aerofoil section, C_D , C_L , and L/D , were assessed using Equation 4.1. The impact of momentum transfer from the ABD flow on the near wall velocity profile downstream to point of flow control was also investigated as well as the impact on the pressure distribution around the aerofoil section. Qualitative assessments of associated flow phenomena was also attempted by flow visualisation using the numerical predictions.

The base case values used in this study are displayed in Table 4.11, where the

Table 4.11: Values for the Common Base Case

Parameter	Value	Unit
Angle of Attack	4.0	$^\circ$
Distance	60.0	%
C_i	1.5	-
Gap-Size	3.0	%
Depth	2.0	%
Reynolds-number	3.4×10^6	-
Shape	parallel	-

geometrical dimensions are related to the chord length of the aerofoil section. The Reynolds-number corresponded to a free stream velocity of 50 m/s, a chord length of 1 m, and ambient conditions of $T = 288$ K and $p_{at.}=1013$ mbar.

4.3.1 Impact of the Parameters on the Aerodynamic Characteristics of the Aerofoil Section

The Angle of Attack

Figure 4.3 shows the percentage change of C_D , C_L and L/D as a result of keeping all the other common parameters constant and changing the angle of attack. The drag coefficient was reduced by $\approx 7\%$ at low angles of attack (e.g. 0° and 4°). Smaller improvements were achieved for -4° and 12° angles of attack. C_L improved only marginally ($\approx 1\%$) at 0° and 4° attack with the greatest improvement occurring at -4° (i.e. under conditions of negative lift). As a result, the improvement in L/D remained almost constant with values of 7.1% and 8.8% at 12° and 0° angles of attack, respectively. Due to the negative lift force at -4° the percentage improvement with respect to L/D was not valid so that this data point is omitted in Figure 4.3. The aerodynamic character-

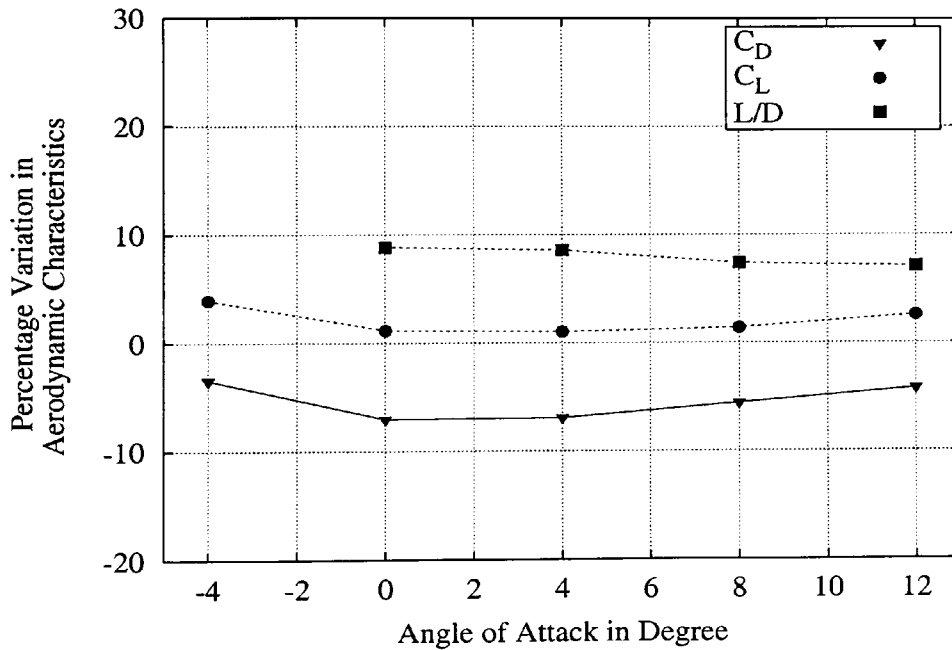


Figure 4.3: Percentage Variation versus Angle of Attack

istics of the aerofoil, C_D and C_L , versus angle of attack for the smooth aerofoil were shown in Figure 3.6 and 3.7. Consequently it is also of interest to examine the absolute improvements in aerodynamic coefficients, see Figure 4.4. The absolute improvement of C_D is almost linear, whilst the lift was augmented at an increasing rate with the

4.3. PARAMETRIC STUDY OF AN ABD ON A NACA65-415 AEROFOIL SECTION

angle of attack. Reductions in drag can also be observed in Figure 4.5¹, which presents velocity distributions in the wake region for aerofoils with and without ABD flow control. The reduced (narrowed and shortened) size of flow disturbance translates directly into changes in aerodynamic resistance. The shifted wake region to lower values of y/c also indicates improved circulation due to the ABD which resulted in the recorded lift augmentation.

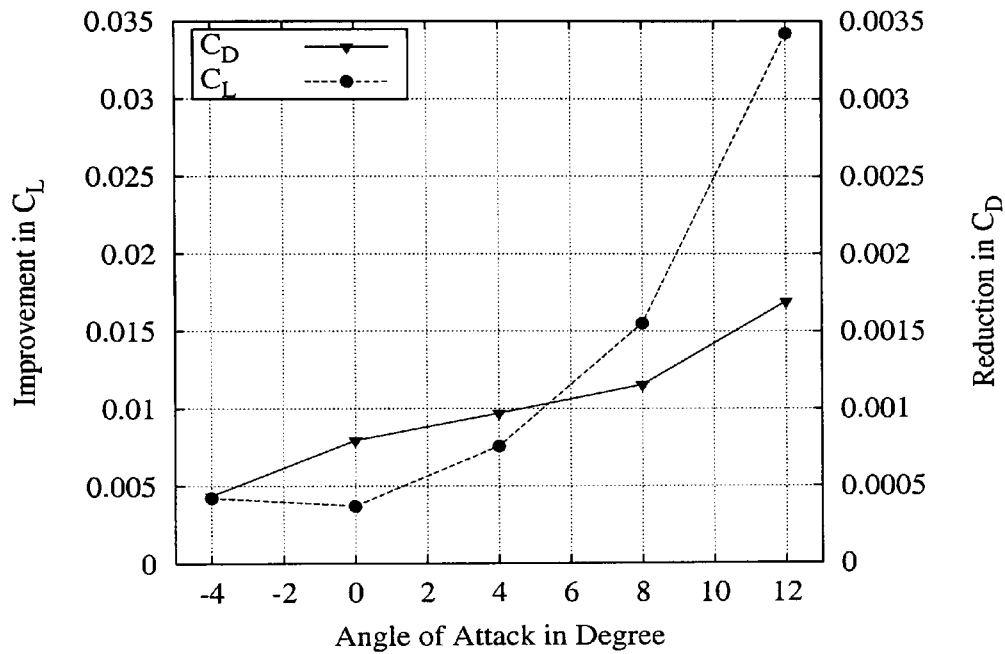


Figure 4.4: Improvements in Aerodynamic Characteristics versus Angle of Attack

¹For clarity only a selected number of discrete samples are shown.

4.3. PARAMETRIC STUDY OF AN ABD ON A NACA65-415 AEROFOIL SECTION

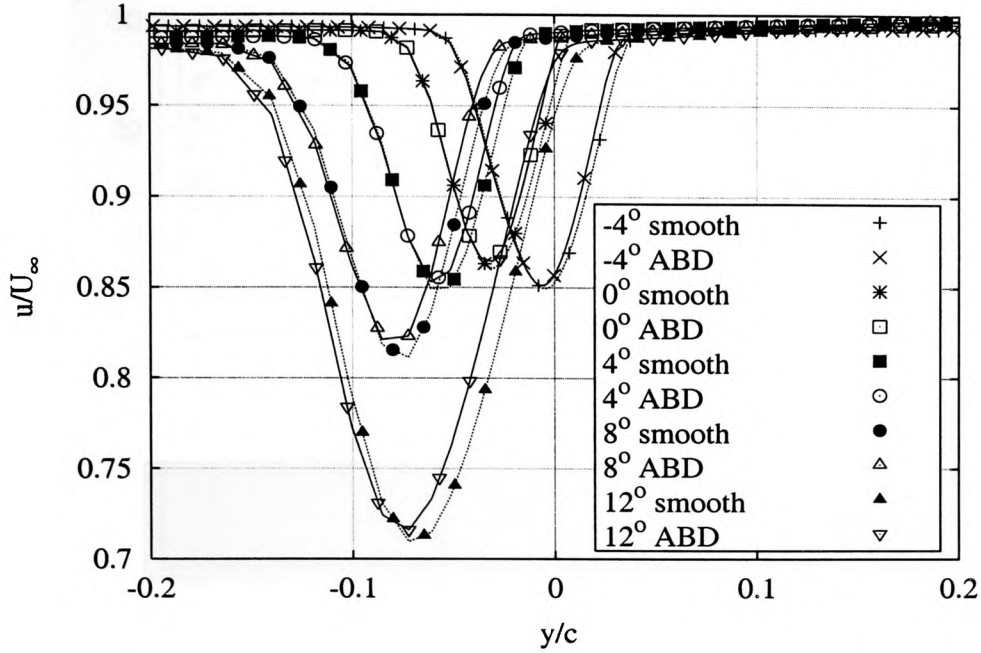


Figure 4.5: Wake U-Velocity Distribution with and without Flow Control

The Location of the ABD

Variation of the ABD position between 50% and 80% chord resulted in improvements in aerodynamic characteristics which increased as the interaction zone was moved closer towards the trailing edge (see Figure 4.6). The enhancements were almost linear so that the increase of L/D at 80% chord is 12.6%, 11.4% and 8.2% for 0° , 4° and 8° angle of attack, respectively. Thus the effects of moving the ABD towards the trailing edge are more pronounced at low angles of attack. As the near wall flow approaches the trailing edge the relative velocity between the ABD stream and the external flow increases and the greater velocity gradient provided greater enhancement of the momentum transfer between the two flows. It is also known that the free stream and slot flow turbulence levels are significant with respect to the performance of tangential injection of momentum [25]. The turbulence intensity with respect to the local mean velocity close to the aerofoil section increases from 50% chord onwards, and this may also have contributed to the better performance at high position to chord ratios. The slightly poorer percentage drag reduction at 8° conforms with the trends shown in Figure 4.3.

4.3. PARAMETRIC STUDY OF AN ABD ON A NACA65-415 AEROFOIL SECTION

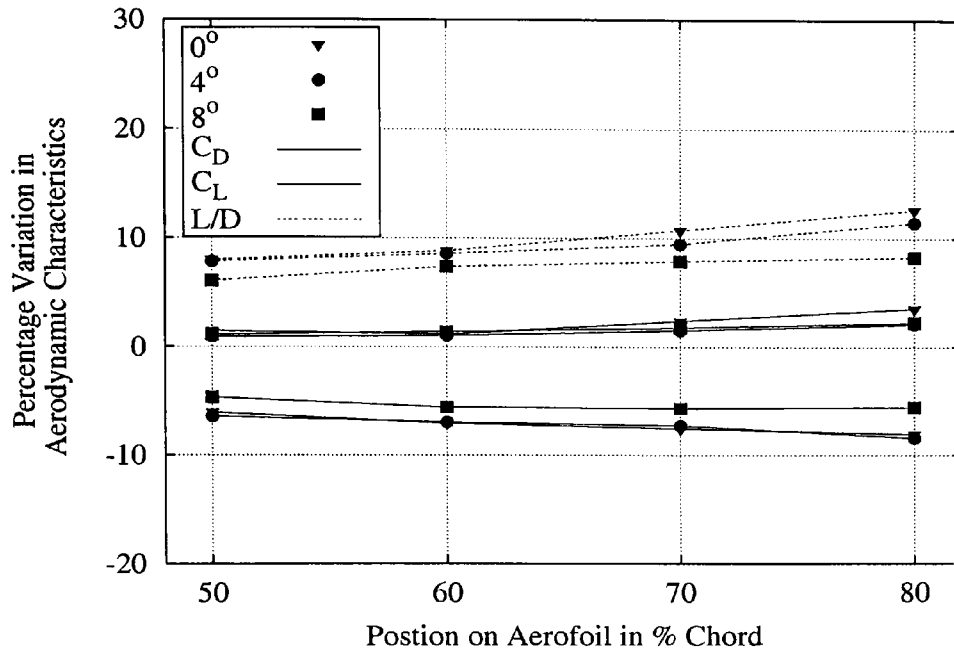


Figure 4.6: The Effects of the ABD Location on the Aerodynamic Characteristics

The Gap-Size i.e the Size of the Interaction Zone

The length of the interaction zone showed significant impact on the aerodynamic characteristics of the aerofoil. A gap-size of 1% chord only achieved minor improvements in drag ($\Delta C_D = -1.57\%$) and the lift coefficient remained almost unaffected, as can be seen in Figure 4.7. Interaction zones greater than 2% showed improvements for all the characteristics. The greatest improvements occurred at a gap-size of 5% chord with a reduction in C_D of 10.8%, an improvement in C_L of 1.7% and the overall performance, L/D , elevated by 14.1%. From the shape of the curve in Figure 4.7 it is apparent that even greater improvements would be obtained with longer gaps. However these extended interaction zones have not been investigated since bigger ABDs would not conform with the basic idea of an air breathing device which is intended to be a compact mechanism with minimum structural disturbance to the wing.

The Velocity Ratio C_i

The strongest impact on all the aerofoil characteristics was achieved by variation of the velocity ratio or injection coefficient, C_i . An arrangement with a 3% gap-size and C_i of 1

4.3. PARAMETRIC STUDY OF AN ABD ON A NACA65-415 AEROFOIL SECTION

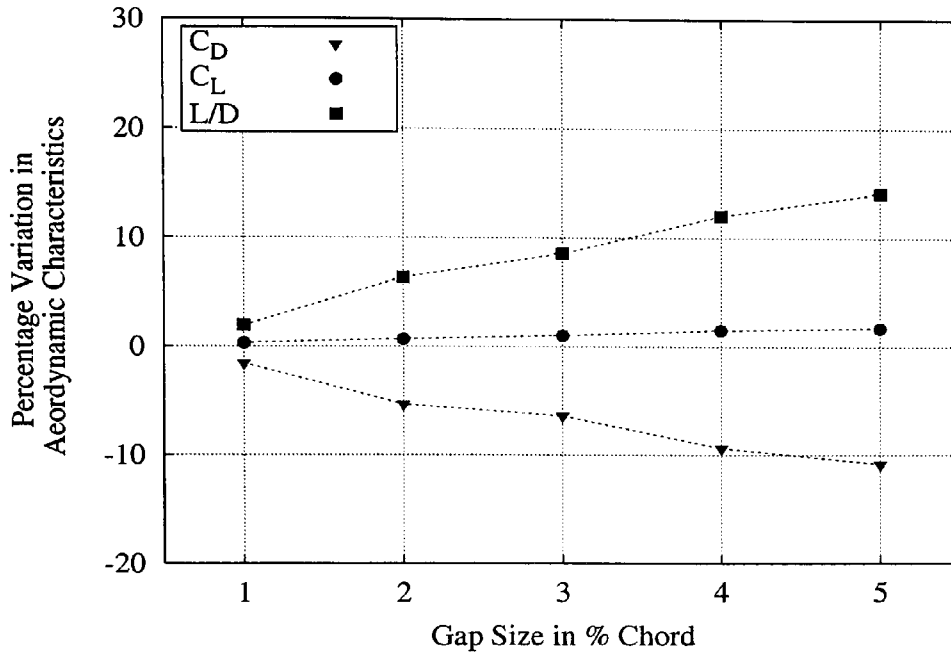


Figure 4.7: The Effect of the ABD Gap-Size on the Aerodynamic Characteristics

lowered the drag by 3.4%. Drag reductions of $\approx 19\%$ were predicted when the injection coefficient was increased to 2.5. Over the same range the lift coefficient was enhanced by 0.3% and 3.5% for $C_i = 1$ and $C_i = 2.5$, respectively. A combination of both features resulted in an improvement of 28.2% for L/D . Even greater improvements are possible at higher C_i s but it must be remembered that the pressure drop in the ABD increases strongly as the inlet velocity is increased. This will undoubtedly place an upper limit on the value of C_i and will be shown below when the power consumption of the ABD will be discussed.

The ABD Shape

In order to assess the impact of different injection and suction angles, three different ABD shapes were implemented in the NACA65-415 aerofoil section. In this study, the upper duct surface revolved around radii of 5%, 10% and 20% of the chord length, respectively, relative to the centre of the interaction zone. The angle between the flow boundaries of the ABD was chosen so that the lengths of the (curved) centreline of the ABDs were of equal magnitude. Figure 4.9 shows the geometry and the grid for

4.3. PARAMETRIC STUDY OF AN ABD ON A NACA65-415 AEROFOIL SECTION

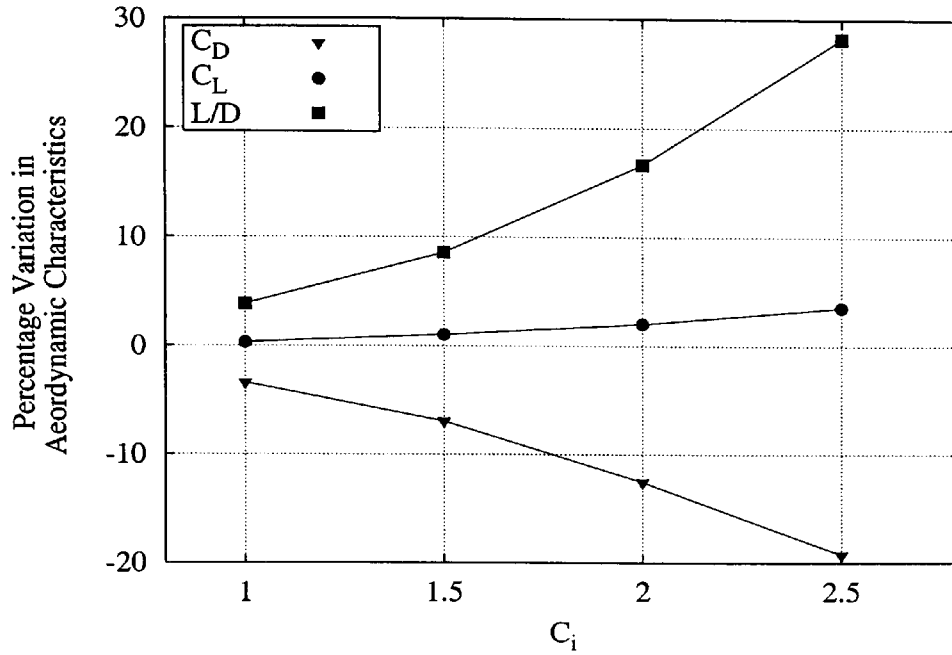


Figure 4.8: The Effects of the Injection Coefficient, C_i , on the Aerodynamic Characteristics

a *curved* ABD with a radius of 5% chord. This variation of the ABD shape had little influence on the lift performance, but the increasing curvature (i.e. the smaller radii) had a positive impact on drag reduction. An ABD with a curvature of $R=5\%$ chord reduced C_D by a further 1 *percentage point*² when compared to the drag reduction for the parallel arrangement with a corresponding improvement in L/D .

²A percentage point refers to the difference between two individual percentage variations.

4.3. PARAMETRIC STUDY OF AN ABD ON A NACA65-415 AEROFOIL SECTION

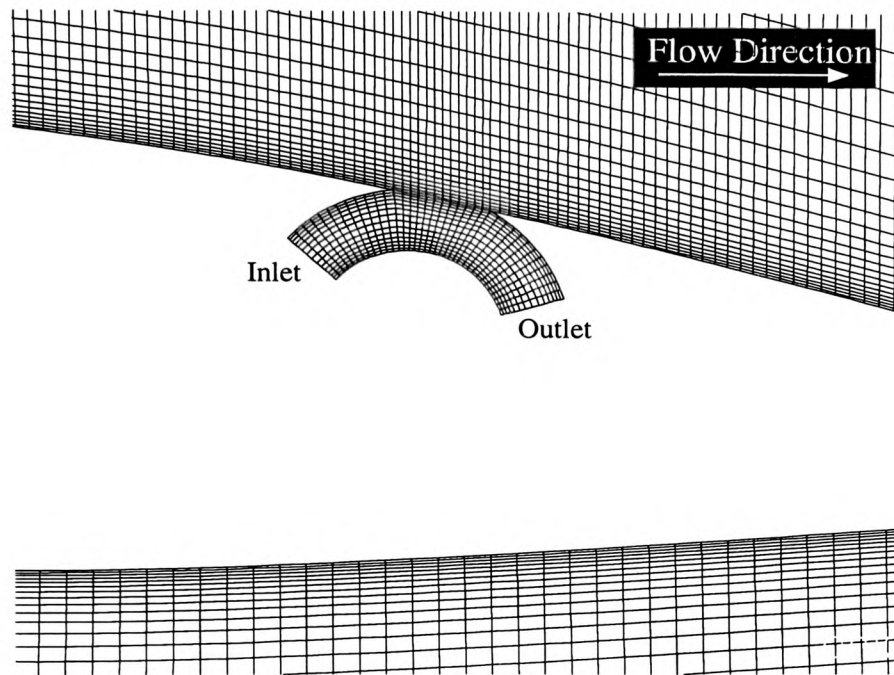


Figure 4.9: Geometry and Grid for a Curved ABD with $R = 5\%$ Chord

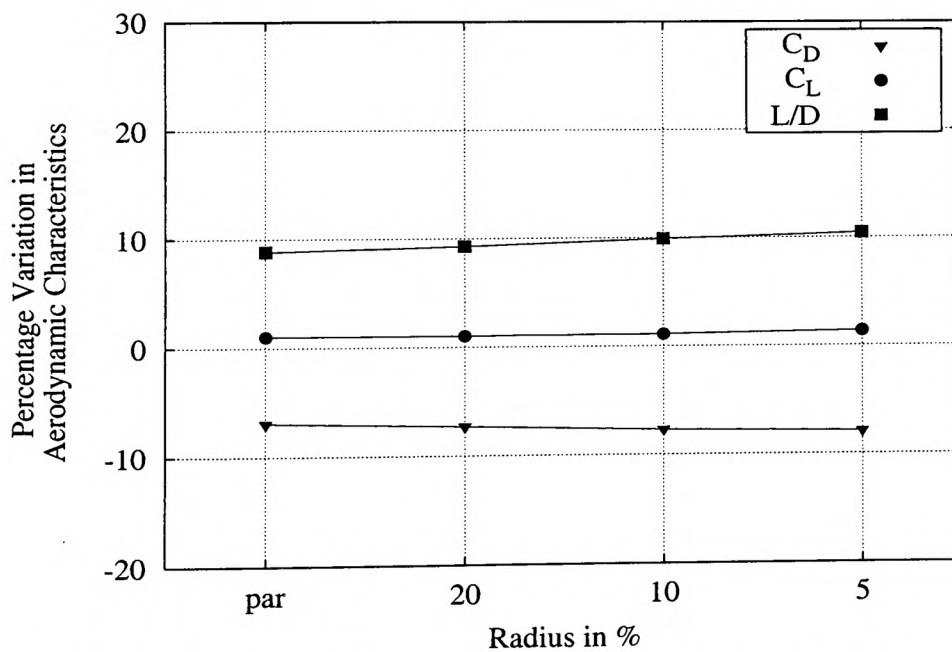


Figure 4.10: The Effect of the Radius of Curvature of the ABD on the Aerodynamic Characteristics

4.3. PARAMETRIC STUDY OF AN ABD ON A NACA65-415 AEROFOIL SECTION

The ABD Depth and the Chord Reynolds-number

The effect of momentum transfer using an ABD was relatively independent of variations in the ABD depth and the Reynolds-number, as shown in Figures 4.11 and 4.12. Here, the Reynolds-number was related to the main flow velocity and the aerofoil chord length. Due to the high Reynolds-numbers on both sides of the interaction zone (i.e. internal ABD flow and near aerofoil flow) it can be assumed that the momentum transfer was mainly driven by turbulent phenomena. For the Reynolds-numbers 0.68×10^6 and 1.3×10^6 the percentage change of C_L and of L/D showed more improvements than for higher Reynolds-numbers. The relatively thick boundary layer at low free stream velocities thus appeared to enhance the effects of flow control on C_L .

Table 4.12: Variation of the Aerodynamic Characteristics with the Reynolds-number

$Re \times 10^{-6}$	C_D	C_L	L/D
0.68	0.0178	0.711	39.89
1.36	0.0157	0.727	46.10
3.40	0.0139	0.739	52.98

The relative insensitivity to the depth of the ABD indicated that only the small fluid layer along the interaction zone was responsible for the fluid interaction. This is a useful feature since it means that the ABD mass flow rate has relatively little effect and this will help to minimise the ABD power consumption.

4.3. PARAMETRIC STUDY OF AN ABD ON A NACA65-415 AEROFOIL SECTION

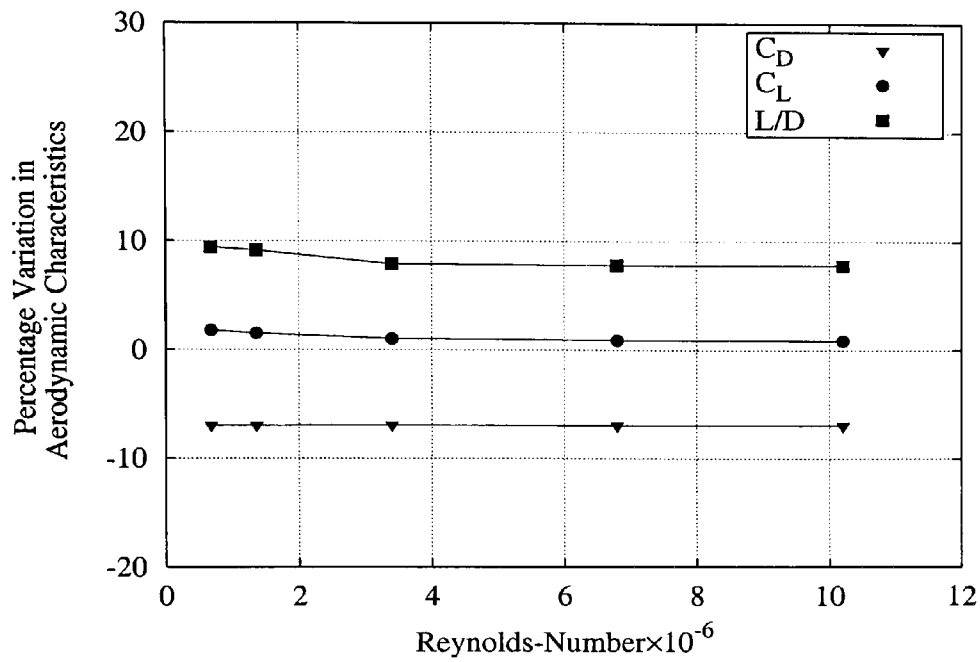


Figure 4.11: The Effect of the Chord Reynolds-number on the Aerodynamic Characteristics

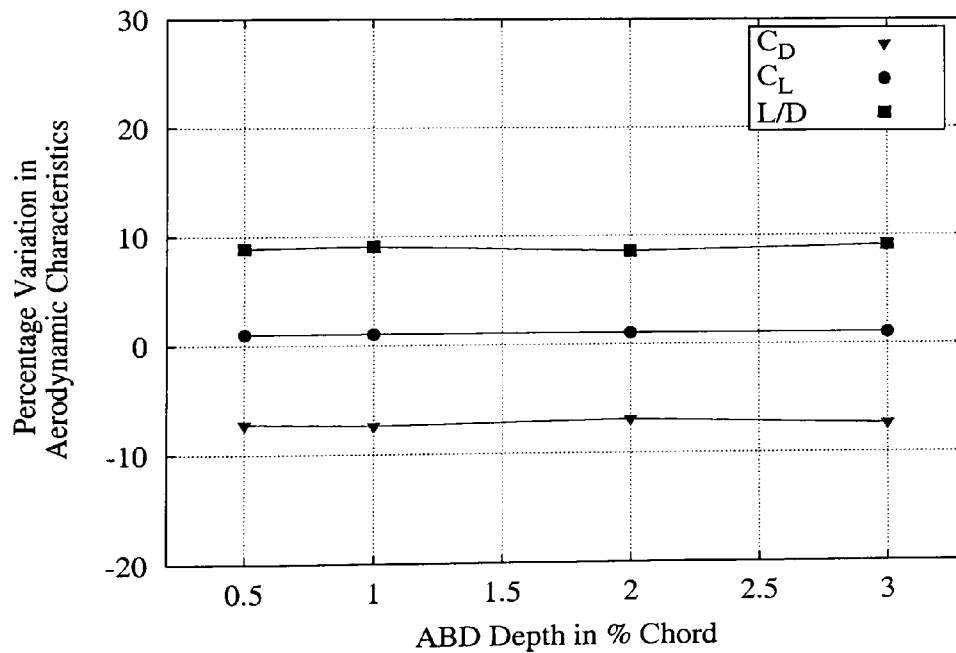


Figure 4.12: The Effects of the ABD Depth on the Aerodynamic Characteristics

4.3. PARAMETRIC STUDY OF AN ABD ON A NACA65-415 AEROFOIL SECTION

The Aerofoil Dimensions

Variation of the aerofoil dimensions by changing the chord length whilst maintaining the Reynolds-number at 3.4×10^6 had marginal impact on the performance of the ABD, as shown in Figure 4.13.

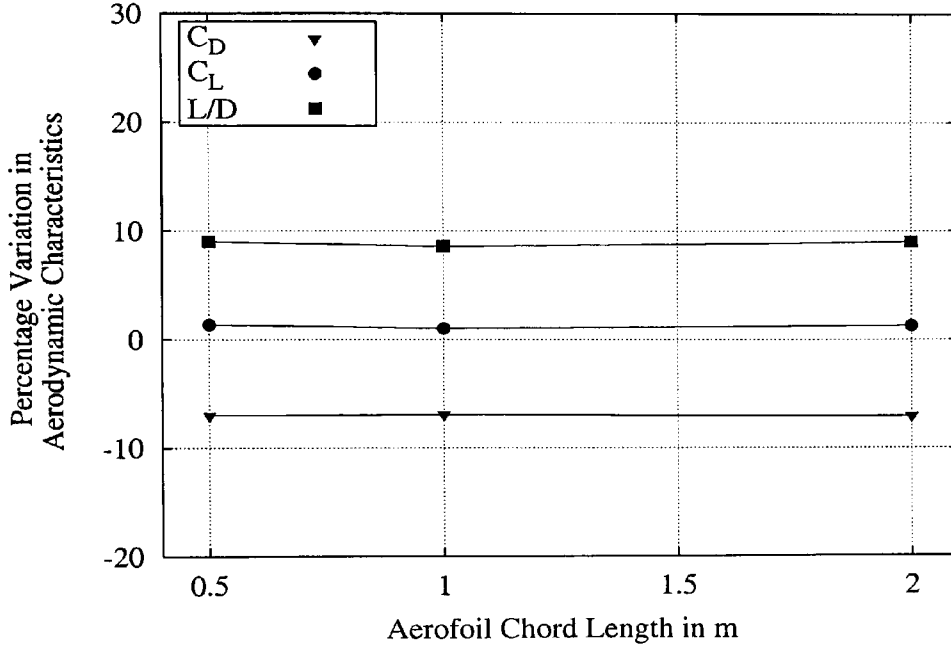


Figure 4.13: Percentage Variation of C_D , C_L and L/D with increasing Chord Length at $Re = 3.4 \times 10^6$

4.3.2 Impact of the ABD on the Near Wall Flow

The momentum introduced on the upper aerofoil surface affected the near wall flow. Figures 4.14 to 4.17 show the velocity profiles at four different locations downstream of the ABD position. These profiles were obtained from the computed velocities plotted along a vertical line at the location indicated by the titles of the individual graphs and the common base case parameters (see Figure 4.11) were applied unless stated otherwise in the graphs.

As shown in Figure 4.5, the momentum introduced into the flow narrowed and shortened the wake region. In all the graphs in Figure 4.14, 4.15 and 4.16 the secondary flow created a ‘nose’ or sharp peak of accelerated fluid at the trailing edge of the

4.3. PARAMETRIC STUDY OF AN ABD ON A NACA65-415 AEROFOIL SECTION

interaction zone. Further downstream the energy content of this ‘nose’ was distributed into the higher regions of the flow and a ‘fuller’ velocity profile remained .

The variation of the gap-size placed the ABD trailing edge at different locations, which need to be considered in Figure 4.14. For a gap-size of 1% chord only a small flow enhancement can be observed leading to the 1.57% reduction in drag (Figure 4.6), whereas the momentum contribution through a 5% gap yielded a noticeably enhanced velocity profile far downstream towards the trailing edge.

The strongest impact on the near wall flow arose at $C_i = 2.5$ (see Figure 4.15). In this case, the velocity peak at the trailing edge of the ABD exceeded the free stream velocity by more than 20%. This momentum was carried downstream so that at 80% chord the boundary velocity profile was still significantly altered.

The shape of the ABD, as defined by the different injection and suction angles had relatively little influence on the downstream velocity distribution (see Figure 4.16). The onset of the new boundary layer showed that the magnitude peak in the accelerated fluid decreased with increasing suction and injection angles (i.e. a decreased radius), whereas the opposite is true for the effect to the radius on the drag reduction. The enhancement into the flow is shifted to higher values of y/c as is marginally noticeable at the upper section of the first graph at 65% chord in Figure 4.16 .

In Figure 4.17 the impact of the ABD location on the boundary layer is shown by plotting the velocities along a line placed at each ABD trailing edge position. The magnitude of the peak velocity in the accelerated fluid decreased the further that the ABD was located towards the trailing edge of the aerofoil section. The relative enhancement of the near wall flow, however, increased as the ABD is moved towards the trailing edge. This is due to a higher velocity gradient between the local external flow and the internal secondary flow. As a result, the velocity profile was brought closer to the aerofoil wall and the beneficial effects also extended to higher y/c . This explains the general tendency in Figure 4.6 for the aerodynamic characteristics to be increasingly enhanced as the ABD is located further back.

As a result the pressure gradient $[dp/dx_1]$ (Figure 4.19) remained unaffected by the influence of the ABD.

4.3. PARAMETRIC STUDY OF AN ABD ON A NACA65-415 AEROFOIL SECTION

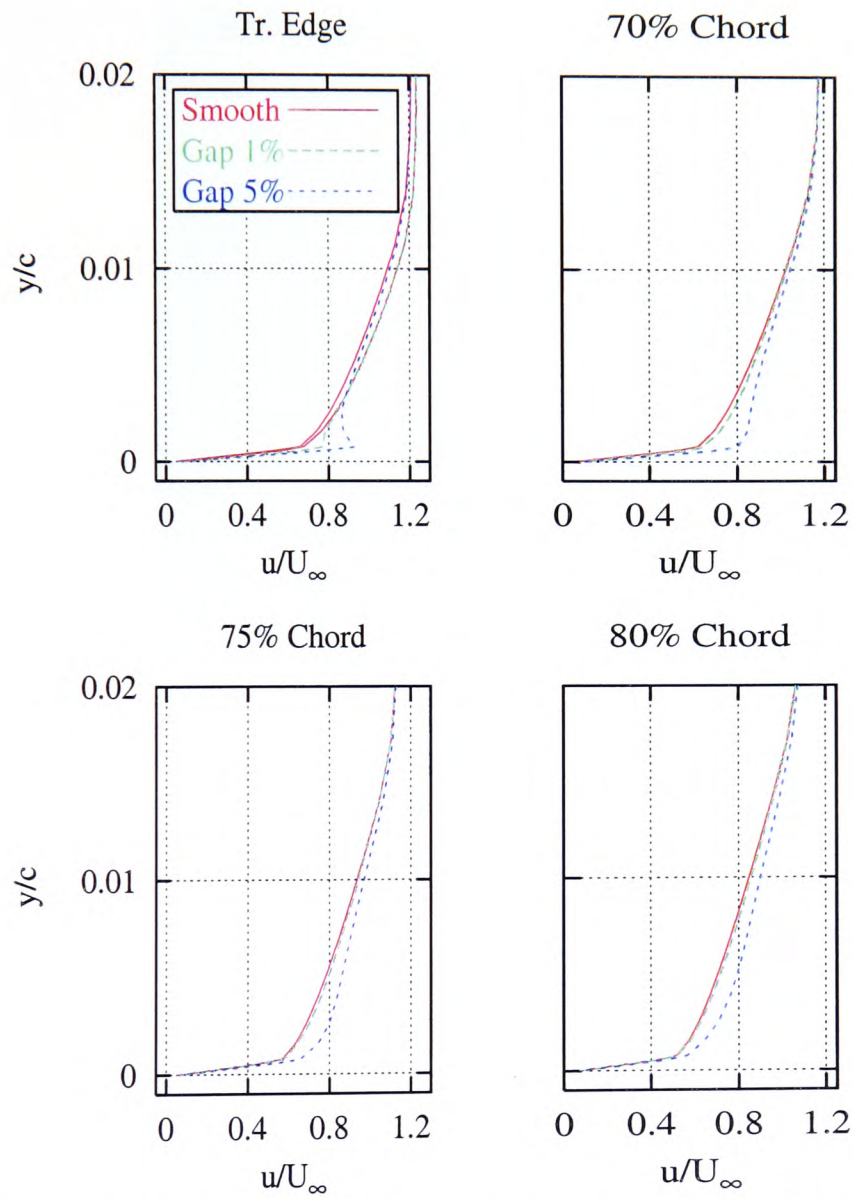


Figure 4.14: Impact of the Gap-Size on the Near Wall Velocity Profile

4.3. PARAMETRIC STUDY OF AN ABD ON A NACA65-415 AEROFOIL SECTION

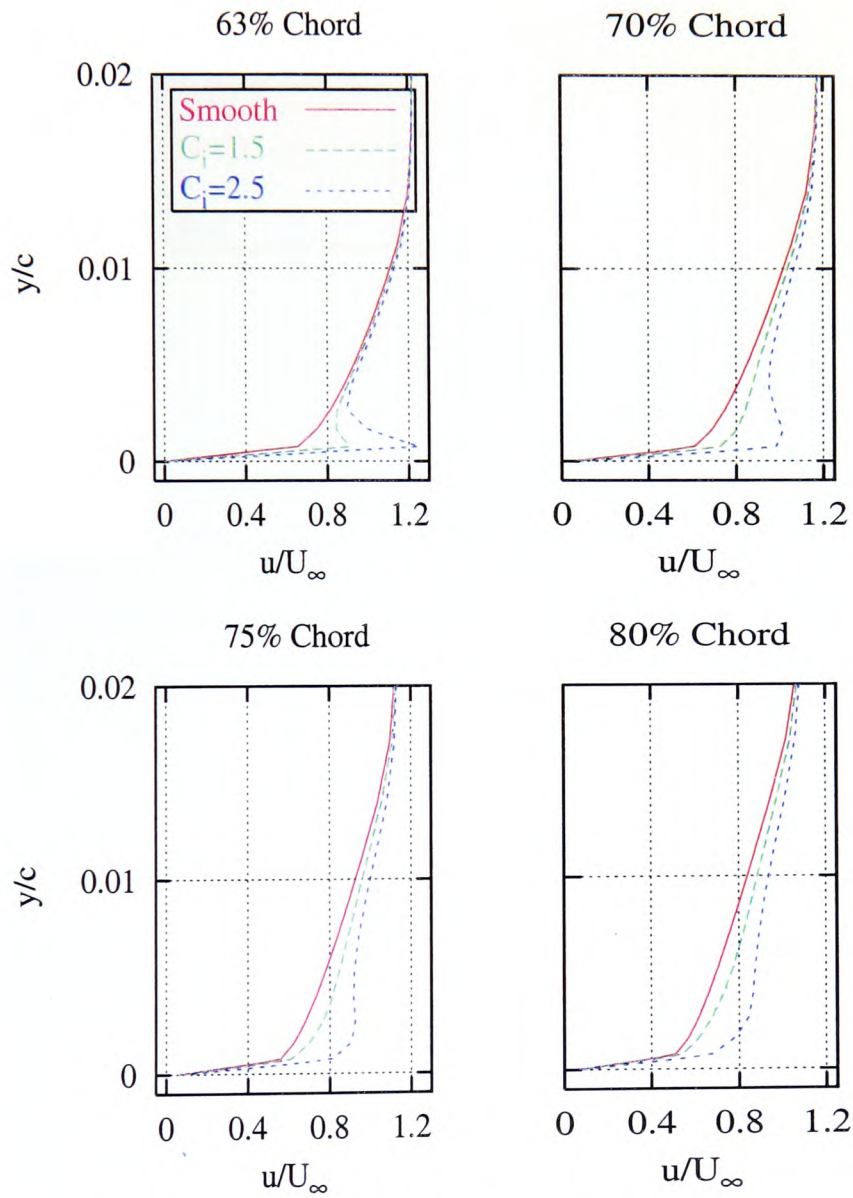


Figure 4.15: Impact of C_i on the Near Wall Velocity Profile

4.3. PARAMETRIC STUDY OF AN ABD ON A NACA65-415 AEROFOIL SECTION

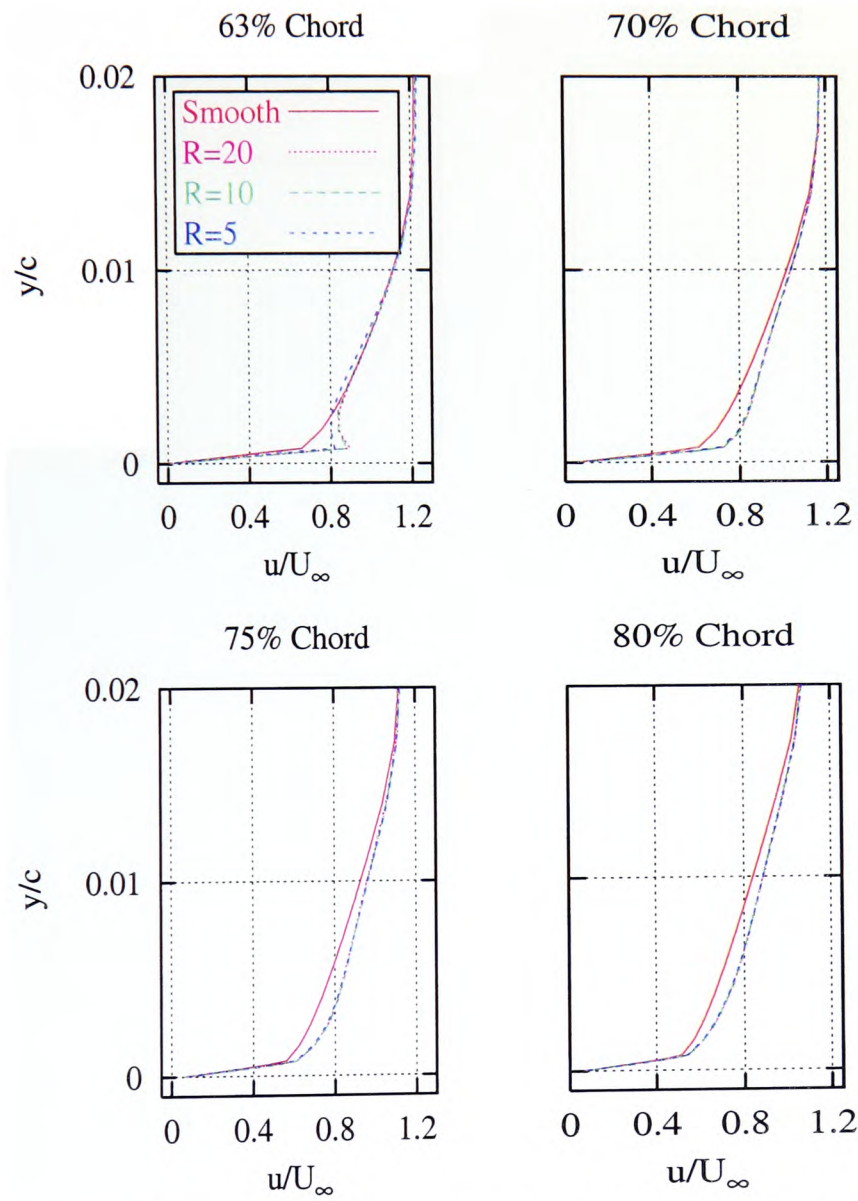


Figure 4.16: Impact of the Shape on the Near Wall Velocity Profile

4.3. PARAMETRIC STUDY OF AN ABD ON A NACA65-415 AEROFOIL SECTION

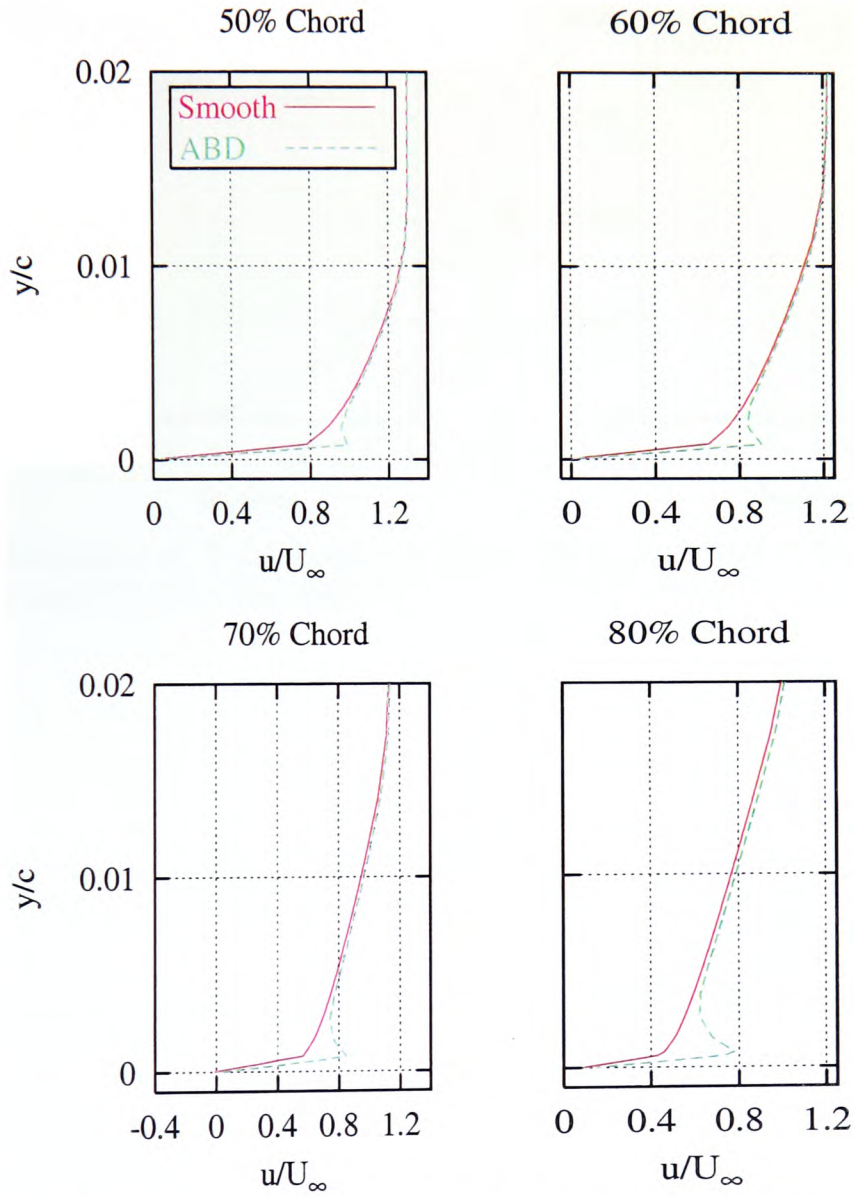


Figure 4.17: Velocity Distribution at the ABD Trailing Edge for Different ABD Locations

4.3. PARAMETRIC STUDY OF AN ABD ON A NACA65-415 AEROFOIL SECTION

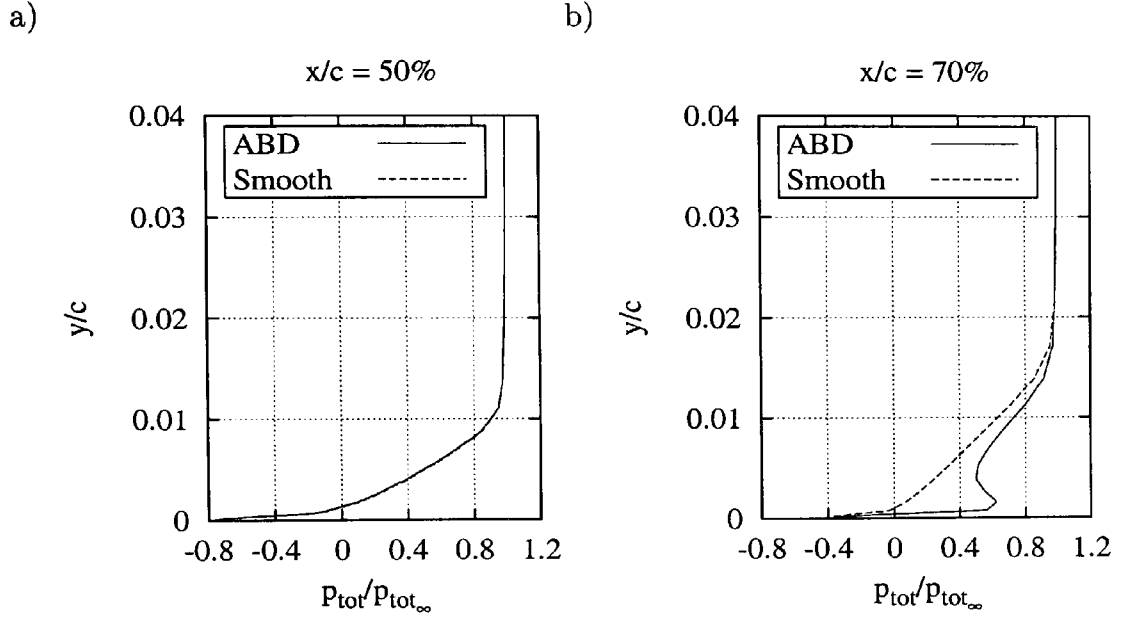


Figure 4.18: Variation of Total Pressure at a) 50% and b) 70% Chord for the Base Parameter Set and $C_i=2.5$. The ABD is located at 60% Chord

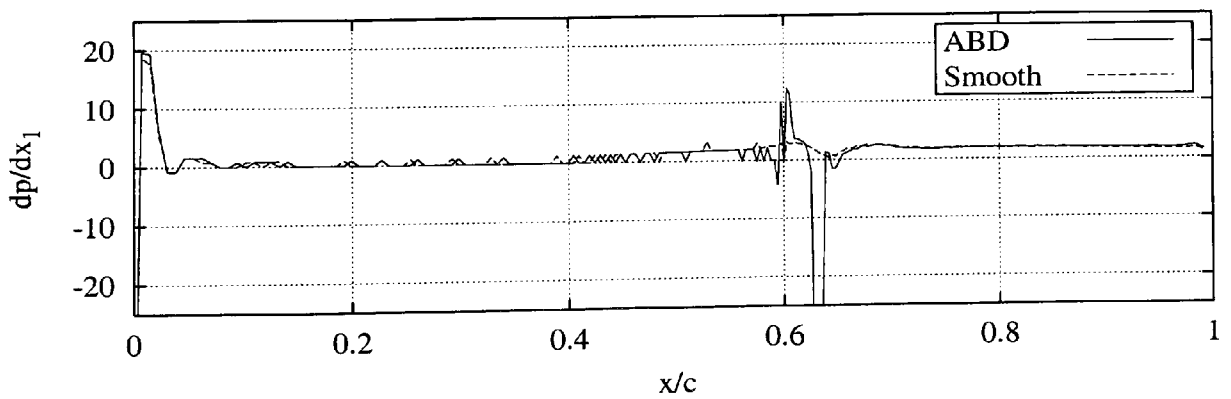


Figure 4.19: Variation of the Pressure Gradient $[dp/dx_1]$ between the Smooth Aerofoil and with an ABD with C_i of 2.5

4.3. PARAMETRIC STUDY OF AN ABD ON A NACA65-415 AEROFOIL SECTION

Upstream of the location of the flow control device the near wall velocity experienced a slight increase and the pressure profile showed a small decrease. Virtually no variation of the total pressure was detected upstream of the ABD. However, the effect of the transferred momentum can be clearly seen as a significant enhancement in the total pressure at 70% chord as shown in Figure 4.18.

4.3.3 Impact on the Pressure Distribution

Since the ABD has relatively little effect on the lift coefficient only small changes to the overall pressure distribution around the aerofoil section could be expected. The ABD had primarily only a local impact on the pressure. Generally, upstream of the interaction zone the lift pressure was positively influenced which indicated an improved circulation around the body of the aerofoil.

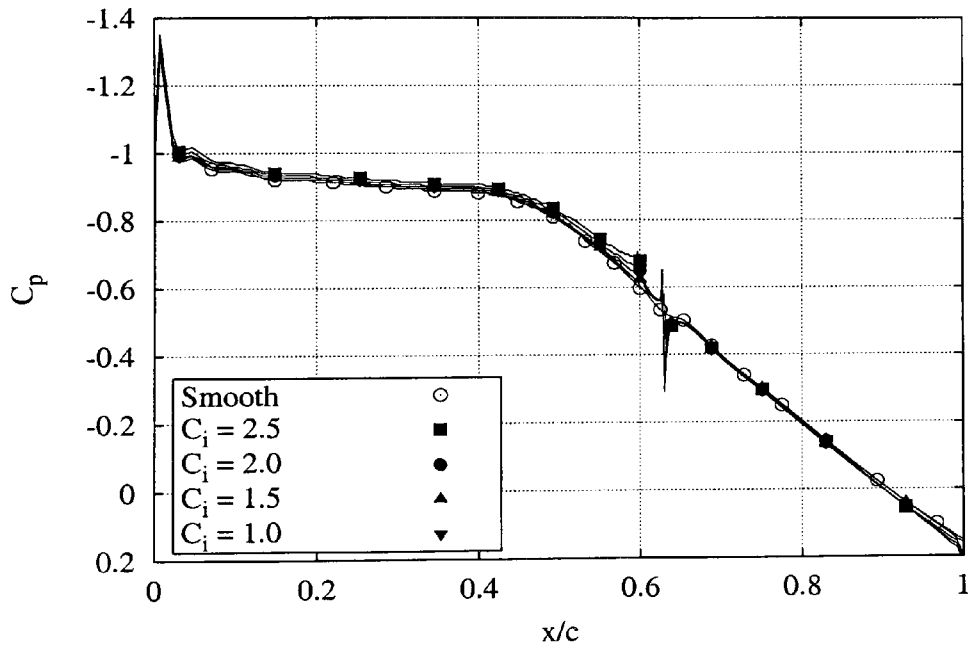


Figure 4.20: Effect of C_i on the Pressure Distribution

In addition the CFD analysis predicted a generally negligible influence on the boundary pressure downstream of the ABD. Although all the cases did show a slight increase in pressure at the trailing edge. Since this increase in pressure did not result from a velocity reduction close to the wall it partially represents the energy introduced into

4.3. PARAMETRIC STUDY OF AN ABD ON A NACA65-415 AEROFOIL SECTION

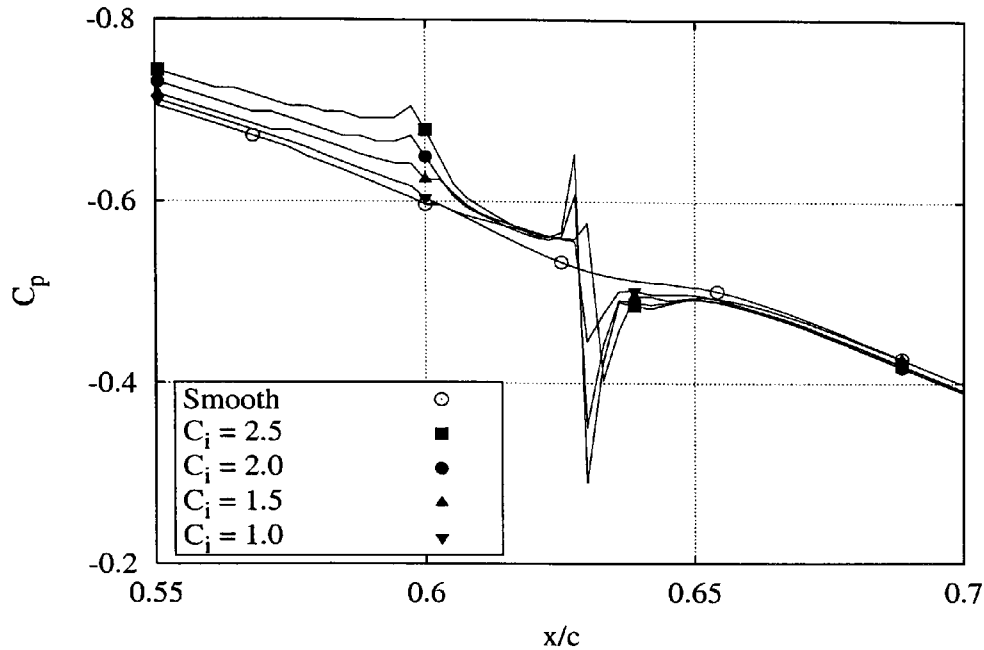


Figure 4.21: Local Effect of C_i on the Pressure Distribution

the flow.

A parallel interaction causes the flow just upstream of the ABD to accelerate and hence the pressure decreases (see Figures 4.20, 4.21, 4.22 and 4.23). Along the interaction zone of the ABD the external fluid velocity was further improved and reached its peak just before the end of the 'gap'. The geometry of the aerofoil wall downstream of the ABD results in a protrusion in the flow which forced the intermediate fluid layer between the external and the ABD stream to stop and this 'impingement' resulted in a rapid pressure change.

4.3. PARAMETRIC STUDY OF AN ABD ON A NACA65-415 AEROFOIL SECTION

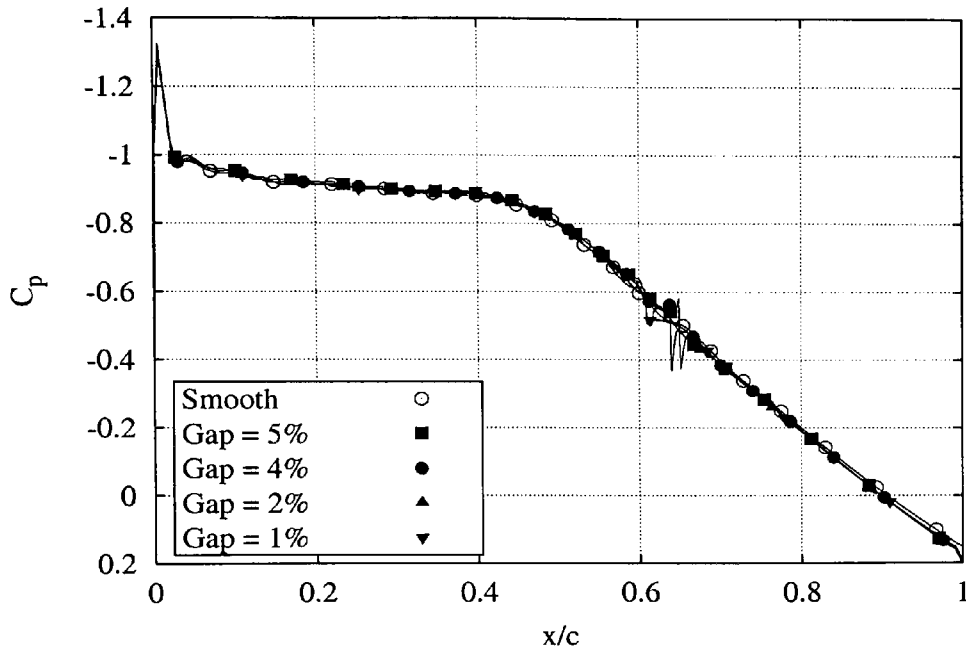


Figure 4.22: Effect of the Gap-Size on the Pressure Distribution

In the case of the non-parallel ABD shapes the duct fluid, to some extent, entered the domain of the external flow. This is exacerbated at the lowest radii, i.e. the steepest injection and suction angles. The large pressure change, shown in Figure 4.24 and 4.25, for $R = 5\%$ thus arose from the static pressure of the secondary flow which entered the external flow domain. At the trailing edge of the ABD a strong pressure increase was caused by the ‘rolling’ motion of the duct flow and the modelling of a ‘real’ wall dividing the two flow regions. An increase of the injection angle caused an increasing penetration of the secondary flow into the external flow domain. From this it can be presumed that the fluid layer at the wall shortly upstream of the ABD probably experienced deceleration, whereas fluid layers further away from the wall are entrained by the transferred momentum.

4.3. PARAMETRIC STUDY OF AN ABD ON A NACA65-415 AEROFOIL SECTION

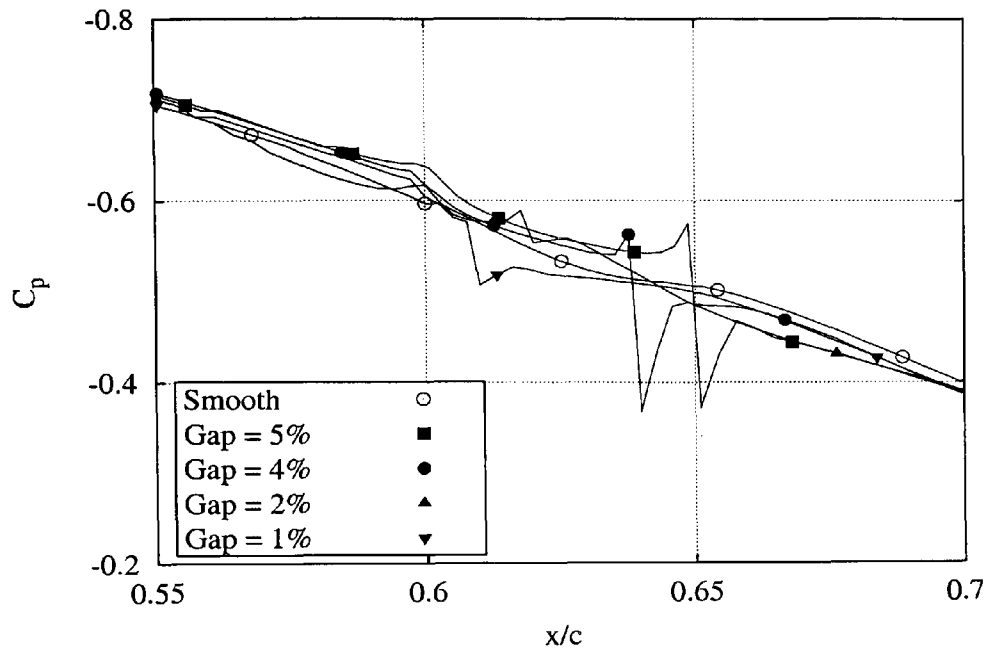


Figure 4.23: Local Effect of the Gap-Size on the Pressure Distribution

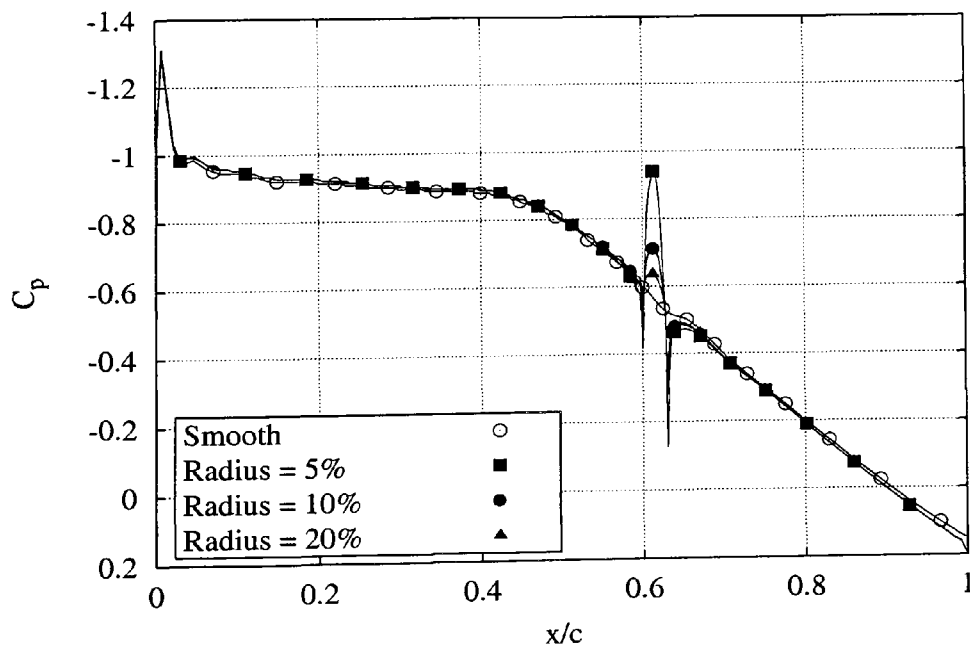


Figure 4.24: Effect of the Injection and Suction Angle on the Pressure Distribution

4.3. PARAMETRIC STUDY OF AN ABD ON A NACA65-415 AEROFOIL SECTION

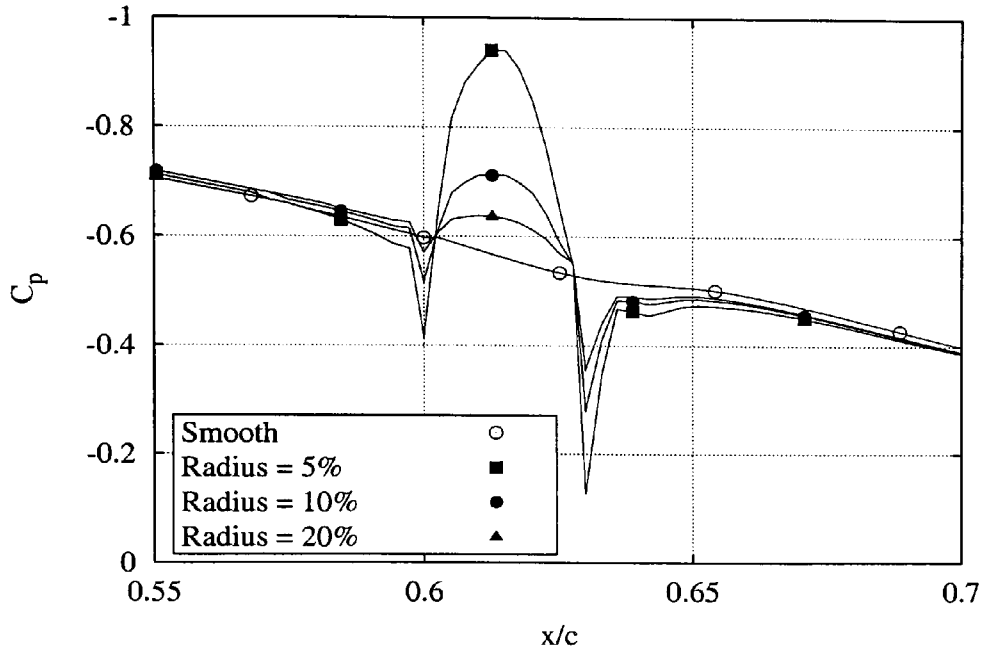


Figure 4.25: Local Effect of the Injection and Suction Angle on the Pressure Distribution

Pressure distributions on the high pressure side of the aerofoil section were not included in the above discussion since this region remained unaffected by the flow control process.

4.3.4 Flow Visualisation

In the previous Subsections (4.3.1, 4.3.2, 4.3.3) the effects of momentum transfer via a secondary flow in the ABD were quantified, whereas the current subsection contains a brief qualitative discussion of the flow control process.

Figure 4.26 shows the velocity vectors at the interaction zone for a parallel and a curved ABD. In both cases the acceleration of the fluid along the interaction zone can be observed as well as the enhanced velocity profiles downstream of the flow control region. In the case of a curved ABD penetration of the duct flow into the external flow domain can be clearly seen. This does not cause any obvious substantial disturbances such as swirling flow or sudden directional changes in the flow direction.

The effects are perhaps more clearly shown in Figure 4.27 where the velocities are represented by shaded contours which clearly identify the shape of the interaction region

4.3. PARAMETRIC STUDY OF AN ABD ON A NACA65-415 AEROFOIL SECTION

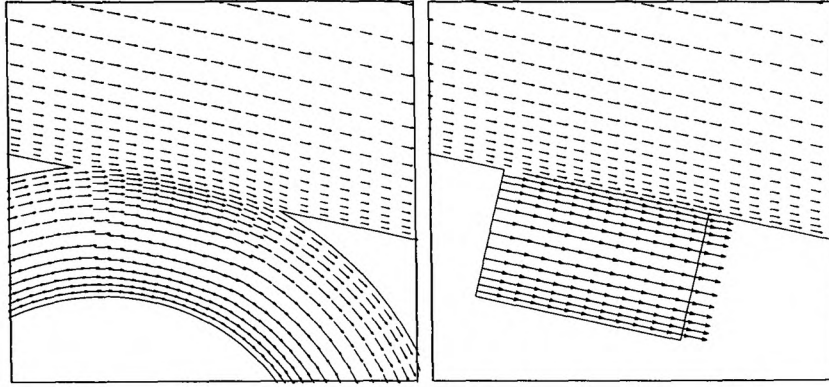


Figure 4.26: Velocity Vector at the location of flow control for a Curved and Parallel ABD Arrangement

as well as the local flow enhancement above the ABD. This visualisation of the flows shows the reduction in velocity which occurs near the upper duct wall downstream of the flow control region due to the transfer of momentum whereas the remaining flow field in the ABD appears to be unaffected. This observation supports the findings that momentum transfer from the ABD is relatively independent of the depth of the device, see Figure 4.12.

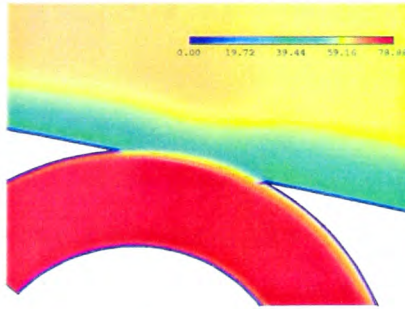


Figure 4.27: Shaded Velocity Contours at the location of flow control

4.3.5 Effect of the ABD Power Consumption on the overall Improvement in Aerodynamic Characteristics of the Aerofoil Section

So far the numerical investigation has concentrated on the impact of the ABD on the aerodynamic characteristics of aerofoil sections, C_D , C_L , and L/D , and no allowance has

4.3. PARAMETRIC STUDY OF AN ABD ON A NACA65-415 AEROFOIL SECTION

been made for the energy required to maintain the flow in the ABD. In order to obtain an estimate of the *overall efficiency*, $P_L/P_{D_{eff}}$, of the device, the power requirements of the ABD must be taken into account. Therefore, the product of the pressure drop and the volume flow rate in the ABD was used to assess the power required to drive this secondary flow. To obtain the ‘efficiency’ of the ABD, i.e. a measure of the improvement of the device when the power consumption by the secondary flow is taken into account, the following ratio was used:

$$\frac{P_L}{P_{D_{eff}}} = \frac{P_L}{P_D + P_{ABD}} \quad (4.5)$$

with

$$P_L = \frac{1}{2}\rho U_\infty^2 \times U_\infty \times C_L \times A \quad (4.6)$$

$$P_D = \frac{1}{2}\rho U_\infty^2 \times U_\infty \times C_D \times A \quad (4.7)$$

and

$$P_{ABD} = \dot{V}_{ABD} \times \Delta p_{ABD} \quad (4.8)$$

In Equation 4.5 the denominator represents the total energy, i.e. the component necessary to overcome the drag forces due to the forward motion of the wing section, as well as the power needed for the secondary flow and the numerator is a parameter which expresses the power requirement to achieve the desired lift. Although the physical meaning of P_L is limited the ratio $P_L/P_{D_{eff}}$ can be used as an L/D -like expression for the aerofoil performance including the energy required for flow control. With negative lift forces when the numerator of Equation 4.5 is negative the assessment of L/D and the effective performance, $P_L/P_{D_{eff}}$, is not valid. In order to obtain a clearer view on the potential and limitations of the flow control process the percentage change of C_D was compared with the percentage change of the power requirement to drive the wing section forward, $P_{D_{eff}}$. In this section of the thesis the effective performance of the ABD was investigated numerically so that detailed consideration of the supply and discharge of the secondary flow was not taken into account. The necessary power requirements

4.3. PARAMETRIC STUDY OF AN ABD ON A NACA65-415 AEROFOIL SECTION

for the ABD only considered the pressure drop and volume flow rate irrespective of the efficiency of the method of producing the secondary flow (aircraft propulsion forces, vacuum pumps etc.). The following parametric study was again based on the common base case (see Table 4.11) and the individual parameters were changed according to the abscissa of the following diagrams.

Figure 4.28 shows that the effective performance increased with increasing angle of attack. Towards higher angles of attack the curves for P_L/P_{Deff} and P_{Deff} converge towards the curves for the aerodynamic characteristics, C_D and L/D , which indicates that the efficiency of the secondary flow process was improved. At -4° the power consumption of the ABD exceeded the benefits of drag reduction for the present configuration so that the overall performance of the aerofoil was reduced.

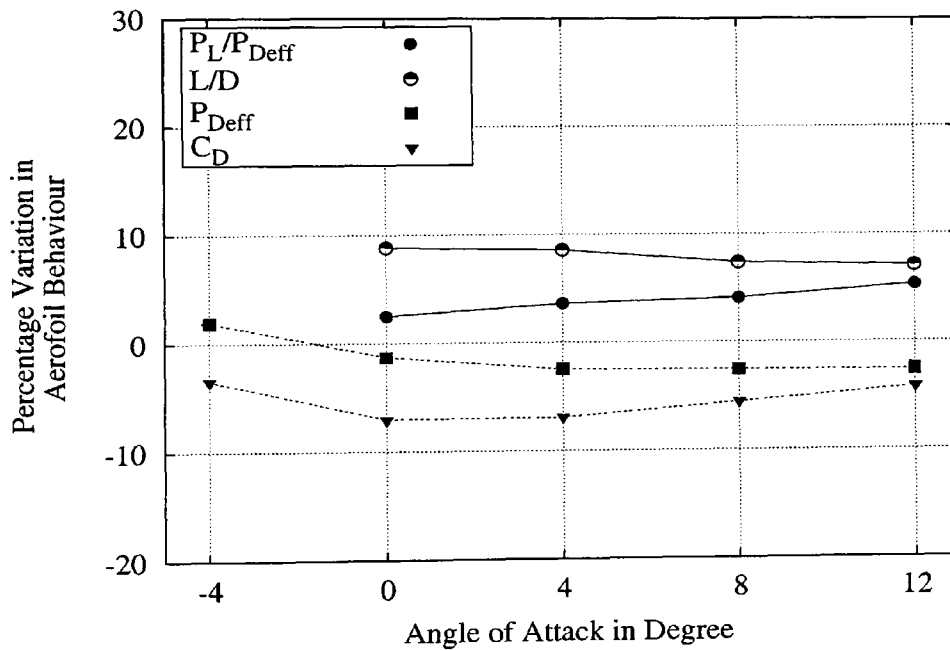


Figure 4.28: Impact of the Angle of Attack on the Effective ABD Performance

The position of the ABD also had great influence on the overall efficiency, see Figure 4.29. The drag coefficient was reduced as the position of the ABD was moved towards the trailing edge with a consequent enhancement in L/D . However the power consumed by the ABD increased as the ABD moved back to the trailing edge and this worked against the aerodynamic benefits so that the highest overall efficiency occurred with

4.3. PARAMETRIC STUDY OF AN ABD ON A NACA65-415 AEROFOIL SECTION

the ABD at 60% chord.

Thus two contradicting phenomena govern the overall effectiveness of the present momentum transfer method. The higher the velocity ratio between the secondary flow and the local external flow the better the transport mechanism. On the other hand the slower the external flow the higher the external static pressure. The numerical results showed that the higher the external static pressure the higher the pressure drop along the ABD and this can explain the general tendency of the relationships in Figure 4.28 and 4.29. However, these phenomena are complex and a straightforward relationship

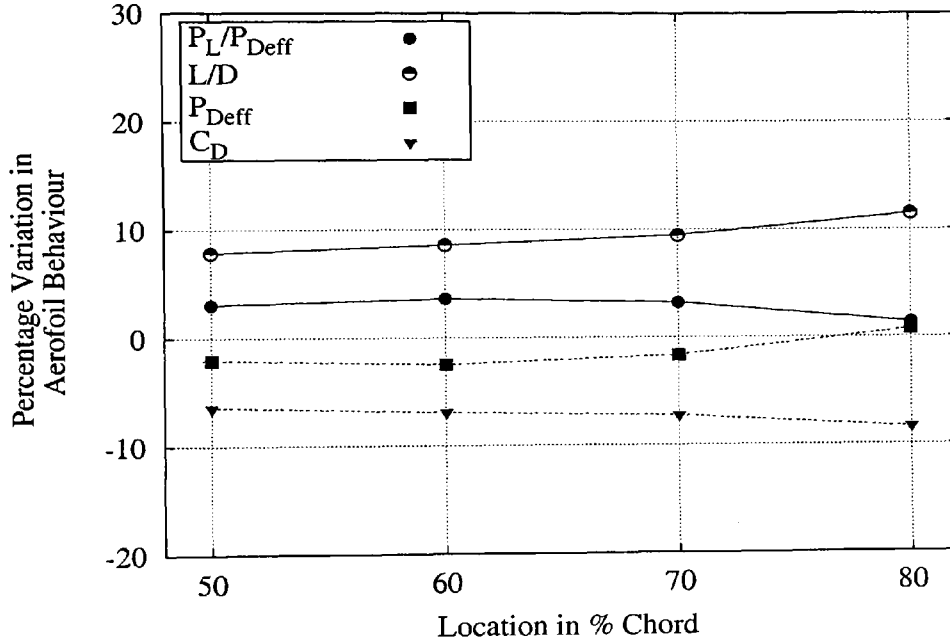


Figure 4.29: Impact of the ABD Location on the Effective ABD Performance

between pressure, velocity and ABD efficiency could not be established.

Figure 4.30 shows the impact of the length of the interaction zone on the effective performance of the ABD and the aerodynamic characteristics of the aerofoil section. For a gap-size of 1% chord the momentum exchange has only a small impact on the characteristics. As the gap-size is increased L/D increased almost linearly and reached its peak with an interaction zone of 5% chord length. The ABD power consumption increased with increasing gap-size. However, the net effect was that P_L/P_{De} increased up to a gap-sizes of 3% chord but remained virtually constant thereafter.

4.3. PARAMETRIC STUDY OF AN ABD ON A NACA65-415 AEROFOIL SECTION

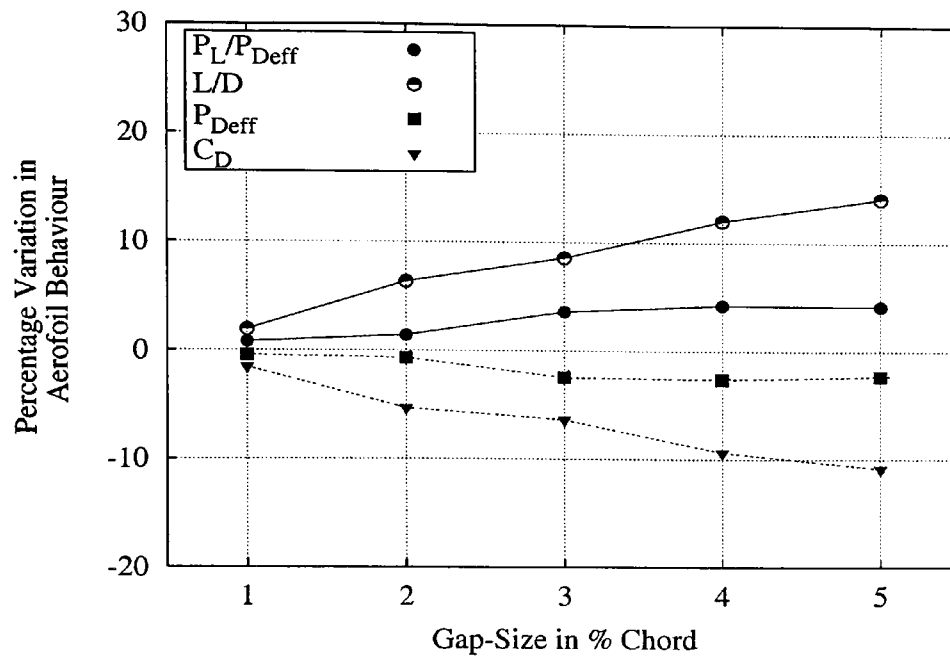


Figure 4.30: Impact of the Gap-Size on the Effective ABD Performance

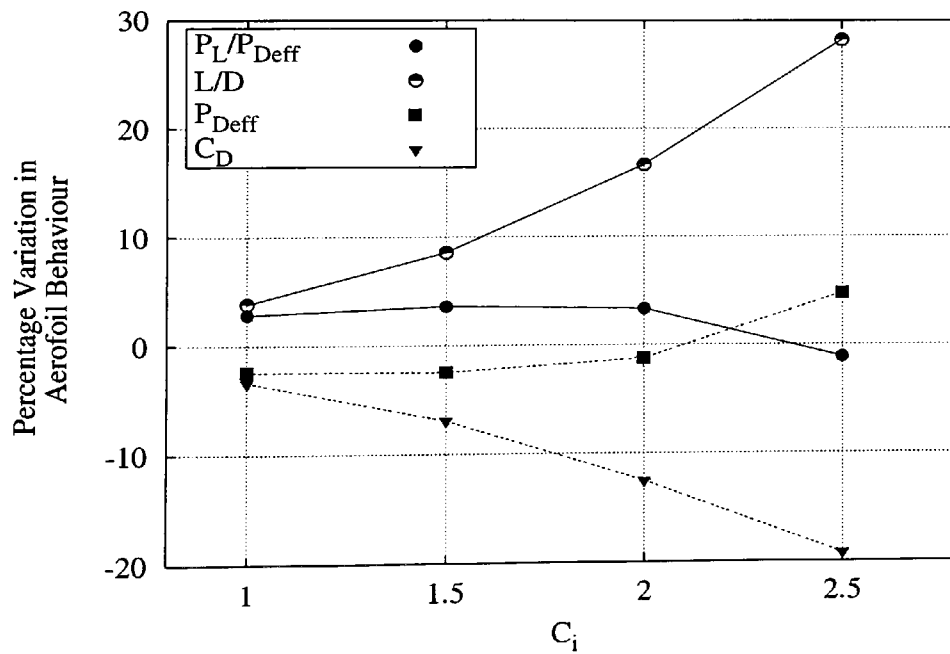


Figure 4.31: Impact of C_i on the Effective Performance

4.3. PARAMETRIC STUDY OF AN ABD ON A NACA65-415 AEROFOIL SECTION

Although high C_i s achieved substantial drag reductions and lift enhancements, the pressure drop and hence the power requirements limited the use of high secondary flow velocities, see Figure 4.31. The most beneficial arrangement was established for $C_i = 1.5$ although the improvement in overall efficiency was virtually constant for $1 \leq C_i \leq 2$. For the current ABD geometry the overall efficiency then fell sharply so that at an injection coefficient of 2.5 there is an overall decrease in performance compared with the smooth aerofoil. Despite this relationship between the ABD efficiency and

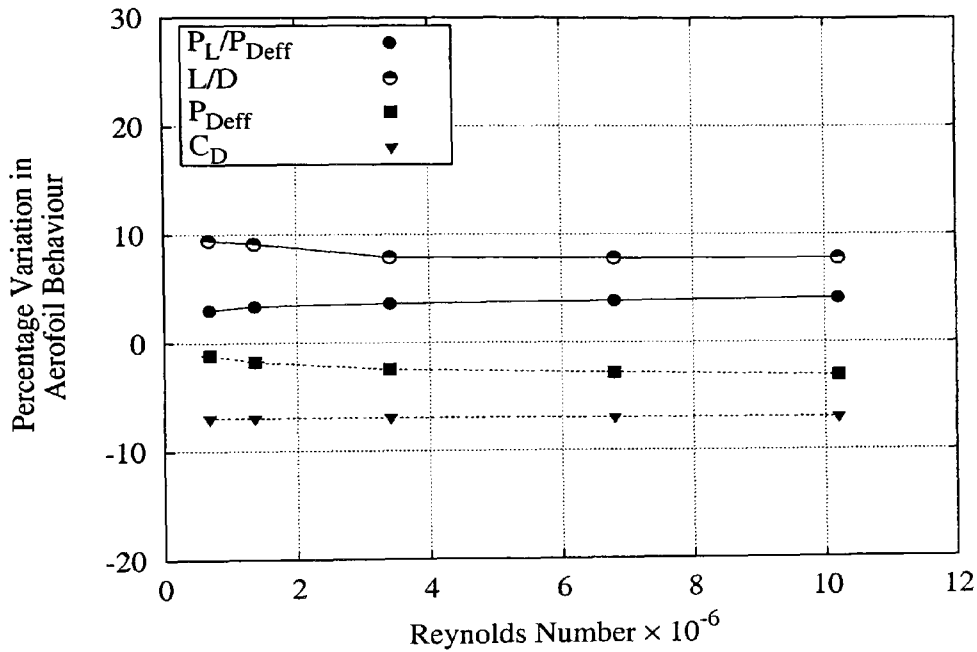


Figure 4.32: Impact of the Reynolds-number on the Effective ABD Performance

C_i an increase of the Reynolds-number yielded very slight improvements in overall efficiency with increased velocities, see Figure 4.32. Here, the Reynolds-number was controlled by the free stream velocity and therefore the free stream velocity associated with a doubled Reynolds-number ($Re = 6.8 \times 10^6$) required an internal velocity that was 20% higher than for the configuration with $Re = 3.4 \times 10^6$ and $C_i = 2.5$. Thus the effective aerofoil performance is only governed by the injection coefficient rather than the magnitude of the secondary velocity. Small Reynolds-numbers (0.68×10^6 and 1.36×10^6) yielded a percentage increase of L/D due to an augmented lift coefficient. Despite decreasing pressure drops across the ABD the required volume flow rate through

4.3. PARAMETRIC STUDY OF AN ABD ON A NACA65-415 AEROFOIL SECTION

the device assumed increasing importance and increased the proportion of P_{ABD} to P_D . Table 4.13 shows the required pumping power as a proportion of the energy required to overcome the drag resistance and this leads to a decrease in $P_L/P_{D_{eff}}$ for the low Reynolds-number range.

Table 4.13: Proportion of P_{ABD} to P_D

Reynolds-number $\times 10^{-6}$	0.68	1.36	3.4	6.8	10.2
Proportion in %	6.25	5.5	4.7	4.4	4.1

Reduction of the ABD depth proved to be beneficial with respect to $P_L/P_{D_{eff}}$ and $P_{D_{eff}}$ due to a reduced volume flow through the ABD (Figure 4.33).

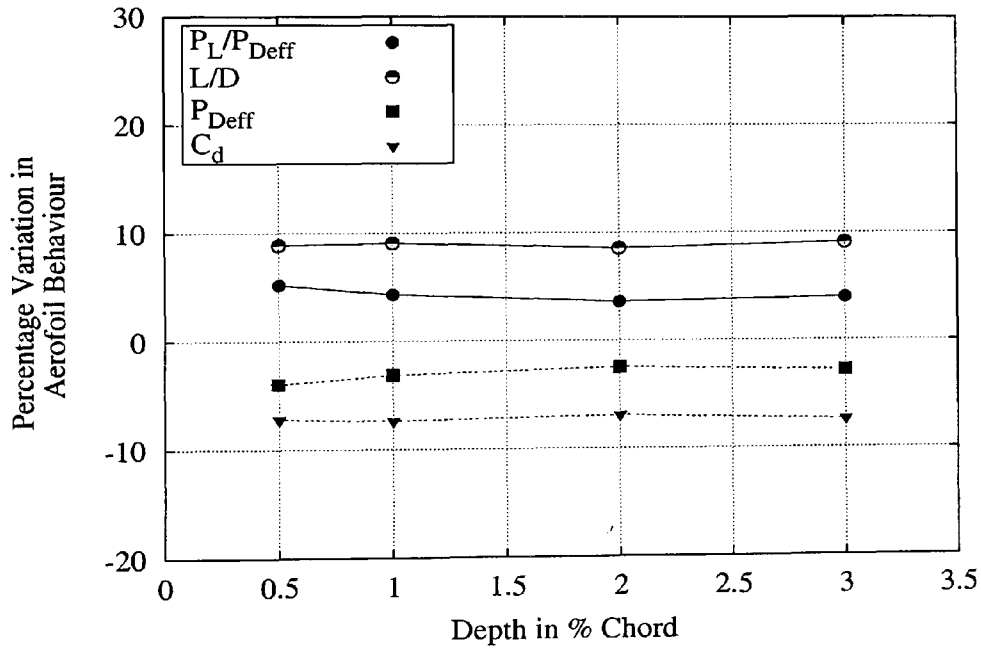


Figure 4.33: Impact of the ABD Depth on the Effective ABD Performance

4.3.6 Notes on the CFD Set-Up

The power consumption for the flow control process was established for a *truncated* ABD structure. In order to ensure that no mass exchange took place between the secondary and main stream flows, ‘inlet’ (i.e. Dirichlet) boundary conditions were assigned to

4.3. PARAMETRIC STUDY OF AN ABD ON A NACA65-415 AEROFOIL SECTION

the injection and suction side of the ABD. At the injection opening the velocities were given a positive sign and the suction velocity was given a negative sign. Thus the mass flow through the ABD was conserved. The predicted turbulence quantities for the suction side with negative inflow need to be regarded with care since in convection dominated outflows non-physical results may occur. They, however, applied only for a very small region at the suction patch and the effects on the remaining flow domain can be neglected [30].

Due to the lack of information on the value of turbulence quantities at the inlet and outlet of the ABD the turbulence intensity ($T_i = \sqrt{\frac{2}{3}}k/U_i$)³ was fixed at 4% and the dissipation length scale was set to the inlet and outlet diameter. Recalculation of T_i within the ABD showed that these settings did not fix the turbulent quantities. Within the ABD flow T_i showed a total variation from the boundary condition ($T_i = 0.04$) of between -73% and +100% for the range of angles of attack studied, and from -73% to +230% for $1 < C_i < 2.5$ and for the variation of the gap-size between 1% and 5% chord T_i varied from -99% and +110%. Therefore it can be presumed that the intuitively chosen turbulence properties at the inlet boundaries did not influence these properties within the ABD and consequently had little affect on the momentum transmission.

The model validation (see Subsection 3.2.2) suggested that a grid independent solution for the model was used in the parametric study. A further refined grid was used to investigate the independence of the momentum exchange to the grid spacing. Therefore, the cell numbers in the tangential direction on the upper aerofoil surface were multiplied by 1.5 and the propagation ratios were kept unchanged. Table 4.14, which presents the resultant predicted aerodynamic characteristics of the aerofoil section, shows a slightly increased momentum transfer. However the computational time increased by about 44% for 1000 outer iterations. Usage of the standard $k - \epsilon$ turbulence model increased the effect of the momentum transfer via the secondary flow by about 1.73 percentage points for C_D and 0.63 percentage points for C_L . The isotropic nature of the $k - \epsilon$ model appears to support the flow control process. This model was not used initially because it predicted higher drag coefficients than the RNG $k - \epsilon$ turbulence model for the smooth aerofoil section. Also the variation of the chord length

³ T_i was computed with respect to ABD velocity $U_i = C_i \times U_\infty$.

4.3. PARAMETRIC STUDY OF AN ABD ON A NACA65-415 AEROFOIL SECTION

at a Reynolds-number of 3.4×10^6 (see Figure 4.13) had no influence on the predicted magnitude of the variations of C_L and C_D . The grid spacing normal to the aerofoil surface was adapted to meet the conditions of the original computation. The chord length and Reynolds-number for this last test ($c = 0.5$ m, $Re = 0.68 \times 10^6$) were chosen due to their significance for the experimental work in Chapter 6.

Table 4.14: Effects of CFD Parameter on Momentum Transfer via a Secondary Flow through the ABD

	$C_{D_{ABD}}$	C_D	ΔC_D	$C_{L_{ABD}}$	C_L	ΔC_L	$Re \times 10^{-6}$
Original	0.0129	0.0139	-6.93%	0.747	0.739	1.02%	3.40
Refined Grid, $\times 1.5$	0.0125	0.0135	-7.13%	0.753	0.743	1.30%	3.40
$k - \epsilon$ Turb. Model	0.0131	0.0144	-8.66%	0.753	0.741	1.65%	3.40
Original, $c = 1$ m	0.0165	0.0178	-6.99%	0.724	0.711	1.79%	0.68
Model Size, $c = 0.5$ m	0.0162	0.0166	-7.41%	0.726	0.713	1.80%	0.68

4.3.7 Discussion

A comprehensive study has been conducted in order to obtain an overall picture of the effects of parameters on the aerodynamic characteristics of the aerofoil flow and ABD flow. This included the determination of the percentage change of the aerodynamic characteristics of the aerofoil section, C_D , C_L , and L/D , as well as quantitative and qualitative studies of pressure and velocity changes in the near vicinity of the aerofoil surface. Attempts were also made to assess the effective augmentation of the aerofoil characteristics, taking into account the power requirements of the flow control device. The outcome of this parametric study was submitted for review [41] and can be summarised as:

- The drag coefficients were strongly affected by the use of momentum transfer from the ABD. Maximum reductions of $\approx 20\%$ were predicted for a C_i of 2.5. The same parameter set yielded a maximum lift augmentation of 3.5%.
- The impact of the ABD on lift at low angles of attack was limited. However due to the magnitude of the lift forces even small percentage changes can translate into significant lift force augmentations.

4.3. PARAMETRIC STUDY OF AN ABD ON A NACA65-415 AEROFOIL SECTION

- Inclusion of the power requirements to drive the secondary flow introduced additional limitations in the effective improvements in aerofoil behaviour. Thus the effects of the important parameters C_i and gap-size (which markedly improved C_L and reduced C_D) were partially offset by the increasing power requirements of the ABD.
- The local velocity gradient between the secondary and external boundary flows is probably the most significant factor in determining momentum transfer from the secondary flow so that:
 - the percentage improvements due to the ABD were virtually independent of the Reynolds-number,
 - the device offers potentially good performance for take-off and landing conditions due to the high angles of attack and the low aircraft velocities.
- Low external pressures enhanced the efficiency of momentum transfer via a secondary flow through the ABD.
- The operation of the ABD did not result in any significant disturbances to the external flow, such as sudden directional changes of the fluid and/or swirling flow.
- The effects of the ABD were similar for a NACA0012 and a NACA65-415 aerofoil section which were considered in this thesis. For example, with a parallel ABD using a C_i of 2.0 a variation of $\Delta L/D = 16.27\%$ ($\Delta C_D = -12.53\%$, $\Delta C_L = 1.66\%$) was achieved with the ABD at 30% chord on the NACA0012 aerofoil section (see Section 4.2, *Taguchi*: Test8). The same ABD parameter at 60% chord on the NACA65-415 section produced $\Delta L/D=16.65\%$ ($\Delta C_D = -12.56\%$, $\Delta C_L = 2.0\%$, see Section 4.3.1).

These findings highlighted the need for further optimisation of the device. Essentially, the geometry of the ABD should aim to provide:

- high local velocity gradients,

4.3. PARAMETRIC STUDY OF AN ABD ON A NACA65-415 AEROFOIL SECTION

- installation at positions of low pressure,
- an ABD with economic and structurally sensible gap-size,
- an ABD requiring a minimum of auxiliary power consumption to drive the flow.

Contrary to the findings of the Taguchi analysis the parametric study indicated that the aerodynamic characteristics of the aerofoil sections were independent of the ABD depth. Therefore, the interaction of the ABD depth with the injection and suction angle was investigated. Calculation of an ABD with a 'shape radius', $R = 5\%$ chord, as shown in Figure 4.9, and an injection and suction opening of 1% chord yielded 2.2 percentage points more drag reduction (9.917%) and 0.75 percentage points more lift improvements as for the shaped ($R = 5\%$) model with 2% depth. Thus the ABD depth is an important parameter only when the ABD is shaped, which was detected correctly by the Taguchi analysis. Placing the ABD shape on low ranks (see Table 4.7) is therefore misleading and the two level Taguchi analysis can only be used as an attempt to summarise the effects of momentum transfer via an ABD on the aerodynamic characteristics of an aerofoil and confirm the trends of previous efforts on flow control using an ABD.

Due to the non-linear interrelationships of the parameters governing the performance of the ABD and the somewhat contradictory aims of maximum flow control effects with minimum costs, a global search tool was employed for optimisation of the ABD geometry. Genetic algorithms (GA) provide a semi-stochastic search method suitable for non-linear optimisation applications. Unlike many search strategies GAs search for global optima without being pre-deterministic. The following section describes the optimisation of the structure of the ABD by means of GAs and CFD.

Chapter 5

Optimisation of the ABD by Genetic Algorithms and CFD

This chapter describes the development of the air breathing device that provides the most efficient and effective structure for momentum transfer via the secondary flow. This was undertaken using a computer based semi-stochastic search method (genetic algorithms) combined with computational fluid dynamics to predict the behaviour of individual ABDs. In the following section the principle of the evolution strategy is explained as well as the way in which CFD was implemented into the optimisation process.

5.1 Genetic Algorithms

Genetic Algorithms (GAs) are powerful optimisation techniques loosely based on the principles of natural evolution and the survival of the *fittest*. Evolution strategies select, recombine and mutate *individuals* from populations and approach an optimal solution by evolving stronger individuals in successive generations of the populations. Individuals consist of a combination of parameters representing possible solutions for the given problem. When encoded as (binary) strings these individuals are called *chromosomes*. Due to the genetic operators (selection, mutation and cross-over) the individuals adapt to an environment that is described by a fitness function. The initial population consists of randomly created individuals and the fitness of each individual, i.e. the performance of each combination of parameters, is assessed. The fitness or the *fitness value* is then

stored and used for the selection process.

A *selection* operator picks individuals for the *mating pool*. Thus for example *Roulette-wheel* selection uses a percentage representation of individuals according to their fitness, from which individuals are picked at random. Due to the larger proportion of individuals with higher fitness strong parameters are more likely to be reproduced. *Tournament* selection, another common technique, freely picks two individuals from the entire population and passes the one with the higher fitness value to the mating pool. The so-selected individuals are subjected to cross-over (recombination) and mutation in the pool before a new generation is created.

Cross-over and *mutation* ensure evolution and diversity throughout the search within successive generations. Cross-over creates new individuals by swapping parts of the chromosome string between a chosen number of individuals. The cross-over location is selected randomly. Whereas, cross-over exploits the already existing volume of search space, mutation feeds the evolution with ‘fresh ideas’ by random alteration of some of the chromosome strings. Both operations are controlled by mutation and cross-over probabilities. Without these genetic operators only the parameter combinations of the initial population would take part in the evolution.

The *fitness function* describes the search space or defines the optimisation problem. Within this function the suitability of each parameter set to solve the given problem is evaluated and represented by a *fitness value*, that is returned to the GA.

Unlike other optimisation techniques GAs are likely to find the global optima due to the non-deterministic initiation (no defined starting point) and the genetic operations. GAs also perform well in noisy search domains [42]. Further robustness is achieved by:

- the search from populations of potential solutions, i.e. off-spring is not produced from successive iterates of a single solution,
- self-repair, i.e. ill-developments will not succeed in the evolution,
- self-guidance, i.e. search direction and starting parameters must not be given.

However, GAs work on the basis ‘better than’ and give no indication about the closeness of a solution to the actual optimum. Also, the generally long search duration (due to

the large number of individuals) and the use of so-called penalty functions may be disadvantageous for evolutionary search. *Penalty functions* are necessary for many engineering application and are used to limit the search space for certain parameters to avoid physically unrealistic solutions. A comprehensive discussion about the operation of GAs is given by Goldberg [42].

Other search methods such as gradient based methods (GM) or simulated annealing (SA) are prone to get trapped in local optima. GMs update the last candidate solution iteratively towards the steepest ascent and perform efficiently in clear and small search domains. Discontinuities in the search function and sharp multiple peaks can lead to failure of the method [43]. SAs also work on an updating principle. The last possible solution is updated when a randomly picked parameter set performs better. They produce efficient solutions and are less likely to find only local optima. Both methods require several restarts which limits their efficiency [43].

Application of GAs in Aero-Engineering

Optimisation of aerodynamic problems by GAs have been the focus of considerable recent attention [44]. Obayashi and Takanori [43] optimised a two-dimensional wing with GMs, SAs and GAs using a penal method to analyse the wing characteristics. They reported a superior performance for the GAs compared to the other methods. Gage and Kroo [45] successfully reduced the induced drag for a fixed lift on three-dimensional multi-element wings using a GA-vortex lattice code combination. Anderson and Gebert [46] used a multi-object (Pareto) GA to simultaneously optimise the structural and aerodynamic performance for a 3D wing. Obayashi and Oyama [47], Doorly et al [48], Periaux et al [49] and Marco et al [50] used Euler or Navier-Stokes codes together with simple or Pareto GAs for design of aerodynamic shapes. All these authors pointed out that the use of GAs in aerospace science is time-consuming but the generally good performance of the optimisation tool can be justified.

For example, Doorly et al [48], used a viscous-inviscid solution algorithm to determine the aerodynamic performance of a two-dimensional aerofoil section. The application of GAs aimed at the optimisation of the cruising L/D for a natural laminar flow aerofoil section at Reynolds-numbers between 0.4×10^6 and 6.0×10^6 , and angle of

attacks between 4° and 7° . Twenty vertices were used to define a B-spline curve which represented the aerofoil surface. Figure 5.1 shows the resultant aerofoil shape of this investigation. A typical pressure distribution for high L/D aerofoils at these Reynolds-numbers was established. The aerofoil shape is therefore flat at the lower surface and the curvature on the upper surface produced an almost constant decrease of C_p , i.e. a negative pressure gradient, along the first third on the aerofoil section. A smooth pressure recovery prevented flow separation and an indicated ‘flap’ at the aerofoil trailing edge maintained high lift forces for low angles of attack. Although, the design of an optimal aerofoil shape seems to be incomplete, all strong features for the desired L/D performance were highlighted by this evolutionary optimisation of the aerofoil section.

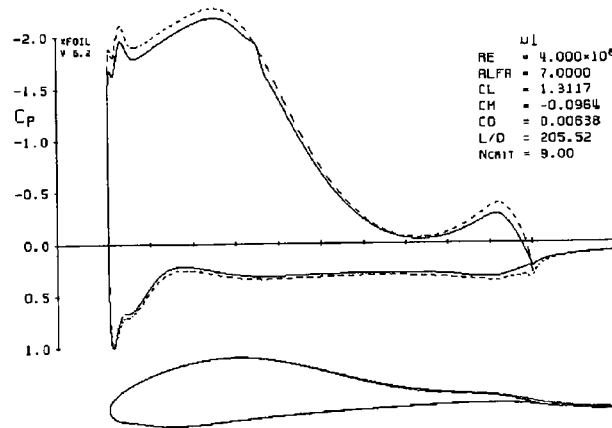


Figure 5.1: Resulting Aerofoil Shape due to GA Optimisation [48]

Optimal shape design for internal flow problems has been described for example by Sharatchandra et al [44] who optimised the structure of micro-pumps. Their combined GA-CFD analysis yielded non-intuitive pumping shapes with vastly superior pump performance than the original ‘straight’ pump. Figure 5.2 shows the original and the optimised micro-pump shape, for which the bulk velocity was multiplied by 2.5.

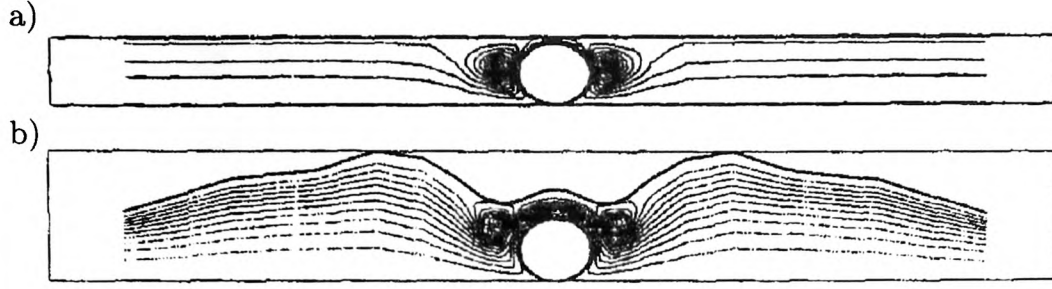


Figure 5.2: a) Straight Micropump before Optimisation and b) Micropump after Optimisation [44]

5.2 Optimisation

5.2.1 Structure and Set-Up

The current optimisation process was aimed at maximising the fitness (Equation 4.5) as described in Chapter 4:

$$\frac{P_L}{P_D + P_{ABD}} = \frac{P \text{ to produce lift}}{P \text{ to overcome drag} + P \text{ for the ABD}}$$

Therefore GA software freely distributed by the Massachusetts Institute of Technology, from Methew Wall, were used. This library called GAlib [52] provided a selection of genetic algorithms and genetic operators written in C++.

A simple genetic algorithm, as described by Goldberg [42], was used. Simple GAs are characterised by the production of an entirely new population for each generation and the assignment of a single fitness value to each individual. A binary-to-decimal genome¹ decoded the information of the chromosomes into a decimal representation suitable for grid generation.

The selection method used was a combination of Roulette-wheel selection and Tournament selection. From two Roulette-wheel spins the individual with the higher fitness was chosen for the mating pool. Within the mating pool one point cross-over and one point flip mutation (see Figure 5.3 and Figure 5.4) were applied to produce the offspring for the next generation. The cross-over and mutation probabilities were set to 80% and 1%, respectively.

¹A genome stands for the sum of all the genes (features) contained in a chromosome [42].

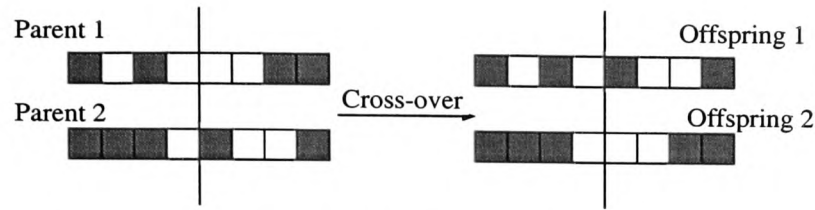


Figure 5.3: Example for Single Point Cross-over

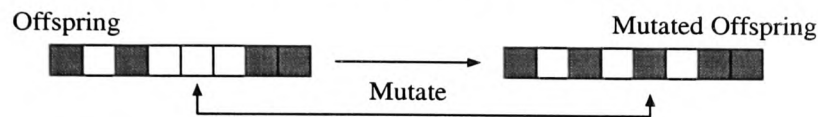


Figure 5.4: Example for Single Point Flip Mutation

Figure 5.5 shows the flow chart for the genetic algorithm. The rhombus in this figure shows the implementation of the fitness function and the flow chart for the fitness function is given in Figure 5.6. The sequence of fitness evaluation of a particular case started with the receipt of an individual from the GA. Thirteen design variables were employed to control the position, interaction zone and shape of the ABD. The internal geometry depended on two variables for the injection and suction angle, two variables for the inlet and outlet diameters and seven variables to define the shape of the lower surface by offsetting the co-ordinate points from a 'base' ABD with an even depth of 0.5% chord.

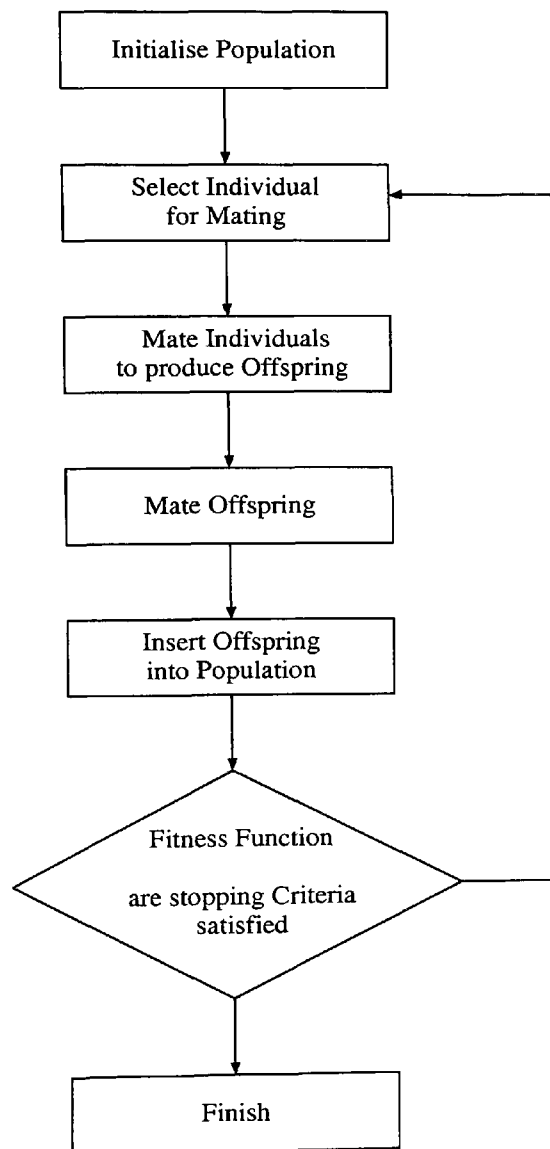


Figure 5.5: Flow Charts for the Genetic Algorithm

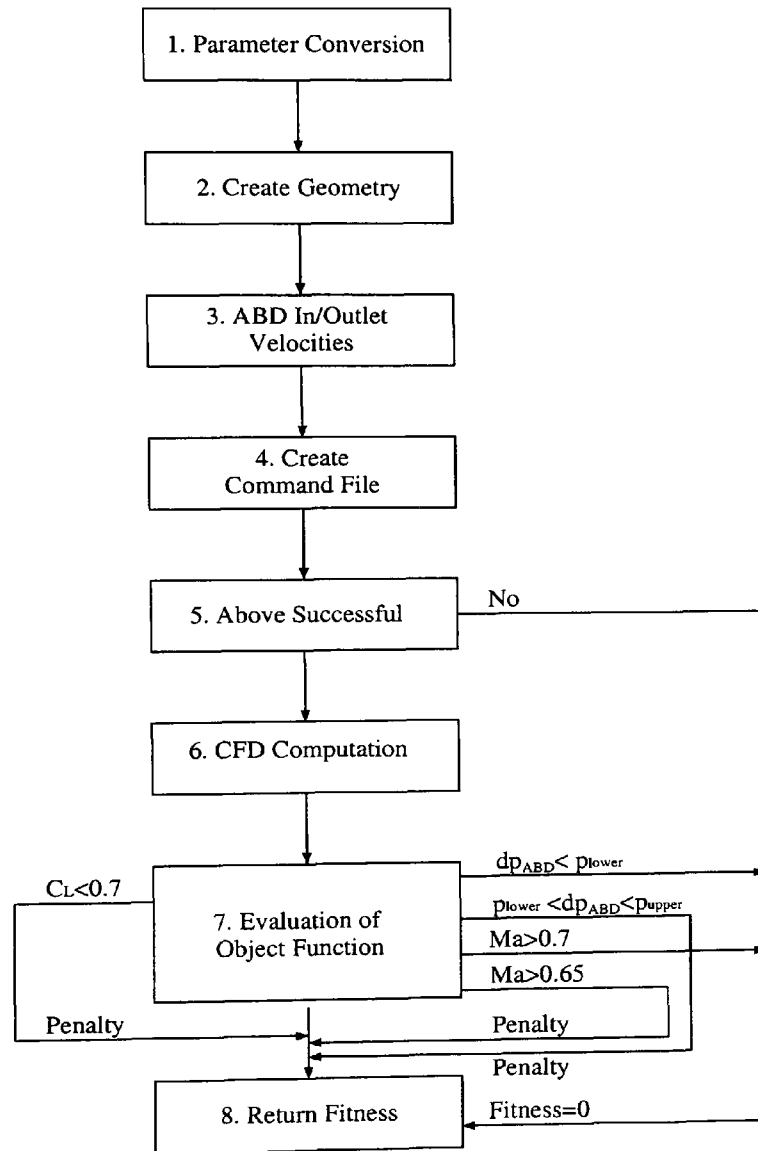


Figure 5.6: Flow Charts for the Fitness Function

Due to the curvature of the ‘base’ ABD the point translation needed to be normal to the bottom surface (see Figure 5.7). In addition it was necessary to limit the degree of freedom of all the variables, in order to produce sensible geometries with no-overlapping ABD contours. The ABD position ranged between 40% and 70% chord, the gap-size from 2% to 5% chord, and the radii for fluid injection and suction between 5% and 30% chord. The remaining points were allowed to translate from the ‘base’ ABD from 0.4% chord inwards to 3% chord outwards, apart from the inlet and outlet diameter which were restricted to 2% chord outwards. B-spline curves were used to connect three neighbouring co-ordinate points and these were subsequently blended to achieve a smooth representation of the lower surface of the ABD. This, in conjunction with further extrusion of the inlet and outlet openings, ensured even ABD inlets and outlets whilst providing geometrical flexibility in the mid-section of the air breathing device. All the centrelines for all the ABD structures were constructed to be of the same length.

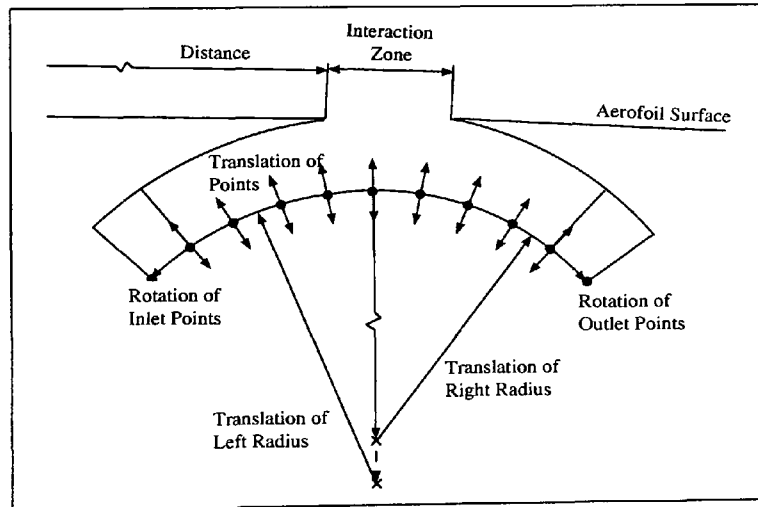


Figure 5.7: Principle Structure for Creation of an Optimal ABD by GAs

In order to reduce the computational times to acceptable length and using the same computational domain and dimensions as in the previous numerical investigations (chord = 1 m, domain height/length = 20 m, $Re = 3.4 \times 10^6$), a dense grid layer was modelled around the aerofoil section. External to this layer strong grid propagation was used (see Figure 5.8). A successful computation was halted following attainment of

a mass source residual of 1×10^{-2} . This computational arrangement required approximately 6 min for each individual set of parameters. Due to the coarser grid slightly different aerodynamic characteristics of the aerofoil section had to be accepted. At 4° angle of attack the Jones traverse method predicted $C_D = 0.0172$ whilst the wall force integration evaluated $C_L = 0.708$ for the smooth aerofoil section. Previous computations with the finer grid resulted in 0.0135 and 0.7433 for C_D and C_L , respectively. However, despite this simplified arrangement the grid was still concentrated at the critical locations, i.e. at the tip of the aerofoil section (the point of high stagnation pressure), at the interaction zone between the ABD and main flow (momentum transfer), and at the trailing edge of the aerofoil section. To ensure adequate performance of the turbulence model, the first grid point layer was kept at the same distance normal to the aerofoil surface as in previous numerical studies (i.e. $y^+ > 30$). Grid generation was achieved by executing CFX-BUILD4 in conjunction with a script file which was produced by the fitness function according to the position of the design variables.

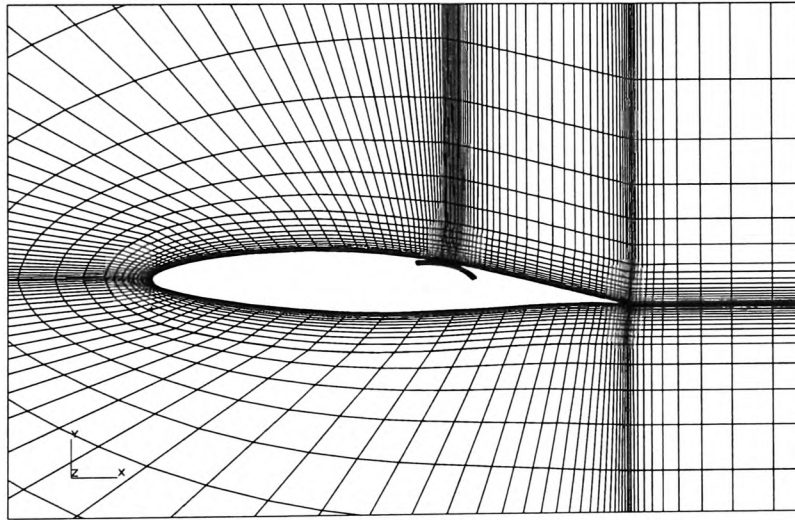


Figure 5.8: Coarse Grid around NACA65-415 Aerofoil Section for GA optimisation

In stage 3. in Figure 5.6 the volume flow rate through the ABD was determined for a fixed C_i at the injection opening of the ABD. Inlet and outlet velocities were evaluated accordingly and inserted into the command file for computation of the CFD problem.

In stage 5. of the evaluation of the fitness function (Figure 5.6) the ‘success’ of

the stages 2 to 4 was monitored. Failure of any of these stages to produce the wanted outcome resulted in the assignment of zero fitness in order to avoid subsequent time consuming steps in the program.

Penalty functions were used to provide smooth transition from non-sensible or unwanted results to physically sensible and useful results. Such measures allowed strong parameter sets to remain in the evolution which would otherwise be eliminated in conjunction with unsuitable parameters of an individual. Following the CFD computation of the particular ABD penalty factors ($PF < 1$) were assigned to the fitness of the ABD in stage 7 in certain cases:

- These limited the inflow or outflow velocities of the ABD to Mach numbers smaller than 0.65, to avoid the need for compressible flow computations. Recalculation of the density throughout the entire domain would increase the computational times enormously and the associated drag contribution from fluid compression or possible shock waves would also limit the use of ABDs at such high velocities. Thus all ABD geometries resulting in the secondary flow velocity exceeding Mach numbers of 0.7 were set to zero fitness,
- Some individual cases yielded negative pressure drops across the air breathing device. This occurred for very high outlet velocities (close to Ma of 0.65) and low inlet velocities with a small injection opening. Two reasons are responsible for this physical unrealistic situation. Firstly, due to the assignment of the same number of grid points at the injection opening, the inlet opening, and the outlet opening a very coarse mesh was generated at the inlet which may have led to increased numerical diffusion. Additionally, the grid spacing at the outlet may not have been sufficient for the very high velocity at the outlet. However, the individuals which resulted in small negative pressure drops were thought to include strong parameters which were worthwhile keeping. Individual parameter sets producing strong negative pressure drops were regarded as physically unrealistic and were taken out of the evolution,
- A penalty was assigned to individuals which produced reduced lift.

- Cases resulting in increased drag coefficients were also assigned a penalty factor.

All the penalty functions used linear penalty progression and were intuitively chosen since their direct impact on the evolution could not be traced back or predicted.

Sequences in the fitness function that are not explicitly mentioned are self-explanatory from Figure 5.6.

5.2.2 Results

The optimisation of the ABD was conducted for different geometrical parameters and injection velocities and the corresponding results are discussed in this section. Three initial optimisation conditions were used, namely:

- The interaction zone (3% chord), the distance from the leading edge (65% chord) and an injection coefficient of 1.5 were all fixed (Evolution 1.1),
- The interaction zone (3% chord), the distance from the leading edge (65% chord) and an injection coefficient of 2.0 were specified (Evolution 1.2),
- Finally, an injection coefficient of 1.5 was specified with all other 13 design parameters free to vary (Evolution 1.3),

Each optimisation required an evolution time of 4.5 days for 20 generations each with populations of 50 individuals.

Figures 5.9 to 5.11 show an example of the convergence for all three optimisations. The curves on the left hand indicate the convergence of the population average of the fitness value (4.5) and the individual components, C_D , C_L , and Δp with respect to the evolution average of these quantities. Due to the great differences in the magnitudes of the fitness values, C_D , C_L , and Δp , a percentage difference was used. The drag and lift coefficients had to be multiplied by a factor of 10 to distinguish their evolution in the proportional diagrams. Due to the small variation of the volume flow rate through the ABD the pressure drop across the ABD was used to show the ‘internal convergence’. On the right hand side of Figures 5.9 to 5.11 all the individual fitness values are plotted chronologically for the entire optimisation.

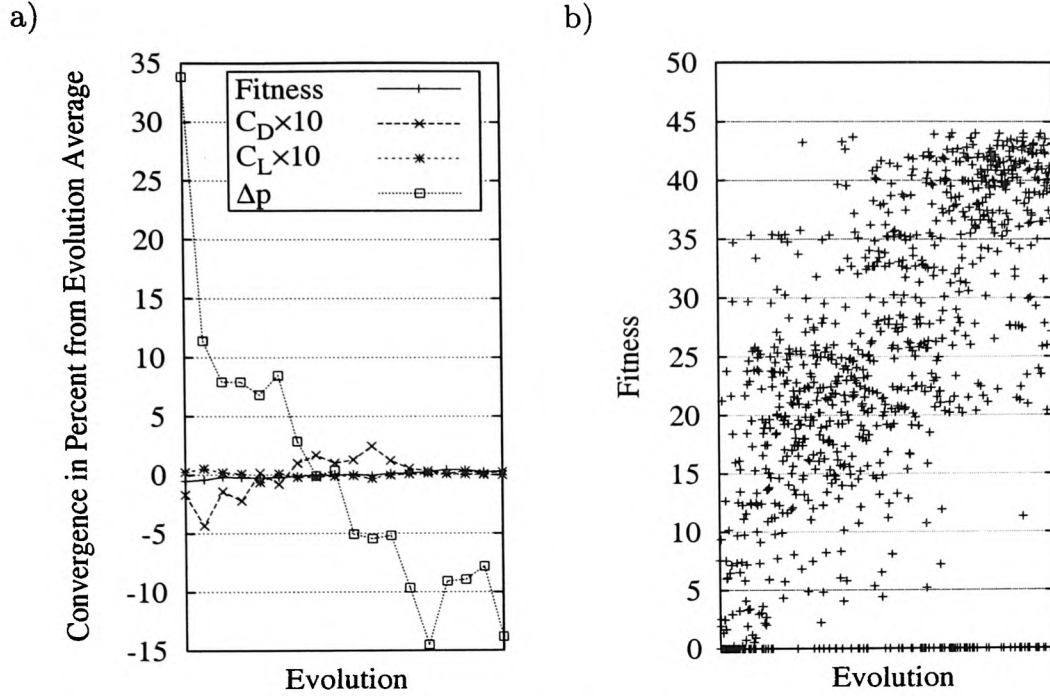


Figure 5.9: a) Convergence of the Averaged Fitness, C_D , C_L and Δp , and b) Convergence of Fitness for Evolution 1.1

The evolution was clearly governed by the change in the pressure drop across the ABD. In all three diagrams (see Figure 5.9a, 5.10a, and 5.11a) it is shown that the features which result in high pressure drops were extinguished within the first few generations. In the earlier generations 1 to 4 very high pressure drops cause high lift and low drag. It is clear from Figure 5.10a that the higher injection coefficient has a strong impact on the evolution of the drag coefficient.

The fitness values for individual cases showed a substantial clustering, at the end of the optimisation, of individuals with high potential benefits (i.e. those points in the top right of the diagram) for Evolution 1.1 (Figure 5.9b) but less so in the other studies. In this evolution the final converged population consisted mainly of individuals with strong parameter sets. The fitness of Evolution 1.2 and Evolution 1.3 were less well clustered at the end of the process. With an injection coefficient of 2.0 many individuals ‘died’ during the optimisation since they violated the constraint of specified maximum velocities at the inlet and outlet of the ABD. These are represented by the number of individuals with zero fitness. The optimisation using all thirteen parameters

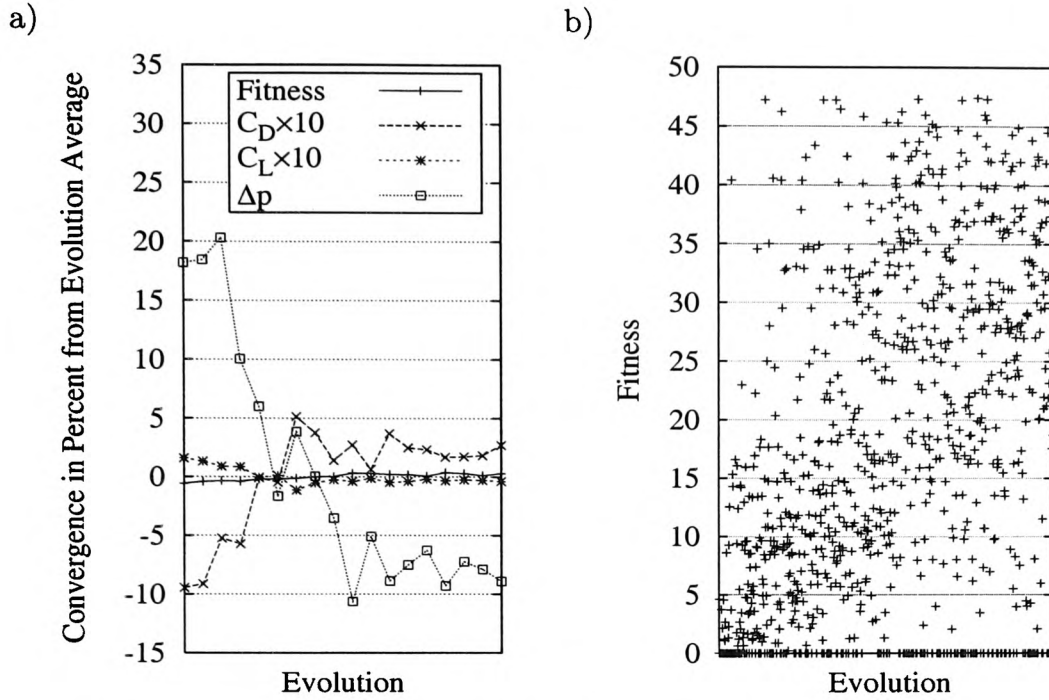


Figure 5.10: a) Convergence of the Averaged Fitness, C_D , C_L and Δp , and b) Convergence of Fitness for Evolution 1.2

showed a tendency to converge, but the number of generations and/or the population size appeared to be insufficient, see Figure 5.11b. All of the optimisations produced individuals with a fitness value >41.16 , which was the value of the corresponding lift-to-drag ratio for the smooth aerofoil section under the simulated conditions. In particular, Evolution 1.2 produced individuals with a fitness of 47.39 despite the high injection velocity and the length of the ABD.

The individuals with maximum fitness in each evolution were re-evaluated with a refined CFD mesh and the resultant absolute velocity contours are plotted in Figures 5.12, 5.13 and 5.14.

These optimised ABDs showed similar features. In all cases a small depth of the ABD at the location of injection provided the required injection coefficient whilst simultaneously keeping the volume flow rate small. In addition the evolutions identified small contractions in the air supply ducting. For the outlet side the optimisations suggested that a greater diameter seemed to be advantageous. With an uniform outlet velocity a pocket of fluid was developed in the outlet duct over which the exiting jet

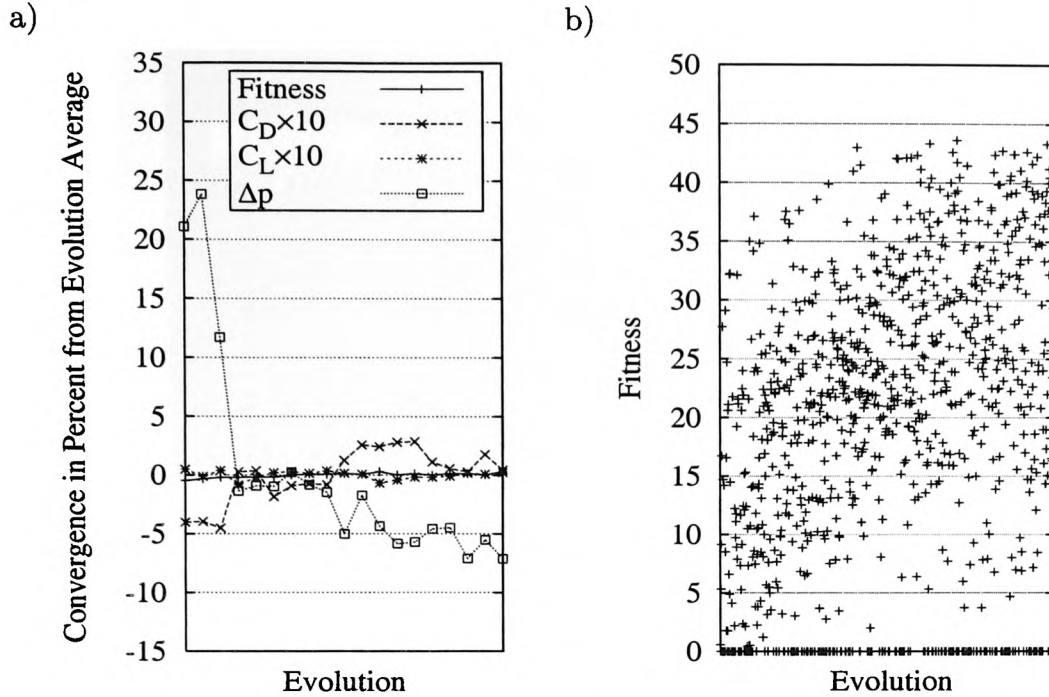


Figure 5.11: a) Convergence of the Averaged Fitness, C_D , C_L and Δp , and b) Convergence of Fitness for Evolution 1.3

seemed to glide. This minimises the shear forces in the exit flow but may not be sensible from a practical viewpoint. The more important features are that only moderate injection angles are needed and these will cause minimal interference between the ABD and external flows. In addition a pocket of rotational flow evolved at the centre of the interaction zone. The relative performance of the best cases from the three different optimisations are presented in Table 5.1. Evolution 1.1 appears to provide the best results so that further discussion is limited to the features of this Evolution.

Table 5.1: Refined Results of Best Individuals

	Evolution 1.1	Evolution 1.2	Evolution 1.3
ΔC_L	3.39%	2.97%	6.8%
ΔC_D	-8.39%	-13.9%	-0.8%
P_{ABD}	105 W	196.1W	129.8W

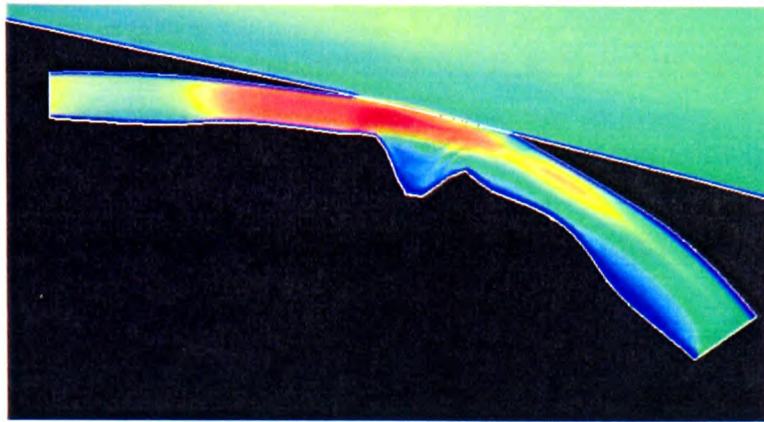


Figure 5.12: Best Individual Case of Evolution 1.1

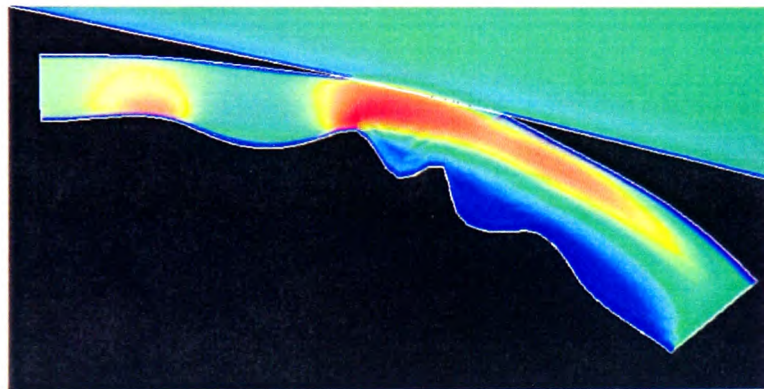


Figure 5.13: Best Individual Case of Evolution 1.2

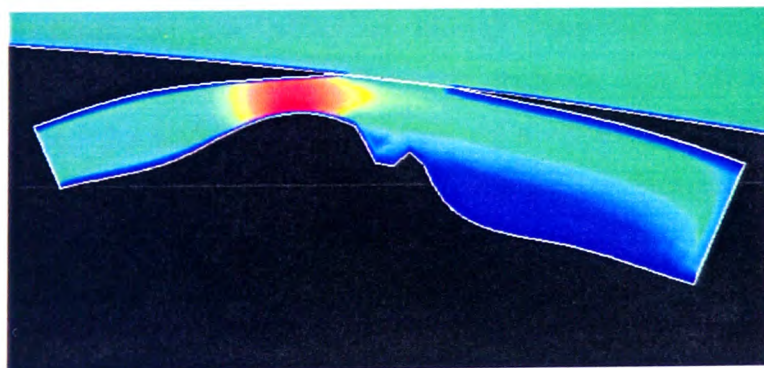


Figure 5.14: Best Individual Case of Evolution 1.3

Analysis of Evolution 1.1

Four additional geometries were analysed by CFD and compared with the best individual case from Evolution 1.1. These geometries are shown in Figure 5.15 and are intended to show:

- the improved performance of Evolution 1.1 over an ABD with even depth (Figure 5.15a),
- the impact of the pocket of rotational flow at the base of the ABD on ΔC_D , ΔC_L and Δp (see Figure 5.15b),
- the impact on the momentum transfer of enlarging the ABD depth within the interaction zone to increase the cross-sectional area of the outlet duct (see Figure 5.15 c).

In contrast, the fourth air breathing geometry was used to study the effects of a contracting ABD duct on the aerofoil characteristics, to confirm the main conclusions of the evolution. In Figure 5.15 red colours represent high velocities and the velocities are declining towards green colours.

Table 5.2 shows the resulting characteristics from the computations for the four cases. An ABD with an even depth performed relatively well and showed the expected drag reduction and lift augmentation. The introduction of a pocket improved the momentum transfer and hence further reduced C_D and increased C_L but also increased the auxiliary power requirements for the ABD significantly. An increase of the ABD depth within the interaction zone absorbed energy from the outer fluid and yielded a negative pressure drop across the ABD. Here the pressure drop was computed from the total pressures at the inlet and outlet openings. As a result the aerodynamic resistance of the body was increased and the lift remained almost unaffected. Computation of the opposite case (Figure 5.15d) predicted high drag reductions and good lift improvements. The pressure drop across this ABD exceeded the values of all the other geometries tested, thus during the evolution these types were extinguished.

The pressure distributions on the upper surface of the aerofoil section due to different ABD models caused only local pressure variations. For all the cases the pressures

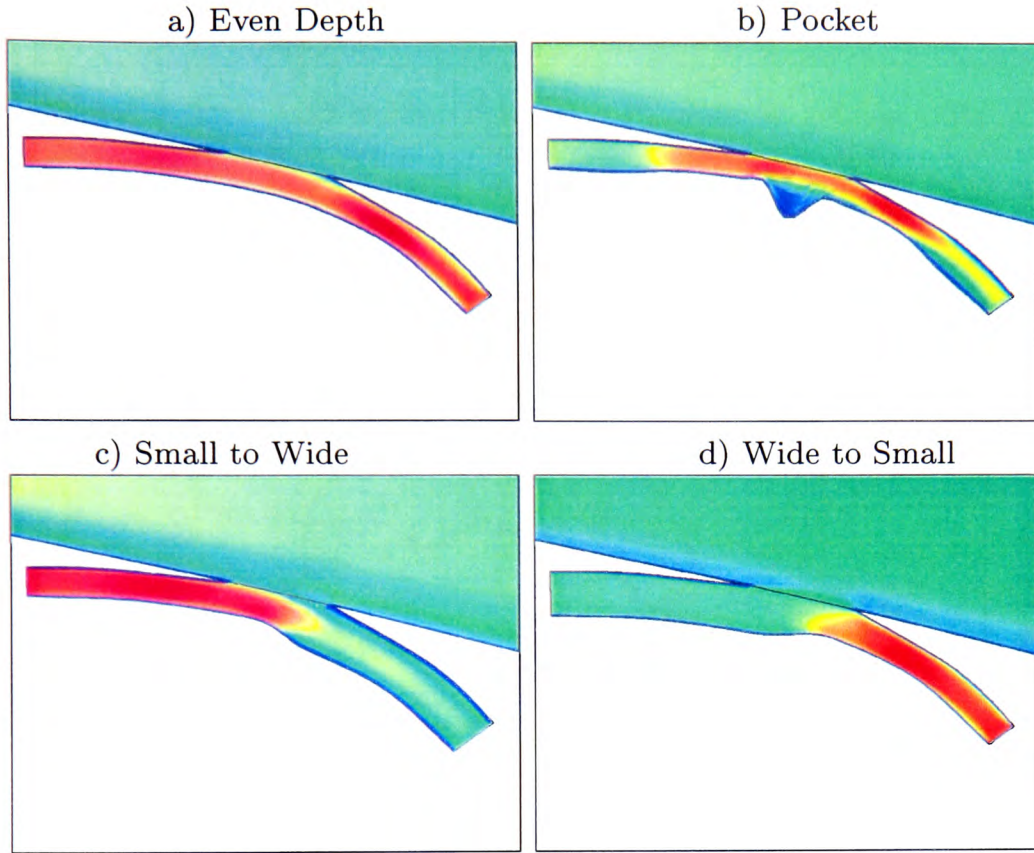


Figure 5.15: ABD Models to Study Characteristics of Evolutionary Results

upstream of the interaction zone were marginally improved and downstream of the ABD pressure variations are not noticeable (Figure 5.16). The local impact of the momentum transfer via the secondary flow at the interaction zone governs the variation of the lift coefficient.

Figure 5.17 shows the total pressure within the first grid point layer on the upper surface of the aerofoil section between 60% and 80% chord. It clearly shows the low energy content of the flow downstream of the point of interaction between the ABD stream and the external flow for an expanding ABD depth. The lower kinetic energy of the near wall flow for this geometry is also illustrated by the velocity profile in Figure 5.18b. From Figure 5.17 and Table 5.2 it can be seen that ABD geometries maintaining a high total pressure content downstream of the interaction zone produce the more desirable effects for flow control and improvement in the aerodynamic performance.

Table 5.2: Results for ABD Models

Model	Δp in Pa	\dot{V} in $\frac{\text{m}^3}{\text{s}}$	P_{ABD} in W	ΔC_D	ΔC_L
Even Depth	567	0.711	404	-6.89	1.35
Pocket	1412	0.677	956	-8.37	2.15
Small to Wide	-1841	0.873	-1607	0.86	0.15
Wide to Small	5262	1.259	6625	-7.04	2.12
Evolution 1.1	155	0.677	105	-8.04	3.39

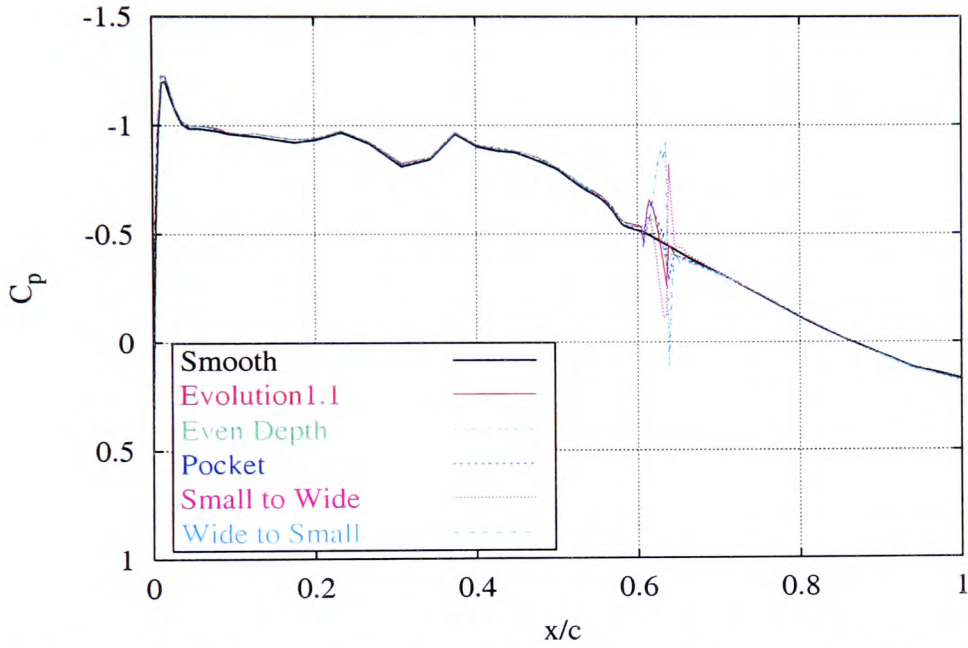


Figure 5.16: Pressure Distribution due to Different ABD Models

Figure 5.18a shows that all the studied ABD configurations had no visible impact on the velocity profile upstream of the position of flow control. However, at 75% chord a significantly ‘fuller’ velocity profile was obtained by the ABD configurations which produced increased total pressure content in the flow downstream of the ABD (see Figure 5.17). Hence, the static pressure was also increased downstream of flow control.

Visualisation of the flow velocity within the ABD with the even depth and the device with a ‘pocket’ (Figure 5.19a and 5.19b) shows that the internal ABD flow was kept in close contact by the presence of the ‘pocket’ with the external boundary layer and

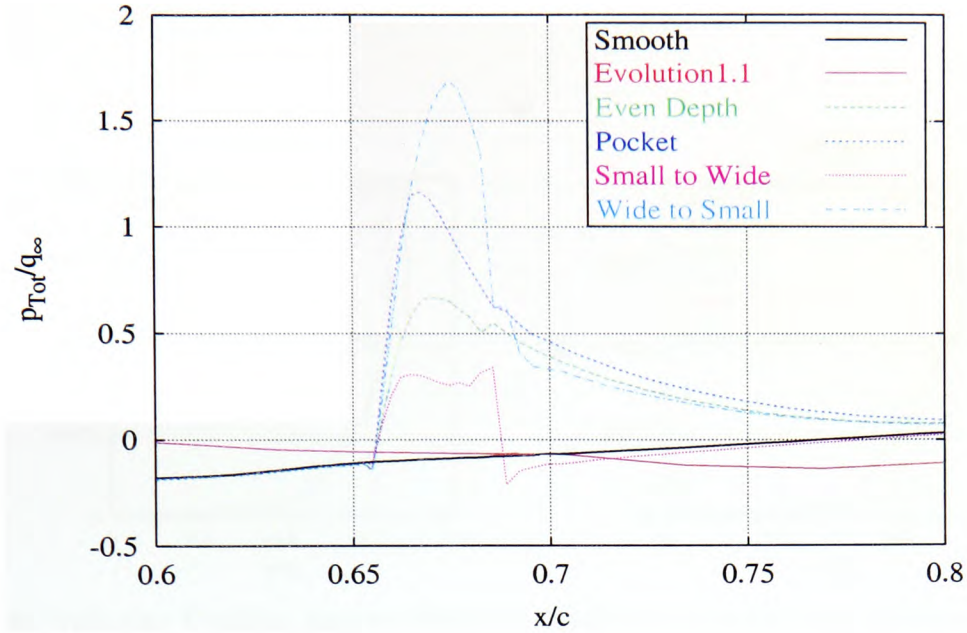


Figure 5.17: Total Pressure Distribution due to Different ABD Models

caused the improved interaction of the flow. The ‘closeness’ to the external flow was achieved by the rotational flow within the ‘pocket’, which guided the secondary flow along a smooth curve across the interaction zone.

During the course of the evolution the geometries which were developed combined the effects of improved momentum transfer due to the presence of a pocket of rotational flow as well as a reduced pressure drop due to a slight increase in the ABD depth within the interaction zone.

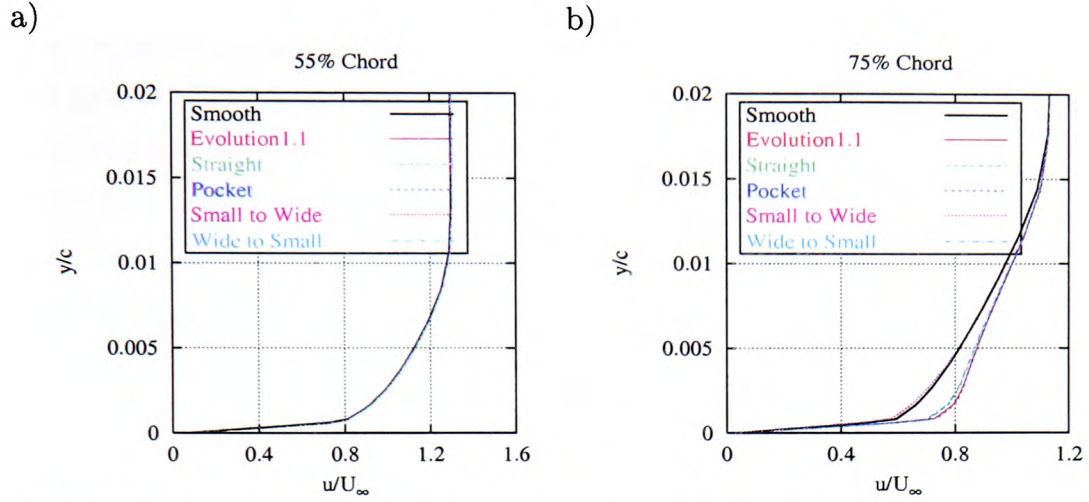


Figure 5.18: Velocity Profiles due to Different ABDs Upstream and Downstream of the Point of Interaction

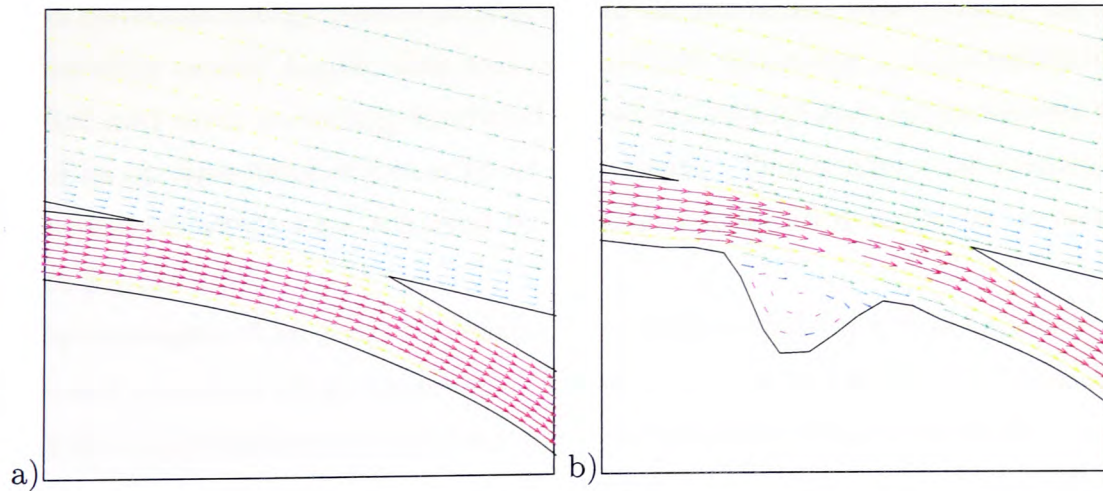


Figure 5.19: Velocity Vectors for a) the ABD Model with an even depth and b) the ABD Model with a 'pocket'

5.2.3 Discussion

An optimisation of the geometry of an ABD has been conducted. The optimisation was based on genetic algorithms, which evolve individuals with favourable features in successive generations. A fitness function based on the power requirements for lift, drag and the pumping power was used to assess the fitness of each parameter combination. All data for this fitness were obtained from numerical CFD predictions.

Despite the long evolution times, which limited the extent of the optimisation process, good convergence levels for the individual numerical computations and the evolution were achieved. Due to the strong influence of the auxiliary power requirements for the ABD on the fitness value the evolutions were governed by the pressure drop across the device. All evolutions showed the presence of a pocket of rotational flow within the interaction zone and an increase in the dimensions of the exit duct were desirable. Optimisations at a fixed ABD location and interaction size produced the same injection and suction angles.

Further study of the influence of the re-circulation pocket and of ABD duct widening showed that the pocket increased the momentum transfer into the boundary layer of the external flow. A widening of the ABD duct within the area of interaction caused a transfer of potential energy (static pressure) into the secondary flow system. On its own such a widening caused higher drag and reduced lift. However, a combination of both (i.e. pocket and duct widening) produced beneficial results and outperformed the behaviour of an air breathing device with an even depth. This configuration exceeded the lift improvements which were achieved by a parallel ABD using an injection coefficient of 2.5 (see Figure 4.8).

The optimisation of an ABD by genetic algorithms produced a ‘non-intuitive’ shape, which showed potential for an improved ABD efficiency and effectiveness. More detailed information on appropriate geometries may be obtained by further research. In particular, the impact of an expanding ABD duct and the resulting apparent negative pressure drop would need confirmation by physical experiments. In practice, a pump must cause a negative pressure at the outlet to withdraw the fluid out of the device, so that it is unlikely that the total pressure at outlet increases.

Chapter 6

Wind Tunnel Experiments

The numerical predictions in this study are validated by trials on a large wind tunnel at the University of Bath. A NACA65-415 aerofoil section was used in the numerical analysis to assess the effects of flow control by an air breathing device. This flow simulation study covered a wide range of parameters all of which could not be tested experimentally. Consequently, in order to confirm the numerical predictions a single air breathing system was investigated experimentally. This experimental programme investigated direct measurements of aerofoil forces and the pressure distribution over the upper surface of the aerofoil section. Flow visualisation using tufts attached downstream of the flow control system were also employed to examine qualitative features such as separation.

6.1 The Wind Tunnel

A low speed wind tunnel, at the University of Bath, with a maximum free stream velocity of 45 m/s was used in the present study. The test section measured 2.12 m in width and 1.51 m in height. The flow turbulence intensity was 0.5% for a velocity of 30 m/s at the centre-line of the section. A virtual axis six-component wind tunnel balance system was located on top of the test section with a support structure reaching through the roof of the tunnel into the test section (see Figure B.3). The six-components measured the forces in all three Cartesian coordinate directions and the three associated moments revolving around these directions. For the present investigation the wing section was mounted vertically in the test section, so that vertical rotation of the balance

system caused changes in the angles of attack. The force balance reference frame was fixed relative to the position of the aerofoil section.

6.2 Construction of the Aerofoil Section

The NACA65-415 wing section with a chord length of 0.5 m and a span of 0.4 m was casted in isocyanate polymer. The dimensions of the aerofoil section were chosen taking into account the following factors:

- The Reynolds-number should be as high as possible,
- The wing span should be as wide as possible,
- The dimensions were limited by the maximum allowable force which can be measured by the balance system (see Appendix B.2),
- Provision must be made to remove the secondary fluid flow out of the aerofoil section.

For the present investigation a maximum velocity of 30 m/s was used, so that the maximum Reynolds-number was:

$$Re = \frac{30 \frac{\text{m}}{\text{s}} \times 0.5 \text{ m}}{14.7 \times 10^{-6} \frac{\text{m}^2}{\text{s}}} = 1.02 \times 10^6$$

Although, the Reynolds-number on the wing of a commercial aircraft would be significantly higher the wing performance, L/D , does not change significantly for $Re > 10^6$ (see Figure 2.2). Therefore, the Reynolds-numbers¹ used for the present application are sufficient to be representative for flow conditions on aircrafts at high altitude.

The span-wise length was influenced by the need to satisfy the following contradicting objectives; (i) The aerofoil was mounted between slitter plates. These will exert forces on the balance system in addition to those from the aerofoil section. Consequently these wall effects associated with the splitter plates should be minimised by maximising the span. (ii) The span should be minimised to limit the air flow rate to

¹The fluid properties were taken from VDI Wärmeatlas [53] for $T = 288 \text{ K}$, $p = 1013 \text{ mbar}$ at dry condition.

6.2. CONSTRUCTION OF THE AEROFOIL SECTION

the ABD. The numerical simulations indicated that the ABD depth had only a small affect on momentum transfer via the secondary flow. Therefore, the injection and suction openings were set to 1% of the chord length in order to minimise the volume flow rate of the secondary flow without choking the supply and discharge devices. The ABD volume flow rate was restricted to $34 \text{ m}^3/\text{h}$ due to the capacity of the fluid extraction facilities and this in turn limited the span-wise length of the wing section to 0.4 m if an injection coefficient of 1.5 was required at $\text{Re} = 1.02 \times 10^6$. The supply of compressed air to the ABD did not exert any additional constrains on the construction of air breathing system.

Figure 6.1 shows the dimensions of the aerofoil section including the internal air supply and discharge ducting for the ABD and the position of the aerofoil section at the support structure. The aerofoil also incorporated a slot in which inserts (either smooth or comprising an ABD) were mounted.

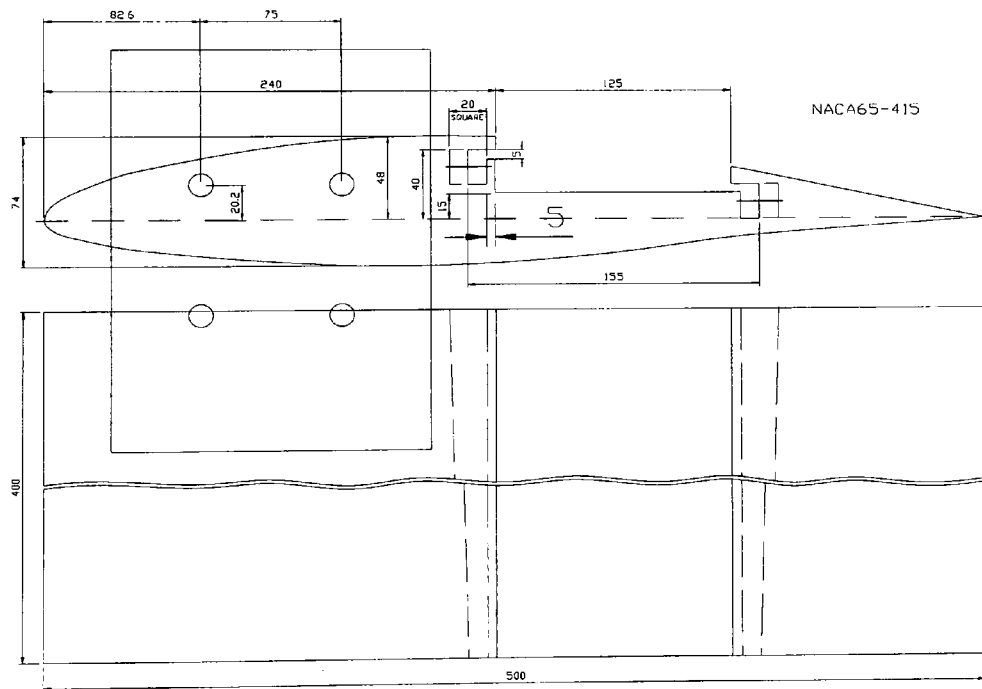


Figure 6.1: Aerofoil Section

The Construction of the ABD

An insert was constructed for the ABD which placed the location of flow control at 65% chord. This also fixed the size of the interaction zone to 3% chord. The injection and suction openings were fabricated to be 1% of the chord length. These parameter settings are a compromise between the limitations of the available space, the need to have a reasonable pressure drop at the suction side of the ducting system, as well as the use of moderate injection and suction angles.

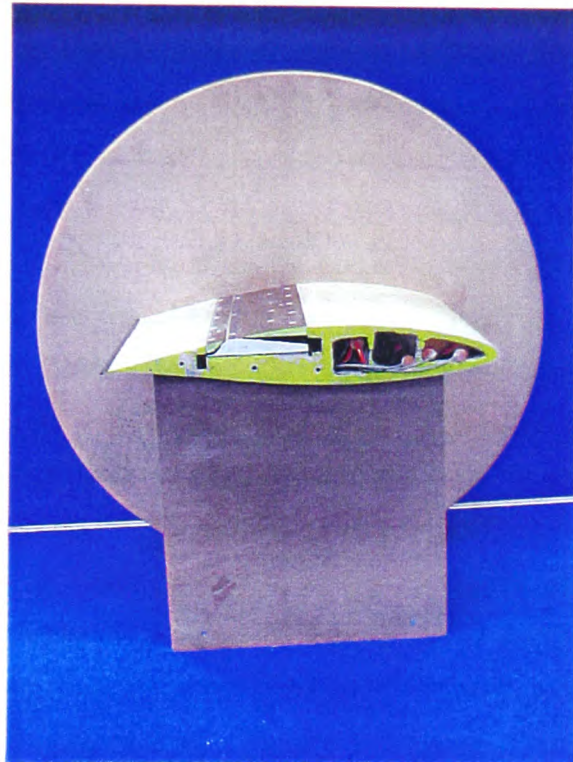


Figure 6.2: NACA65-415 Aerofoil Section With ABD Insert

The ABD model consisted of a MDF (medium density fibre) base and extensions which were fitted smoothly into the aerofoil surface. These extension pieces were made out of Phenol-formaldehyde paper composite (TufnolTM). Screws were used to fix the MDF base with the TufnolTM extensions or blades and to align the blades with the aerofoil surface as well as to adjust the injection and suction openings. Once the blade position was adjusted the holes for the embedded screw heads were filled with resin and subsequently smoothed with the aerofoil surface. In Figure 6.2 the aerofoil section with

the inserted ABD model is depicted. The lighter spots on the upper surface show the position of the screw heads.

Internal Ducting System

It was essential that the test configuration was two dimensional. Consequently, the span-wise injection and suction velocity should be uniform. Space limitations required that the secondary air was introduced and removed from the aerofoil ‘box’ in a span-wise direction. Therefore, various internal ducting systems with different tapers and shapes were simulated by CFD to try to give a uniform flow across the span of the system. An internal duct with a rectangular cross-section and taper ratio of 2 (Figure 6.1) was found to provide an optimal distribution (see Appendix B.1). To check this an acrylic model was build and tested. However, the resultant velocity distribution at the injection opening of the ABD proved to be non-uniform. Therefore the acrylic model was modified by means of a flexible back wall to investigate the effects of different tapers. Variation of the inclination of the back wall had no significant influence on the velocity distribution at either fluid suction or injection. The fluid was extracted uniformly at the suction side for all back wall positions. However, obtaining a uniform injection across the span of the ABD proved to be more difficult. The external air supply produced a jet-like flow into the delivery system. This jet resulted in most of the air being discharged at the span-wise far side of the ABD from the external air supply. In order to achieve an even air injection an ‘air distribution system’ was incorporated into the internal aerofoil supply duct. Figure 6.3 shows the principle of the injection

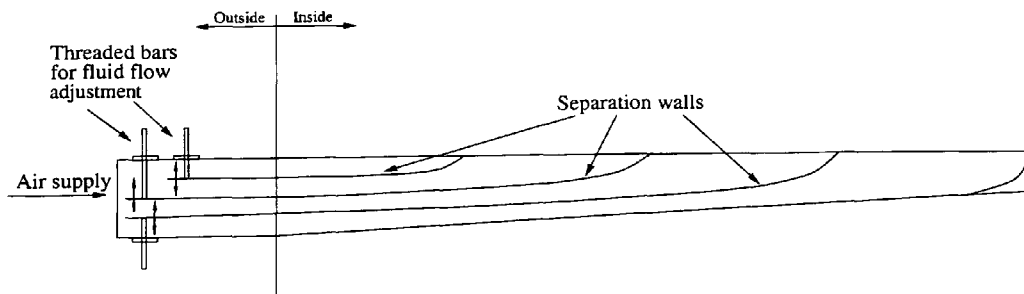


Figure 6.3: Injection Air Distributor System

air distribution system. A series of internal walls were used to distribute the flow more

6.2. CONSTRUCTION OF THE AEROFOIL SECTION

uniformly in the span-wise direction, i.e. they acted as flow straighteners. As shown on the left hand side of the distributor in Figure 6.3 threaded bars were attached to the separation walls to adjust the flows in each section. This part was located outside the test section, so that the velocity distribution along the injection opening into the ABD could be adjusted whilst the test were conducted. The separation walls inside the model were fixed so that only the size of the air supply inlets were adjusted. Additionally, an acrylic sheet flow straightener with 3 mm bore holes at a pitch of 10 mm was placed between the span-wise distributor and the ABD model. Both the flow straightener and the air distribution system are shown in Figure 6.4.

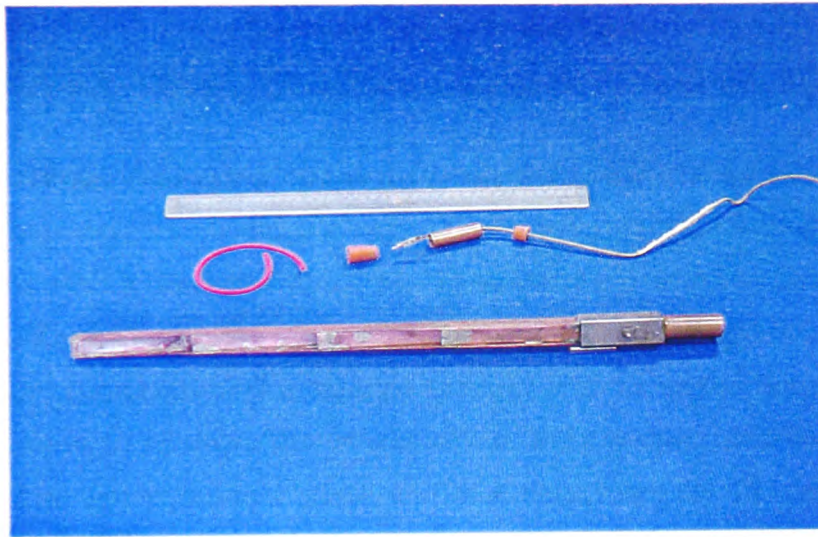


Figure 6.4: From bottom to top: Pressure Distributor, Pressure Tapping System, and Separation Wall with 3mm bore holes

As a result of these modifications a relatively even velocity distribution at the inlet opening to the ABD, as shown in Figure 6.5, was established. The graph shows the percentage velocity variation about the average value. These velocities were measured with a 3 mm diameter pitot static tube which was placed in front of the injection slot at 20° attack with respect to the aerofoil centre line.

Mounting of the Aerofoil Section

The aerofoil section was built with a slot for the insertion of the ABD or of a blank insert to maintain a smooth aerofoil section, as shown in Figure 6.1 and 6.6. The fixed

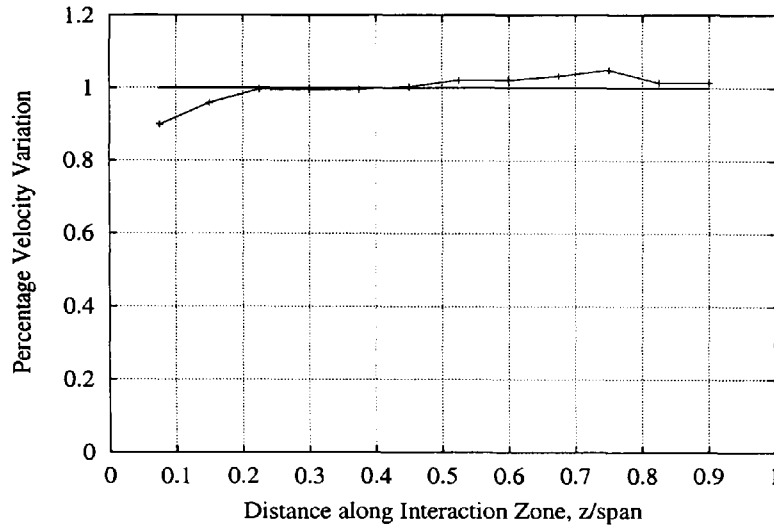


Figure 6.5: Velocity Distribution along the Interaction Zone

position of the external air supply connections ensured that the aerodynamic effects of the presences of these conditions did not vary. The aerofoil section was mounted between two splitter plates with a diameter of 0.7 m. These were attached to the aerofoil section to maintain two-dimensional flow. The aerofoil section was linked with two threaded bars to the support structure of the balance system. The threaded bars were embedded in the aerofoil section to support the weight of the wing section and to ensure stability during testing. The upper splitter plate was also connected by the two bars and two additional countersunk screws to the support structure of the balance system. The assembled test rig with the splitter plates, aerofoil section and support structure of the balance system (i.e. the beam) is shown in Figure 6.6.

Assessment of the effects of the use of the ABD required the measurement of the aerodynamic characteristics of the smooth aerofoil section for comparison purpose. Therefore, a smooth isocyanate polymer² insert was mounted in the slot, as shown in Figure 6.7, in this case.

²Use of an aluminium filler resulted in the insert having a different colour to the main aerofoil section.

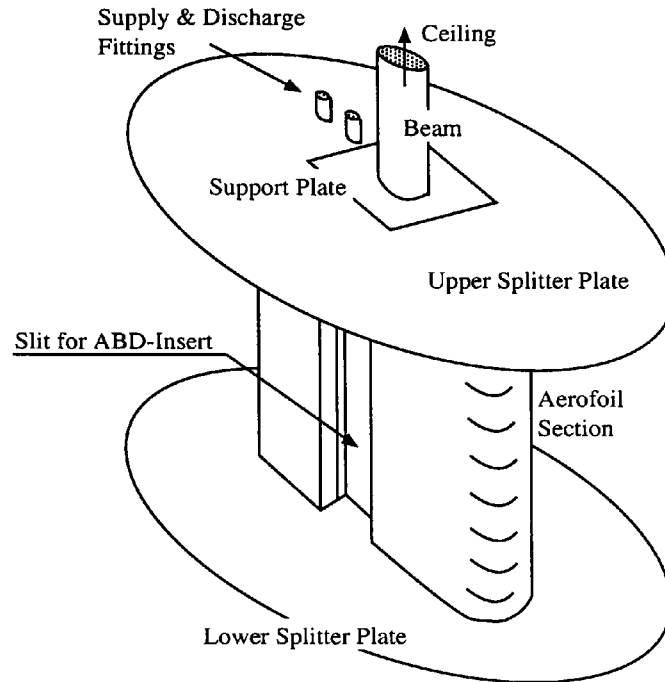


Figure 6.6: Model Structure

6.3 Aerodynamic Characteristics of the Aerofoil

Quantitative assessment of the effects of the ABD was undertaken using direct force measurements to determine the variations of lift and drag forces as well as by integrating the static pressure on the suction side of the aerofoil. The direct force measurements are discussed in Section 6.3 of this chapter and Section 6.4 describes the pressure variations as a result of flow control and the resulting lift augmentation.

The lift and drag coefficients were determined by measuring the absolute forces using the force balance system (see Appendix B.2). Due to the vertical placement of the wing section only the ‘side force’, the ‘drag force’ and the ‘yawing moment’ were used in this study. The side force represented the lift of the aerofoil section. Interaction between these forces and the moments required separation of the individual components, as shown in Appendix B.3. The resulting forces are initially those with respect to the balance system and these are subsequently resolved into forces related to the main flow direction.



Figure 6.7: Aerofoil Section with Blank Insert

The aerofoil characteristics were recorded for two different wind tunnel velocities namely 30 m/s and 20 m/s which corresponded to $Re = 1.02 \times 10^6$ and $Re = 0.68 \times 10^6$, respectively. A range of injection coefficients from 0 to 2.5 were also studied. These experiments were aimed at studying:

- the dependency of the performance of the ABD on the Reynolds-number and
- the effect of varying C_i on the drag and lift.

The aerodynamic characteristics of the aerofoil section were determined for angles of attack ranging from -8° to the stall angle in increments of 2° . The drag and lift coefficients in Figure 6.8 and 6.9 are the average of two sets of measurements. Error-bars are omitted in these graphs, since the small variations between the readings did not provide any useful information. The forces exerted on the balance system by the splitter plates and support structure were measured individually for all angles of attack and wind tunnel flow velocities and were subtracted from the overall force balance

readings to yield the forces acting on the aerofoil. Stall occurred for the aerofoil section subjected to $Re = 0.68 \times 10^6$ between 18° and 20° angle of attack and at the higher $Re = 1.02 \times 10^6$ between 20° and 22° (see Figure 6.9).

6.3.1 The Smooth Aerofoil Section

The curves for both the lift and drag characteristics are clearly defined and show a typical shape for a NACA65-415 aerofoil section, see Figures 6.8 and 6.9. The lift coefficient coincides with the maximum C_L as published by Abbott and von Doenhoff but $C_{L_{max}}$ is shifted to higher angles of attack. For the higher Reynolds-number (i.e. $Re = 1.02 \times 10^6$) the experimental $C_{L_{max}}$ was determined at 20° angle of attack and for $Re = 0.68 \times 10^6$ at 18° angle of attack. The difference between the individual lift curves may well be due to the different Reynolds-numbers and test conditions for which lift of the NACA65-415 aerofoil section was measured.

Figure 6.8 shows the drag coefficient measured in this experimental study, C_D from Abbott and von Doenhoff [26] and C_D from the numerical analysis from Chapter 4. The diagram shows a strong difference between the drag curves from this experimental investigation and the two other curves. The lower Reynolds-number which was used in this study, the Reynolds-numbers used in the numerical analysis and the Reynolds-number from Abbott and von Doenhoff [26] are all different and may have influenced the results. It should be noted, that the previously published data used an aerofoil with a rough surface to initiate early transition. The stronger impact on the drag data probably arose from the difficulties to separate the individual drag contribution of the splitter plates, the supply and discharge piping and the support structure of the force balance system. Furthermore, the effect of the tunnel vibration and inaccuracies of the hand manufactured aerofoil section are not known. Drag measurements are very sensitive to small disturbances due to their low magnitude. Overall both aerodynamic characteristics of the NACA65-415 aerofoil section showed similar results for two successive measurements. Variation of the Reynolds-number in this experimental study showed expected effects on C_D and C_L .

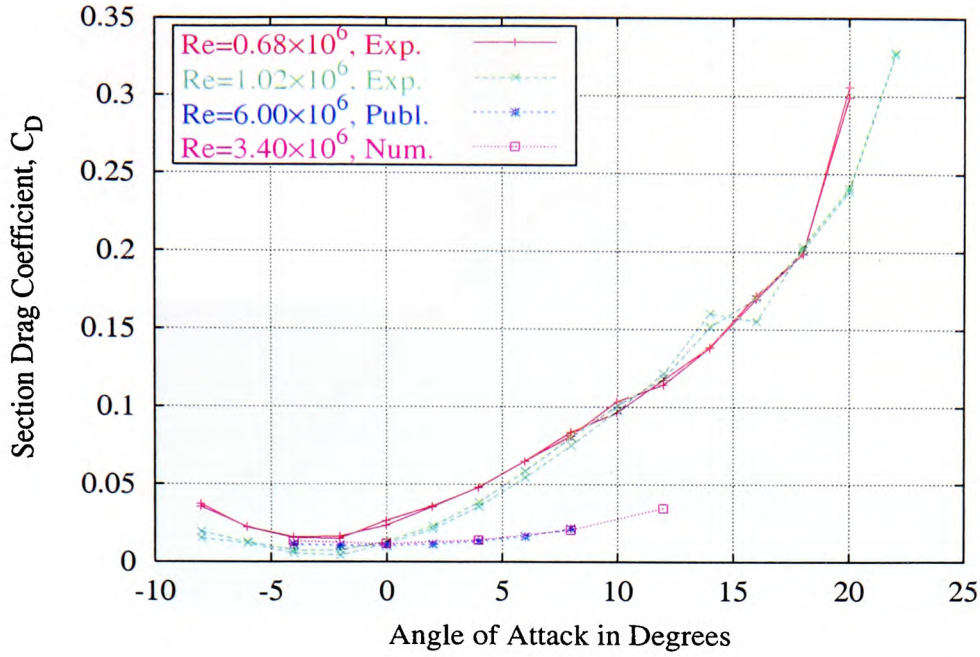


Figure 6.8: Drag Coefficient versus Angle of Attack

6.3.2 Effect of the ABD on the Aerofoil Performance

The aerofoil section was tested at two different Reynolds-numbers ($Re = 1.02 \times 10^6$ and $Re = 0.68 \times 10^6$). The limited capacity of the secondary air supply restricted the study of the effects of higher values of C_i on the performance to the lower Reynolds-number. The injection coefficients of 2.5, 2.0 and 1.5 used in the test were achieved by volume flow rates through the ABD of $34 \text{ m}^3/\text{h}$, $28.8 \text{ m}^3/\text{h}$ and $21.6 \text{ m}^3/\text{h}$, respectively. For the higher Reynolds-number the maximum volume flow rate ($34 \text{ m}^3/\text{h}$) provided a C_i of 1.5. The following graphs show the aerodynamic characteristics for the smooth aerofoil section (Smooth), an aerofoil fitted with a non-operational ABD (No Flow), and an ABD operating with different injection coefficients, C_i .

The lift coefficient was enhanced for angles of attack $> 6^\circ$ for both Reynolds-numbers and at all C_i s (see Figures 6.10 and 6.11). These increases can be seen more clearly in Figure 6.12 which shows the percentage change (see Equation 4.1) in the lift coefficient with respect to that for the smooth aerofoil. Thus, a C_i of 1.5 augmented the lift coefficient by 2% at 4° angle of attack for a Reynolds-number of 1.02×10^6 . This lift improvement continues and reaches a peak of approximately 11% at 16° angle of attack.

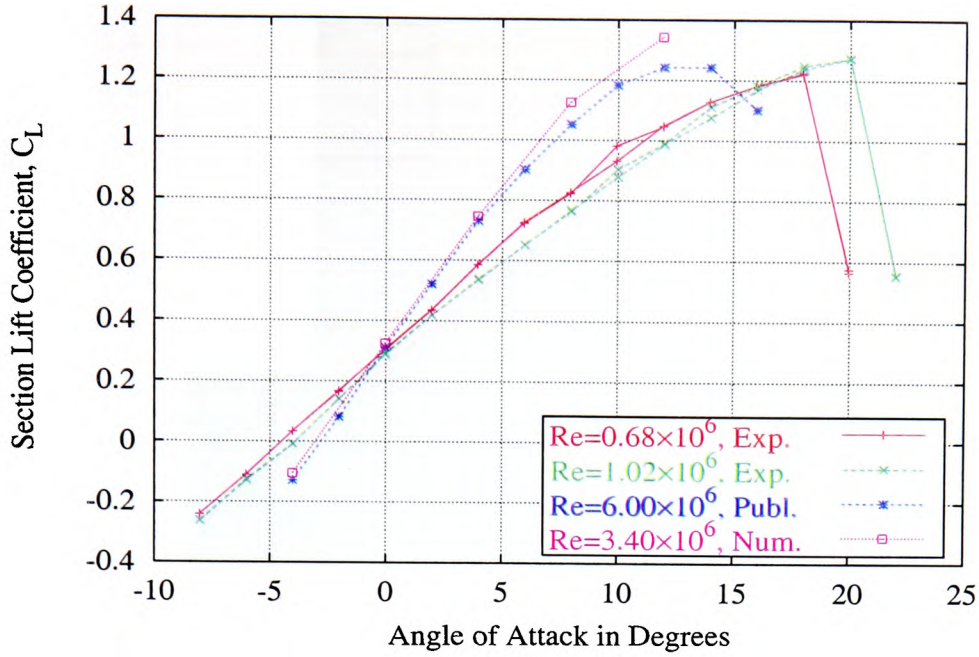


Figure 6.9: Lift Coefficient versus Angle of Attack

A generally similar change in C_L with the angle of attack was observed for the same C_i at $Re = 0.68 \times 10^6$, although, the magnitudes of the changes were much lower, reaching a peak of 6.8% lift augmentation at 16° angle of attack. Higher values of C_i substantially improved the lift characteristics with the maximum improvement of 14.9% occurring at 18° for $Re = 0.68 \times 10^6$ and $C_i = 2.5$. The discontinuity at 10° angle of attack may indicate a significant change in the location of separation on the aerofoil section which can only be controlled with difficulty, especially for low C_i s and low Reynolds-numbers.

At lower angles of attack ($< 6^\circ$) and $Re = 0.68 \times 10^6$ the ABD caused a slight decrease in C_L . The additional forces due to the splitter plates and the support structure make the determination of the benefits of the ABD difficult. Comparison with the numerical results is therefore difficult. However, the strong effects of the ABD on the flow at high angles of attack were shown.

It should be noted, however, that the a non-operational ABD affected the lift coefficient adversely compared to that for the smooth aerofoil section. The ABD gap caused a disturbance in the near wall flow and increased the drag. For higher angles of attack this flow disturbance was less significant.

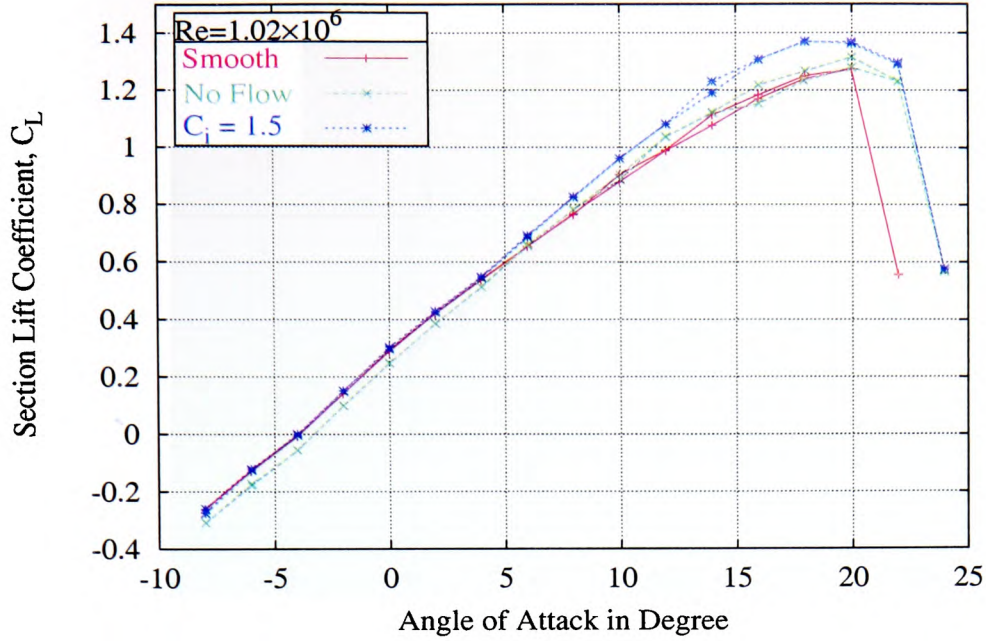


Figure 6.10: Effect of the ABD on C_L at various Angles of Attack ($Re = 1.02 \times 10^6$)

The aerodynamic drag measurements were more strongly influenced by small disturbances than the lift forces. In Figure 6.14 the smooth aerofoil section exhibits slightly poorer performance than an arrangement with a non-operational ABD at low C_i s. Differences in the surface structure, small variations in the shape and/or disturbances due to the transition from the ‘base’ aerofoil section to the inserts may have caused the discrepancy. Furthermore, high drag forces of the peripheral equipment (e.g. the splitter plates, the support structure etc.) compared with the small variations of the aerofoil drag contributed to the unclear effects of the ABD on drag. To avoid negative effects on the readings when the angles of attack was changed the supply and discharge pipes were fixed at the roof of the tunnel (Appendix B.4). Although, the reference readings for the force balance (non-operational wind tunnel) were undertaken with and without ABD flow for all aerofoil positions and in the case of flow control with the three different C_i s, a suspicion remained that the flow dynamics within the supply and discharge pipes may have influenced the variations of C_D and C_L . During the testing period this influence could neither be determined nor could the experimental set-up be changed to avoid a possible influence of the pipes. Thus direct comparisons of the aerofoil drag for

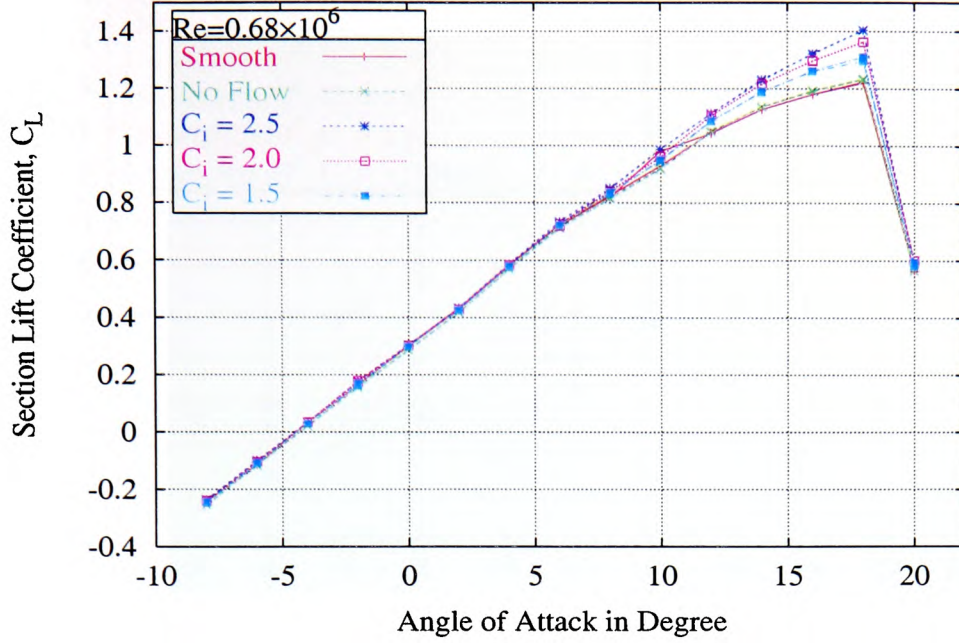


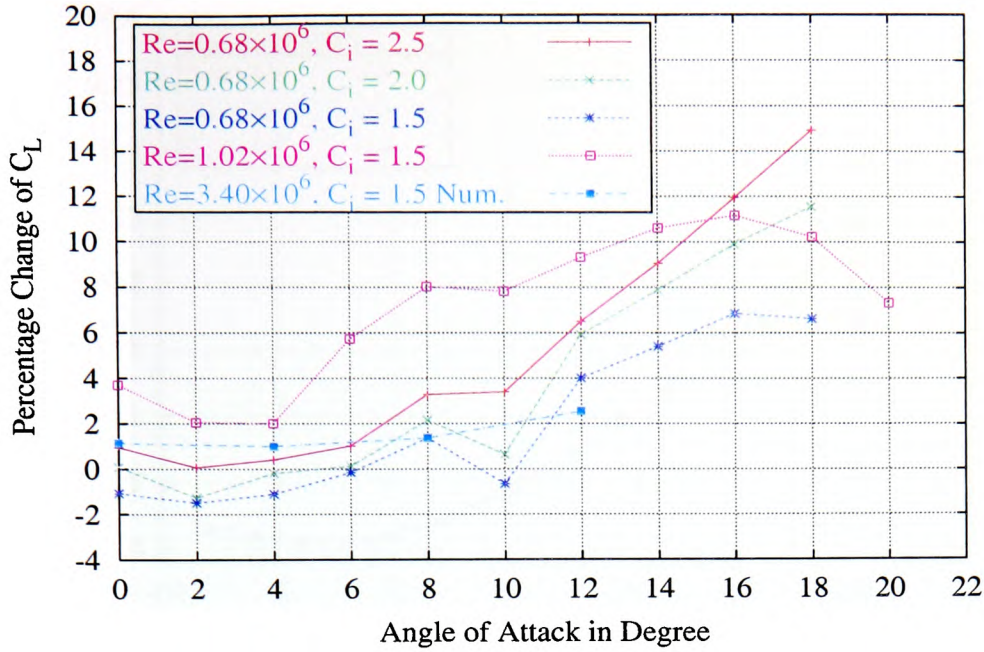
Figure 6.11: Effect of the ABD on C_L at various Angles of Attack ($Re = 0.68 \times 10^6$)

the smooth and ABD cases is limited. Due to these difficulties a quantitative analysis, as for the lift augmentation, was omitted.

6.4 Pressure Distributions

To improve the understanding of the effects of the ABD the pressure distributions on the suction side of the aerofoil were studied. Pressure transducers (see Appendix B.4) were used to measure the pressures at six discrete locations along the span-wise centre line of the wing section. These pressure readings were used to:

- compare the experimental and numerical pressure distributions,
- describe the quantitative effects of the ABD on the pressure distribution,
- calculate the lift coefficient between 3% and 78% chord length and hence the percentage change in C_L due to the ABD,
- compare the percentage changes in C_L with data from the numerical analysis and the direct force balance readings.

Figure 6.12: Percentage Change of C_L

Pressure measurements provide particularly valuable information since they are directly related to the flow field over the aerofoil section.

6.4.1 Installation of the Pressure Transducers

Plastic tubes were used to connect the ‘tappings’ on the aerofoil surface with the pressure transducers. The transducers were inserted in copper tubes with an inner diameter of 10 mm, which were sealed with two rubber plugs, as shown in Figure 6.15 (see also Figure 6.4). In this way a constant reference pressure was maintained for each pressure transducer. Use of the correct pressure tapping tubes assisted the production of a smooth aerofoil surface and ensured minimal flow disturbance due to the small tube bore of 0.8 mm. The copper tubes were placed in the aerofoil chamber (Figure 6.2) and the cables for signal transmission were guided along the support structure out of the wind tunnel. Further details of the transducers are presented in Appendix B.4.

The transducer signals were amplified by a factor of 750 and processed by means of a LABVIEWTM program. One hundred measurements were taken every second at a sampling rate of 200 samples per second. The remaining 0.5 seconds ensured quasi

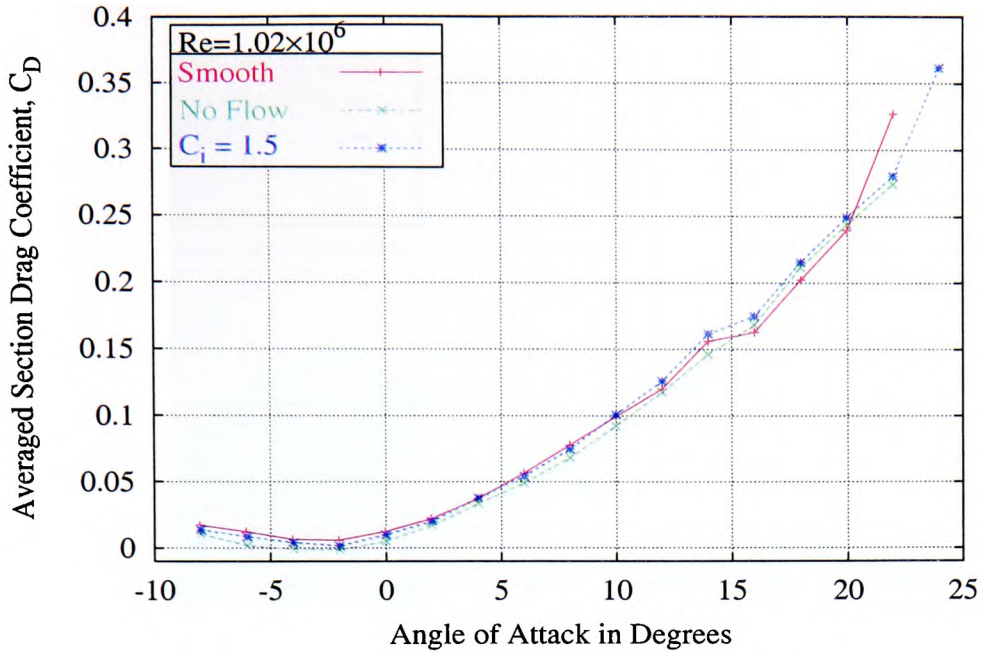


Figure 6.13: Effect of the ABD on C_D at various Angles of Attack ($Re = 1.02 \times 10^6$)

simultaneous storage of the data from all the transducers. Each average pressure value in the following diagrams was assembled from a series of ten readings.

Due to a malfunction of the transducer at 25% chord length only five pressure acquisition locations were used in this study.

6.4.2 Validation of the Pressure Measurements

In Figure 6.9 the numerical predictions were shown to be in good agreement with published lift coefficients and hence suggested that the numerical pressure distributions were reliable. In the current section of the thesis these numerical pressure distributions were further validated by the experimental pressure readings.

Figures 6.16 and 6.17 show good agreement between experimental and predicted data for pressure coefficients between 3% and 53% chord length for the smooth aerofoil. Although, there are significant differences in the predicted and measured values at 78% chord overall the pressure distributions were generally consistent with the predicted values at the different angles of attack (see Figure 6.17). Possible causes of the differences near the rear of the aerofoil may arise from variations in the aerofoil shape and

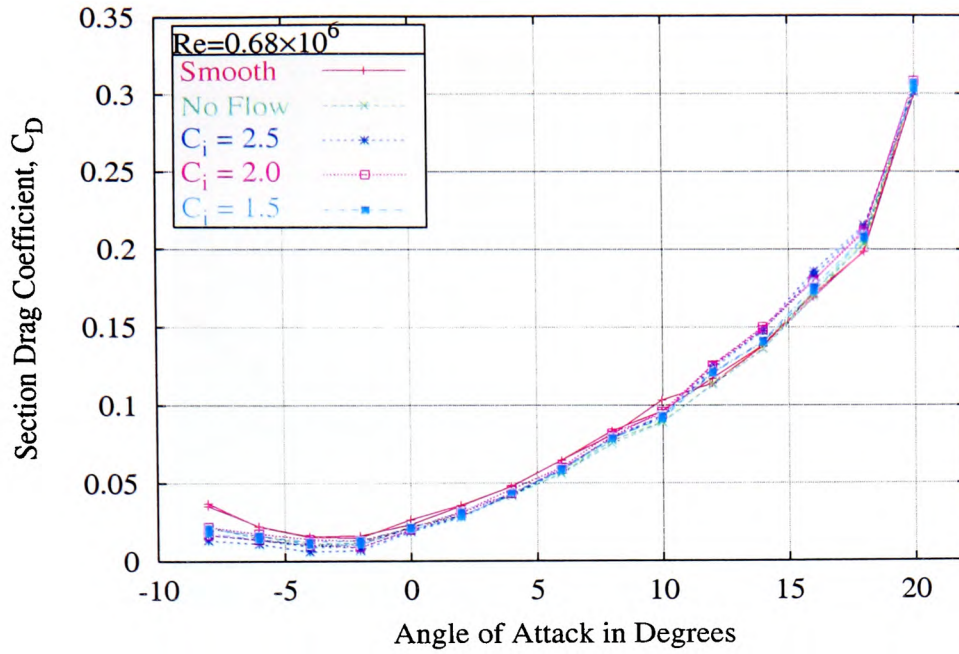


Figure 6.14: Effect of the ABD on C_D at various Angles of Attack ($Re = 0.68 \times 10^6$)

the presence of disturbances due to the ‘inserts’. The difference in flow conditions for the numerical ($Re_{Num.} = 3.4 \times 10^6$) and experimental ($Re_{exp.} = 0.68 \times 10^6$ and $Re_{exp.} = 1.02 \times 10^6$) work may also need to be taken into consideration when comparing the experimental results with the predicted data. Overall, however, the data for the smooth aerofoil appears to be reliable so that the pressure measurements provide a sound basis for comparing the effects produced by the ABD.

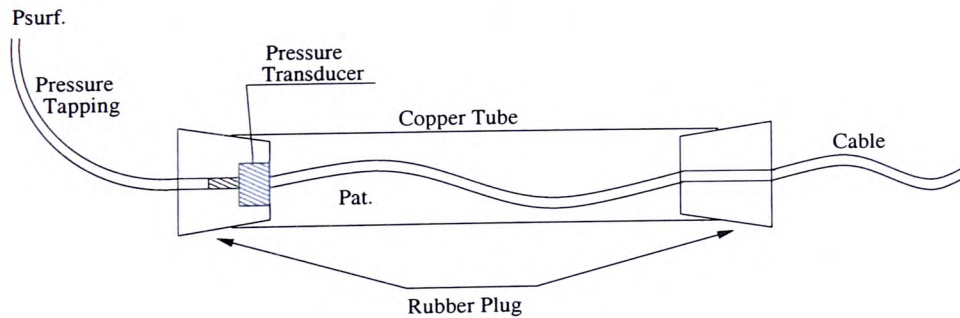
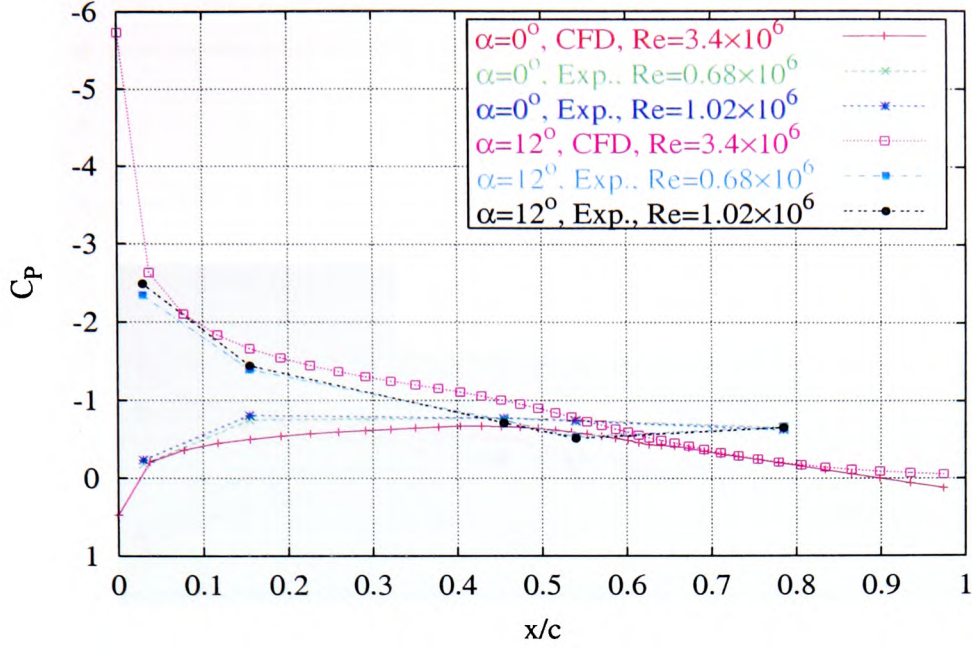


Figure 6.15: Principle of Pressure Tapping

Figure 6.16: Validation of Pressure Readings for 0° and 12°

6.4.3 Effects of the ABD on the Pressure Distributions

Qualitative Assessment

This section of the thesis discusses the effects of momentum transfer via the secondary flow in the ABD on the pressure distributions measured on the suction side of the NACA65-415 aerofoil section. The pressure distributions for $Re = 0.68 \times 10^6$ at -8° , 0° , 8° , and 16° angle of attacks are shown. Similar pressure distributions were recorded for $Re = 1.02 \times 10^6$. A detailed discussion of the higher Re data would not contribute to the overall understanding of the effects but they are shown in Appendix B.6.

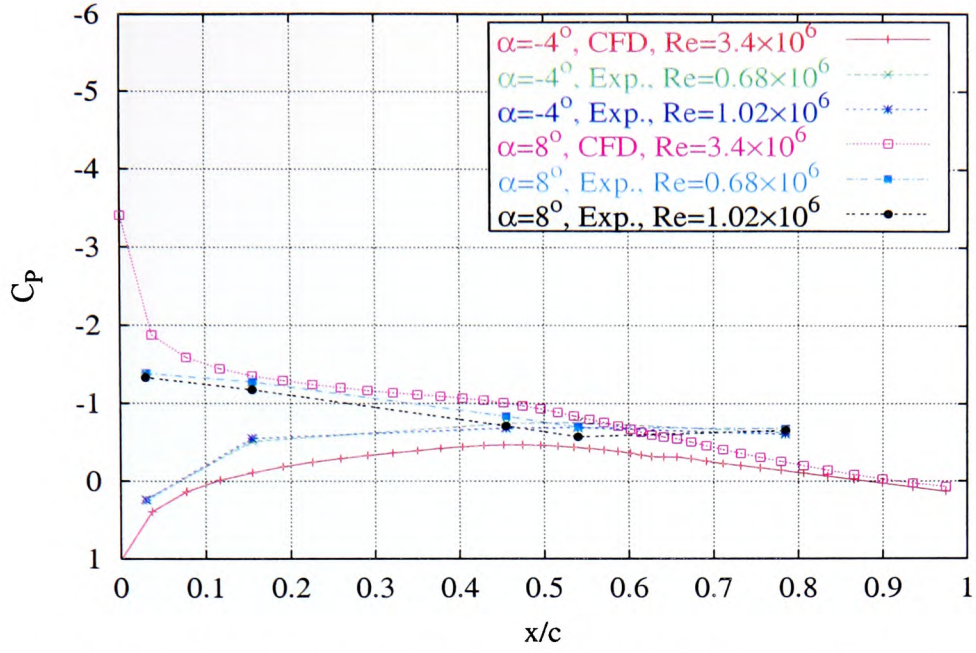


Figure 6.17: Validation of Pressure Readings for -4° and 8°

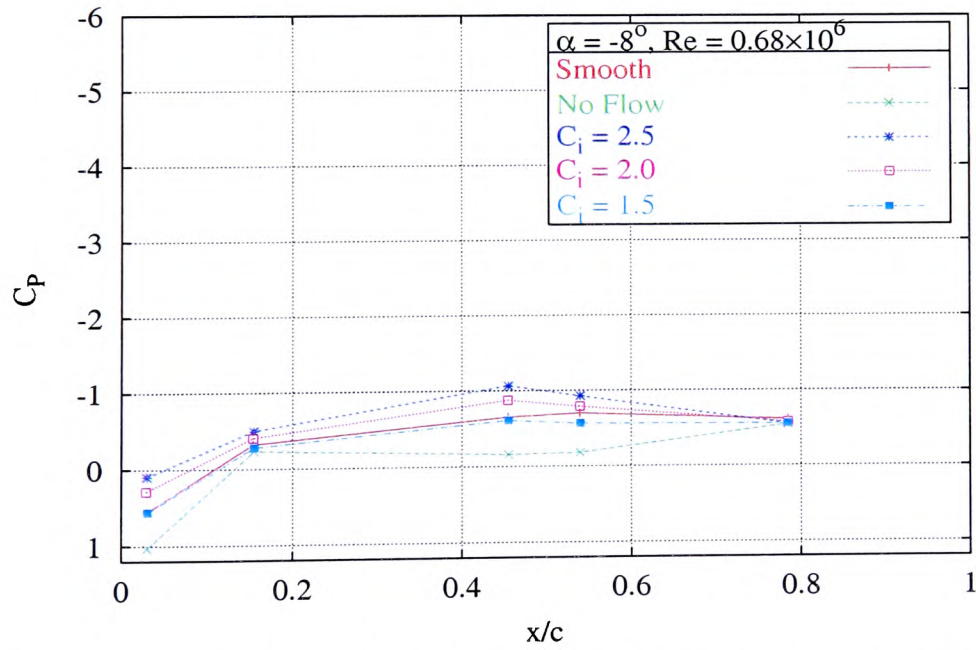
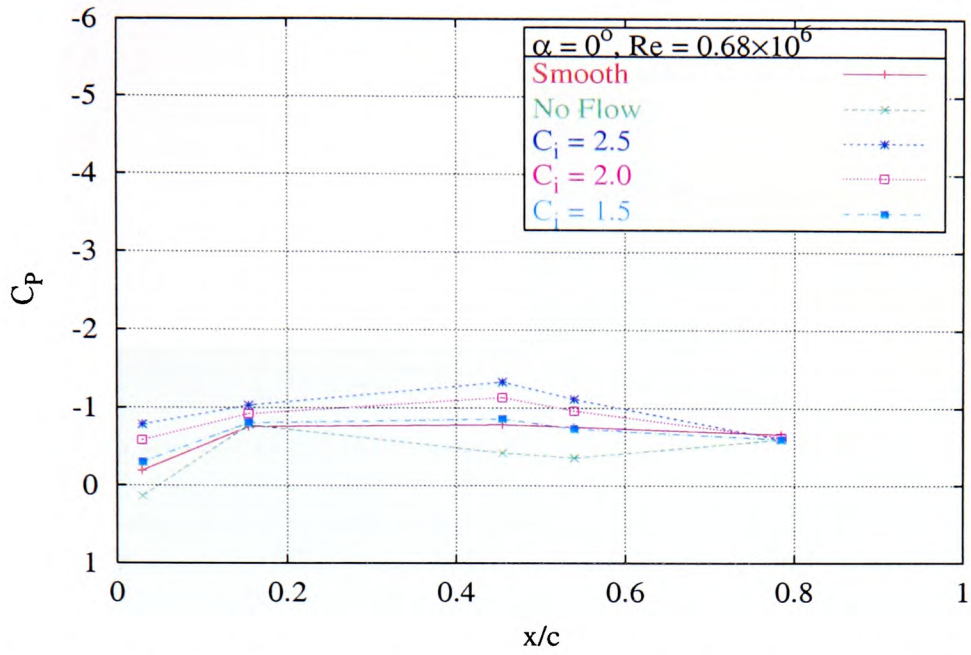
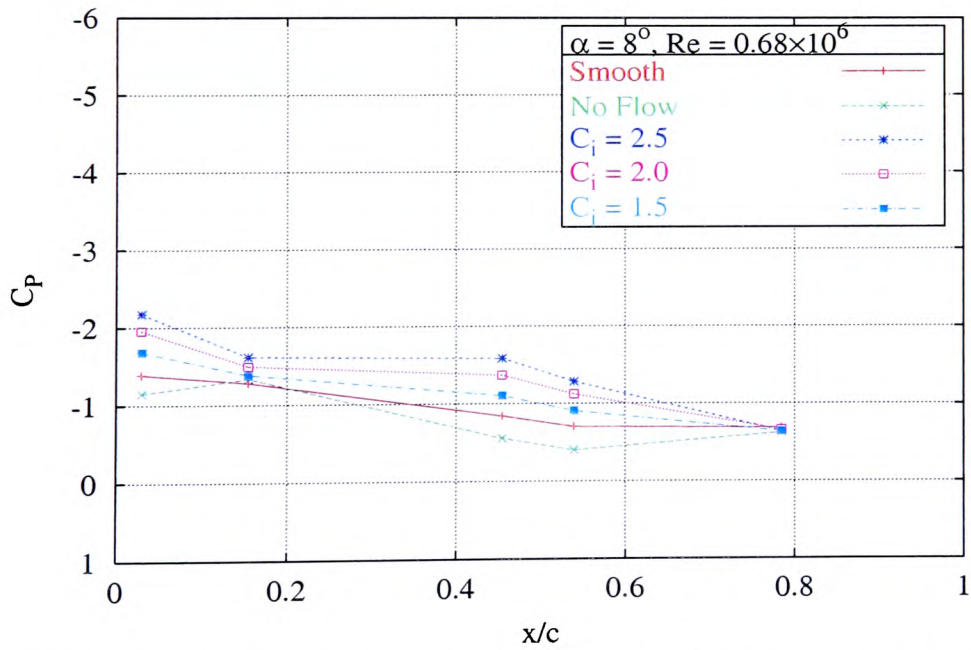


Figure 6.18: Effects of the ABD on the Pressure Distribution at -8° Angle of Attack

Figure 6.19: Effects of the ABD on the Pressure Distribution at 0° Angle of AttackFigure 6.20: Effects of the ABD on the Pressure Distribution at 8° Angle of Attack

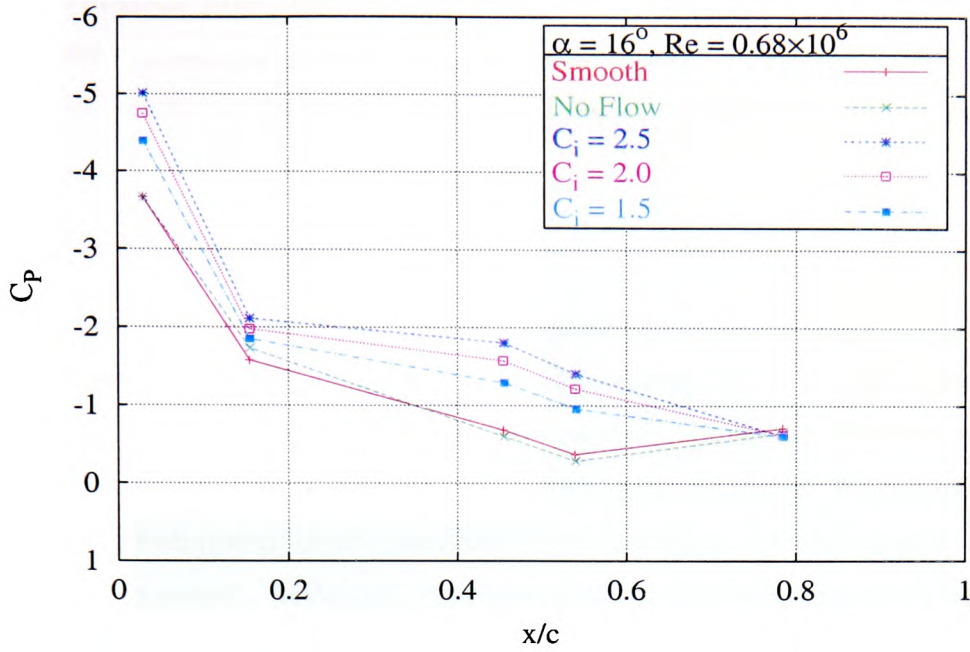


Figure 6.21: Effects of the ABD on the Pressure Distribution at 16° Angle of Attack

At -8° angle of attack, see Figure 6.18, the pressure on the suction side of the aerofoil section was decreased at the higher injection coefficients of 2.0 ($\dot{V} = 28.8 \text{ m}^3/\text{h}$) and 2.5 ($\dot{V} = 34 \text{ m}^3/\text{h}$). These changes are noticeable between 3% and 53% chord length, whereas the pressures measured close to the trailing edge experienced only small variations. A C_i of 1.5 increases the pressure slightly near the region of interaction with the secondary flow. This confirms the conclusion about the impact of the velocity difference of the ABD flow and the external flow at the location of interaction. This velocity difference is small at low and negative angles of attack and the flow in the vicinity of the aerofoil surface can not be enhanced. The expected disturbance of the main flow occurred for a non-operational ABD, as indicated by the higher pressures in this case. In Figures 6.11 to 6.14 this effect was not detected which shows the direct measurements only detected large variations in lift forces.

For angles of attack greater than 0° enhancement of lift for all C_i s were observed, see Figures 6.19 to 6.21. Between 3% and 53% chord the pressure coefficients are significantly decreased (i.e. they become more negative). Thus for an angle of attack of 16° at 53% chord C_p substantially improved for C_i s of 1.5 and 2.5, which confirms

the lift augmentation presented in Figure 6.11. However, the pressures close to the trailing edge were marginally increased for all test cases. It should also be noted that the disturbance due to a non-operational ABD largely disappeared at very high angles of attack.

Quantitative Assessment

The qualitative assessment of the pressure variation due to flow control suggest a somewhat stronger impact on C_L as detected by the direct force balance measurements. The pressure decrease on the aerofoil suction side, as shown in Figures 6.18 to 6.21, indicated significant lift improvements. In the current section of this thesis the contribution to the lift behaviour of the aerofoil of the pressure measurements between 3% and 78% was determined. Although, the information obtained from the integration of only five static pressure readings is limited, it nevertheless, provides a reasonable basis for estimating the changes in C_L due to the ABD.

The lift force contribution of the upper aerofoil surface between 3% and 78% was obtained from the numerical integration of the five discrete pressures, as:

$$\cos\beta \times span \times \int_{3\%c}^{78\%c} \overline{p_{n,n+1}} dc \quad (6.1)$$

where β represents the angle between the position of the individual pressure sampling location and the free stream direction (taking into account the angle of attack).

In Table 6.1 the validity of the method compared with a ‘more continuous’ variation of the pressures is assessed for the smooth aerofoil. Here, the columns (from left to right) represent:

1. angle of attack,
2. the lift coefficient from the integrated wall forces as give by the CFD simulation,
3. C_L obtained by integrating over the entire upper surface (as defined in Equation 6.1) using 125 discrete pressure values from the numerical study,
4. C_L obtained by integrating the numerical pressure between 3% and 78% chord length,

5. C_L obtained by integrating the numerical pressures for the five discrete locations (3%, 15%, 45%, 53%, and 78% chord),
6. the percentage variation between the fine (125 points) and the coarse (five points) integration of pressures to indicate the likely error in using only a few discrete points,
7. and 8. C_L obtained from the integrated experimental pressures at five discrete locations (3%, 15%, 45%, 53%, and 78% chord) for $Re = 0.68 \times 10^6$ and $Re = 1.02 \times 10^6$.

Table 6.1: Values of Lift Coefficients by Different Techniques for a Smooth Aerofoil Section

Inc.	Numerical C_L					Exp. C_L	
	Wall Force	Integr. 100%	Integr. 3%-78%	5 Point	%	5 Point	
						0.68×10^6	1.02×10^6
-4	0.1627	0.1654	0.1902	0.1708	-10.1	0.4370	0.2919
0	0.3728	0.3699	0.3721	0.3539	-4.8	0.5130	0.4121
4	0.6147	0.5952	0.5624	0.5525	-2.1	0.6102	0.5287
8	0.8626	0.8148	0.7394	0.7405	0.15	0.6879	0.5715
12	1.0220	0.9414	0.8179	0.8382	2.5	0.7166	0.7034

Integration of pressures is in close agreement with the wall force predictions (columns 2 and 3 in Table 6.1) which suggests that pressure integration is a valid method of determining C_L . The small difference in the prediction of C_L by the integration method (column 3) may be due the negligible contribution of shear forces on the lift. Ignoring the first 3% and the last 22% of the aerofoil section alters the lift contribution only relatively slightly. The use of only five pressure readings in the integration between 3% and 78% over the span of the aerofoil results in changes in C_L of -10.1% at -4° and 0.15% at 8° angle of attack (i.e. compared to the results in column 4). Thus, despite this coarse approach the difference in predicted values of C_L between 0° and 12° angles of attack is minor. The numerical and experimental 'five point integration' data are generally in reasonable agreement except at -4° and 0° angles of attack. In these cases substantial differences were found particularly at $Re = 0.68 \times 10^6$. From

Subsection 6.4.2 it can be seen that the experimental results for the pressures were lower than the numerically calculated values at low angles of attack. Thus the differences in numerically calculated and experimentally determined values of C_L were caused by the differences of the pressure distributions and not by the integration method. The thickness of a boundary layer decreases with the Reynolds-number, thus the pressure difference was probably caused by the different thicknesses of the experimental and the numerically predicted boundary layers on the aerofoil surface.

Using the above 5 point integration method on the experimental pressure distributions over the aerofoil surface yielded the lift coefficients in Figures 6.22 and 6.23.

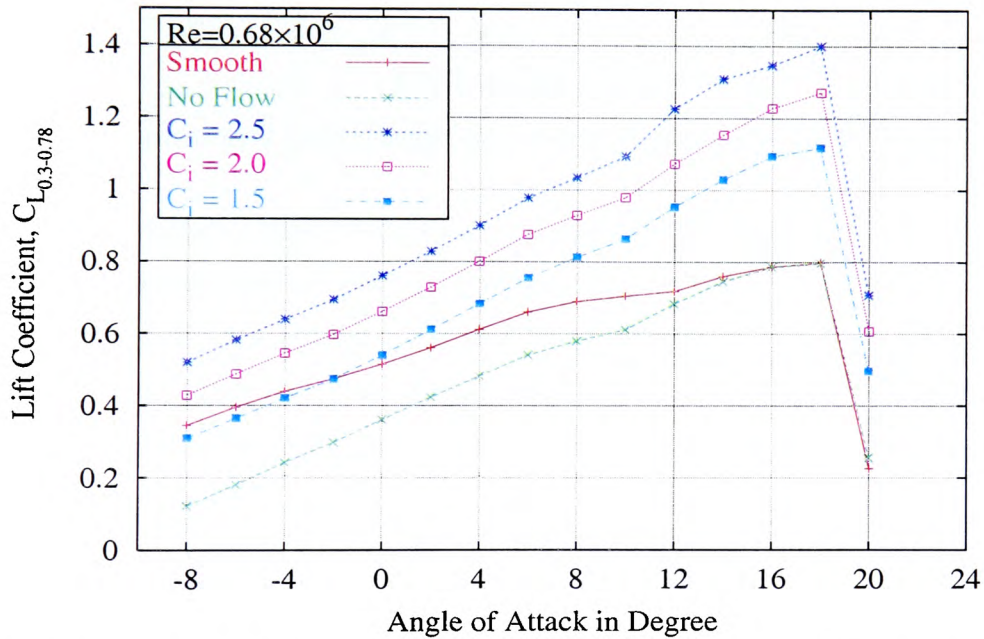


Figure 6.22: Experimental Lift Coefficient versus Angle of Attack ($Re = 0.68 \times 10^6$)

At low or negative angles of attack the downwards force due to the fluid acceleration over the lower aerofoil surface is not accounted for so that the lift coefficients are likely to be over estimated. In contrast, for high angles of attack neglecting the lift contribution from the wing tip and the high pressure side produces lower measured C_L s. The lift curves for both test conditions exhibited similar trends with increasing angle of attack.

In both diagrams (Figures 6.22 and 6.23) the presence of the non-operational ABD

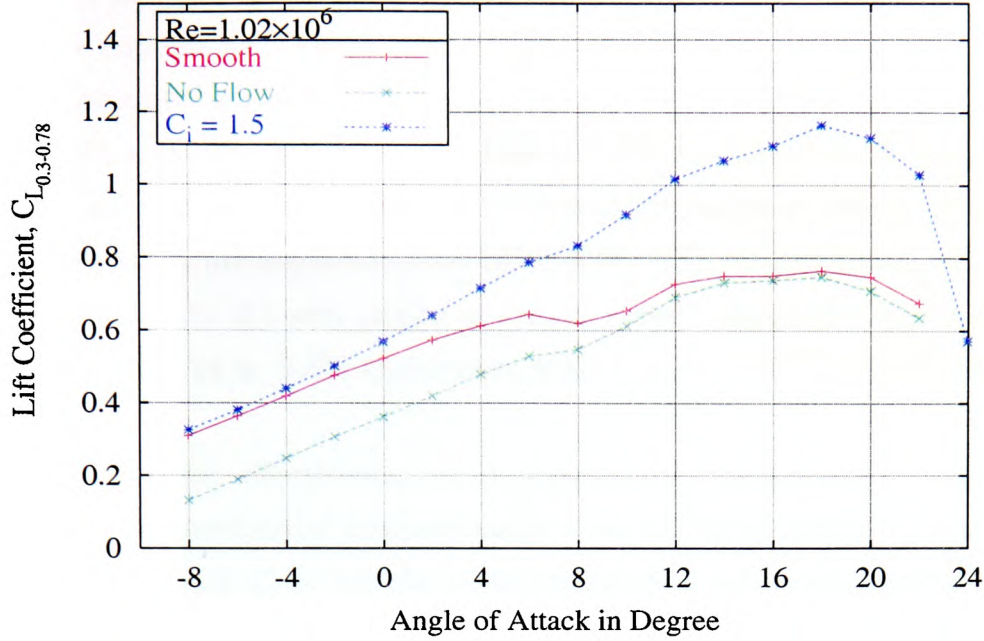


Figure 6.23: Experimental Lift Coefficient versus Angle of Attack ($Re = 1.02 \times 10^6$)

caused flow disturbances that resulted in a reduced lift performance. This effect decreased with increasing angle of attack. For very high angles of attack the flow separated upstream of the ABD interaction zone and the impact of the non-operational ABD is less significant. The presence of an operational ABD produced enhancement of the lift coefficient except for a C_i of 1.5, an angle of attack $< -2^\circ$ and $Re = 0.68 \times 10^6$, due to the high local velocity of the external flow.

The beneficial impact of the ABD increased with C_i , the angle of attack, and the Reynolds-number. For $Re = 1.02 \times 10^6$ the stall was delayed to higher angles of attack and a smooth transition towards aerodynamic failure of the aerofoil was observed. In Figures 6.22 and 6.23 the relation between the local velocity on the aerofoil and C_i is clearly shown. At low and negative angles of attack the flow velocity near the interaction zone with the ABD is high, so that the local velocity ratio is relatively small. With increased angles of attack the higher velocity gradient between the two flows resulted in an elevated transport of momentum into the external boundary layer. The local flow velocity on the aerofoil section also influenced the disturbance by a non-operational ABD with this effect becoming more prominent as the local velocity increased.

Figures 6.24 and 6.25 show the aerodynamic advantages and disadvantages for the individual flow conditions. These are presented as percentage changes from the lift coefficient of the smooth aerofoil section. A maximum lift improvement (based on the data between 3% and 78% chord length) of about 76% was found at 18° angle of attack, $C_i = 2.5$, and $Re = 0.68 \times 10^6$. Between -8° and 10° angle of attack these values of C_i and Re resulted in lift augmentations of $\approx 50\%$. Lift enhancements of $>50\%$ were also achieved with $C_i = 2.0$ and angles of attack greater than 12° . The maximum lift reduction in Figure 6.24 is -9.8% and occurs with $C_i=1.5$, -8° angle of attack, and $Re = 0.68 \times 10^6$.

The improved ABD effectiveness at the higher Reynolds-number is presented in Figure 6.25. Again substantial improvements were obtained except at some negative angles of attack and with $C_i = 1.5$. As mentioned above, at low angles of attack and $C_i = 1.5$ the local velocity ratio reached is low and the external flow was not accelerated. At an angle of attack of 18° the improvement in lift is about 12 percentage points greater than at $Re = 0.68 \times 10^6$.

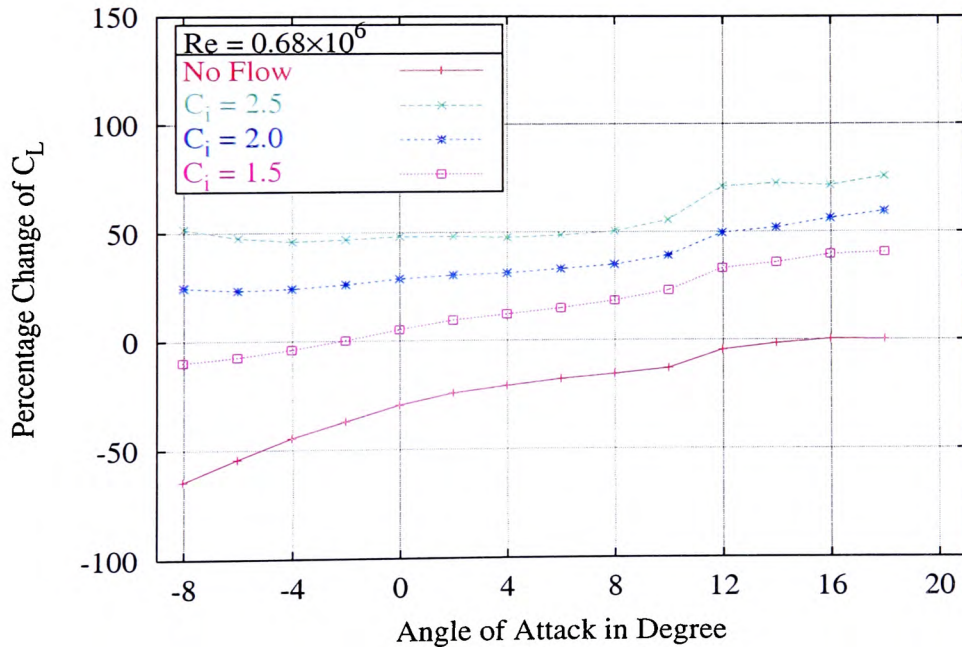


Figure 6.24: Percentage Variation of C_L due to the Experimental Pressure Distribution

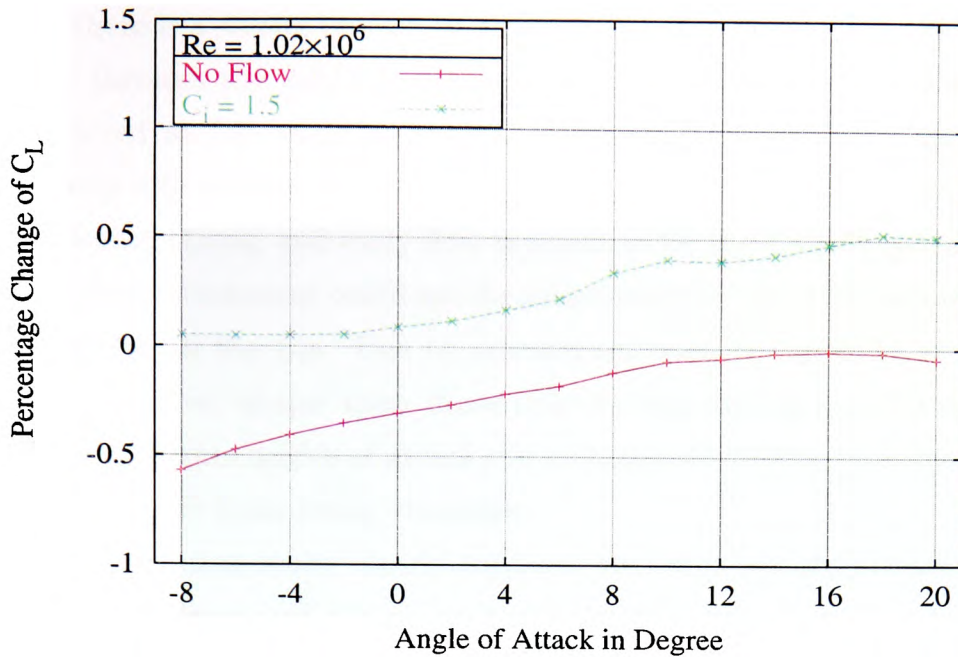


Figure 6.25: Percentage Variation of C_L due to the Experimental Pressure Distribution

Overall lift improvements were observed for all angles of attack. Associated drag reductions can also be expected as a result of improved flow circulation and delayed flow separation due to the ABD. The strong lift improvements obtained from the pressure data indicate that direct force measurements under-predicted the lift improvements.

6.5 Flow Visualisation

This section of the thesis attempts to corroborate the previous findings by means of flow visualisation. Tufts attached downstream of the interaction zone between the main stream and ABD flows were used to visualise the impact of momentum transfer. Pictures for the range between 10° to 20° angles of attack were obtained but only those in which there was a visible alteration to the flow (12° , 14° , 16° and 18°) are presented in Figures 6.26, 6.27, and 6.28.

The flow straightening properties of the ABD are clearly visible in all the pictures. For both Reynolds-numbers initial instabilities occurred with the smooth aerofoil at 12° angle of attack, as indicated by the fluctuating outer tufts. All values of C_i prevented these disturbances. At 14° angle of attack the trailing edge separation moves further

upstream and there is a strong impact on the tufts for the smooth aerofoil section. The secondary flow through the ABD, however, maintained fully attached flow. A similar behaviour occurred at 16° angle of attack, where the flow over the smooth aerofoil section is severely affected by flow separation. The tufts showed recirculating flows for 18° , which indicated strong and early flow separation for the smooth geometry. In this case, complete flow attachment could not be maintained by the ABD although the flow is 'straightened' for all the C_i s. Due to momentum transfer the tufts at 18° angle of attack are still in better 'shape' than those tufts on the smooth aerofoil section at 14° angle of attack. At higher angles of attack the strength of the flow separation prevented the impact of the ABD from being visualised.

This flow visualisation study clearly supports the recorded improvements of C_L by the force balance readings and the pressure distribution study.

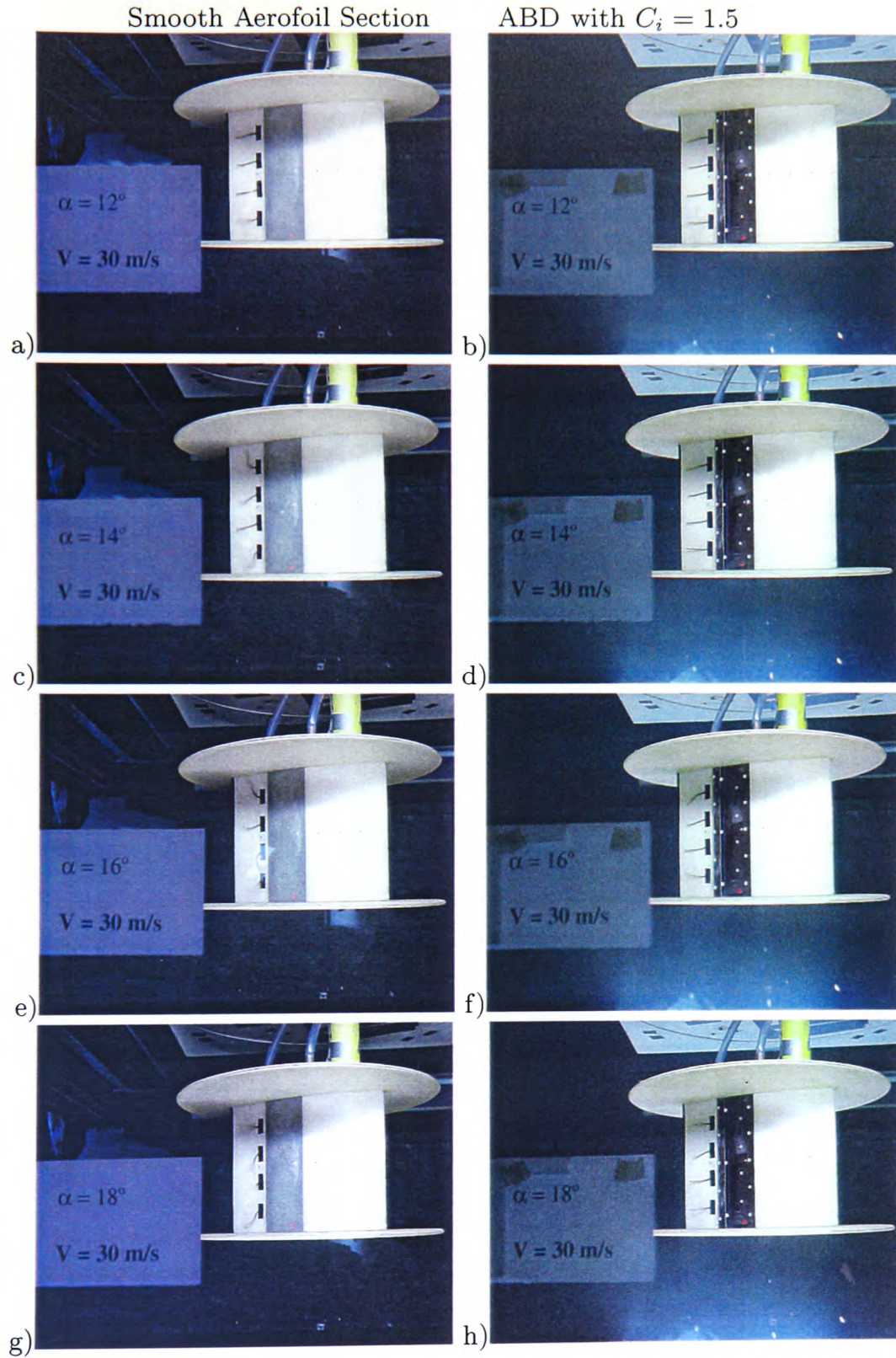


Figure 6.26: Flow Visualisation for $Re = 1.02 \times 10^6$ for the Smooth Aerofoil Section and the ABD with $C_i = 1.5$, (i.e. $\dot{V} = 34 \text{ m}^3/\text{h}$)

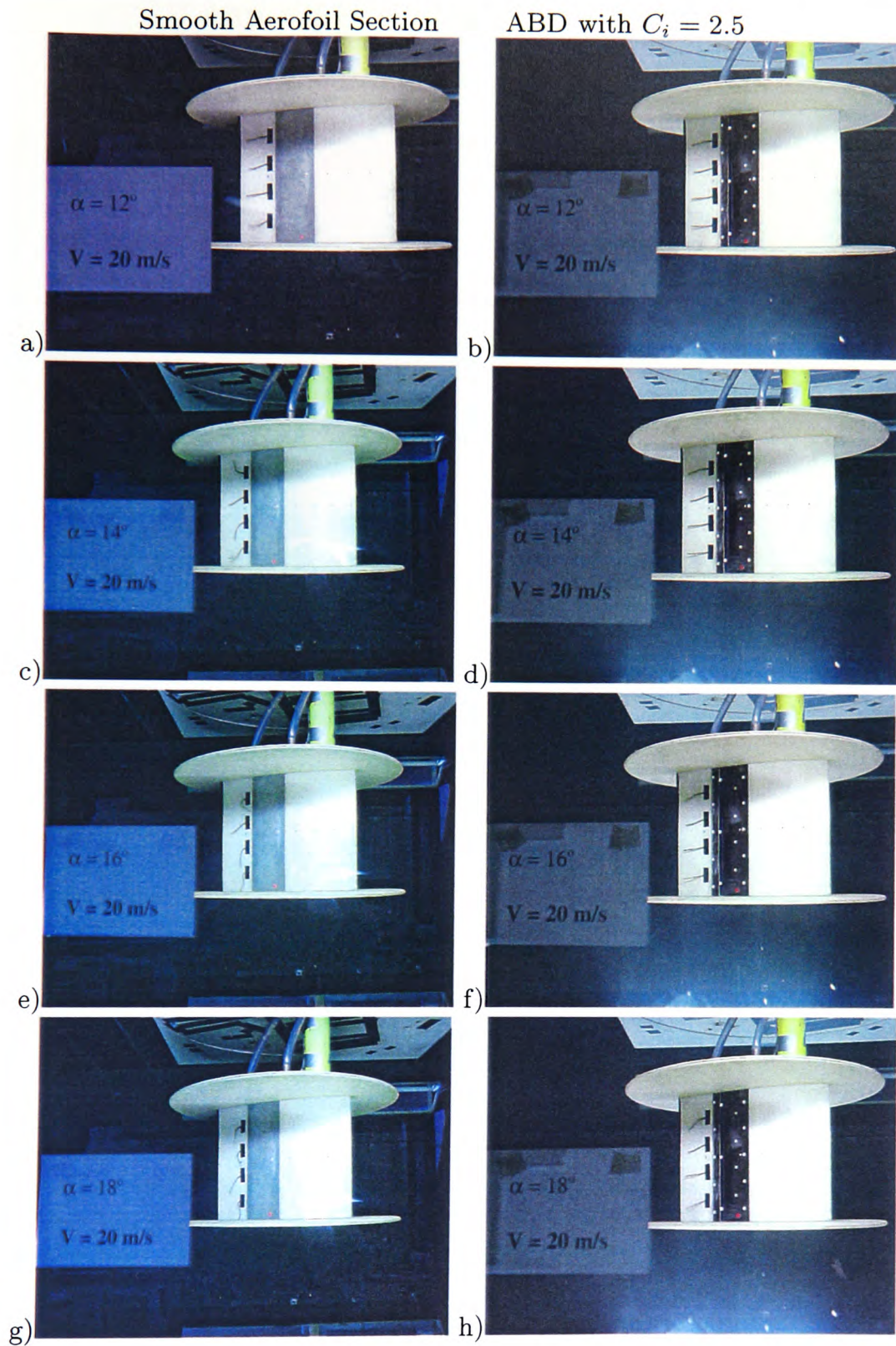


Figure 6.27: Flow Visualisation for $Re = 0.68 \times 10^6$ for the Smooth Aerofoil Section and the ABD with $C_i = 2.5$ (i.e. $\dot{V} = 34 \text{ m}^3/\text{h}$)

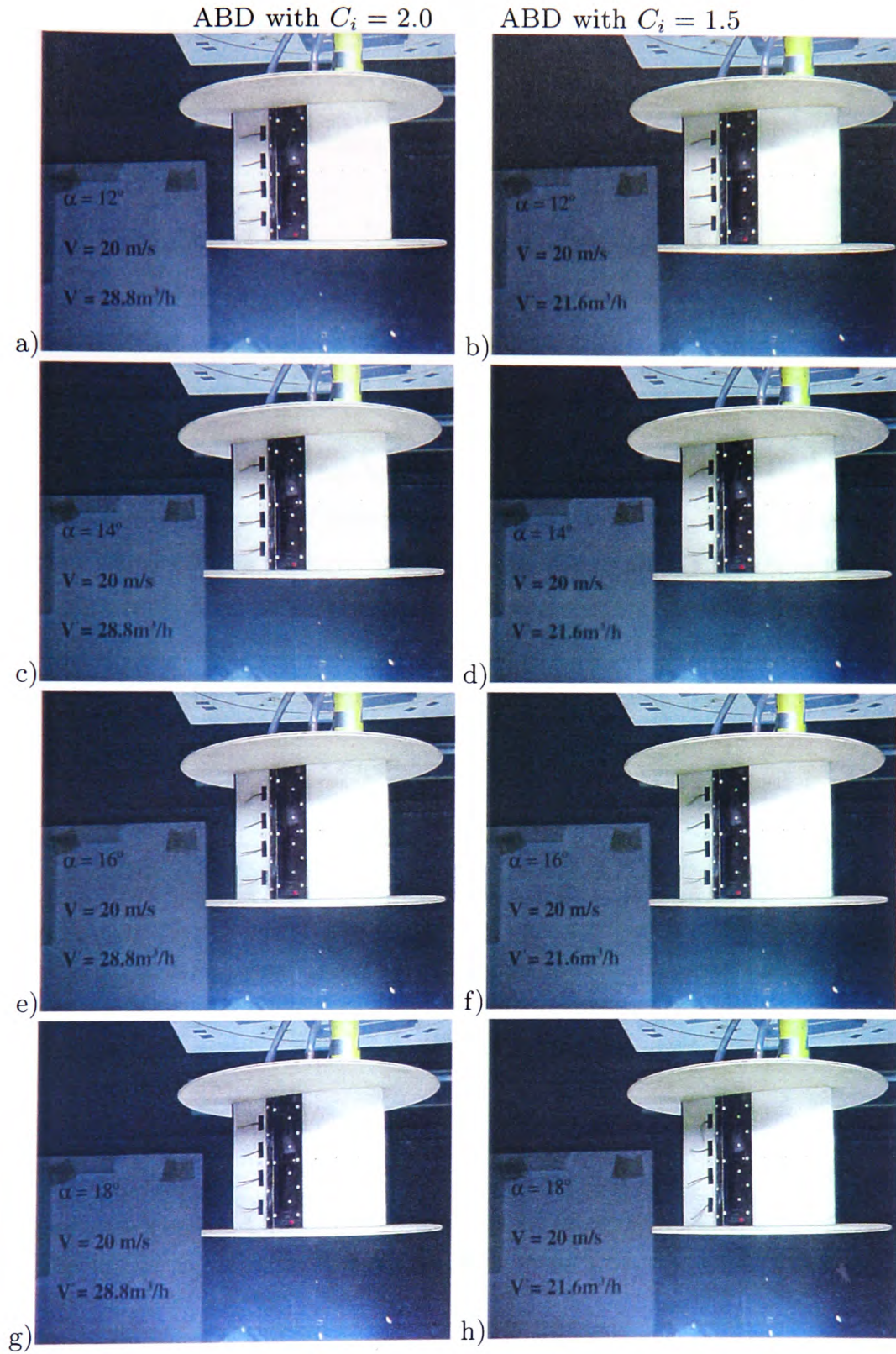


Figure 6.28: Flow Visualisation for $Re = 0.68 \times 10^6$ for the ABD with $C_i = 2.0$ (i.e. $\dot{V} = 28.8 \text{ m}^3/\text{h}$) and the ABD with $C_i = 1.5$ (i.e. $\dot{V} = 21.6 \text{ m}^3/\text{h}$)

6.6 Power Requirements

The power requirements for the ABD were estimated using the difference in static pressures at the supply and discharge ducting and the volume flow rate through the device.

$$P_{ABD} = \Delta p \times \dot{V} \quad (6.2)$$

The experimental set up prohibited measurement during wind tunnel operation, so that the pressure drop between inlet and outlet was measured at ambient pressure in the absence of an external flow. Figure 6.29 shows a linear increasing power requirement of the ABD with increasing C_i . The power requirement of ≈ 45 W to achieve a C_i of 2.5 at $Re = 0.68 \times 10^6$ is relatively low. Tangential air supply into the ‘wing’ box may not be the most efficient way of providing the secondary flow. Thus the more spacious conditions in a bigger wing section would enable larger sized air supply and discharge ducting to be used, and this increases the efficiency of the ABD. The ducting system also needs optimisation to improve the efficiency of the ABD. Insufficient data on drag reduction prevented the determination of net savings due to the ABD.

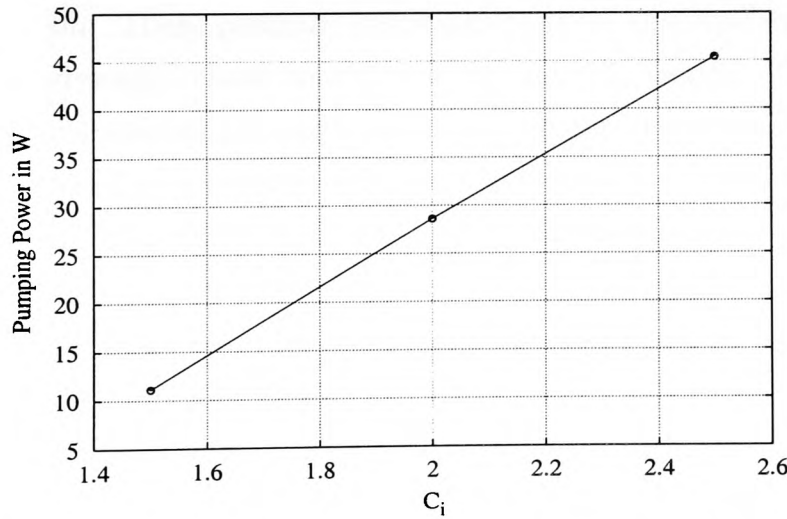


Figure 6.29: Power Requirements for the ABD versus C_i ($Re = 0.68 \times 10^6$)

6.7 Discussion

An experimental study on aerodynamic flow control via an air breathing device has been conducted. The injection of momentum into the boundary layer of the external flow around a NACA65-415 aerofoil section was found to modify the aerofoil performance. Direct force balance readings, pressure measurements and flow visualisation were used to assess the benefits of the flow control method. The content of this chapter is intended to be submitted for publication in the Journal of Aerospace Engineering [54].

The force balance readings showed a beneficial impact on the lift coefficient at high angles of attack for all the test cases, reaching a maximum percentage increase of 15% (see Figure 6.12). Drag reductions could not be explicitly and reliably determined reliably by the direct force balance readings due to the sensitivity of the comparatively small drag forces to disturbances and irregularities within the experimental set up. This difficulty in estimating drag reduction was exacerbated since the splitter plates and support structure contributed substantially to the overall drag. It was thus difficult to separate the aerofoil drag from the overall drag.

The ABD, however, strongly affected the pressure distributions on the suction side of the aerofoil section. These pressure variations suggest that the device had a great impact on the aerodynamic characteristics of the aerofoil section. Integration of the pressure distributions yielded lift augmentations greater than those detected by the direct force balance readings. Despite using only five discrete locations between 3% and 78% chord to sum up the overall effects the method can be seen as sufficiently accurate to show clear tendencies in the effects of the ABD. Lift improvements exceeding 50% prior to the stall angle were obtained with injection coefficients greater than 2.0 at $Re = 0.68 \times 10^6$ and for $C_i \geq 1.5$ at $Re = 1.02 \times 10^6$.

The flow visualisation by tufts attached close to the trailing edge of the aerofoil section supported the findings of the pressure distributions. These results indicated likely drag reductions due to flow attachment as well as reduced ‘displacement effects’ by the re-energised boundary layer on the suction side of the aerofoil section.

The difference between the results from the directly measured aerofoil forces and the pressure distribution may be due to:

- the flow dynamics within the external supply and discharge pipe-work to the aerofoil which exerted variable forces on the balance system, probably resulting in an under-prediction of the effects of flow control,
- the contribution of the splitter plates and the support structure ‘swamping’ the comparatively small variations due to flow control,
- the possible disturbing influence of the slow moving secondary fluid close to the splitter plates (Figure 6.5) which reduced the lift improvements and drag reductions.

The outcome of this experimental study on the effects of the ABD on the aerodynamic characteristics of the NACA65-415 aerofoil section can be summarised as:

- the benefits increased with the Reynolds-number,
- the benefits increased with the injection coefficient,
- the benefits increased with the angle of attack.

These effects can be explained by two phenomena. Increased Reynolds-number and flow velocities increased the turbulence levels in the free stream and hence within the boundary layer. This resulted in improved mixing between the two fluid streams and improved the transport of momentum. Secondly, increased injection coefficients and/or reduced flow velocities on the aerofoil section at higher angles of attack increased the local velocity gradients at the interaction zone between the ABD stream and the external flow and again resulted in improved momentum transport. The two latter conclusions confirm the numerical analysis on the variation of the aerodynamic characteristics of the aerofoil section with angle of attack (Figure 4.3) and C_i (Figure 4.8)

This investigation demonstrated that the numerical analysis probably under-predicted the effects of the use of the ABD. At high Reynolds-numbers as in the present study, transport of momentum was primarily based on turbulent phenomena and the local velocity ratio. The use of wall functions and the turbulence models included in the computations may have caused the difference between the numerical and the experimental results. The computations also did not model the same free stream turbulence

as in the experiments and this may have resulted in the opposite trends for the variation of C_L with the Reynolds-number in the two cases. In Figure 4.11 the improvement in C_L decreased as the Reynolds-number was increased for $0.68 \times 10^6 < Re < 1.36 \times 10^6$. For the numerical results it was assumed that the increasing thickness of the external boundary layer with a decreased Reynolds-number improved the shear stress due to a higher local velocity gradient at the location of flow control.

Overall, the strong impact of momentum transfer via the ABD on the aerodynamic characteristics of the NACA 65-415 aerofoil section was clearly demonstrated by this experimental study. It thus highlighted the potential of this flow control method overall, and the trends of the numerical analysis have been confirmed by the experiments, although the magnitude of the benefits due to the presence of the ABD are more pronounced than those predicted numerically.

Chapter 7

Conclusions and Recommendations for Further Work

7.1 Conclusions

The present work concentrated on the introduction of momentum into the boundary layer of the flow over the suction side of aerofoil sections. Momentum transfer was provided by a secondary flow that passed through an air breathing device (ABD). The device was embedded near the aerofoil surface, so that an almost tangential and uni-directional fluid interaction re-energised the the boundary flow. Injection velocities greater than the free stream velocity were essential for the excitation of the external flow.

Flow control using momentum transfer via the ABD resulted in the reduction of drag and the improvement of lift. The energy efficiency of air traffic is enhanced by drag reductions and lift improvements can benefit take-off and landing performance of large aircraft. Greater take-off weights, lowered noise levels due to reduced thrust and shorter take-off and landing distances are amongst the benefits from improving the lift of aerofoil sections.

The work presented in this thesis used both numerical and experimental methods to assess the potential benefits using an ABD to transfer momentum via a secondary flow. The numerical work included the study of the parameters governing the flow control process with respect to the aerodynamic characteristics of aerofoil section, C_L , C_D and L/D , as well as on the power requirements for the fluid interaction.

A Taguchi technique was used to obtain an overall assessment of the parameters governing flow control by an air breathing device. This technique indicated that the most important factors were the gap-size, i.e. the distance in flow direction over which the secondary stream interacted with the external flow on the aerofoil section, the injection coefficient of the secondary flow into the ABD, and the depth of the ABD. The flow and geometrical parameters of the ABD were then studied in greater detail.

Optimisation of the ABD geometry was attempted using genetic algorithms. The data for this optimisation was obtained from computational fluid dynamics. Finally, experimental work was conducted in a closed-loop low speed wind tunnel to confirm the numerical predictions.

Momentum transfer via the ABD secondary flow significantly reduced the aerodynamic resistance of the aerofoil section. The numerically predicted lift forces were only marginally improved. In contrast the experimentally measured pressure variations on the suction side of the aerofoil section confirmed the trends of the computational results but indicated more substantial benefits. Thus the predicted trends were confirmed although the magnitude of the experimentally measured benefits were significantly greater than expected.

The numerical analysis established drag reductions of up to 20% and lift improvement of about 3.5%. These were achieved with an injection coefficient of 2.5 for a parallel air breathing device, located at 60% chord and transferring momentum through a gap-size of 3% chord. Variation of the gap-size, the distance from the leading edge (i.e. the location) and the ABD shape can provide further improvements. Inclusion of the power requirements for the ABD reduced the benefits of drag reduction. Consequently, there was a need to optimise the ABD parameters to minimise the power consumption. A non optimised parallel ABD for an injection coefficient of 1.5 produced drag reductions of about 7% and lift improvements of 1%.

Using an evolutionary optimisation technique (genetic algorithm) in conjunction with the CFD determination of the aerodynamic characteristics of the aerofoil produced a more efficient air breathing geometry. The momentum transfer was enhanced so that lift improvements of 3.39% and drag reductions of 8.39% were established, whilst maintaining low volume flow rates (i.e. an C_i of 1.5) and pressure a drop of 155 Pa per

unit span. A non optimised ABD achieved with a C_i of 1.5 lift improvements of 1.35%, drag reductions of 6.89% and pressure drop of 567 Pa per unit span. The key was the geometrical modification of a pocket of rotational air flow within the interaction zone. This appeared to ‘guide’ the secondary fluid in a smooth fashion along the interaction zone.

The experimental work confirmed the trends of the numerical study. Direct force measurements with a force balance system showed lift improvements for high angles of attack, reaching a maximum improvement of 15% with a C_i of 2.5 at $Re = 0.68 \times 10^6$ and 18° angle of attack. A Reynolds-number of 1.02×10^6 showed lift improvements of about 11% using a injection coefficient of 1.5 at 16° angle of attack, compared to lift augmentation of about 7% at the lower Reynolds-number and the same angle of attack. This suggests improved performance of the ABD at higher Reynolds-numbers. Injection coefficients greater than 1.5 were not used at $Re = 1.02 \times 10^6$ in the experimental study. Drag reductions were not accurately determined by direct force measurements. Lift forces were also measured using the pressure distribution on the suction side of the aerofoil section between 3% and 78% chord. These pressures were integrated and the lift forces improved about 50% with injection coefficients greater than 2.0 at $Re = 0.68 \times 10^6$ and for $C_i = 1.5$ at $Re = 1.02 \times 10^6$. Flow visualisation by tufts attached close to the trailing edge of the aerofoil section supported the findings of the pressure distributions.

Momentum transfer via the secondary ABD flow is mainly governed by the local velocity gradient at the interaction zone, which depended in turn on variations of the flow conditions in the external boundary layer as well as on the internal ABD velocity. As a result the effects of using the ABD improved with:

- increasing the angle of attack,
- increasing the injection coefficient,
- an increase in the distance of the ABD location from the leading edge.

Contradicting results were obtained for the effects of the Reynolds-number. The experimental study showed increased benefits on lift for $Re = 1.02 \times 10^6$ compared to Re

$= 0.68 \times 10^6$. Within this range of Re the numerical work showed the opposite trend. This may be caused by the different turbulence intensities in the wind tunnel and the numerical flow domain. Hefner [25] suggest a similar effect for tangential slot-injection. Increased turbulence intensity of both the external flow on the aerofoil and the injected flow caused improved mixing between the two fluids which resulted in an improved excitation of the external flow. The increasing benefits from the ABD with the angle of attack, locating the ABD closer to the trailing edge of the aerofoil section and the injection coefficient is due to the difference in velocity at the location of flow control. Further benefits on lift and drag can be obtained by the size of the interaction zone (i.e. the gap-size) and the relative injection and suction angles.

The simplicity and the resultant improvements in the aerodynamic characteristics of the aerofoil section suggested that the ABD is an attractive means for aerodynamic flow control, which should be studied in further detail.

7.2 Recommendations for Further Work

Further investigations of the use of an ABD should concentrate on the details of the fluid interaction and the associated transport phenomena. Knowledge of this will be essential for further optimisation of this novel method for aerodynamic flow control. In particular the impact of turbulent properties and the local static pressure should be studied since these are important parameters. In-depth experimental investigation on the detailed transport phenomena will provide data for further numerical studies on the local impact of momentum transfer via a secondary flow. An improved understanding of the process will also help in ‘adjusting’ the CFD models to simulate ‘real’ conditions. In this respect, it should be investigated whether or not the wall function approach which was used in the present study affected the momentum exchange between the ‘donor’ and ‘receiver’ fluids. Two layer boundary flow models may provide a better approach for the study of the effects of an ABD on lift and drag.

In Chapter 5 an ABD structure was produced as a result of an optimisation process using genetic algorithms. The improved geometrical structure, however, requires confirmation by physical experiments in order to demonstrate the validity of the optimisation

and the effectiveness of the resultant ABD geometry.

Unsteady flow around wings causes flutter which adversely affects the structure of the flow around the wing. Due to the likely beneficial flow straightening properties of the ABD (shown in Chapter 6) the effects of the device on flutter and large scale turbulence should be investigated.

Flight conditions need to be simulated for the application of an ABD to aircraft wings. The variation of fluid properties due to low temperatures and ambient pressure will affect the momentum exchange.

The success of the ABD will depend on the efficiency and the energy consumption of the device. Thus the determination of the required power consumption of the air supply and discharge should be a focus of future attention.

If net savings can be confirmed practical engineering issues will need further study prior to incorporation of the device in the aircraft structure. This will involve changes to the design of the required size of the ABD and the the placement of air supply and discharge facilities.

Bibliography

- [1] Al-Shihry A. *The Development of a Novel Air Bearing Device for Aerodynamic Flow Control*. PhD thesis, University of Glamorgan, School of Design and Advanced Technology, 1997.
- [2] Schlichting H. *Boundary-Layer Theory*. McGraw-Hill, London, 7th edition, 1979.
- [3] Beitz W. and Grote K.-H. *DUBBEL-Taschenbuch für den Maschinenbau*. Springer-Verlag, 19th edition, 1997.
- [4] Gersten K. Schlichting H. *Grenzschicht-Theorie*. Springer-Verlag, Berlin, 9th edition, 1997.
- [5] Prandtl L. Über Flüssigkeitsbewegung bei sehr kleiner Reibung. In *Proc. Third Int. Math.*, pages 484–491, Heidelberg, 1904.
- [6] Klebanoff P.S, Tidstrom K.D, and Sargent L.M. The three-dimensional nature of boundary-layer instability. *Journal of Fluid Mechanics*, 12:1–34, 1962.
- [7] Gad el Hak M. Flow control. *Applied Mechanic Review*, 42(10):261–293, 1989.
- [8] Gad el Hak M. Control of low-speed airfoil aerodynamics. *AIAA Journal*, 28(9):1537–1552, 1990.
- [9] McLean J.D., Crouch J.D., Stoner R.C., Sakurai S., Seidel G.E., Feifel W.M., and Rush H.M. Study of the application of separation control by unsteady excitation to civil transport aircraft. Technical Report CR-1999-209338, NASA, Langely Research Center, 1999.

- [10] National Academy Press, Washington, D.C. *Technology for the United States Navy and Marine Corps, 2000-2035: Becoming a 21st-Century Force, (Volume 6 Platforms)*, 1997.
- [11] Gad el Hak M. Modern developments in flow control. *Applied Mechanics Review*, 49(7):365–379, 1996.
- [12] Gad el Hak M. Boundary layer interaction with compliant coatings: An overview. *Applied Mechanical Review*, 39(4):511–523, 1986.
- [13] Joslin R.D. Overview of laminar flow control. Technical Report TP-1998-208705, NASA, Langley Research Center, 1998.
- [14] Collier F.S (Jr.). An overview of recent subsonic laminar flow control flight experiment. Technical Report AIAA Paper 93-2987, AIAA, NASA Langley Research Center, 1993.
- [15] Maddalon D. V. and Braslow A. L. Simulated-airline-service flight test of laminar-flow control with perforated-surface suction system. Technical Report NASA Tech. Paper 2966, NASA, 1990.
- [16] ELFIN. First laminar flow flight test prove drag reduction potential. *Aircraft Engineering*, pages 5–7, 1992.
- [17] Bushnell D. M. Viscous drag reduction in aeronautics. In *ICAS'94 Guggenheim*, volume 1, pages XXXIII–LV. ICAS, 1994.
- [18] M. J. Walsh. Effect of detailed surface geometry on riblet drag reduction performance. *Journal of Aircraft*, 27(6):572–573, 1990.
- [19] Prandtl L. Magnuseffekt und Windkraftschiff. *Naturwissenschaften*, 13(6):93–108, 1925.
- [20] Modi V.J., Munshi S.R., and Mokhtarian F. Multi-element aerofoils with moving surfaces boundary layer control wind tunnel, numerical and flow visualizastion

- studies. In *Proc. of 19th Congress of the Int. Council of the Aeronautical Science*, volume 1, pages 80–103, 1994.
- [21] Chew Y.T., Pan L.S., and Lee T.S. Numerical simulation of the effect of a moving wall on separation of flow past a symmetrical aerofoil. In *Proc. Instn. Mech. Engrs. (Part A)*, volume 212, pages 69–77. IMechE, 1997.
- [22] Tennant J.S., Johnson W. S., and Krothapalli A. Rotating cylinder for circulation control on an airfoil. *Journal of Hydrodynamics*, 10(3):102–105, 1975.
- [23] Modi V.J., Sun J.L.C., Akutsu T., Lake P., McMillian, Swinton P.G., and Mullins D. Moving-surface boundary-layer control for aircraft operation at high incidence. *Journal of Aircraft*, 18(11):963–968, 1981.
- [24] Wygnanski I. Boundary layer and flow control by periodic additon of momentum. *AIAA*, (97-2117), 1997.
- [25] Hefner J. N. and Bushnell D. M. Viscous drag reduction via surface mass injection. In *AIAA Progress in Astronautical and Aeronautics*, volume 123, pages 457–476, Washington, D.C., 1990. AIAA.
- [26] Abbott I.A and Von Doenhoff A.E. *Theory of Wing Sections*. Dover Publications, INC. New York, 1959.
- [27] Seifert A. and Pack G.P. Oscillatory excitation of unsteady compressible flows over airfoils at flight reynolds numbers. *AIAA*, (99-0925), 1999.
- [28] Ravindran S.S. Active control of flow separation over an airfoil. Technical Report TM-1999-209838, NASA, Langley Research Centre, 1999.
- [29] Maksoud T.M.A, Al-Shihry A., and Ward J. Theoretical/experimental analysis of a novel air breathing device for flow control. *Journal of Aircraft*, 38(1), January-February 2001.
- [30] AEA Technology plc. *CFX-4.2-: Solver Manual*.

- [31] Jr. Anderson J.D. *Computational Fluid Dynamics: The Basics with Application*. McGraw-Hill, Inc., 1995.
- [32] Abbot M.B. and Basco D.R. *Computational Fluid Dynamics: An Introduction for Engineers*. Addison Wesley, 1997.
- [33] Ferziger J.H. and Peric M. *Computational Methods for Fluid Dynamics*. Springer-Verlag, Berlin, 2nd edition, 1999.
- [34] Anderson D.A., Tannehill J.C., and Pletcher R.H. *Computational Fluid Mechanics and Heat Transfer*. Henspere Publishing Corporation, 1984.
- [35] Versteeg H. K. and Malalasekera W. *An Introduction to Computational Fluid Dynamics*. Addison-Wesley, 1995.
- [36] Street R.L, Watters G.Z, and Vennard J.K. *Elementary Fluid Mechanics*. John Wiley and Sons Inc., 1996.
- [37] Jones B.M. Measurement of profile drag by the pitot-transverse method. Technical Report 1688, Cambridge University, 1936.
- [38] Rhie C. M. and Chow W.L. Numerical study of the turbulent flow past and airfoil with trailing edge separation. *AIAA Journal*, 21(11):1527–1532, 1983.
- [39] S.M Klausmeyer and J.C Lin. Comparitive results from a cfd challenge over a 2d three-element highe-lift aerofoil. Technincal Memorandum 112858, NASA, Langley Research Center, 1997.
- [40] G.S. Peace. *Taguchi Methods, A Hands-On Approach*. Addison-Wesley Publishing Company, Inc, 1993.
- [41] Breitfeld O., Maksoud T.M.A., and Ward J. A novel method for improving the flow around aerofoil sections. *Journal of Aerospace Engineering*, submitted in 2002.
- [42] Goldberg D. E. *Genetic Algorithms in Serach, Optimization and Machine Learning*. Addison-Westley Publishing Company, Inc., 1989.

- [43] Obayashi S. and Takanori T. Comparison of optimization algorithms for aerodynamic shape design. *AIAA*, (96-2394-CP):181–187, 1996.
- [44] Sharatchandra M.C., Sen M., and Gad el Hak M. New approach to constrained shape optimisation using genetic algorithms. *AIAA Journal*, 36(1):51–61, 1998.
- [45] Gage P. and Kroo I. A role for genetic algorithms in preliminary design environment. *AIAA*, (93-3933):1–11, 1993.
- [46] M.B Anderson and G.A. Gebert. Using pareto genetic algorithms for preliminary subsonic wing design. *AIAA*, (AIAA-96-4023):363–371, 1996.
- [47] Obayashi S. and Oyama A. Three-dimensional aerodynamic optimisation with genetic algorithm. In *Proceedings ECCOMAS*, pages 420–424. Wiley, New York, 1996.
- [48] Doorly D.J., Peiró J., and Oesterle J-P. Optimisation of aerodynamic and coupled aerodynamic-structural design using parallel genetic algorithms. *AIAA*, (96-4027-CP):401–409, 1996.
- [49] Periaux J., Sefrioui M., Stoufflet B. Mantel B., and Laporte E. Robust genetic algorithms for optimisation problems in aerodynamic design. In *Genetic Algorithm in Engineering and Computer Science (Eds Winter G. et. al.)*, pages 371–395, Chichester, 1995. J Wiley.
- [50] Marco N. and Désidéri J. Lanteri S. Mult-objective optimization in cfd by genetic algorithms. Technical Report 3686, INRIA, 1999.
- [51] Fan H-Y. An inverse design method of diffuser blades by genetic algorithms. In *Proc. Instn. Mech. Engrs. (Part A)*, volume 212, pages 261–268. IMechE, 1998.
- [52] Wall M. *GAlib: A C++ Library of Genetic Algorithm Components*. Massachusetts Institute of Technology, 1996.
- [53] *VDI-Wärmetlas*. Verein Deutscher Ingenieure, 1983.

- [54] Breitfeld O., Maksoud T.M.A, and Ward J. Experimental study on a novel method for improving the lift of aerofoil sections. *Journal of Aerospace Engineering*, to be submitted in 2002.

Appendix A

CFD

A.1 Differencing Schemes

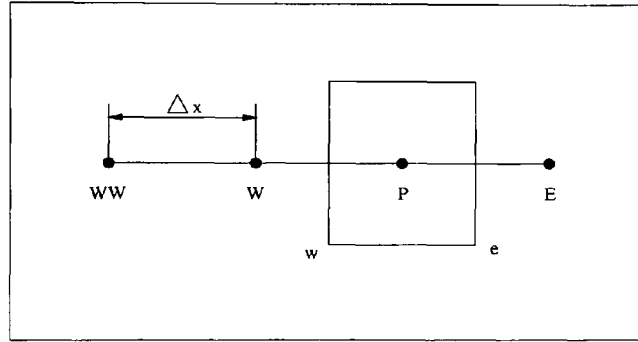


Figure A.1: Control Volume Notation

To obtain an approximate solution of the governing equations by the finite volume or control volume method integration of the general differential equation is required. The equation is subsequently discretised, i.e. an algebraic expression is derived, and this expression is passed to an equation solver. The principle discretisation for convection and diffusion of Φ is briefly discussed below.

$$\underbrace{\frac{\partial}{\partial x_j}(\rho \bar{u}_j \bar{\phi})}_{convection} = \underbrace{\frac{\partial}{\partial x_j} \left(\Gamma_{eff} \frac{\partial \bar{\phi}}{\partial x_j} \right)}_{diffusion} \quad (A.1)$$

Equation A.1 shows the general differential conservation equation for ϕ for steady state and incompressible flow.

The Diffusion Term

Integration of the diffusion term of Equation A.1 in horizontal direction leads to the following expression

$$\left(\Gamma \frac{d\Phi}{dx} \right)_e - \left(\Gamma \frac{d\Phi}{dx} \right)_w$$

Discretisation of this expression by the central differencing scheme uses a linear profile assumption for Φ between nodes. For an equally spaced, rectangular grid the above expression becomes:

$$\Gamma_e \left(\frac{\Phi_E - \Phi_P}{\Delta x} \right) - \Gamma_w \left(\frac{\Phi_P - \Phi_W}{\Delta x} \right)$$

From this expression an equation for the computation of the diffusion of Φ_P can be derived:

$$\left(\frac{\Gamma_e}{\Delta x} + \frac{\Gamma_w}{\Delta x} \right) \phi_P = \left(\frac{\Gamma_w}{\Delta x} \right) \phi_W + \left(\frac{\Gamma_e}{\Delta x} \right) \phi_E \quad (\text{A.2})$$

The Convection Term

The convection term determines the accuracy of the computation. The control volume method allows the use of different differencing schemes with different accuracies for the convection term. The accuracy of a differencing scheme is usually determined by the rate of reduction of the discretisation error when the node distance (i.e. the grid spacing) is reduced.

Integration of the convection term in Equation A.1 gives:

$$(\rho u \Phi)_e - (\rho u \Phi)_w$$

Below some discretisation schemes for the convective flux of Φ are given. These equations are introduced into the above expression. An equation for the convection of Φ_P can be derived and this is done similarly as for the diffusion of Φ .

Central Differencing Scheme

Central differencing uses a linear profile assumption for Φ between nodes. This scheme is rarely used for convection driven problems due to instabilities and it may produce non-physical or oscillatory solutions. Central differencing is second-order accurate.

$$\Phi_e = \frac{1}{2}(\Phi_E - \Phi_P)$$

$$\Phi_w = \frac{1}{2}(\Phi_P - \Phi_W)$$

Upwind Schemes

The order of nodes used for upwind schemes depends on the direction of the flow. In the following examples the flow proceeds from the left hand side, W, to the right hand side, E, of the page. If the flow is reversed the order of the node notations has to be changed, accordingly.

First-Order-Upwind

$$\Phi_e = \Phi_P$$

$$\Phi_w = \Phi_W$$

This scheme is first-order accurate.

Second-Order-Upwind

$$\Phi_e = \frac{3}{2}\Phi_P - \frac{1}{2}\Phi_W$$

$$\Phi_w = \frac{3}{2}\Phi_W - \frac{1}{2}\Phi_{WW}$$

This scheme is second-order accurate.

QUICK (Quadratic-Upwind-Differencing)

$$\Phi_e = \frac{3}{8}\Phi_E + \frac{3}{4}\Phi_P - \frac{1}{8}\Phi_W$$

$$\Phi_w = \frac{3}{8}\Phi_P + \frac{3}{4}\Phi_W - \frac{1}{8}\Phi_{WW}$$

QUICK is third-order accurate and uses a quadratic profile assumption between three neighbouring nodes.

A.2 Specification of Grid Types

Figure A.2 shows different block arrangements to structure the domain for a CFD problem.

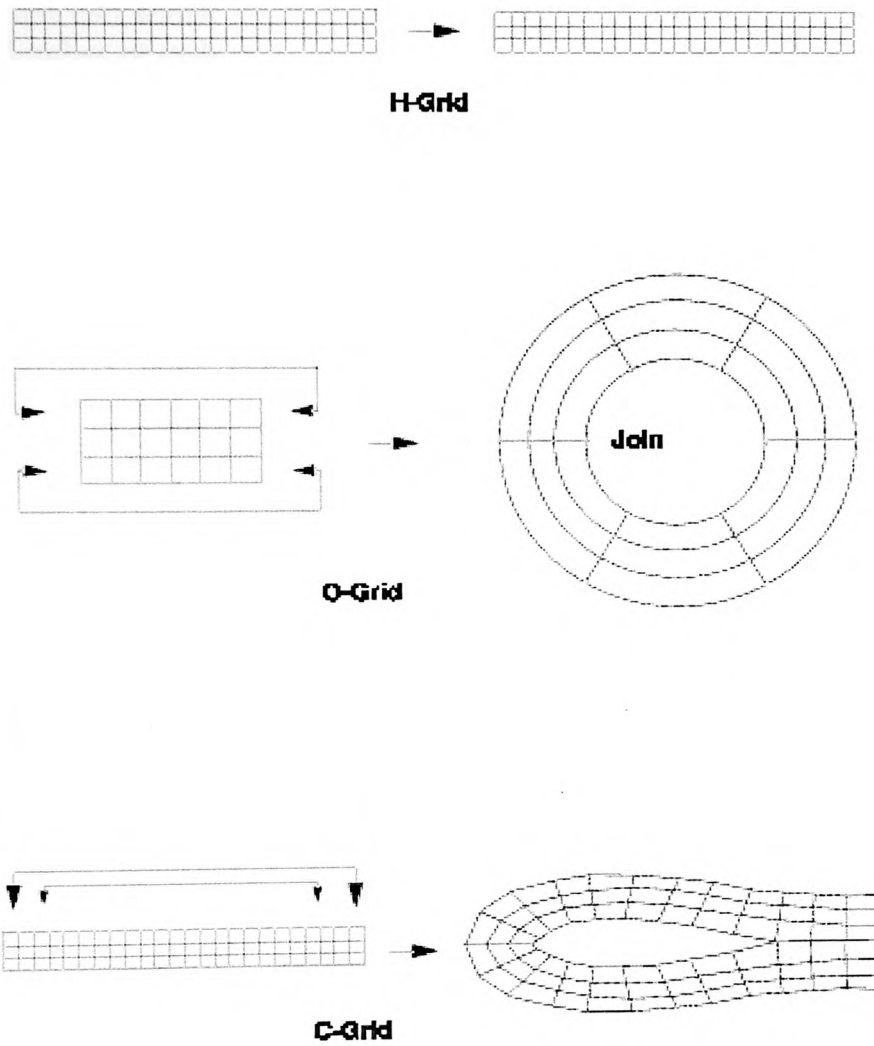


Figure A.2: Specification of Grid Types

A.3 Grid Geometric Propagation Formulae

$$D = \sum_1^n ar^{i-1} = a + ar + ar^2 + ar^3 + \dots + ar^{n-1}$$

Where:

D	Block edge length
a	Last cell width
ar^{n-1}	First cell width
n	Number of cells
r	Propagation ratio

From the above the propagation ratio can be computed as:

$$r = \frac{a-D}{ar^{n-1}-D}$$

and the number of cells along the block edge:

$$n = \frac{\log_{10}\left(D\frac{r-1}{a}+1\right)}{\log_{10}r}$$

A.4 Command File

A typical command file specification to read by the CFX-4.3 solver for a smooth aerofoil section.

```

>>CFX4
>>OPTIONS
TWO DIMENSIONS
BODY FITTED GRID
CARTESIAN COORDINATES
TURBULENT FLOW
ISOTHERMAL FLOW
INCOMPRESSIBLE FLOW
STEADY STATE
USE DATABASE
>>MODEL DATA
>>DIFFERENCING SCHEME
U VELOCITY 'VAN LEER'
V VELOCITY 'VAN LEER'
PRESSURE 'VAN LEER'
K 'HYBRID'
EPSILON 'HYBRID'
>>MATERIALS DATABASE
>>SOURCE OF DATA
PCP
>>FLUID DATA
FLUID 'AIR'
MATERIAL TEMPERATURE 2.8800E+02
MATERIAL PHASE 'GAS'
>>TITLE
PROBLEM TITLE 'CFX4 COMMAND FILE'
>>PHYSICAL PROPERTIES
>>TURBULENCE MODEL
TURBULENCE MODEL 'RNG K-EPSILON'
>>SOLVER DATA
>>PROGRAM CONTROL
MAXIMUM NUMBER OF ITERATIONS 1000
MASS SOURCE TOLERANCE 1.0000E-03
ITERATIONS OF VELOCITY
AND PRESSURE EQUATIONS 3
ITERATIONS OF TURBULENCE EQUATIONS 3
SOLVER DEBUG PRINTING

TRACE MAXIMUM RESIDUALS
>>UNDER RELAXATION FACTORS
U VELOCITY 4.0000E-01
V VELOCITY 4.0000E-01
PRESSURE 5.00000E-01
VISCOSITY 5.0000E-01
K 3.0000E-01
EPSILON 3.0000E-01
>>MODEL BOUNDARY CONDITIONS
>>INLET BOUNDARIES
PATCH NAME 'INLET1'
U VELOCITY 5.0000E+01
V VELOCITY 0.0000E+00
K 1.0000E-04
EPSILON 1.0000E-04
>>PRESSURE BOUNDARIES
PATCH NAME 'PRES'
PRESSURE 0.0000E+00
>>OUTPUT OPTIONS
>>FRONTEND PRINTING
NO TOPOLOGY STRUCTURE
>>PRINT OPTIONS
>>WHAT
U VELOCITY
V VELOCITY
PRESSURE
DENSITY
VISCOSITY
K
EPSILON
>>WHERE
K PLANES 1
ALL BLOCKS
>>WHEN
FINAL SOLUTION
>>STOP

```

Appendix B

Experimental Details

B.1 ABD Velocity Distribution

Figure B.1 shows the geometry for the internal ducting with a taper ratio of 2. The two cylinders represent the supply and discharge fittings which were attached on the upper splitter plate (Figure 6.6). The interaction zone was covered by a small flow domain subjected to ambient pressure and zero free stream velocity. The resulting velocity distribution is shown in Figure B.2, which was measured along the stream-wise centre line of the box at half ABD depth (0.25 mm).

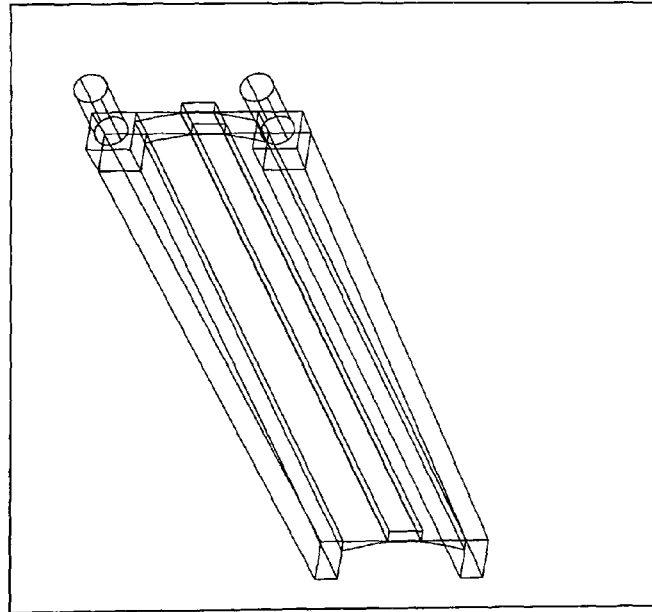


Figure B.1: Model for Tapered Internal Ducting

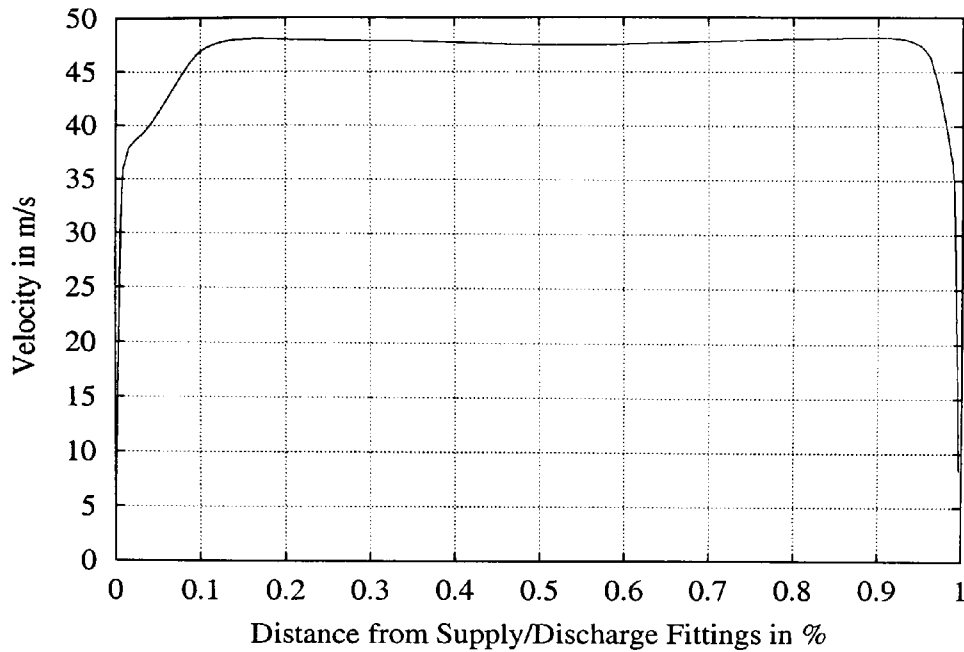


Figure B.2: Predicted Velocity Distribution along Interaction Zone Centre Line

B.2 Details of the Force Balance System

The force balance system was designed for the following maximum loads.

Lift	: 700N
Drag	: 200N
Pitch	: 30Nm
Roll	: 60Nm
Side Force	: 270N
Yaw	: 38Nm

All forces are mutually perpendicular. At zero rotation of the force balance system the drag force points in the main flow direction and the side force horizontally in the cross stream direction. The lift force is the normal force in cross stream direction. The pitch moment, roll moment and the yaw moment are centred around the lift, drag and side force axes, respectively. All loads are related to the position of the balance system.

The accuracy of the balance system was:

B.2. DETAILS OF THE FORCE BALANCE SYSTEM

Lift	:	0.08%	full scale
Drag	:	0.07%	"
Pitch	:	0.10%	"
Side Force	:	0.10%	"
Yaw	:	0.10%	"
Roll	:	0.08%	"

Figure B.3 shows the force balance structure mounted on top the testing chamber:



Figure B.3: Virtual Axis Six-Component Wind Tunnel Force Balance System with Vacuum Pump for Fluid Removal

B.3. CORRECTION PROCEDURE FOR THE FORCE BALANCE SYSTEM

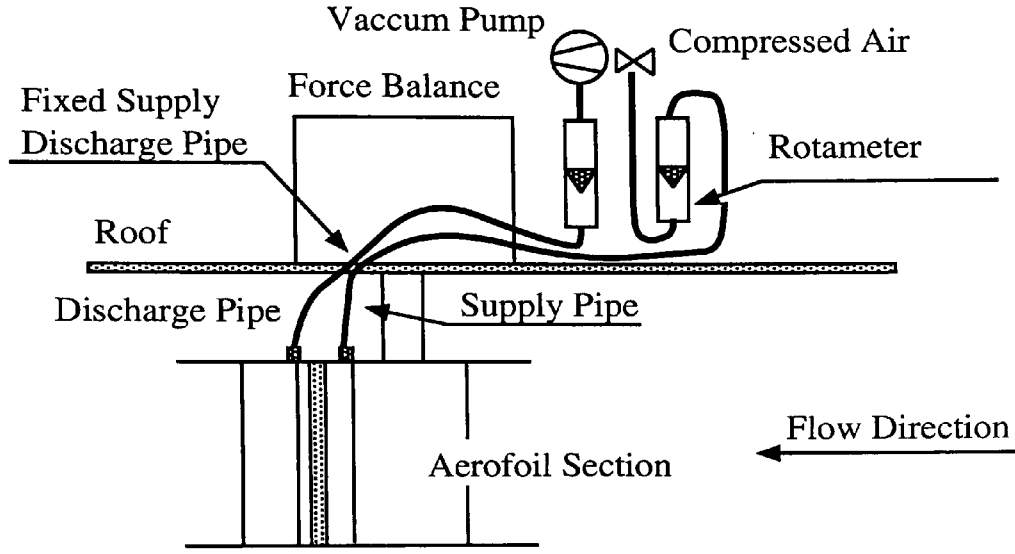


Figure B.4: Experimental Set Up

B.3 Correction Procedure for the Force Balance System

Due to interaction of the forces and moments of the force balance system the following correction procedure was applied to recorded values or 'counts':

- $\text{Lift}_B \text{ (N)} = (\text{Lr} + 0.029 * \text{Yr}) * 0.34256$
- $\text{Drag}_B \text{ (N)} = (\text{Dr} + 0.12 * \text{Yr}) * 0.10418$
- $\text{SideForce}_B \text{ (N)} = (\text{Sr} + 0.029 * \text{Yr}) * 0.15215$
- $\text{Yawing Moment}_B \text{ (Nm)} = (\text{Yr} + 0.13 * \text{Lr} + 0.13 * \text{Dr} - 0.72 * \text{Sr}) * 0.02894$
- $\text{Rolling Moment}_B \text{ (Nm)} = (\text{Rr} + 0.017 * \text{Lr} + 0.08 * \text{Sr}) * 0.04127$

Where Lr , Dr , etc. are zero corrected readings of Lift, Drag etc. taken directly from the digital displays. ' B ' refers to the orientation to the balance system.

The angel of attack, α , affects the steam-wise forces as follows:

- $\text{Drag}_{\text{Aerofoil}} \text{ (N)} = \text{Drag}_B * \cos\alpha + \text{SideForce}_B * \sin\alpha$

$$\bullet \text{ Lift}_{Aerofoil} \text{ (N)} = \text{Lift}_B * \cos\alpha - \text{SideForce}_B * \sin\alpha$$

In the above the correction procedure is based on the notation of the force balance system, whereas $\text{Drag}_{Aerofoil}$ and $\text{Lift}_{Aerofoil}$ are related to the aerofoil forces with respect to the main wind tunnel flow.

B.4 Pressure Transducer CTQH-187

The pressure transducers had the following main specifications:

Rated Pressure	10 psi (\cong 689 mbar)
Operational Mode	Gauge
Full Scale Output	100 mV nominal
Excitation	10 V DC or AC constant voltage
Bridge Independence	2500 Ω

B.4.1 Calibration

The pressure transducers were calibrated with a DruckTM DPI 610 pressure calibrator. Ten different pressures were applied to the transducers within the range of output voltages between +4V and -4V. The obtained calibration functions and the coefficient of correlation are displayed below.

Date	10/12/00
Location	University of Glamorgan
Device	Druck DPI 610 Pressure Calibrator

Results

Probe 1:	V=	0.0008261p	+	0.104758,	r=1
Probe 2:	V=	0.0008466p	-	2.155342,	r=1
Probe 3:	V=	0.0008253p	-	1.904993,	r=1
Probe 4:	V=	0.0008447p	-	1.587543,	r=1
Probe 6:	V=	0.0008226p	-	3.008356,	r=1
Probe 7:	V=	0.0008466p	-	1.337603,	r=1

B.5 A/D-Card

The A/D-card used to acquire the pressure readings had the following specification:

Manufacturer	National Instruments
Board	LAP-PC+

B.6 Pressure Distributions for various Angles of Attack ($Re = 1.02 \times 10^6$)

The following diagrams show the effects of the ABD on the pressure distributions of the NACA 65-415 aerofoil section at $Re = 1.02 \times 10^6$. These data show similar trends as the pressure variations at $Re = 0.68 \times 10^6$. At -8° angle of attack the impact of a secondary flow with a velocity $C_i = 1.5$ on the pressure distribution was relatively small but the flow is disturbed by an non-operational ABD, indicated in the legend of the figures by 'No Flow'. As the angle of attack increases the flow enhancing properties of the ABD becomes more visible and the disturbing influence of the ABD gap for a non-operational ABD is reduced.

Pressure Distributions at $Re = 1.02 \times 10^6$ from -8° to 20° Angle of Attack

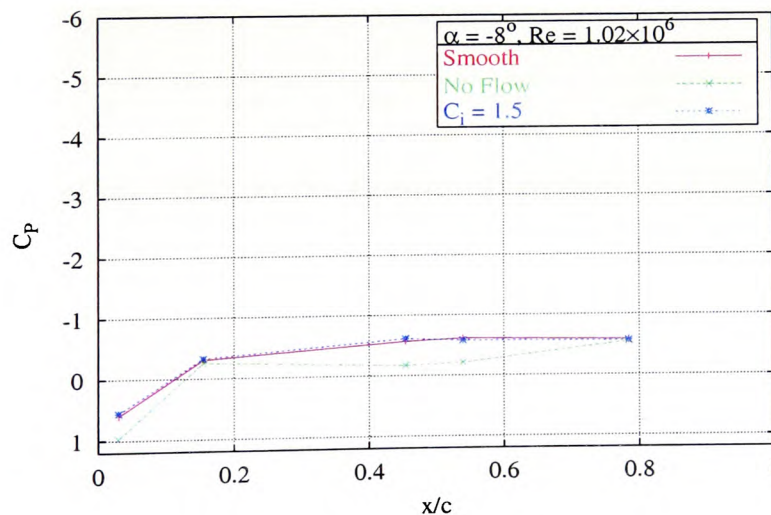


Figure B.5: Effect of the ABD on the Pressure Distribution at -8° Angle of Attack ($Re = 1.02 \times 10^6$)

B.6. PRESSURE DISTRIBUTIONS FOR VARIOUS ANGLES OF ATTACK ($Re = 1.02 \times 10^6$)

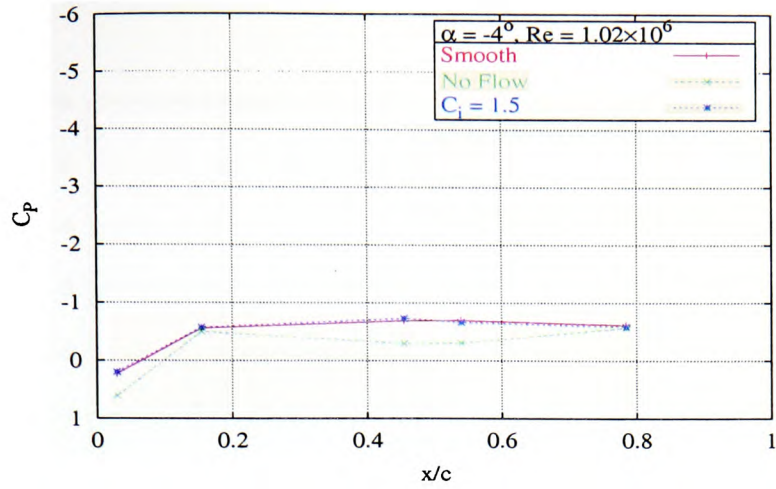


Figure B.6: Effect of the ABD on the Pressure Distribution at -4° Angle of Attack ($Re = 1.02 \times 10^6$)

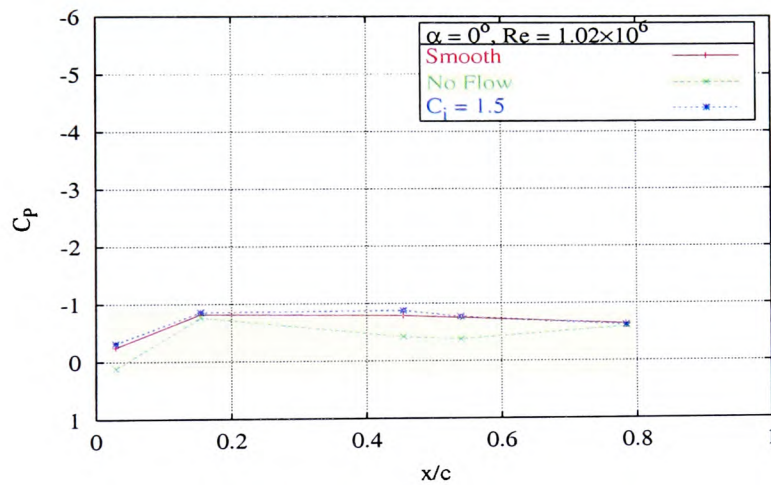


Figure B.7: Effect of the ABD on the Pressure Distribution at 0° Angle of Attack ($Re = 1.02 \times 10^6$)

B.6. PRESSURE DISTRIBUTIONS FOR VARIOUS ANGLES OF ATTACK ($Re = 1.02 \times 10^6$)

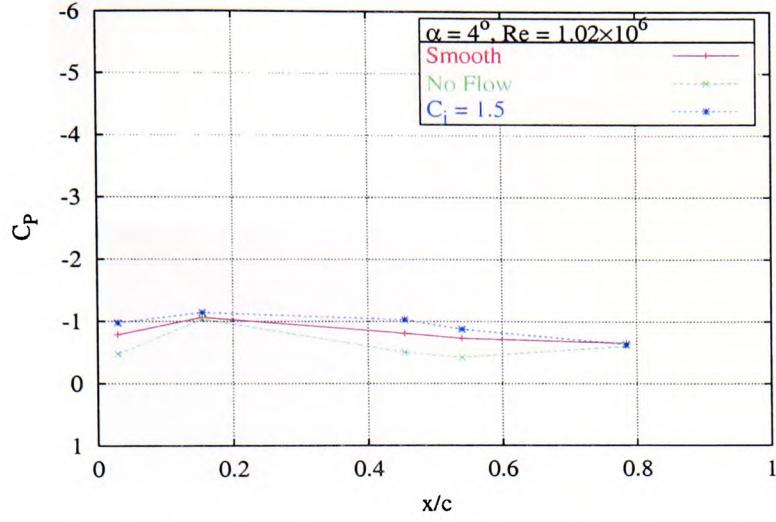


Figure B.8: Effect of the ABD on the Pressure Distribution at 4° Angle of Attack ($Re = 1.02 \times 10^6$)

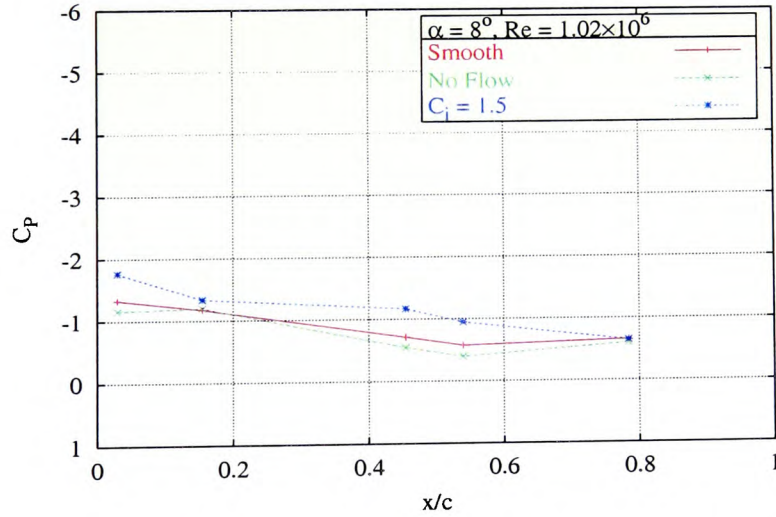


Figure B.9: Effect of the ABD on the Pressure Distribution at 8° Angle of Attack ($Re = 1.02 \times 10^6$)

B.6. PRESSURE DISTRIBUTIONS FOR VARIOUS ANGLES OF ATTACK ($Re = 1.02 \times 10^6$)

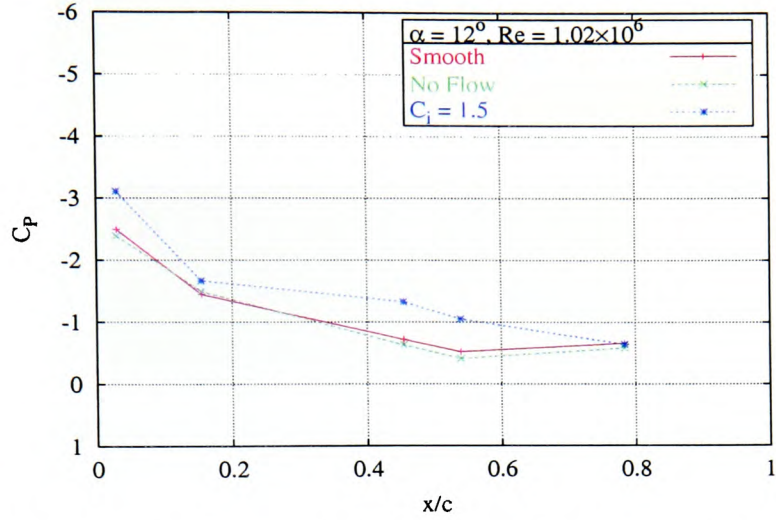


Figure B.10: Effect of the ABD on the Pressure Distribution at 12° Angle of Attack ($Re = 1.02 \times 10^6$)

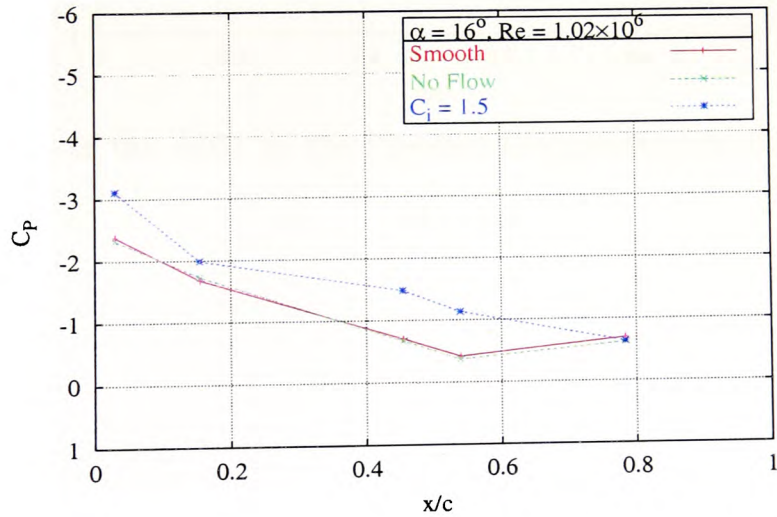


Figure B.11: Effect of the ABD on the Pressure Distribution at 16° Angle of Attack ($Re = 1.02 \times 10^6$)

B.6. PRESSURE DISTRIBUTIONS FOR VARIOUS ANGLES OF ATTACK ($Re = 1.02 \times 10^6$)

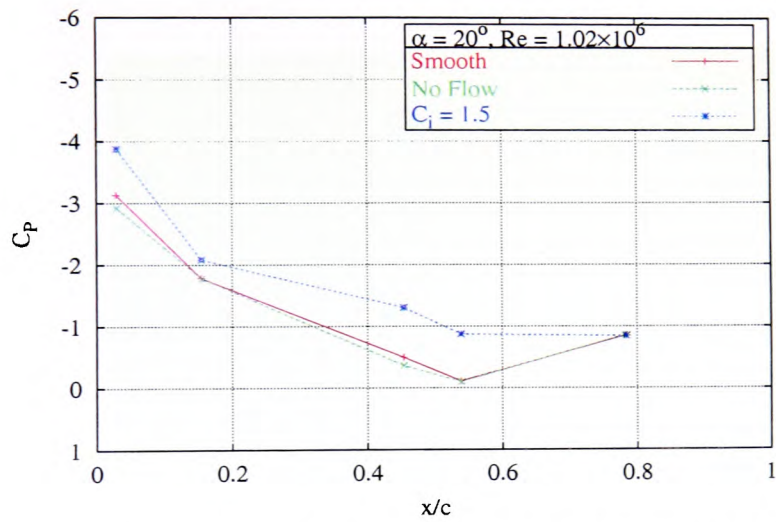


Figure B.12: Effect of the ABD on the Pressure Distribution for 20° Angle of Attack ($Re = 1.02 \times 10^6$)